LASER FREQUENCY COMBS FOR HIGH RESOLUTION SPECTROGRAPH CALIBRATION

Dissertation zur Erlangung des
mathematisch-naturwissenschaftlichen
Doktorgrades
”Doctor rerum naturalium”
der Georg-August-Universität Göttingen
im Promotionsstudiengang Physik
der Georg-August University School of Science
(GAUSS)

vorgelegt von

Michael Debus

aus Lich

Göttingen, 2021

BETREUUNGSAUSSCHUSS

Prof. Dr. Ansgar Reiners, Institut für Astrophysik, Universität Göttingen
Prof. Dr. Claus Ropers, Max-Planck-Institut für Biophysikalische Chemie
Prof. Dr. Philipp Huke, Institut für Laser und Optik, Hochschule Emden/Leer

MITGLIEDER DER PRÜFUNGSKOMMISSION

Referent:
Prof. Dr. Ansgar Reiners, Institut für Astrophysik, Universität Göttingen

Korreferent:
Prof. Dr. Claus Ropers, Max-Planck-Institut für Biophysikalische Chemie

Weitere Mitglieder der Prüfungskommission:
Prof. Dr. Stefan Dreizler, Institut für Astrophysik, Universität Göttingen
Prof. Dr. Philipp Huke, Institut für Laser und Optik, Hochschule Emden/Leer
Prof. Dr. Stefan Mathias, I. Physikalisches Institut, Universität Göttingen
Prof. Dr. Alec Wodtke, Max-Planck-Institut für Biophysikalische Chemie

Tag der mündlichen Prüfung: 9. September 2021

ABSTRACT

While laser frequency combs (LFCs) are in principle ideal calibration light sources for high resolution spectrographs, they are still not regularly used. This is not only due to high cost and maintenance, but also persistent technological challenges. One of these challenges is the high variability and instability of the spectral envelope of the LFCs. This issue is caused by underlying physical effects and the sensitivity of the nonlinear broadening process used to generate the supercontinuum spectrum.

In the context of ELT-HIRES and the Göttingen solar observatory, we aim to improve the calibration of high resolution spectrographs using an LFC. To mitigate the adverse effects of the variability and instability of the spectral envelope we explore three different approaches.

The first is to design a tapered nonlinear fiber which yields a more stable and flat spectral envelope. This is done by creating a grid of simulations for various fiber taper parameters and then judging the quality of the simulated spectra. Results from the simulation are promising and the designed fiber was manufactured. First measurement results of a spectral broadening are still pending.

The second approach is specific to the Fourier transform spectrograph (FTS). We develop a method to calculate the comb frequencies necessary for calibration directly from the interferogram. Thereby, we aim to simplify and improve the calibration process. This method is faster since we do not have to perform a phase correction and subsequently fit the individual comb lines in the spectrum. We show that the method of retrieving the comb frequencies from the interferogram and a calibration is possible. However, the precision is lower than for the conventional method. By calculating simulated interferograms and introducing different types of measurement errors into the simulation, we find that the main reason for reduced precision in this method is the change of the spectral envelope during the measurement. Additionally, phase errors and a dispersion depending on the optical path length difference are causing systematic errors.

Last, we develop, construct and characterize a spectrum control setup to stabilize and manipulate the spectral envelope of the LFC. This is the first demonstration of such a setup in the near infrared. Using this setup, the stability of the resulting spectral envelope is increased and the dynamic range is decreased. In high resolution spectrograph measurements, more comb lines are thus detectable. However, the spectrum control setup causes systematic noise in the FTS measurements. Thus, this approach does not lead to an improvement in calibration precision and further work is necessary to remove this noise from the measurements. For echelle spectrographs this problem does not apply and this setup could therefore be suitable to improve LFC calibration of an astronomical spectrograph in the near infrared.

CONTENTS

LIST OF FIGURES

LIST OF TABLES

ACRONYMS

BIC	Bayesian information criterion
CEO	carrier-envelope-offset
FP	Fabry-Pérot
FTS	Fourier transform spectrograph
FWHM	full width at half-maximum
GDD	group dispersion delay
GNLSE	generalized nonlinear Schrödinger equation
GVD	group velocity dispersion
HCL	hollow cathode lamp
ILS	instrumental line shape
LC	liquid crystal
LCOS	liquid crystal on silicon
LFC	laser frequency comb
MFD	mode field diameter
NA	numerical aperture
OPD	optical pathlength difference
PAN	parallel aligned nematic
PBS	polarizing beam splitter
PCF	photonic crystal fiber
PLL	phase locked loop
RV	radial velocity
SLM	spatial light modulator
SNR	signal-to-noise-ratio
VAN	vertically aligned nematic
VCO	voltage controlled oscillator

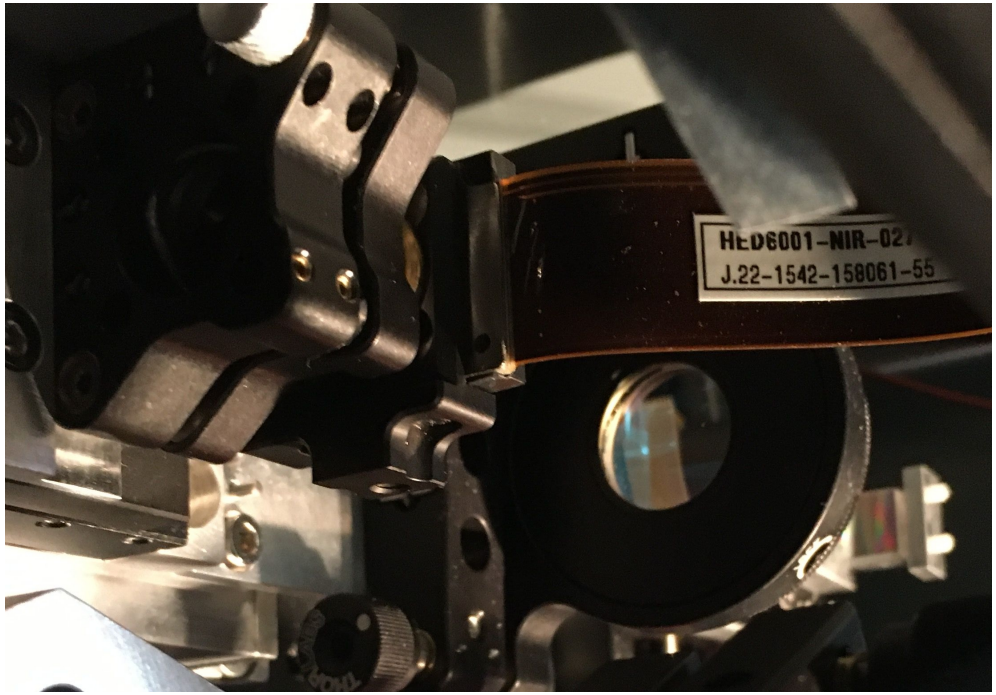
J.22-1542-158061-55

1

INTRODUCTION

One major field in astronomy and astrophysics is the study of exoplanets and exoplanetary systems. This is a fairly young field. The first exoplanet was discovered in 1992 in routine observations of the pulse time of arrival of the pulsar PSR1257 + 12 (Wolszczan and Frail, 1992). The first exoplanet discovered around a main-sequence star was 51 Peg b found in 1995 (Mayor and Queloz, 1995). This was also the first detection in an actual planet search program. Since then, a total of 4777 planets and 3534 planetary systems have been confirmed [1].

Several different methods to find exoplanets exist. The different methods are sensitive to different combinations of stellar type, and planet parameters such as period, radius and mass. Some of these require special conditions and thus only led to few discoveries so far. For example, planets can be found through gravitational microlensing events. These occur when an object moves across our line of sight to a bright background object, e.g., a star or quasar, and the light of the background object is lensed by the mass of the transiting object. If the lensing object is a star accompanied by a planet, the exoplanet can be inferred from the lensing lightcurve (Bond et al., 2004; Beaulieu et al., 2006). For some cases, even the direct motion of stars, caused by the gravitational pull of a planet can be measured (Muterspaugh et al., 2010; Dupuy et al., 2018; Curiel et al., 2020). More planets have been found via direct imaging, which is possible for planets which are comparably large and in comparably wide orbits (Kalas et al., 2008; Marois et al., 2008; Lagrange et al., 2010b). The method which led to by far the most discoveries is transit photometry (Henry et al., 1999; Udalski et al., 2002). If an exoplanet moves in between its host star and our line of sight a slight darkening is observed in the light curve. If such an event occurs at periodic intervals it is likely caused by a planet. The Kepler mission alone has led to more than 2600 discovered exoplanets (Borucki et al., 2010). From timing variations in the occurrence of transits further planets can be inferred (Ballard et al., 2011).

1 www.exoplanet.eu, 1. July 2021

The other main method is the radial velocity (RV) method which was used by Mayor and Queloz in their seminal discovery of 51 Peg b. For this discovery they were awarded half a Nobel prize in 2019. While conceptually more complex than transit photometry or direct imaging, the basic principle behind the technique is straightforward. If a planet orbits a star, they orbit the common center of gravity. Thus, the planet induces a slight reflex motion of the star. The component of this motion along our line of sight causes a Doppler shift of the wavelengths in the observed optical spectrum of the star. Using spectral features, such as atomic absorption lines, the motion of the star can be measured with high resolution spectrographs (see Fig. 1.1). If a periodic variation is discovered in these measurements, a Keplerian orbit solution can be fitted to the data and an upper mass limit of the planet can be inferred. To determine the exact mass, the angle of inclination of the planets orbit i has to be known, as the velocity component towards the observer scales with $\sin(i)$. The method is also highly complimentary with transit photometry. If it is possible to measure a transit and the RV amplitude, the exact mass, the radius and thus also the planets density can be obtained.

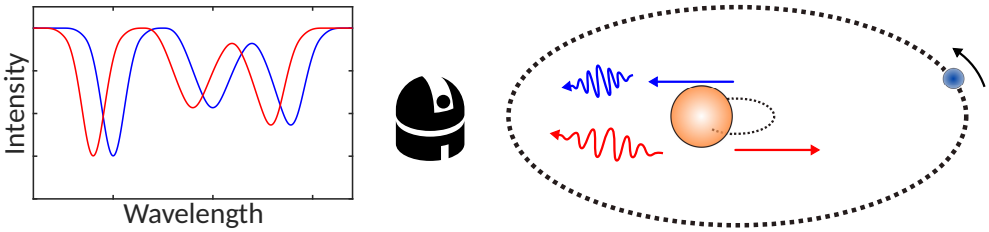

Figure 1.1: Schematic star planet system with an exaggerated Doppler shift in the spectrum observed from the star.

The RV technique has been used to identify binary systems of stars for more than a century. The first observation of such a spectroscopic binary was done by Hermann Carl Vogel as early as 1889 (Aitken, 1898). In these systems, the RV amplitude can reach magnitudes of up to hundreds of km s^{-1}. For planets, however, the expected RV amplitudes are much lower. The RV amplitude depends on the movement of the star around the common center of gravity and a larger mass companion shifts the common center of gravity further away from the star. For example, the highest RV amplitude in our solar system is caused by Jupiter, with a magnitude of about 12.4 m s^{-1}. Thus, a much higher measurement precision is required to detect exoplanets than stellar binaries. The early surveys for exoplanets towards the end of the 20th century were

expecting Jupiter analogs, i.e., planets with radial velocity amplitudes of 10 to 20 m s^{-1} and periods of multiple years for sun-like stars (Walker, 2012; Hatzes, 2016). These endeavors managed to reach sufficient measurement precision and even led to some suspicious signals, which were much later confirmed to be due to planets (Campbell et al., 1988; Hatzes and Cochran, 1993; Walker et al., 1995; Hatzes et al., 2003, 2006). Mayor and Queloz, however, discovered a very different type of planet which was not expected to exist by the community: A planet with about half the mass of Jupiter and a period of only 4.2 days, which is much easier to detect than a true Jupiter analogue.

The detection of 51 Peg b increased interest in the search for exoplanets and sparked a desire for more precise and more stable high resolution spectrographs. With today's high resolution spectrographs, even the characterization of exoplanet atmospheres becomes possible (Redfield et al., 2008; Snellen et al., 2010; Brogi and Line, 2019). With the next generation of extremely large telescopes and the planned high resolution spectrographs such as ELT-HIRES, the search for signatures of habitability or possibly even life becomes feasible (Marconi et al., 2020; Snellen et al., 2015; Hawker and Parry, 2019).

These measurements and discoveries are only possible because of the constant improvement of instruments for measuring precise RVs and high resolution spectra. To reach the highest level of precision, the calibration of the spectrographs is crucial. For calibration standard light sources or absorbing media are used. These are measured in parallel or in sequence with the stellar light. The calibrator must have well known, reproducible spectral features, which then allow to discern the Doppler shift from the instrument drift.

The present work is concerned with improving calibration of high resolution spectrographs using one particular calibration light source, the laser frequency comb (LFC).

1.1 Evolution of calibration of astronomical spectrographs

There are many different techniques for calibrating high resolution spectrographs, but all of them require a reference. In the following, we list the properties that an ideal calibration light source or absorber should have (Kerber et al., 2007; Fischer et al., 2016):

- The wavelength and lineshape of the calibration lines should be stable.
- The calibration lines should cover the whole spectral range the spectrograph is capable of observing.

- The calibration lines should have a dense, equal spacing, which can be adapted to the respective instrument.
- All calibration lines should have an equal strength. Even better, the calibration spectrum should be designable to account for the wavelength dependent efficiency of the spectrograph.
- The calibration lines should be known accurately. Since RV is a relative measurement this is not strictly necessary. However, a high accuracy makes measurements across different epochs and instruments more easily comparable. Additionally, science cases not strictly related to RV measurements may require a high accuracy.
- The calibration lines should not be resolved by the spectrograph. Then the calibration lines provide a measurement of the instrumental line shape. This information can be used to improve the calibration (Cornachione et al., 2019; Pepe et al., 2021).

While, thus far, no perfect calibrator has been devised, the improvement in calibration techniques throughout the last half century has been remarkable. We now give an overview of the evolution of different calibration techniques for high resolution spectrographs in the context of exoplanets.

1.1.1 Early calibration techniques

The first calibration light sources for high resolution spectrographs were arc lamps or hollow cathode lamps (HCLs) (see e.g. Sanford (1933) and Hewitt et al. (1968)). These produce a spectrum consisting of many sharp emission lines, defined by atomic transitions of the arc material (in the case of arc lamps) or cathode material and the filling gas in the case of HCLs. The lamps were used to illuminate parts of the entrance slit of the spectrograph not illuminated by stellar light. Regardless of the light source, early calibration techniques all suffered from similar drawbacks. Most importantly, the path of the calibration light was different from that of the stellar light, which limited the precision of the calibration (Griffin, 1973). Additionally, the exposures were often taken before or after the observation and not in parallel. The environment of the instruments was only weakly stabilized, if at all. Thus, the instrument could drift between the observation and calibration exposure. With these methods stabilities of a few 100 m s^{-1} could be reached. While HCLs are still in use today, the calibration techniques have since then evolved.

1.1.2 Telluric absorption lines

The first major improvement in spectrograph calibration was the calibration with telluric absorption lines introduced by Griffin in 1973. These lines are imprinted on the stellar spectrum during the passage of the light through earth's atmosphere. Therefore, this technique can be used in any ground-based observatory. The improvement is that the calibration lines follow the exact same light path as the stellar light and therefore do not suffer from any geometrical differences in the light path (Griffin, 1973; Osterbrock et al., 1996). Making use of telluric lines allowed an improvement in the RV precision from hundreds of $\mathrm{m\,s^{-1}}$ down to tens of $\mathrm{m\,s^{-1}}$.

However, the telluric lines depend on the altitude of the target at the time of the observation as well as the atmospheric conditions in the line of sight. Changes in pressure or local wind conditions can cause changes to the telluric absorption lines (Campbell and Walker, 1979). This can be mitigated to some extent by observing an RV standard star, i.e., a star with no RV variability, for a nightly zero point correction (Marcy and Benitz, 1989). Yet, this ultimately limits the achievable precision of this technique. Furthermore, the spectral coverage and thus the calibration is limited to regions where this absorption occurs.

1.1.3 Gas cells

Another major improvement of the calibration for precision RV measurements was the usage of gas cells introduced by Campbell and Walker in 1979. The gas cell is placed in the beam of stellar light coming from the telescope. Similar to the telluric lines, the absorption spectrum of the gas is then imprinted on the stellar spectrum. The absorption lines from the gas cell are more stable and less broad than telluric lines, since there are no winds or strong pressure gradients in the gas cell.

The first gas being used was hydrogen fluoride. It has well spaced molecular absorption features in the visible, without any additional weak lines in between. However, hydrogen fluoride is a dangerous gas which can cause blindness or death. Moreover, it requires inert materials for containment due to its corrosive nature and therefore has to be handled with care (Campbell and Walker, 1979).

Because of these issues, hydrogen fluoride cells were abandoned and iodine cells became the standard in the early nineties (Marcy and Butler, 1992). Iodine

is not toxic, easier to handle and has more usable lines for calibration. The iodine absorption lines have a another advantage. Since they are not resolved by the spectrograph, they can be used to model drifts of the instrumental line shape (ILS) during an exposure (Valenti et al., 1995; Butler et al., 1996). Thus, an additional error source can be corrected. They offer excellent long term stability of the line centers with single cells sometimes operating for more than a decade, e.g., at the 2.1 m telescope at McDonald Observatory (Hatzes et al., 2006). In older surveys, a precision of 10 to 15 m s^{-1} was achieved. Iodine cell measurements can still give very relevant data today, e.g., from the UVES spectrograph at VLT, where a reanalysis of older measurements resulted in precisions better than 4 m s^{-1} (Butler et al., 2019).

However, they also suffer some significant drawbacks. As the iodine cells absorb a part of the stellar light, the throughput is reduced. Therefore, observations using gas cells are limited to brighter stars. Also, the iodine lines blend with the stellar lines, which prevents a modeling of stellar activity (Fischer et al., 2016). Since stellar activity also causes RV signals, the modeling is essential to prevent false detections and to detect planets masked by stellar activity (Queloz et al., 2001). Additionally, the absorption spectrum of iodine only covers a fairly small wavelength range in the visible of 510 to 620 nm and does not extend into the near infrared. Despite some of their shortcomings gas cells are still actively used in some observatories, e.g., UVES at the VLT. Even new gas cells containing a mixture of the gases acethylene, ammonia and methane were developed to cover the H- and K-bands in the infrared for the upgrade of the spectrograph CRIRES (CRIRES+) (Seemann et al., 2014).

1.1.4 Simultaneous fiber calibration

Using a fiber instead of a slit was first tested in 1979 (Hubbard et al., 1979), but it took time for this technology to be developed. With the ELODIE spectrograph at the Observatoire de Haute-Provence the method of simultaneous fiber calibration was established in the early nineties. The spectrograph is fed with light from two fibers, where one fiber is injected with stellar light, while light from a Thorium-Argon HCL is simultaneously injected into the second fiber (Baranne et al., 1996). A more detailed review on HCLs is given by Kerber et al. (2007). While the calibration light source is not new, the method of using two optical fibers in parallel eliminates major issues. The geometrical properties of the light exiting the fiber are similar to the stellar light and thus

do not suffer different aberrations in the spectrograph. Additionally, the design enables easy simultaneous calibration. Subsequently, this design was used for other spectrographs such as FEROS (Stahl et al., 1999) or HARPS. The HARPS spectrograph, the first instrument wholly dedicated to exoplanet detection, set a new standard for RV measurements (Pepe et al., 2002; Mayor et al., 2003). It achieved new levels of stability, due to a temperature and pressure controlled vessel for the spectrograph. With this instrument the calibration precision using HCLs was pushed to the limit, reaching RV precisions of 20 cm s^{-1} (Lovis and Pepe, 2007).

Besides Thorium-Argon HCLs, other types also exist, such as Uranium-Argon or Uranium-Neon, which cover different spectral bands to a different degree. Particularly Uranium-Neon is more suitable for instruments operating in the infrared such as CARMENES or CRIRES+ (Quirrenbach et al., 2012, 2016; Sarmiento et al., 2014; Seemann et al., 2014).

HCLs also have some properties which are undesirable for a calibration light source. First of all, the lines are not equally distributed, leading to only a few or no calibration lines in some spectral orders. Secondly, the lines have strong variations in intensity, so that some of the strong gas lines saturate the spectrograph detector and even lead to unwanted blooming effects, while others are barely detected. Additionally, some of the lines become weaker as the lamp ages, which induces calibration errors. To make datasets from different epochs comparable, a cross calibration with a master lamp is required. Furthermore, new regulations caused manufacturers to use metaloxids instead of metals in the production of HCLs, which can lead to a contamination of the lamp spectra with additional lines (Nave et al., 2018).

1.1.5 Fabry–Pérot etalons

Another calibration method uses Fabry-Pérot etalons or Fabry-Pérots (FPs) for short. For applications in astronomy, FPs with two semitransparent coplanar mirrors with a well defined spacing are used. This spacing defines an interference condition, so that only light of wavelengths fulfilling this condition passes the FP. The FP is illuminated by a white light source, e.g., a halogen lamp. When choosing the distance between the mirrors correctly, this yields a spectrum which has a dense coverage of spectral lines in each order. The spectrum is uniform in intensity and has a broad spectral coverage if an adequate white light source is chosen. Usually, FPs are used in dual fiber spectrographs. The

dense coverage of the FP spectrum enables a measurement of pixel position and size inhomogenities on the detector as well as discontinuities caused by the manufacturing process (Bauer et al., 2015).

While the use of white light illuminated FPs for calibration is not a new invention (see e.g. Connes et al. (1996)), the first high precision RV measurements were reported in 2011 from measurements with HARPS (Wildi et al., 2011). FPs are routinely employed in the latest generation of spectrographs, e.g., CARMENES and ESPRESSO. In these spectrographs, internal precisions of 10 cm s^{-1} can be reached (Schäfer and Reiners, 2012; Schäfer et al., 2018; Pepe et al., 2021).

The drawback of FPs is that even with a great degree of passive stabilization of the mirror spacing, the line positions can drift over time. Furthermore, the exact wavelength of the calibration lines is not known. Therefore, FPs only give a relative calibration, but do not provide an absolute reference. Thus, they are used in combination with HCLs. The absolute wavelength reference is provided by the HCL and the FP is then used for simultaneous calibration during the observations to correct the drift of the instrument. Other proposed schemes include monitoring or controlling the FP drift using a Rubidium referenced laser locked to an FP-mode (Reiners et al., 2014; Schwab et al., 2015). The method of monitoring the FP drift is being used at the MAROON-X spectrograph (Stürmer et al., 2017).

1.1.6 Laser frequency combs

A calibration light source which has many of the properties of an ideal calibration light source described above is the LFC. LFCs were first proposed as a calibration light source for astronomical spectrographs a little over 10 years ago (Murphy et al., 2007; Schmidt et al., 2007; Li et al., 2008). They emitt a broad spectrum of narrow emission lines whose position can be controlled with high accuracy and precision. Contrary to the FP they can give a full wavelength solution on their own, since the line positions are well defined. Also, the comb lines have line widths on the order of 100 kHz or less, so that they are not resolved and can be used for ILS modeling. They are also used in the standard dual fiber configuration.

First observations with high resolution spectrographs using an LFC for calibration were done at VTT (Doerr et al., 2012), Pathfinder (Ycas et al., 2012), HARPS (Probst et al., 2014, 2016), HARPS-N (Phillips et al., 2012; Glenday et

al., 2015) and HRS (McCracken et al., 2017b). LFCs are foreseen as the main calibration light source for the next generation high resolution spectrograph ELT-HIRES (Huke et al., 2017). One of the science cases of the HIRES spectrograph is the Sandage test (Marconi et al., 2020), which is a measurement of the expansion of the universe (Sandage, 1962). This science case requires a large telescope and accurate RV measurements of distant quasars on a 2 cm s^{-1} scale for at least two decades. Such a feat can likely only be accomplished using LFCs (Liske et al., 2008). An overview over the development of ”astrocombs”, i.e., LFCs optimized for calibration of high resolution spectrographs, is given by McCracken et al. (2017a).

Despite a development effort of more than a decade, they are not routinely used at the newest instruments such as ESPRESSO due to continuous technological challenges (Pepe et al., 2021). Issues which remain include reliability, insufficient spectral coverage and variable background light (Pepe et al., 2021; Schmidt et al., 2021). Additionally, the comb lines are usually spaced so closely that they could not be resolved by the spectrographs. Thus, a large number of lines has to be filtered using FPs. Insufficient suppression of side modes can then lead to RV errors. They are also by far the most expensive calibration light source.

1.2 Scope of this work

The present thesis is part of a larger project with the aim of devising a calibration unit for the spectrograph ELT-HIRES, a second-generation instrument at the ELT. We aim to improve the calibration of both echelle spectrographs and a Fourier transform spectrograph (FTS) using an LFC.

While FTSs currently are hardly used in astronomical observations, they have been used successfully in astronomy in the 1960s and 1970s (Connes and Connes, 1966; Beer et al., 1971; Connes and Michel, 1975). Since the advent of the CCD, grating spectrographs greatly outperform FTSs in terms of efficiency. Thus, there was no real use case for an FTS in the photon-starved field of astronomy anymore. For solar observations however, where the amount of photons is not an issue, a commercial FTS can outperform even ESPRESSO by a factor of ten in resolution, while simultaneously covering a broad wavelength range from the visible to the near-infrared. In Göttingen an FTS is used to perform observations both of the integrated and the resolved Sun (Reiners et al., 2016a,b; Schäfer et al., 2020b).

While counterintuitive at first, solar observations have come to play an important role in the field of exoplanets. Observing the Sun as a star is a natural testbed to improve models for stellar activity phenomena, which are now often a limiting factor for the detection of exoplanets (Meunier et al., 2010; Lagrange et al., 2010a). The Sun is the only main-sequence star which can be spatially resolved in the optical regime. This enables matching what happens on the stellar surface to RV signals and other spectroscopic measurements and thus reveals which proxy measurements can be used to remove the stellar RV jitter from measurements (Haywood et al., 2016). Some astronomical echelle spectrographs are now used to observe the Sun during the daytime such as HARPS-N or PEPSI (Dumusque et al., 2015; Strassmeier et al., 2018).

While LFCs are the optimal calibration light source for high resolution spectrographs on paper, some issues still remain. In the case of echelle spectrographs, the mode filtering can be problematic. For the calibration of an FTS, this is not an issue (Huke et al., 2019b). Because of its extremely high resolution, the FTS is able to resolve comb modes with a spacing of 1 GHz. This is a large advantage since it eliminates the need to filter the comb lines and thus errors caused by suppressed side modes are eliminated.

There are, however, other issues when using an LFC with an FTS. Due to the multiple interference fringes present in the interferogram (Huke et al., 2019a), the phase correction requires additional steps.

For the FTS as well as echelle spectrographs, there are problems related to the spectral envelope. For fiber-laser based LFCs a full spectral coverage is an issue. For Ti:Sapphire based LFCs the high dynamic range in the output spectrum can be problematic.

In both cases, the temporal variability of the spectral envelope is detrimental to the calibration precision. Calibration measurements of the LFC with the FTS show a large amount of systematic structure in the residuals of the line fit position (see Fig. 1.2). These patterns follow the intensity modulation of the spectrum. However, sometimes they are correlated and sometimes anti-correlated. The underlying cause seems to be intensity modulations in the spectral envelope of the LFC during the measurement. Due to the multiplex type of measurement in the FTS, light source intensity variations cause noise in all spectral channels. Typically, the spectral envelope of an LFC is not stable

in time due to the sensitivity of the nonlinear broadening process used to generate the broadband spectrum of the LFC.

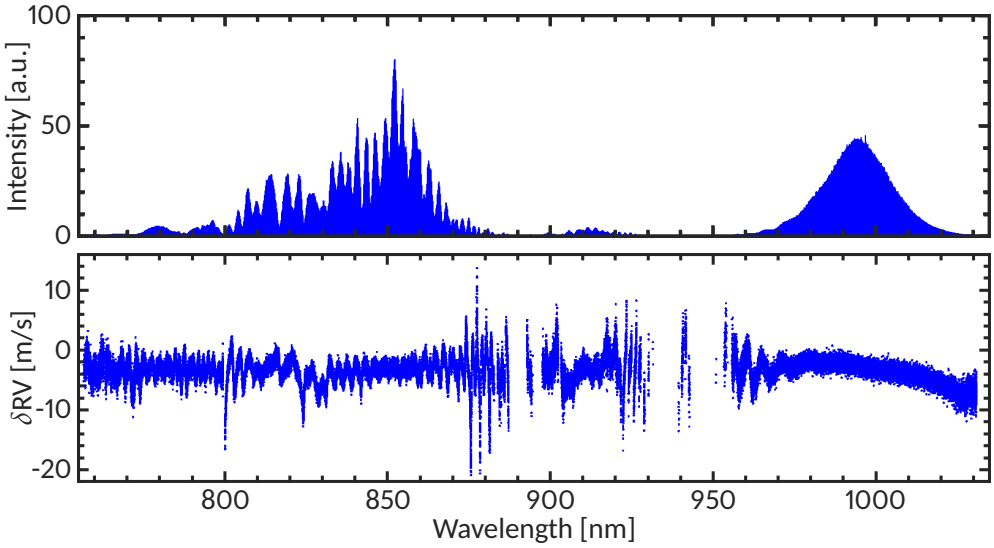

Figure 1.2: Top panel: The measured spectral envelope of an LFC. Bottom panel: The corresponding line center fit devation in terms of radial velocities (adapted from Huke et al. (2019b))

In the present work, some strategies for mitigating these adverse effects to the calibration are investigated. At the heart of our setup and considerations is a Ti:Sapphire laser frequency comb. A schematic overview of the overall setup is given in Fig. 1.3.

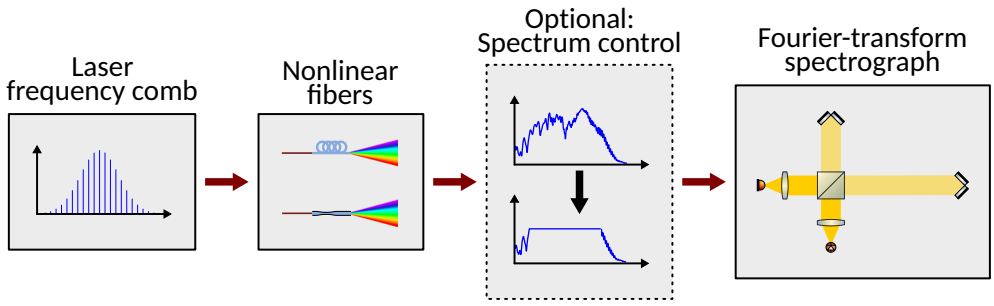

Figure 1.3: A schematic overview of the overall setup in this thesis.

We first investigate the possibility of affecting the nonlinear broadening process of the comb to generate a more stable supercontinuum. For this, we design a tapering geometry for a nonlinear fiber for our specific setup using a grid of simulations. We devised a scheme to evaluate the simulations and find the best possible fiber geometry for our setup.

Second, we are concerned with the interaction between the LFC and the FTS. Due to the pulsed, coherent nature of the comb light, much can be learned

from the interferogram, i.e., the raw measurement, rather than the spectrum. We investigate whether it is possible to calibrate the FTS without considering the spectrum of the LFC. For this, we devise a method to retrieve the position of the comb lines or rather the repetition rate and offset frequency directly from the interferogram. Since the values retrieved from the interferogram differ from those measured in the spectrum, we attempt to identify possible error sources using simulated interferograms.

Last, we design a Fourier transform optical pulse shaping setup, enabling a control of the spectral envelope of the LFC. While similar setups exist for the visible wavelength ranges, this is the first demonstration of such setup for the near infrared (Probst et al., 2013, 2015, 2020; McCracken et al., 2017a). We give an in-depth overview of the design-considerations, alignment and calibration procedures and characterize the setup. Furthermore, we measure the spectrally controlled LFC with an FTS and describe some of the pitfalls of such a spectrum control setup for FTS measurements.

1.3 Outline

This work consists of two parts. Part one is a description of the current LFC and FTS setup. Part two is concerned with improving the calibration of the FTS using the LFC.

Chapter 2 describes the setup of the LFC we use and gives some general background on LFCs and the stabilization of the comb lines.

Chapter 3 gives some background on FTSs, how they may be calibrated and a description of the setup of our FTS.

In part two, Chapter 4 explores the possibility of designing a nonlinear fiber and thereby the resulting supercontinuum spectrum of the LFC with the goal of achieving a broad and stable spectrum.

Chapter 5 is concerned with a new method of calibrating an FTS using an LFC by calculating the calibration factors directly from the measured interferogram, rather than the optical spectrum.

Chapter 6 deals with the development and characterization of a Fourier transform optical pulse shaping setup for the near infrared. This setup enables a control of the spectral envelope of the LFC.

Chapter 7 summarizes the results and provides conclusions from the present work.

Part I

IAG SETUP FOR HIGH RESOLUTION SPECTROSCOPY

2

LASER FREQUENCY COMB

Laser frequency combs (LFCs) are very versatile tools used in multiple disciplines in physics, e.g., metrology, molecular spectroscopy or astrophysics (Diddams, 2010; Picqué and Hänsch, 2019). They are lasers, with a spectrum consisting of many narrow emission lines resembling a comb. The line positions can be controlled with high precision and accuracy. The line spacing can range from tens of MHz to tens of GHz. Furthermore, frequency comb lines can cover a large spectral range of a few hundred THz. Frequency combs spanning up to six octaves (13.3 to 856.5 THz) are possible (Lesko et al., 2021).

The first theoretical description and initial demonstration of an optical laser comb was published in 1978 (Eckstein et al., 1978; Eckstein, 1978). However, there was one thing preventing a successful use of the comb. The position of the lines could not be stabilized easily. There are two main technological advances which enabled today's LFCs. The first one was the Kerr-lens mode locking of the Ti:sapphire laser, which allows generating high energy ultra short pulses (Spence et al., 1991). The shorter the pulse, the broader the resulting optical spectrum. But even with Ti:sapphire lasers initially only a few tens of THz could be reached. The invention of photonic crystal fiber which nonlinearly broadens the optical spectrum to more than a full octave was the final missing piece for the LFC (Ranka et al., 2000; Hänsch, 2006). This enabled the f-2f self-referencing technique, which enabled full control of the comb line positions (Diddams et al., 2000; Jones et al., 2000). Thus, the LFCs could be stabilized to any given radio frequency reference, e.g., a caesium atomic clock. The first demonstrations of what is now called an LFC, a highly stable and accurate frequency ruler, was published around the millenium (Reichert et al., 1999; Diddams et al., 2000; Jones et al., 2000; Holzwarth et al., 2000). This led to a Nobel Prize for John L. Hall and Theodor W. Hänsch in 2005. The press release succinctly describes the importance of this discovery:

"The important contributions by John Hall and Theodor Hänsch have made it possible to measure frequencies with an accuracy of fifteen digits. Lasers with extremely sharp colours can now be constructed and with the frequency

comb technique precise readings can be made of light of all colours. This technique makes it possible to carry out studies of, for example, the stability of the constants of nature over time and to develop extremely accurate clocks and improved GPS technology." – Nobel Prize press release (The Royal Swedish Academy of Sciences, 2005)

Before LFCs were developed, optical spectroscopy of arbitrary frequencies was restricted to large facilities like NIST where frequency chains could be maintained (Hall, 2006; Hänsch, 2006). These frequency chains translated the frequency standard from a caesium clock at 9.2 MHz to the optical regime by forming a ladder of stabilized masers and lasers. With the advent of the LFC, this can be done in a single step giving these capabilities to many small university labs around the world. The high precision and accuracy, coupled with a very broadband spectrum, enables heterodyning measurements at arbitrary frequencies without complicated changes to the setup. Due to the high accuracy of LFCs, it is expected that optical atomic transitions will be used for the definition of the SI-second in the future. Recently, a decade old record in frequency accuracy was broken using LFCs (Beloy et al., 2021). Since metrology is the field for which LFCs were originally developed, it is no surprise that they also arguably had the largest impact in this field.

This chapter describes some of the theoretical background of LFCs as well as the LFC setup we use. Additionally, the frequency stability of the setup is characterized in the context of the calibration of astronomical spectrographs.

2.1 **Comb generation**

The most important property of an LFC, its comb-like spectrum can be understood using Fourier analysis, as laid out in the standard work ‘’Lasers” by Siegman (1986). A frequency comb can be generated from a pulsed laser, if one important requirement is met: The pulse envelope must remain unchanged over many pulse cycles. This requirement can be fulfilled in passively modelocked lasers. This can be understood as all modes allowed by the laser cavity—which are spaced regularly in frequency—being locked in phase. This overlap of many harmonic, sinussoidal modes oscillating in phase is then actually what gives rise to the formation of a pulse in the first place.

In the following, we will derive the comb spectrum from the viewpoint of a pulse with a fixed carrier frequency exciting the laser cavity. We extend the ansatz made by Siegman (1986, p. 1044) in order to include the offset

frequency and arrive at the comb equation. Let $E(t)$ be the electrical field of a single optical pulse generated by a laser as a function of time. We can describe it in terms of a carrier wave with frequency f_c and a slowly varying envelope function $A(t)$

$$E(t) = A(t)e^{-i2\pi f_c t}. \tag{2.1}$$

If we want to describe the pulse train of the laser, we do so by multiplying the carrier wave with repetitions of the pulse envelope function $A(t)$ spaced in time by the laser cavity roundtrip time T

$$E^{(N)}(t) = e^{-i2\pi f_c t} \sum_{n=0}^{N-1} A(t - nT). \tag{2.2}$$

To calculate the Fourier transform of the pulse train, we make use of the convolution theorem and calculate the Fourier transform of each factor in Eq. 2.2 separately.

$$\mathcal{F}(e^{-i2\pi f_c t}) = \delta(\omega - 2\pi f_c) \tag{2.3}$$

$$\mathcal{F}(\sum_{n=0}^{N-1} A(t - nT)) = \sum_{n=0}^{N-1} \widetilde{A}(\omega)e^{-inT\omega}, \tag{2.4}$$

where $\widetilde{A}(\omega)$ is the Fourier transform of the envelope function $A(t)$. Using the convolution theorem the Fourier transform of $E^{(N)}(t)$ is then:

$$\widetilde{E}(\omega) = \mathcal{F}(E^{(N)}(t)) \tag{2.5}$$

$$= \mathcal{F}(e^{-i2\pi f_c t}) * \mathcal{F}(\sum_{n=0}^{N-1} A(t - nT)) \tag{2.6}$$

$$= \delta(\omega - 2\pi f_c) * \sum_{n=0}^{N-1} \widetilde{A}(\omega)e^{-inT\omega}. \tag{2.7}$$

Carrying out the convolution integral is simple due to the properties of the Dirac-function:

$$\widetilde{E}(\omega) = \sum_{n=0}^{N-1} \widetilde{A}(\omega - 2\pi f_c)e^{-inT(\omega - 2\pi f_c)} \tag{2.8}$$

$$= \widetilde{A}(\omega - 2\pi f_c) \sum_{n=0}^{N-1} e^{-inT(\omega - 2\pi f_c)}. \tag{2.9}$$

The carrier frequency f_c can be rewritten in terms of the offset frequency f_{CEO} and the repetition rate f_{rep}:

$$f_c = f_{\text{CEO}} + k_c f_{\text{rep}}, \tag{2.10}$$

where k_c is an integer number and f_{rep} is the inverse of the cavity roundtrip time T. The definition of f_c is motivated by the empirical finding that the comb lines are usually not at frequencies which are integer multiples of the repetition rate, as one would naively expect. Instead, they all share a common offset f_{CEO}. Plugging Eq. 2.10 into Eq. 2.9 and simplifying then leads to

$$\widetilde{E}(\omega) = \widetilde{A}(\omega - 2\pi f_c) \sum_{n=0}^{N-1} e^{-inf_{\text{rep}}^{-1}(\omega - 2\pi(f_{\text{CEO}} + k_c f_{\text{rep}}))} \tag{2.11}$$

$$= \widetilde{A}(\omega - 2\pi f_c) \sum_{n=0}^{N-1} e^{-inf_{\text{rep}}^{-1}(\omega - 2\pi f_{\text{CEO}})} e^{i2\pi n f_{\text{rep}}^{-1} k_c f_{\text{rep}}} \tag{2.12}$$

$$= \widetilde{A}(\omega - 2\pi f_c) \sum_{n=0}^{N-1} e^{-inf_{\text{rep}}^{-1}(\omega - 2\pi f_{\text{CEO}})} \underbrace{e^{i2\pi n k_c}}_{=1}. \tag{2.13}$$

As n and k are integers, the last term will always be one and can be omitted. Using the partial sum of the geometric series, this can be further simplified to

$$\widetilde{E}(\omega) = \widetilde{A}(\omega - 2\pi f_c) \frac{1 - e^{-iNf_{\text{rep}}^{-1}(\omega - 2\pi f_{\text{CEO}})}}{1 - e^{-if_{\text{rep}}^{-1}(\omega - 2\pi f_{\text{CEO}})}}. \tag{2.14}$$

Rewriting this in terms of ordinary frequency leads to

$$\widetilde{E}(f) = \widetilde{A}(2\pi(f - f_c)) \frac{1 - e^{-i2\pi N \frac{f - f_{\text{CEO}}}{f_{\text{rep}}}}}{1 - e^{-i2\pi \frac{f - f_{\text{CEO}}}{f_{\text{rep}}}}}. \tag{2.15}$$

The spectral intensity is then given by

$$I(f)^{(N)} \equiv \left|\widetilde{E}(f)\right|^2 \tag{2.16}$$

$$= I(2\pi(f - f_c)) \frac{1 - \cos(2\pi N \frac{f - f_{\text{CEO}}}{f_{\text{rep}}})}{1 - \cos(2\pi \frac{f - f_{\text{CEO}}}{f_{\text{rep}}})}. \tag{2.17}$$

The first term of Eq. 2.17 is the spectral envelope, centered around the carrier frequency f_c. The second term is a comb of lines with a spacing of $f_{\text{rep}} = T^{-1}$, with the lines becoming narrower with increasing N, approaching a Dirac-comb for N going to infinity. The comb is offset from an integer multiple of f_{rep} by the offset frequency f_{CEO}.

This leads to the comb equation, describing the frequencies f_k of allowed comb modes:

$$f_k = f_{\text{CEO}} + k f_{\text{rep}}. \tag{2.18}$$

with an integer k. The physical meaning of the offset frequency is illustrated in Fig. 2.1. The pulse envelope repetition period is much longer than the period

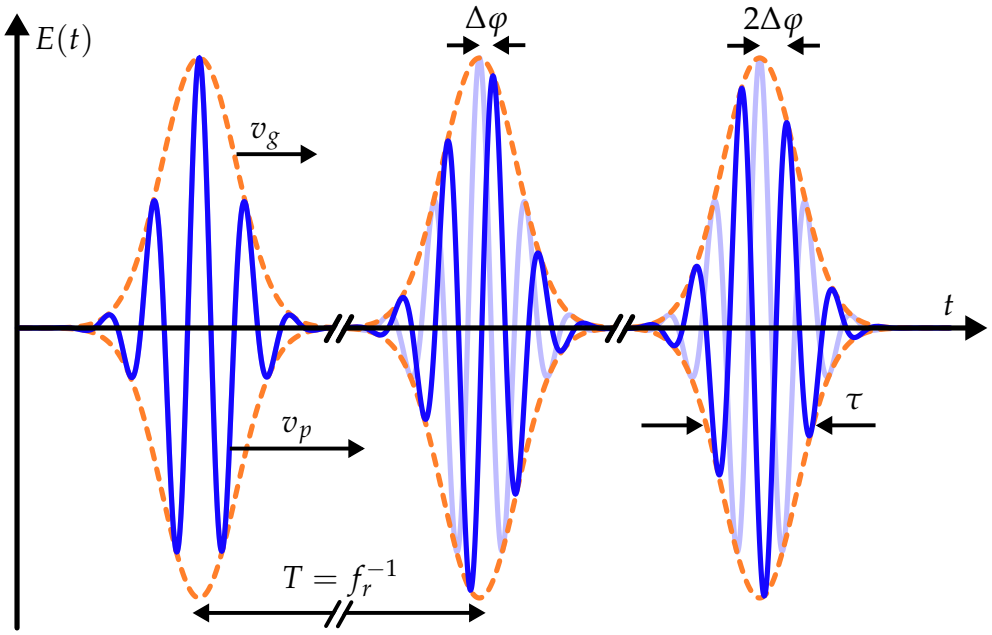

(a) Time domain

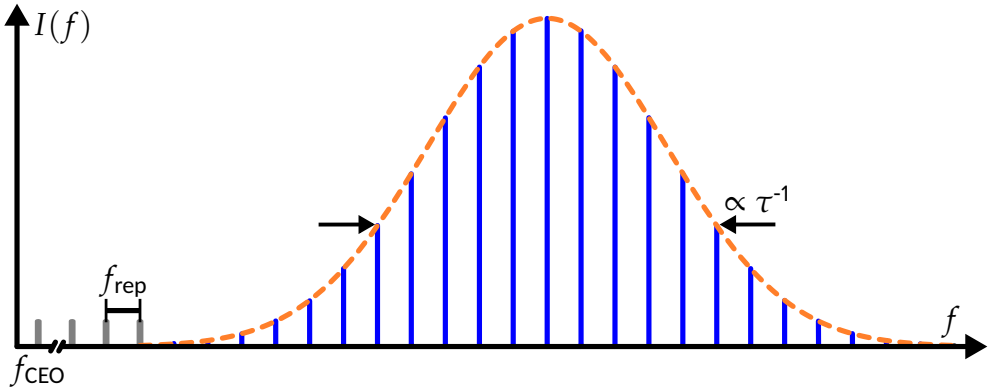

(b) Frequency domain

Figure 2.1: Panel (a): Schematic of the electric field output of an LFC in the time domain. The pulse envelope is shown in dashed orange and the carrier wave as the dark blue line. The light blue line indicates the position of the carrier wave with respect to the envelope of the first pulse to illustrate the carrier-envelope-offset-phase shift $\Delta\varphi$. The broken x-axis is to indicate that the pulse separation is much larger than the pulse duration. Panel (b): Schematic intensity spectrum of an LFC in the frequency domain. The comb lines are shown in blue, while the hypothetical extension of the comb lines is shown in grey. The width of the spectral envelope (dashed orange line) is inversely proportional to the pulse length in time τ. Both figures were adapted from Jones et al. (2000).

of the carrier wave. Thus, the carrier wave undergoes many cycles in between pulses. A subsequent pulse envelope will be almost identical to its predecessor. The carrier wave, however, will undergo a slight phase shift with respect to the pulse envelope. The carrier wave moves with the phase velocity v_p and the pulse envelope with the group velocity v_g. The difference between both velocities is a result of the dispersion in the laser cavity. The phase shift caused by the dispersion is given by

$$\Delta\varphi = \frac{f_{\mathrm{CEO}}}{f_{\mathrm{rep}}} 2\pi. \tag{2.19}$$

The offset frequency is thus a result of the dispersion and depends on the phase shift between the carrier wave and the pulse envelope. Generally, a laser pulse does not oscillate with a constant carrier frequency, but it is chirped. This means, that the instantaneous frequency changes over the duration of a pulse. The comb equation Eq. 2.18 still holds for chirped pulses, even though $\Delta\varphi$ is not well defined anymore (Reichert et al., 1999).

Whether or not a mode with frequency f_k is present in the spectrum depends on the envelope function $I(f)$ (the first term in Eq. 2.17). The spectral envelope corresponds to the spectrum of a single pulse. Assuming the pulse has a Gaussian shape, we can calculate the spectral envelope using the Fourier transform:

$$A(t) = e^{-t^2/(2\tau)^2} \tag{2.20}$$

$$\mathcal{F}(A(t)) = \sqrt{2\tau^2} e^{-\omega^2\tau^2}, \tag{2.21}$$

with the pulse width τ. The Fourier transform of a Gaussian is also a Gaussian but scaling inversely with the pulse width p. For shorter pulses, the width of the spectral envelope increases. While the exact relation is different for non-Gaussian pulse shapes, this generally holds true. To increase the spectral bandwidth of the LFC, the length of the pulse must therefore be reduced. Usually, this spectral broadening is achieved using nonlinear optics. The relevant processes will be introduced in chapter 4.

2.2 **Frequency stabilization**

To make the LFC usable as a frequency standard or calibration light source, the positions of the comb lines have to be controlled with a high accuracy and precision. Especially the stability of the repetition rate is crucial, as any error is magnified in the optical regime by the factor k in Eq. 2.18. Luckily, this is the

parameter which is also easier and more straightforward to control. Before the methods for controlling the repetition rate and the offset frequency are described, the Allan deviation and phase locked loops are introduced in the following sections.

2.2.1 Allan deviation

The Allan deviation is a statistical measure for the stability of an oscillator (Allan, 1966). It was introduced as the regular standard deviation diverges for some frequency dependent noise types present in oscillators. In contrast, the Allan deviation converges even if an oscillator drifts over longer timescales. Using the Allan deviation, the different types of noise and the timescales on which they dominate can be identified. The overlapping Allan deviation, a generalization of the Allan deviation, is now the most widely used in frequency stability analysis (Snyder, 1981; Riley, 2008). There are multiple other statistical measures used in different cases, but most of the time the general-purpose overlapping Allan deviation is sufficient.

We use the Allan deviation, to verify the stability of the phase locked comb frequencies and to identify noise sources by the signatures they create in the Allan deviation. To calculate the Allan deviation we consider an oscillator as described by Vig et al. (1999):

$$A(t) = (A_0 + \varepsilon(t)) \sin(2\pi f_n t + \Phi(t)), \tag{2.22}$$

where A_0 is the peak amplitude, $\varepsilon(t)$ the amplitude noise, f_n is the nominal frequency, t is the time and $\Phi(t)$ is the phase noise. The instantaneous frequency $f(t)$ of this oscillator is given by

$$f(t) = f_n + \frac{1}{2\pi}\frac{\mathrm{d}\Phi(t)}{\mathrm{d}t}. \tag{2.23}$$

The fractional frequency of an oscillator is defined as

$$y(t) \equiv \frac{f(t) - f_n}{f_n} = \frac{1}{2\pi f_n}\frac{\mathrm{d}\Phi(t)}{\mathrm{d}t}. \tag{2.24}$$

The definition of the Allan deviation is then

$$\sigma_y(\tau) = \left[\frac{1}{2(M-1)}\sum_{k=1}^{M-1}\left(\langle y_{k+1}\rangle_\tau - \langle y_k\rangle_\tau\right)^2\right]^{\frac{1}{2}}, \tag{2.25}$$

where M is the number of frequency measurements, τ is the time averaging interval and $\langle y_k\rangle_\tau$ is the fractional frequency averaged over the k-th interval.

The time averaging interval τ can be any multiple of the sampling interval as long as it is smaller than twice the total measurement time. There should be no dead time in between frequency measurements, as there will be a bias in the result otherwise (Vig et al., 1999).

Fig. 2.2a shows a simulated dataset of fractional frequency measurements with some Gaussian noise and a cubic drift. Fig. 2.2b shows the corresponding value of the standard deviation and the Allan deviation as a function of measurement time. While the Allan deviation is almost constant, the regular standard deviation increases with measurement time due to the drift of the oscillator.

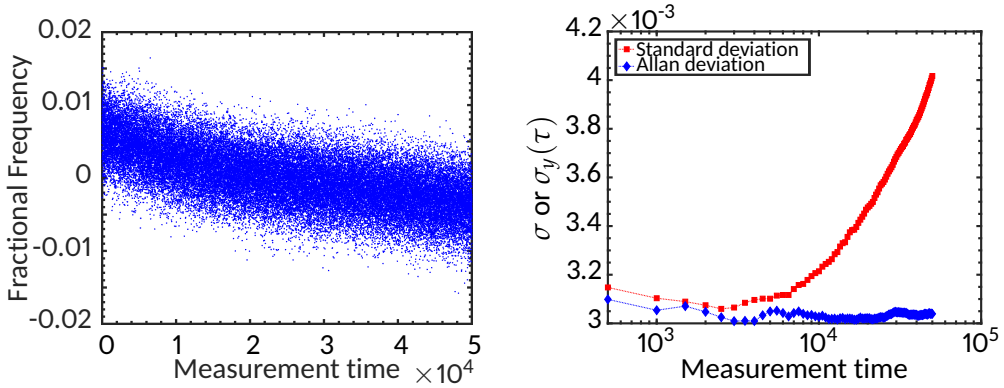

(a) Simulated oscillator frequency

(b) Standard deviation and Allan deviation

Figure 2.2: Panel (a): A simulated oscillator frequency data set with noise and drift. Panel (b): A comparison of the standard deviation (red squares) and Allan deviation (blue diamonds) of the simulated data set as a function of measurement time.

The confidence of the Allan deviation, especially for large time averaging intervals, can be increased when the overlapping Allan deviation is used (Vig et al., 1999). It is defined as (Riley, 2008)

$$\sigma_y(\tau) = \left[\frac{1}{2m^2(M-2m+1)} \sum_{j=1}^{M-2m+1} \left[\sum_{k=j}^{j+m-1} \left(\langle y_{k+m} \rangle_\tau - \langle y_k \rangle_\tau \right)^2 \right] \right]^{\frac{1}{2}}, \tag{2.26}$$

where $\tau = m\tau_0$ with the averaging factor m and the basic sampling interval τ_0. The overlapping Allan deviation computes the relative differences between two sliding windows over the frequency data, rather than using fixed chunks for the whole evaluation process. The difference between standard and overlapping Allan deviation is illustrated in Fig. 2.3. For small averaging times the difference is marginal, but as averaging times increase, the number of samples drops dramatically for the regular Allan deviation. Thus, we will only use the

overlapping Allan deviation in order to characterize the frequency stability of our setup. In this work, both Allan deviation and overlapping Allan deviation were calculated using the code provided by Hopcroft (2016, 2017).

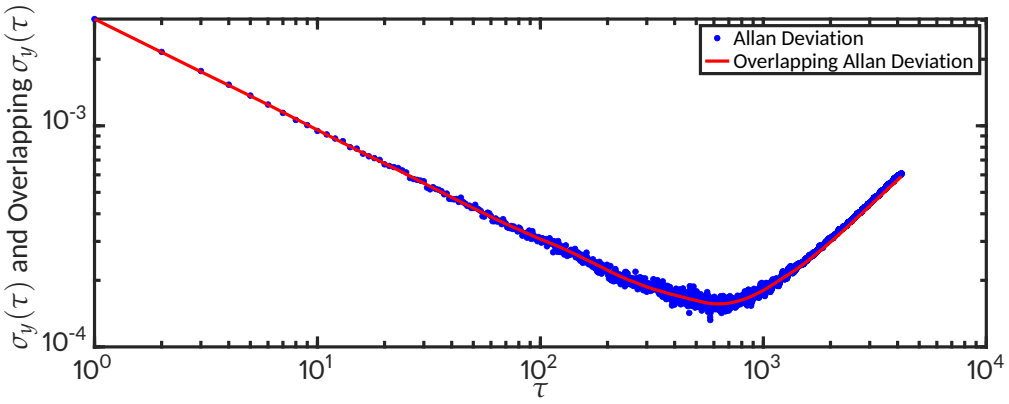

Figure 2.3: Comparison of the regular Allan deviation (blue dots) and the overlapping Allan deviation (red line) for the simulated data set shown in Fig. 2.2.

Fig. 2.3 also shows how the Allan deviation may be used to characterize different noise sources and the time scales over which they dominate measurement errors. For lower averaging values there is a $\tau^{-1/2}$ dependence. This indicates that the white (or Gaussian) frequency noise we simulated is dominant over time scales up to about 200 to 300 times the sampling interval. Over long timescales the frequency drift with a τ^1 dependence becomes dominant and the Allan deviation increases again.

The Allan deviation can also be used to identify low frequency modulations of the oscillator (low frequency with respect to the carrier frequency). A sinussoidal frequency modulation of the oscillator leads to characteristic oscillations in the Allan deviation. The averaging time of the first peak of the first oscillation τ_p can be related to the half cycle of the period of the frequency modulation. For the overlapping Allan deviation the relation is given by Carson and Haljasmaa (2015)

$$\frac{\tau_p}{\tau_{hc}} = \frac{\tan\left(\frac{\pi\tau_p}{2\tau_{hc}}\right)}{\pi} \tag{2.27}$$

$$\approx 0.742. \tag{2.28}$$

The modulation frequency f_m is thus given by

$$f_m = \frac{1}{2\tau_{hc}} \approx \frac{0.371}{\tau_p}. \tag{2.29}$$

2.2.2 Phase locked loops

In order to stabilize the repetition rate and offset frequency of the LFC phase locked loops (PLLs) are used. A PLL is used to lock an oscillator to a frequency reference. The oscillator is stabilized by comparing the phase difference, rather than the frequency difference between oscillator and reference. Fig. 2.4 shows a diagram of a PLL. The phase of the reference and the oscillator under control (or voltage controlled oscillator (VCO)) are compared in the phase comparator. Depending on the phase difference, an error signal is generated. A loop filter generates the control signal from the error signal which then drives the frequency of the VCO in the desired direction. In case the frequency difference between VCO and reference is large the frequency of the VCO may be divided before comparison with the reference. The stability of the reference oscillator is then directly transferred to that of the VCO (Gardner, 2005).

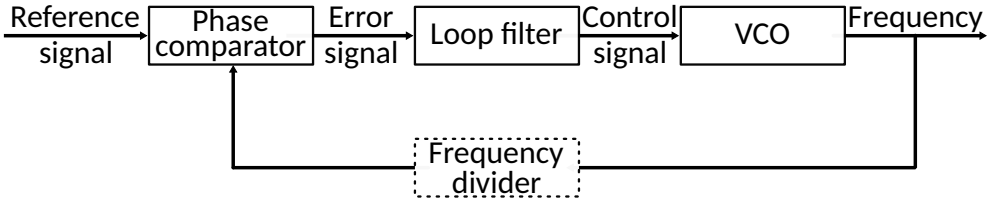

Figure 2.4: Flow diagram of a phase locked loop.

2.2.3 Stabilizing the repetition rate

Passive mode-locking of lasers and control over the repetition rate f_{rep} of pulsed lasers was established by 1970 (Osterink and Foster, 1968; Hillman et al., 1970) and is straightforward. The first step is to measure the repetition rate. This can be done with a fast photodiode, which will generate a signal with the frequency of the laser pulses. The second step to achieve a stable control is to use a physical parameter which influences the repetition rate. The repetition rate is given by

$$f_{\text{rep}} = \frac{c}{nL}, \tag{2.30}$$

with the speed of light in vacuum c, the refractive index n and the laser cavity length L. The speed of light in vacuum is hard to change, natural constants are stubborn quantities after all (Tiesinga et al., 2021). While the refractive index may be changed, i.e., via the optical Kerr effect, the possible change is small, corresponding to an additional optical path length on the order of a

wavelength (Siegman, 1986, p. 34). The most direct way is by changing the cavity length. This can be done by mounting one of the cavity mirrors on a piezo. The cavity length can then be controlled by changing the voltage applied to the piezo. This gives a very fast response time and enables a direct electronic control of the repetition rate of a pulsed laser.

2.2.4 Stabilizing the offset frequency

As with the repetition rate, the first step in stabilizing the offset frequency is measuring it. Initially, this was only possible by using several frequency dividing and mulitplication steps (Udem et al., 1997). With the discovery of nonlinear optical fibers, the f-2f technique was invented (Reichert et al., 1999; Jones et al., 2000). For this technique, the LFC spectrum must be broadened to at least one octave. This means, that the highest frequency value is at least twice the lowest frequency. As an alternative to nonlinear fibers, it is possible to reach a full octave with, e.g., Ti:sapphire lasers using double-chirped mirrors to compress the pulses (Morgner et al., 2001; Matos et al., 2004).

The principle optical layout of an f-2f interferometer used for measuring the offset frequency is shown in Fig. 2.5a. The light of the LFC is first broadened to a full octave in a nonlinear fiber. The output of the fiber is split up with a dichroic mirror. The part of the light with the lower frequency is frequency doubled using a second harmonic generation crystal. Both beams are then recombined and detected with a photodiode, resulting in a beat frequency (Forrester et al., 1955). Fig. 2.5b illustrates the idea behind the f-2f interferometer. The frequencies of the frequency doubled comb modes are given by

$$f_{k_d} = 2f_{\mathrm{CEO}} + 2k_d f_{\mathrm{rep}}. \tag{2.31}$$

The difference between the original and the frequency doubled comb modes is then

$$f_{k_d} - f_k = f_{\mathrm{CEO}} + (2k_d - k) f_{\mathrm{rep}}. \tag{2.32}$$

For each frequency doubled comb mode, there will be a mode for which $k_d = 2k$ and thus the fundamental beat mode detected by the photodiode will be the offset frequency f_{CEO}.

In order to affect f_{CEO}, we must change the dispersion of the cavity, as it depends on the relation between phase and group velocity of the pulses (Reichert et al., 1999). There are multiple methods of actively controlling the dispersion. One way is using pairs of dispersive elements, typically gratings

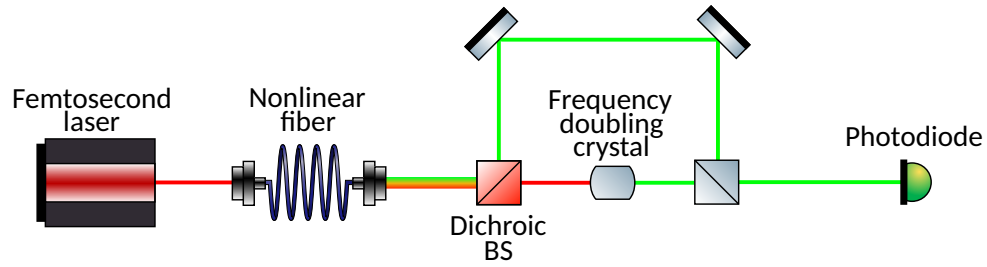

(a) Schematic f-2f setup

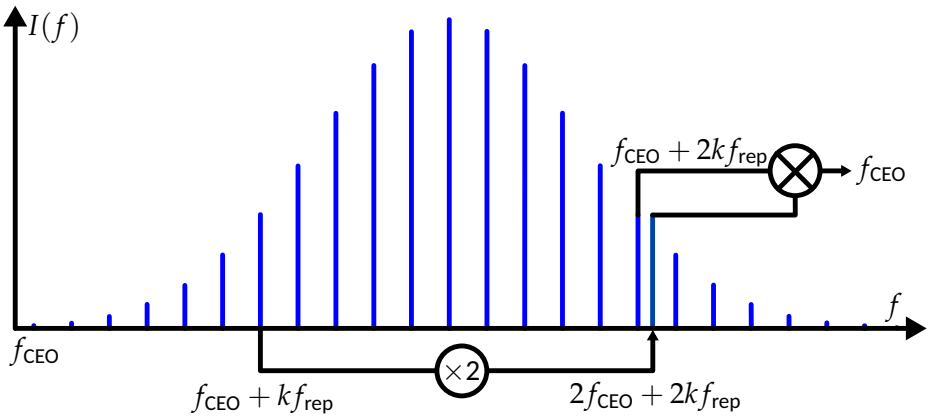

(b) Spectrum of light incident on photodiode

Figure 2.5: Panel (a): Schematic of an f-2f interferometer. The laser output is broadened in a nonlinear fiber. It is then split up using a dichroic beam splitter. The low frequency part is frequency doubled. Both beams are then recombined and measured by a photodiode. This and subsequent optical schematics were created using "ComponentLibrary" (Franzen, 2006). Panel (b): Frequency domain illustration of the light incident on the photodiode. The frequency doubled comb lines differ from the regular ones by exactly f_{CEO}.

or prisms, as illustrated in Fig. 2.6 (Reichert et al., 1999). This creates a beam where the different frequency components are parallel but displaced. The optical path length is then frequency dependent. By adjusting the angle of the end mirror or the prism insertion depth the optical path length is changed depending on the frequency. Instead of an end mirror, a second prism or grating pair may be used.

Another method exploits the optical Kerr effect. Strong electrical fields make slight changes to the refractive index of a material (Kerr, 1875; Holzwarth et al., 2000). By changing e.g., the pump power, the refractive index of the laser medium is changed. This change is very small but is on the order of one wavelength (Siegman, 1986, p. 34). As the necessary phase adjustment is half a

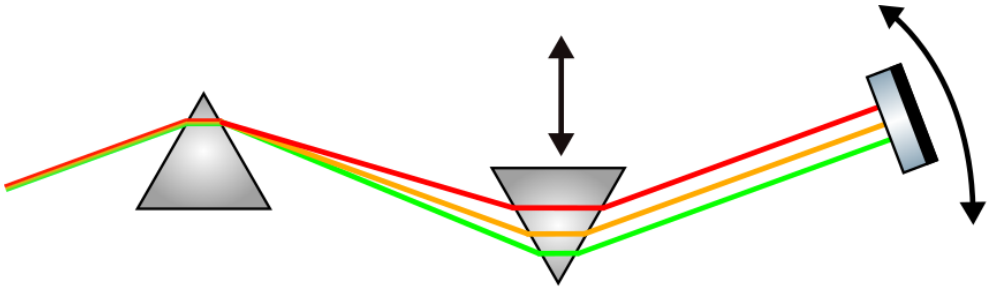

Figure 2.6: Schematic of a dispersion control inside a laser cavity used to stabilize f_{CEO}. The dispersion can be controlled either by tilting the end mirror or by changing the insertion depth of the second prism.

wavelength at most, this is in the correct order of magnitude for a stabilization of the offset frequency.

Our setup combines both approaches. For large scale adjustments, a prism pair is used. For the active control and small range adjustments, the pump power is changed. The reason for this dual approach is that the pump power can be adjusted on much shorter timescales, but its control range is limited. For our laser, a change in pump power by 400 mW changes the offset frequency by 31 MHz which corresponds to 3 % of the range of f_{CEO} (see Fig. 2.7). Since the laser is only stable in a pump power range from about 9600 to 10600 mW, only a small range of f_{CEO} can be scanned without changing environment parameters such as temperature. Since this is undesirable, we use a prism pair for coarse adjustment of f_{CEO} so that we can match it to the auxiliary electronic components we use. For the actual stabilization we then use the pump power.

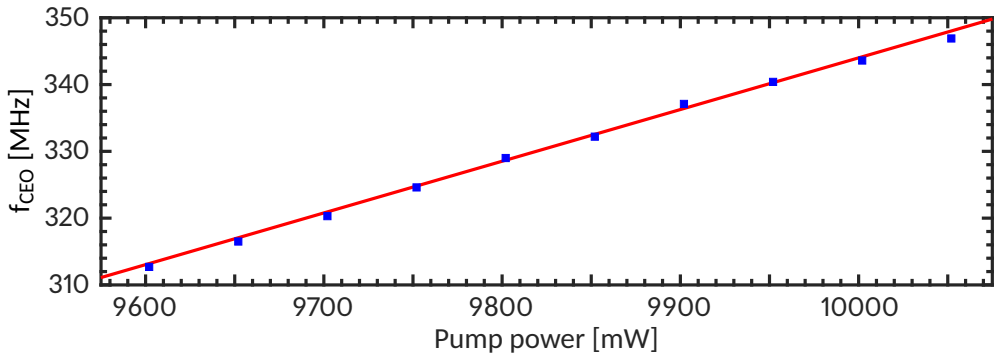

Figure 2.7: Measurement of the offset frequency f_{CEO} as a function of pump power (blue squares). A linear fit (red line) shows good agreement.

2.3 **Laser frequency comb setup**

In the following a short description of the optical setup of our laser frequency comb, as well as the respective electronics to stabilize the repetition rate and the offset frequency is given.

2.3.1 Optical setup

We use a taccor power 10 laser (LaserQuantum) which is a passively mode-locked Ti:sapphire laser. Its main properties as measured by the manufacturer are displayed in Tab. 2.1

The optical setup after the main laser compartment is shown as a schematic in Fig. 2.8a and a photograph in Fig. 2.8b. The polarization of the incoming light may be adjusted using the first λ/2-plate before it hits a chirped mirror pair. The chirped mirrors compress the pulse to a shorter duration to improve the subsequent supercontinuum generation in the nonlinear fibers. After passing an alignment mirror and a lens pair the light is split up by a power beam splitter with a slight polarization dependence. Thus, the power split ratio can be adjusted using the $\lambda/2$-plate. However, this also affects the group velocity dispersion (GVD) properties of the chirped mirrors. From the beam splitter, one part of the light is guided into a photonic crystal fiber via two piezo mounted mirrors and a second λ/2-plate. The piezo mounted mirrors and the λ/2-plate plate enable a fine control of the incoupling parameters to optimize the nonlinear broadening.

An f-2f interferometer as described in Sec. 2.2.4 follows after the spectral broadening in the photonic crystal fiber. The light is split up using a dichroic beam splitter. The low frequency part of the light is frequency doubled. It

Table 2.1: Taccor power specifications

Output power	1955 mW
Power stability	0.2 %
Wavelength	797 nm
Bandwidth	39 nm
Pulse duration	19 fs
Repetition rate	1 GHz
Beam diameter FWHM	0.8 ± 0.3 mm

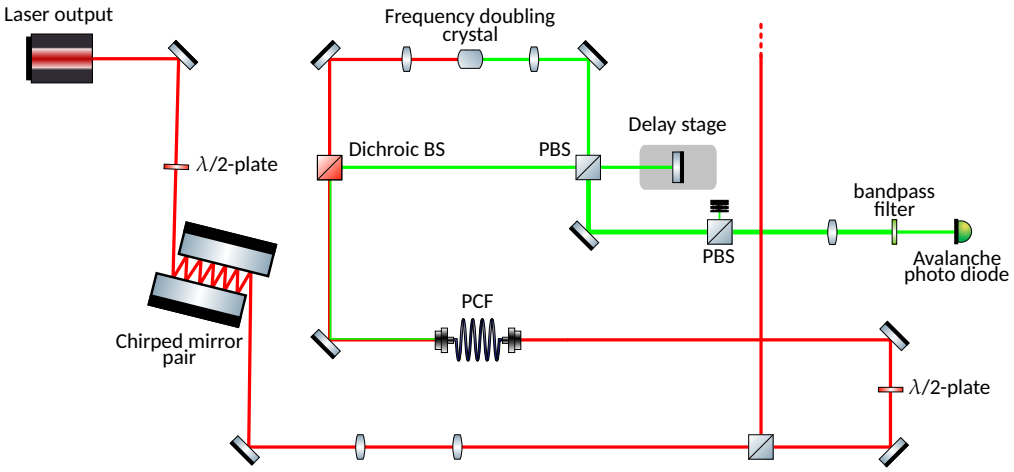

(a) Schematic of the optical setup

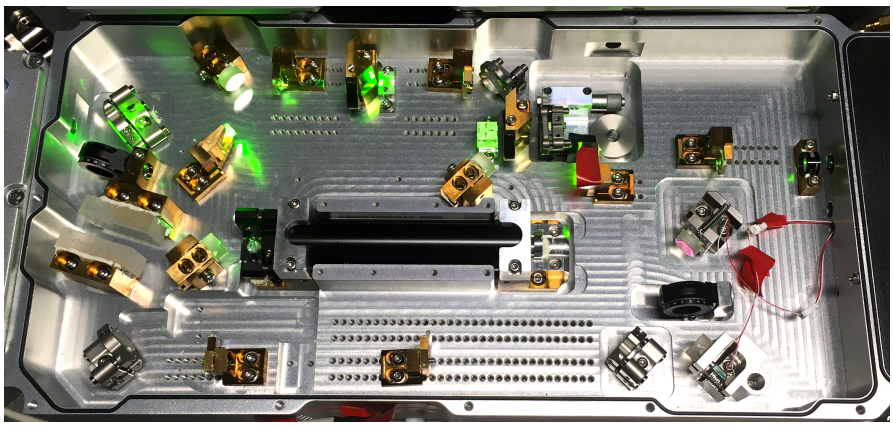

(b) Photograph of the optical setup

Figure 2.8: Panel (a): Schematic overview of the accessible optics of the taccor comb unit. Besides an f-2f interferometer the chirped mirrors are the crucial parts. Panel (b): Photograph of the actual setup.

is recombined with the high frequency part, whose optical path length may be adjusted on a µm level using the delay stage. The path length adjustment ensures that the pulses of both arms of the interferometer overlap after recombination. The light is filtered with a polarizing beam splitter and a band-pass filter (Thorlabs FL05532-10) with a center wavelength of 532 nm and a full width at half-maximum (FWHM) of 10 nm. The filtering ensures that only the spectral region with light both from the frequency doubled and the high frequency part can pass through. This reduces noise in the signal from the avalanche photo diode which is located directly behind the filter. The f-2f interferometer setup is quite stable once it is well aligned. After one year, a realignment only improved the signal amplitude by about 2 dBm. The photonic crystal fiber (PCF), however, is very sensitive to changes in the input. Therefore,

the preceding optics and the $\lambda/2$-plate usually should be realigned before use. Otherwise the f_{CEO} signal is usually too weak for a permanent lock.

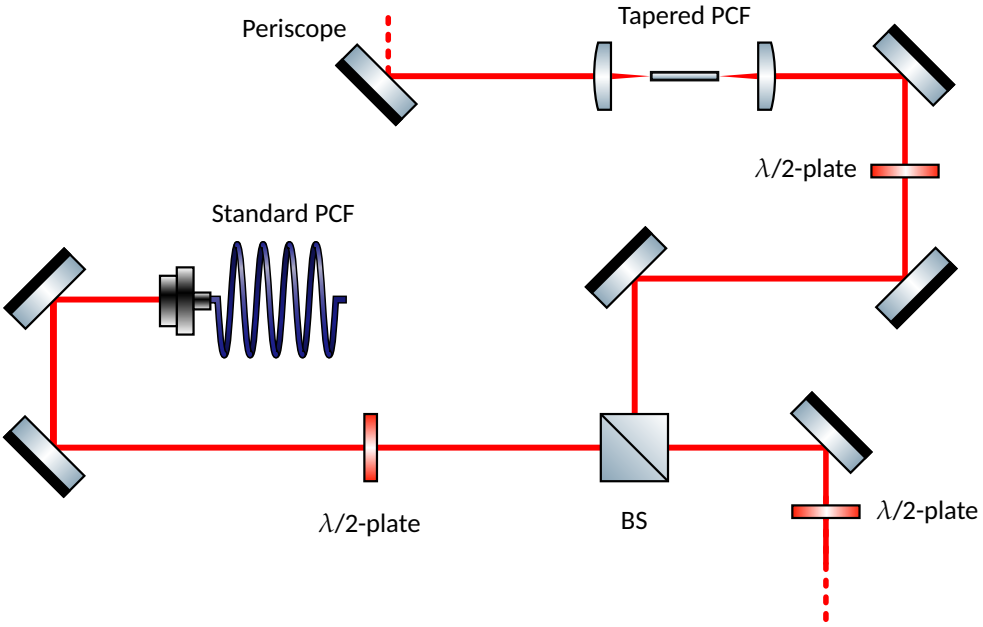

Figure 2.9: Schematic overview of the supercontinuum broadening compartment.

The fraction of light which was split off before the PCF exits through a hole in the compartment and enters the second compartment where supercontinuum broadening of the science light takes place (see Fig. 2.9). A 50:50 power beam splitter splits the light into two different arms. We added an additional $\lambda/2$-plate before the beam splitter to adjust the power in each arm. Both arms have $\lambda/2$-plates and two piezo mounted mirrors to guide the light into the nonlinear fibers and manipulate its polarization. Originally, one arm led to a 100 cm nonlinear fiber and the other to a 50 cm fiber (both NL-PM-750). We subsequently replaced the 100 cm nonlinear fiber with a setup for a designed tapered nonlinear fiber (see Ch. 4). Since the space at the outcoupling port is limited, only one of the arms can be used at a time in this configuration.

2.3.2 Pulse broadening in the setup

We calculate an estimation of the pulse length at the incoupling to the two nonlinear fibers by calculating the overall group dispersion delay (GDD). The GDD is a measure of the chromatic dispersion, i.e., how the different spectral components of the pulse are delayed. We calculate most of the GDD values of the optical components by using tabulated GVD values. [1] The GVD is the

1 www.refractiveindex.info

amount of GDD per unit length and is defined as the derivative of the inverse group velocity with respect to frequency. There are two regimes of GVD, the normal dispersion regime, for which the group velocity is antiproportional to the frequency and the anomalous dispersion regime, for which the group velocity is proportional to the frequency. Thus, the contribution of glasses and other materials, which are mostly in the normal GVD regime, can be compensated by using optical elements which cause a negative GDD. In our setup, a pair of chirped mirrors is used to accomplish this. Using the GDD, the final pulse length t_{out} can be calculated by

$$t_{\text{out}} = \frac{\sqrt{t_{\text{in}}^4 + 16\log(2)^2 \text{GDD}_{\text{all}}^2}}{t_{\text{in}}}, \tag{2.33}$$

where t_{in}=19 fs is the initial pulse length and GDD_{all} is the sum of the GDD caused by the air and the optical components (see Tab. 2.2).

Table 2.2: The GDD of the optical components and air along the beam path. The glass type and exact dimensions of the beam conversion lenses were not known. We thus included two typical glass types, one with a low and one with a high GVD. The contribution of the polymer in the $\lambda/2$-plate was omitted, as the material is not known.

Component	GVD [fs mm^{-1}]	length [mm]	#	GDD [fs^2]
Air [Ciddor]	0.021233	800	1	16.986
$\lambda/2$-plate [BK-7]	44.65	2	2	179.6
C240TMD [D-ZK3]	54.027	3.43	1	185.313
Chirped mirrors				-1330 or -720
Lens [BK-7]	44.65	$\approx$ 3	2	267.9
Lens [CAF-2]	27.873	$\approx$ 3	2	167.238
Sum				-781 to -71

Since the manufacturer provided us with conflicting values of the GDD of the chirped mirrors, the overall range is quite large. This results in a final pulse length between 21 to 101 fs. However, the pulse length is increased because the GDD is actually negative, so there is a significant cushion to allow for further added GDD from other optical elements such as mirrors and beamsplitters. The GDD contribution of the beam splitters is not known. In addition, that of

the mirrors is highly variable for both polarization and wavelength, thus they were not included in the estimation. It would likely be beneficial to carry out a measurement of the pulse duration. This would also enable a check whether the overall GDD before incoupling is negative or positive by introducing an element with known GDD into the beam.

2.3.3 Repetition rate electronics

The repetition rate stabilization is almost fully implemented by the manufacturer. Inside the main laser compartment, a photodiode records the repetition rate signal and feeds it to the loop filter control box (LaserQuantum TL-1000). The only additional component which has to be provided is the frequency reference. We use the SMB100A frequency synthesizer (Rohde&Schwarz), which is locked to the main frequency reference, the GPS-8 (MenloSystems) via a 10 MHz reference signal. The GPS-8 uses an ultra-stable quartz oscillator to ensure the short term stability of the 10 MHz frequency reference signal. To correct for long term drifts, the signal from GPS-satellites is averaged and the quartz oscillator corrected accordingly. This follows the design principle described by Helsby (2003).

2.3.4 Offset frequency electronics

The offset frequency stabilization requires additional steps compared to the repetition rate. The ULC-16 unit controlling the laser has an input port which accepts a control signal of ± 5 V. This control signal adjusts the laser pump power and thus, via the Kerr effect, enables a control of f_{CEO}. The other parts of the control, the phase comparator, amplifying & filtering electronics as well as the PI-controller and frequency reference are not contained in the ULC-16.

To reduce any sources of noise, we pass the f_{CEO} signal from the f2-f interferometer photodiode to a tunable bandpass filter (Lorch Microwave tunable bandpass filter) with a range from 250 to 500 MHz and a passband width of 20 MHz. As this filter is manually controlled, we built a stepping motor controlled by an Arduino for remote control. After the bandpass, the f_{CEO} signal is amplified (MiniCircuits ZFL-1000LN+). An attenuator prevents reflected signals from disturbing the amplifier. A DC-block (MiniCircuits BLX-99-S+) protects the following frequency divider chip (Analog Devices HMC705LP4), which divides the f_{CEO} frequency signal by 17. Both the divided f_{CEO} signal and the reference signal from the HMF2500 (Rohde&Schwarz) frequency synthesizer are fed to

the phase comparator chip (AD9901). Like the SMB100A for the repetition rate stabilization, the HMF2500 is disciplined to the 10 MHz reference signal from the GPS-8 unit. The phase comparator chip automatically switches to a frequency discriminator mode if the frequency difference between the reference and VCO is too high. This increases the catch range of the PLL, i.e., the range of frequency difference in which the control loop is able to establish a phase lock. The error signal from the phase comparator chip is lowpass filtered (MiniCircuits BLP-10.7+) before the PI-controller (New Focus LB1005). From this error signal, the LB1005 generates the control signal which is fed into the ULC-16 and directly adjusts the laser pump power to control f_{CEO}. We usually set the proportional part of the PI-controller close to a gain of unity and the PI-corner frequency to a value of 3 kHz.

2.4 **Frequency stability measurements**

We use a frequency counter (Picotest U6200A) to measure the stability of both the repetition rate f_{rep} and the offset frequency f_{CEO}. A schematic of the setup is shown in Fig. 2.10. The frequency counter is referenced to one of the frequency synthesizers, which in turn are referenced to the GPS-8 10 MHz frequency standard. The frequency counter does not directly accept the GPS-8 output due to an impedance mismatch.

We made multiple measurements of the stabilized and unstabilized f_{rep} and f_{CEO}, with the frequency counter referenced to each frequency synthesizer. Additionally, we also measured the frequency output of the two frequency synthesizers directly to compare the results to the stabilized f_{rep} and f_{CEO}. All measurements had to be done in sequence, as the frequency counter can only measure a single input.

2.5 **Results - Frequency stability**

Fig. 2.11 shows the Allan deviation (see Sec. 2.2.1) of the unstabilized offset frequency and repetition rate. The repetition rate is inherently more stable by about three orders of magnitude. Also, the noise floor is reached at a 1 s averaging time for f_{CEO}, while the drift of f_{rep} starts to come into effect at about 10 s averaging time. The offset frequency exhibits a $\tau^{\frac{1}{2}}$ trend corresponding to random walk noise, while the repetition rate shows a steeper τ^{1} trend corresponding to frequency drift. Both frequencies reach the noise floor at an averaging time of about 1 s.

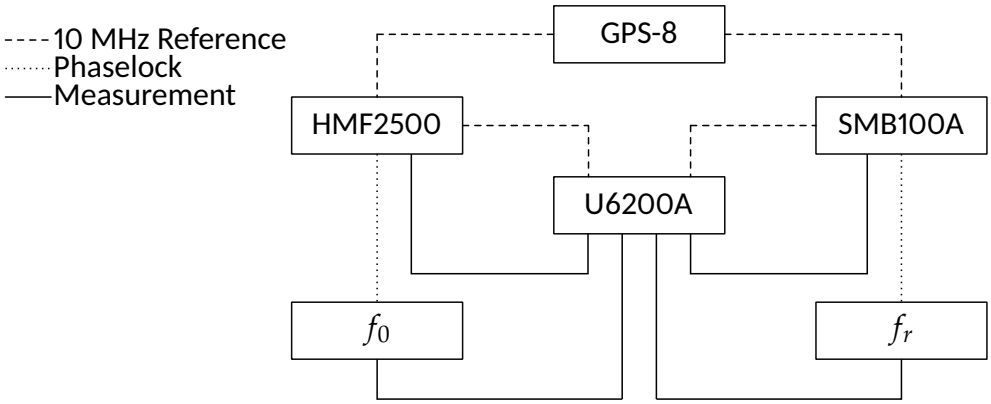

Figure 2.10: Schematic overview of the frequency stabilization setup. The GPS-8 unit is the master reference. Both frequency synthesizers are directly referenced to the GPS-8. The frequency counter U6200A may be referenced to either synthesizer. The HMF2500 is used to phaselock f_{CEO} and the SMB100A is used to phaselock f_{rep}. Both frequency synthesizers and both comb frequencies can be measured using the U6200A.

In Fig. 2.12 the overlapping Allan deviation of the SMB100A frequency synthesizer and the repetition rate are shown. In one measurement, the SMB100A is referenced to the GPS-8, while in the other it is using its internal frequency reference. For the repetition rate measurement the SMB100A is referenced to the GPS-8. For all three measurements, the U6200A is referenced to the SMB100A. This shows that the measured stability is not affected by whether the frequency counter is referenced to the GPS-8 if the frequency counter is referenced to the synthesizer generating the measured frequency signal. However, we can also see that a true phase lock is achieved, as no additional noise is observed in the stabilized repetition rate compared to the direct frequency synthesizer output. The slope follows a clear $\tau^{-\frac{1}{2}}$ trend, corresponding to white (Gaussian) frequency noise (see also Fig. 2.14b).

We made additional frequency measurements of the repetition rate, the offset frequency and both frequency references. In all of these measurements, the frequency counter was referenced to the frequency counter which does not correspond to the measured frequency. E.g., for the measurements of the repetition rate and the SMB100A, the frequency counter was referenced to the HMF2500A. Fig. 2.13 shows that there are oscillations in the Allan deviation calculated from these measurements. These oscillations are characteristic of a low frequency sinusoidal modulation of the phase. Using the Eq. 2.29, we can determine the frequency of this phase modulation. The integration time of

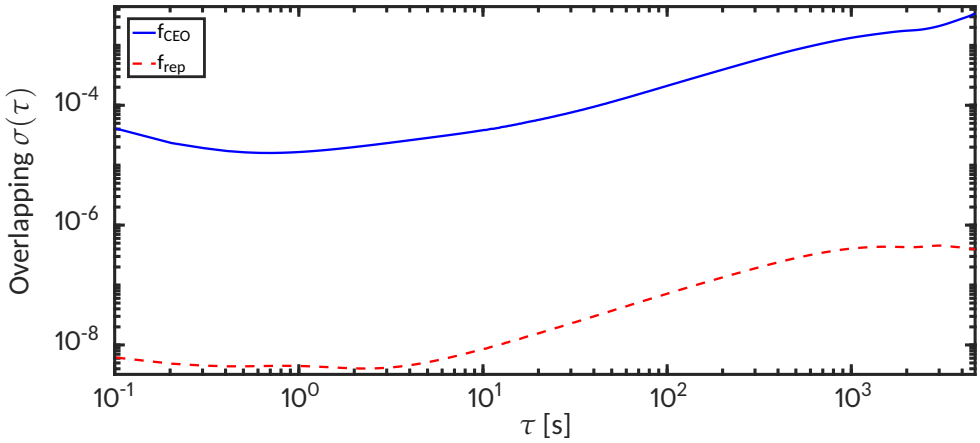

Figure 2.11: Allan deviation of the unstabilized offset frequency f_{CEO} (blue solid line) and repetition rate f_{rep} (red dashed line).

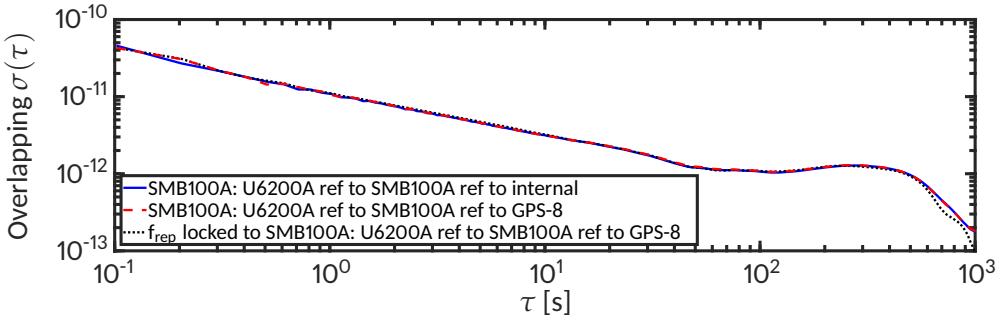

Figure 2.12: Overlapping Allan deviation of the SMB100A referenced to its internal oscillator (blue solid line), of the SMB100A referenced to the GPS-8 (red dashed line) and of the repetition rate f_{rep} referenced to the SMB100A referenced to the GPS-8 (black dotted line) are shown. All measurements are nearly indistinguishable.

the peak is estimated by calculating the logarithm of the integration time and the Allan deviation and then subtracting a linear fit from the logarithmic Allan deviation. Then we fit a quadratic polynomial to the three points around the maximum. This leads to an estimated modulation frequency of 0.73 Hz for the HMF2500 and 0.79 Hz for the SMB100A. Despite this modulation frequency, all measured frequencies are still more stable than the GPS-8 as measured by the manufacturer. The oscillations in the Allan deviation could not be observed if the frequency counter was referenced to the same frequency synthesizer it was measuring (see Fig. 2.12).

With the comb equation (Eq. 2.18) we can use the frequency measurements to calculate the frequency stability of a comb line in terms of radial velocities at 300 THz, corresponding to a wavelength of 1 µm. The expected distribution in the optical is shown in Fig. 2.14. As f_{rep} is multiplied with an integer of

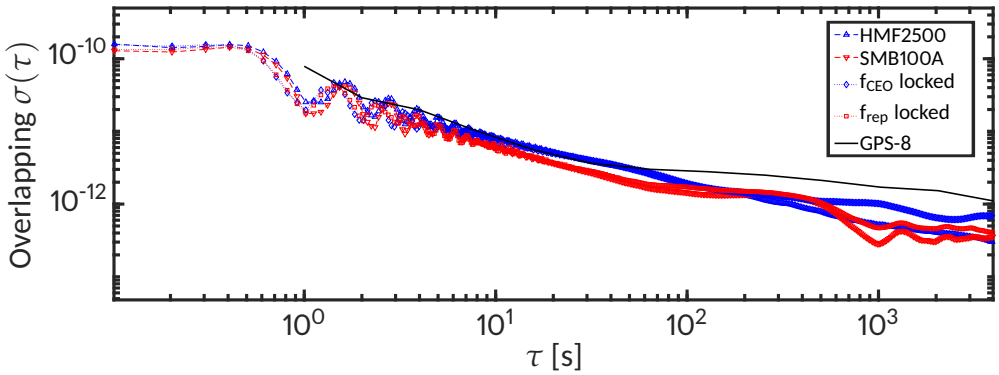

Figure 2.13: Comparison of the Allan deviation of measured comb frequencies and the respective frequency synthesizers to which they were stabilized as well as the specified Allan deviation of the GPS-8 frequency reference.

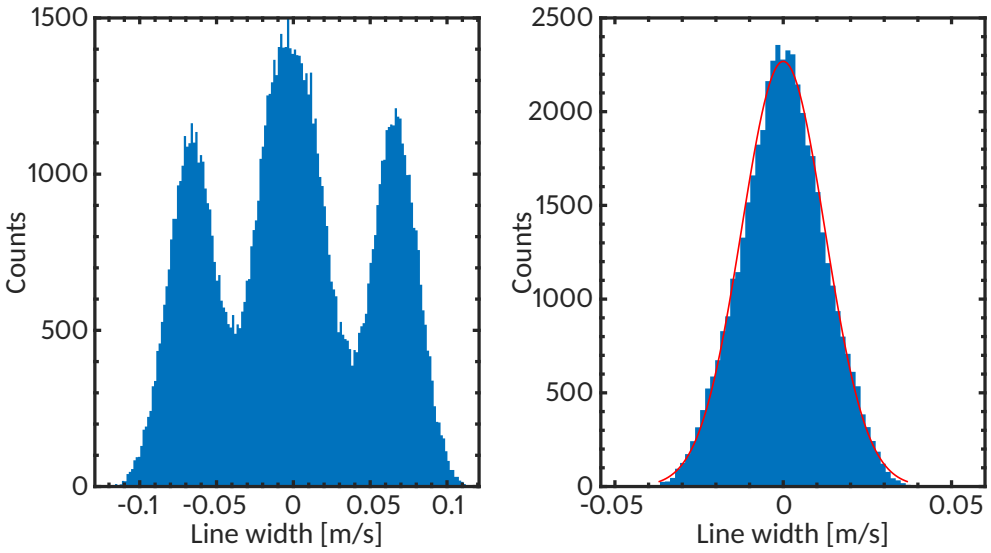

(a) With modulation

(b) Without modulation

Figure 2.14: Expected comb line center distribution in the optical regime. Panel (a): Distribution assuming the phase modulation measured in f_{rep} is not a measurement artifact. Panel (b): Distribution without the phase modulation. The red line shows a Gaussian distribution fit to the data.

about 300,000 its impact on the line position uncertainty also scales with this factor. Both comb frequencies have a similar stability so that the line position uncertainty contribution of f_{CEO} becomes negligible. In case the modulation is not a measurement artifact and transferred to the optical regime we can expect a single comb line to have a frequency uncertainty corresponding to 52 mm s^{-1}. If the modulation is not transferred to the optical, a single comb line would have a line position uncertainty of about 24 mm s^{-1}.

2.6 Discussion

The frequency stability measurements are limited by two factors. First, on short time scales the frequency counter seems less stable than the frequency synthesizer. Ideally, the difference frequency to another, more stable oscillator should be measured. As we do not have an additional reference oscillator in this frequency regime available this was not an option.

The second factor is the phase modulation introduced by the 10 MHz reference chain (see Fig. 2.10). This could be due to an impedance mismatch—two devices (HMF2500 and U6200A) have 1 kΩ terminated 10 MHz input port instead of the standard 50 Ω—or a lack of internal signal separation. We made sure that all instruments are grounded via a star topology to prevent ground loops. It could be that a ground loop is somehow introduced in the 10 MHz reference signal, as we are only using a simple BNC-tee to split the signal. A daisy chain setup of the 10 MHz reference however led to worse results, so we kept the scheme as shown in Fig. 2.10. Additional errors can be introduced by attaching a (terminated) cable to an unrelated port on the frequency counter during a measurement. The splitting of the reference signal with a simple BNC-tee is not good practice. A real signal splitter and an appropriate impedance matching would be better but also more costly.

We were able to phaselock the offset frequency and the repetition rate to the frequency synthesizers. There is some residual noise, caused by a problem in the 10 MHz reference chain or even the frequency counter itself and not in the comb. As both the frequency counter and the frequency reference are stabilized to the 10 MHz signal from the GPS-8, we can only claim that the repetition rate is as stable as the GPS-8 unit. For the GPS-8 stability we have to rely on the manufacturers specifications. A second measurement of the LFC stability is planned: Currently, a heterodyning experiment with a high precision, iodine stabilized Nd:YAG laser is being developed.

Even in the worst case, the frequency uncertainty of a single comb line in the optical regime only corresponds to 52 mm s^{-1}. Assuming that the stability of the GPS-8 reference is the actual limiting factor and the sinusoidal oscillations a measurement artifact, a single comb line in the optical regime would have a line position uncertainty of about 24 mm s^{-1}.

3

FOURIER TRANSFORM SPECTROGRAPH

Fourier transform spectrographs (FTSs) are a standard tool for high resolution infrared spectroscopy in different fields, e.g., physics, chemistry or biology. They are used for many different applications, from molecular spectroscopy to atmospheric monitoring or even for the detection of explosive substances from fingerprints (Davis et al., 2001; Griffiths and Haseth, 2007; Mou and Rabalais, 2009). An FTS is an interferometer, in which the optical pathlength difference (OPD) between two interferometer arms can be varied. Recording the output intensity of the interferometer pattern as a function of OPD results in a so called interferogram. The optical spectrum of the light is obtained by calculating the Fourier transform of the interferogram.

In the 1950s, when the modern FTS were invented, no photographic plates in the infrared existed for the use with dispersive spectrographs. Only single cell detectors were available in this wavelength range. Thus, monochromators where each wavelength is measured successively were used to record infrared spectra. Fellgett proposed the method which is now known as Fourier transform spectroscopy to measure all wavelengths simultaneously on a single detector and thus rapidly decrease the measurement time (Fellgett, 1958; Jacquinot, 1960). This had the advantage that measurements could be performed faster and with lower noise. This advantage is called multiplexing or Fellgets advantage. For this reason, FTSs used to be very capable instruments for infrared astronomy in the 1960s and 1970s (Connes and Connes, 1966; Beer et al., 1971; Connes and Michel, 1975).

With the advent of the CCD Fellgets advantage was no longer in place. While FTSs are able to cover larger spectral ranges at higher resolutions than dispersive spectrographs, they are not as efficient. This is not an issue in laboratory measurements where bright enough light sources are available. The importance of FTSs in astronomy, however, has since diminished. In an astronomical context, they are nowadays typically just used to characterize calibration light sources.

Another use case for FTS are solar observations (the Sun is very bright after all). There is a long, ongoing history of FTS measurements of the sun in the visible and near infrared (Kurucz, 1984; Wallace et al., 2011; Reiners et al., 2016b). While the Sun is an interesting study object by itself, solar observations can also help to better understand stellar observations. The Sun is the only star which can be studied in detail, with a high spatial and temporal resolution. Using an integrating sphere, the light from the whole Sun can be averaged and released as a point source, so that the point spread function resembles that of a star. Combining spatially resolved measurements with integrated measurements of the Sun helps us to understand which effects cause specific characteristics or changes in the solar spectrum (Meunier et al., 2010; Lagrange et al., 2010a; Haywood et al., 2016). This may help to improve our understanding of processes on other stars (Dumusque et al., 2015; Strassmeier et al., 2018; Schäfer et al., 2020b).

The solar observatory in Göttingen offers both, the possibility of spatially resolved as well as integrated solar measurements using an FTS. Solar FTS measurements thus far have been calibrated using telluric lines, reaching a precision of 10 m s^{-1} (Reiners et al., 2016b). To improve the precision and accuracy of these measurements, we aim to use a laser frequency comb (LFC) as a wavelength calibration light source.

This chapter gives a theoretical background on FTSs, possible measurement error sources and the calibration procedure. It also describes the setup used throughout the present work.

3.1 Working principles

The most commonly used form of an FTS is a so called rapid-scan interferometer based on the classical Michelson interferometer (Griffiths and Haseth, 2007). It consists of a beam splitter, two retroreflectors (one of them movable), a monochromatic reference light source and a detector (see Fig. 3.1).

The light source under investigation and the reference light are launched in parallel into the interferometer. At the beam splitter, the light is split in half with each half going into a different arm of the interferometer. Both parts are reflected by the retroreflectors at the end of their respective arms and recombined at the beam splitter. Finally, the light is focused onto the detector.

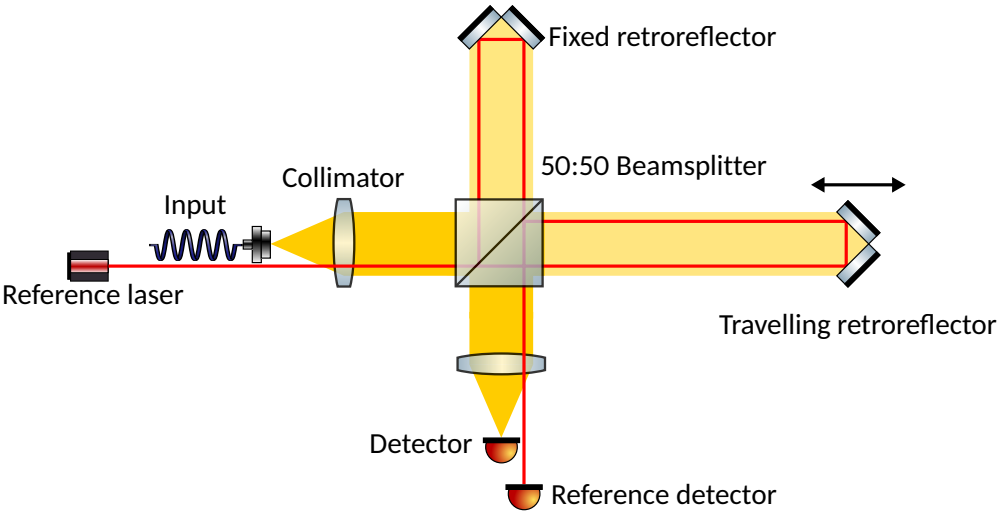

Figure 3.1: Schematic of a Michelson type FTS.

The electric field incident on the detector can be written as a superposition of the field coming from each arm (Davis et al., 2001):

$$E = E_0 e^{i2\pi ft} R_m R_b T_b (e^{-i2\pi f c^{-1} x_1} + e^{-i2\pi f c^{-1} x_2}), \tag{3.1}$$

where R_m is the mirror intensity reflection coefficient, R_b is the beam splitter reflection coefficient, T_b is the beam splitter transmission coefficient, f is the frequency of the light, c is the speed of light in vacuum and x_1 and x_2 are the lengths of each interferometer arm. Calculating the time averaged intensity of this leads to

$$I = \langle E \rangle^2 = I_0 2 R_m^2 R_b^2 T_b^2 (1 + \cos(2\pi f c^{-1} (x_1 - x_2))), \tag{3.2}$$

where $I_0 = E_0^2$ is the intensity amplitude. Defining the attenuated intensity amplitude $\tilde{I}_0 = I_0 2 R_m^2 R_b^2 T_b^2$ and the OPD $x = x_1 - x_2$ leads to

$$I = \tilde{I}_0 (1 + \cos(2\pi \frac{fx}{c})). \tag{3.3}$$

If one mirror is moved along the optical axis, the OPD changes. This also changes the intensity recorded at the detector. This measurement, the intensity as a function of OPD, is called an interferogram. For a monochromatic light source, e.g., the reference laser, this is a simple cosine function. By counting the number of fringes, the interferogram of the reference laser is used to measure the OPD. If the light is polychromatic, the recorded intensity is the superposition of all monochromatic light intensities:

$$I'(x) = \int_{-\infty}^{\infty} \tilde{I}(f)(1 + \cos(2\pi \frac{fx}{c}))df. \tag{3.4}$$

By subtracting the constant term and calculating the inverse Fourier transform, the optical spectrum of the light source under investigation is obtained:

$$\tilde{I}(f) = \int_{-\infty}^{\infty} I(x) \cos(2\pi \frac{fx}{c}) dx. \tag{3.5}$$

Following the Shannon-Nyquist sampling theorem, the highest optical frequency which can be measured with an FTS is given by half the sampling rate (Nyquist, 1928; Shannon, 1949). If we sample the interferogram at the zero-crossings of the fringes of a reference laser with a given frequency, then the highest measurable frequency is exactly that of the reference laser, as we are sampling with twice the laser frequency or wavelength.

3.2 **Resolution**

The resolution of an FTS is determined by its instrumental line shape (ILS), i.e., the lineshape of an unresolved line. The width of the ILS is determined by multiple factors. There are three main factors limiting the resolution in principle (Davis et al., 2001).

1. The maximum OPD, which is always limited. In a real FTS the interferogram has to be truncated at some point, which corresponds to multiplying the ideal infinite interferogram with a boxcar function. In frequency space, this is then a convolution with a sinc-function. The width of the sinc-function decreases with the size of the boxcar function or maximum OPD and scales with a constant factor η. This limits the resolution to
$$\delta f = \frac{\eta c}{\mathrm{OPD}} \approx \frac{1.20671 c}{\mathrm{OPD}}. \tag{3.6}$$
2. The diameter of the entrance aperture d_{ap} is always larger than an ideal point source. Depending on the focal length of the collimator f_{col}, this changes the solid angle which is observed at the detector. The finite extension of the source leads to a decrease in fringe contrast scaling with a sinc function of the OPD and frequency. The resulting resolution limit is thus frequency dependent and given by
$$\delta f = f \frac{d_{\mathrm{ap}}^2}{8 f_{\mathrm{col}}^2}. \tag{3.7}$$
3. Lastly, self apodization also plays a role. Apodization means that the fringe amplitude decreases over the length of the interferogram. Self apodization may be caused by misalignment or limited coherence of

the light source, which leads to a decrease in fringe contrast for longer OPDs. An apodization may also be applied on purpose to change certain characteristics of the ILS, usually the strength of the sidelobes. A detailed review on apodization or windowing functions was given by Harris (1978).

Each of these factors changes the ILS. The first one is a sinc function in the frequency domain, while the second is a boxcar function. The third can be more complex. Each of these are convolved with the true spectrum of the light source, which broadens all spectral lines and thus limits the resolution.

Usually, the aperture diameter is chosen, so that the resolution is limited by the maximum optical path length difference, because otherwise not only the resolution is limited, but noise is also increased (Davis et al., 2001).

3.3 **Measurement errors and correction**

Measurement errors in the FTS can arise from multiple causes: systematic errors in the OPD determination, the interferogram not being sampled at exactly zero OPD, the zero OPD point being wavelength dependent due to optical or electrical dispersive effects, misalignment or asymmetries in the interferometer arms (Porter and Tanner, 1983; Learner et al., 1995). These errors may shift apparent line position and affect the ILS, leading to asymmetries and typically a shift to lower frequencies (Saarinen and Kauppinen, 1992).

3.3.1 Interferometer errors

There are multiple ways in which the interferometer can be misaligned, or imperfect:

- The aperture is never a perfect point source. This leads to aperture broadening, which is a frequency dependent broadening of the ILS (Ahro et al., 2000).
- The aperture or light source may not be in the focus of the collimator, or in focus but not on the optical axis. This leads to a line shape distortion, where the side-lobe on the lower frequency side merges into the main peak (Saarinen and Kauppinen, 1992).
- The retroreflector travelling in one interferometer arm may not follow the optical axis perfectly, also broadening and distorting the ILS (Kauppinen and Saarinen, 1992) .

- The detector position may be off-axis, leading to a change in ILS, depending on the shape of the detector (Genest and Tremblay, 1999).
- The OPD may be measured incorrectly, due to laser instability or non-parallel alignment of science and reference beam (Ahro et al., 2000). The latter leads to a stretching or compression of the frequency axis of the spectrum.
- General optical aberrations, e.g., spherical aberrations, coma, field curvature, astigmatism and distortion affect the ILS (Genest and Tremblay, 2002).

3.3.2 Phase correction

Due to these errors, the interferogram is not symmetric around zero OPD anymore. The phase of the spectral components is shifted with respect to zero OPD and thus leads to asymmetric components. The asymmetric components in the interferogram lead to a complex valued spectrum when calculating the Fourier transform. The aim of a phase correction is to correct these errors, or the phase, so that the correct, physical, real valued spectrum is obtained.

Multiple phase correction methods exist. The easiest one, in a mathematical sense, is to record a double-sided interferogram. This means that the retroreflector travels equal distances on both sides of the zero OPD point. In such an interferogram the full asymmetric contribution is recorded as well and no special phase correction after the Fourier transform is required (Connes, 1963). This of course increases the instrument size, as for the same resolution the maximum OPD that has to be scanned in both directions.

Two main methods exist to correct single-sided interferograms, i.e., interferograms with differing lengths on the opposite sides of zero OPD. Both methods require at least a small symmetric section around zero OPD to obtain a low resolution phase spectrum. Therefore, it is not possible to start recording the interferogram at zero OPD if a phase correction is to be applied.

For the Forman method, a symmetric section of the interferogram around zero OPD is Fourier transformed. The resulting phase spectrum is truncated to the wavelength region under investigation (Forman et al., 1966). Then the inverse Fourier transform of the truncated phase spectrum is calculated and convolved with the original full interferogram. The process may be iteratively repeated to improve the phase correction.

The Mertz method also makes use of the phase spectrum of a symmetric interferogram section around zero OPD (Mertz, 1966). For the phase correction the Fourier transform of the full spectrum is multiplied with a complex exponential which has the phase spectrum of the symmetric interferogram part as its argument.

The two algorithms are similar operations in different domains and can be related by the convolution theorem. However, it was found that the Forman method performs worse, if an inadequate weighting function around zero OPD is chosen (Sanderson and Bell, 1973). This weighting function is necessary, as otherwise the double-sided part of the interferogram would be counted twice.

The Mertz method of phase correction was later extended as it was found to be erroneous for emission line spectra (Learner et al., 1995). In emission spectra, the phase is often ill-defined as large regions of the spectrum have zero intensity. As a remedy, Learner et al. (1995) suggested the following approach: Only the phase values of strong emission lines should be considered and then fitted by a polynomial to interpolate the phase data. Since a small symmetric interferogram leads to a low resolution phase spectrum, this requires using a symmetric region around zero OPD which is as large as possible. There were two reasons, to keep the symmetric part of the interferogram small. One reason was the additional space required for the interferometer. The other reason was the additional required computation time. Due to faster computers and the invention of the fast Fourier transform algorithm (Cooley and Tukey, 1965), the computation time was not an issue anymore. Subsequently, newer FTSs often allow the recording of a larger symmetric section of the interferogram.

The phase correction of LFC spectra requires a further extension of the Mertz phase correction method (Huke et al., 2019a). The initial steps of this method are similar to those used in the sub-nominal method for FTSs. The sub-nominal method leverages the unique spectrum of the LFC to measure absorption spectra with a resolution much better than the nominal resolution of the FTS (Maslowski et al., 2016; Rutkowski et al., 2016). The first step of both the sub-nominal method and the phase correction is a truncation of the interferogram so that each comb line is sampled by the same number of points. Then a complex phase shift is applied, to shift the sampling, so that sampling point is always at the peak of the comb line (see Fig. 3.2). After these two steps, the phase spectrum exhibits not just a single phase trend, but multiple

”phase strings” as shown in Fig. 3.2c (Huke et al., 2019a). Each phase string corresponds to one sample point of the comb line. The phase spectrum for the Mertz phase correction is obtained as follows: First, a polynomial is fitted to the data points in the phase spectrum corresponding to the sample point at the line peak. For each of the remaining phase strings, this polynomial fit is then shifted by a constant offset to match each phase string. This is then the phase spectrum used for the phase correction.

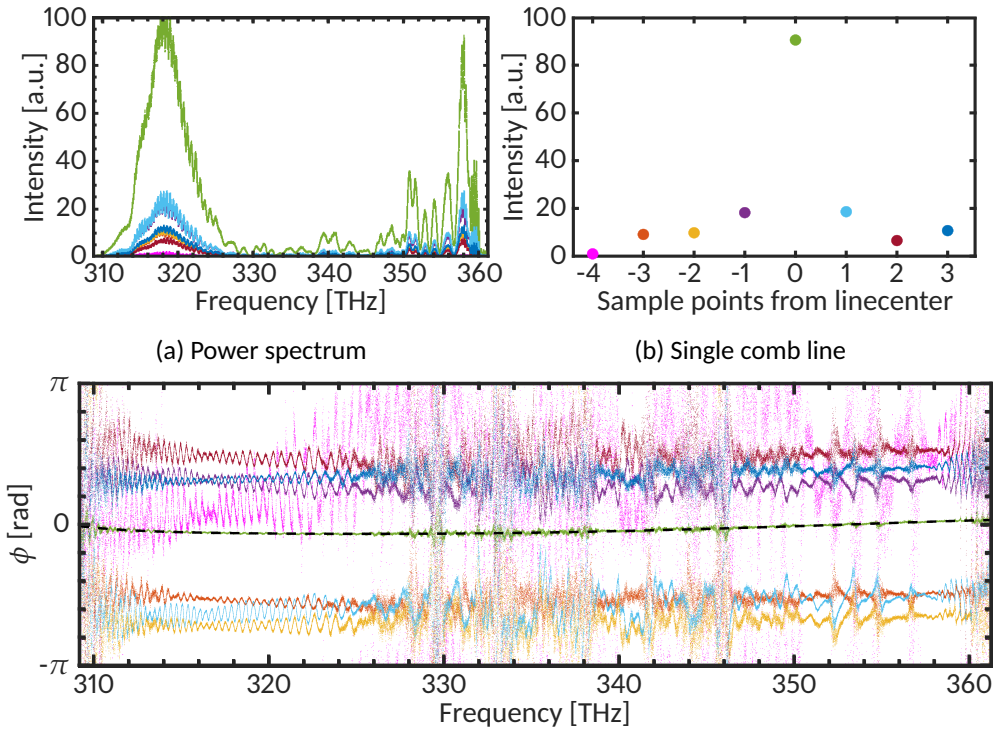

(a) Power spectrum

(b) Single comb line

(c) Phase spectrum

Figure 3.2: Illustration of the phase correction method for LFC spectra. Panel (a): A single measured power spectrum of the LFC, sampled at exactly eight times the repetition rate. Panel (b): A single comb line illustrating how each line is sampled and correspondingly color-coded. Panel (c): The detected phase spectrum, showing the individual ”phase strings”, each corresponding to a different sampling point on the comb lines and the fit to phase string corresponding to the peak sample points (black dashed line).

These phase correction methods only correct linear phase errors (Kauppinen et al., 1978). Some issues like an asymmetric ILS can remain, because the phase errors which depend on the OPD are not corrected for (Saarinen and Kauppinen, 1992). These phase errors can be identified by isolating a single unresolved line and calculating the inverse Fourier transform of this single line. The phase of the complex result is then a measure of this OPD dependent

phase error (Kauppinen and Saarinen, 1992; Saarinen and Kauppinen, 1992). This result can be used as an indicator to improve the FTS alignment (Ahro et al., 2000) and thus eliminate these errors or to calculate a correction of the interferogram (Kauppinen et al., 1978). Alternatively, a matrix inversion method exists to correct these errors (Desbiens et al., 2006).

Since we are mainly concerned with measuring an LFC we used the phase-correction method given by Huke et al. (2019a) whenever possible. We did not use the correction method for OPD-dependent phase errors as the comb lines in our spectra are all influenced by the side lobes of their corresponding neighbors and it is thus not feasible to calculate the Fourier transform of a single line.

3.3.3 Spectral intensity variations

Spectral intensity variations of the light source are more detrimental in FTSs compared to dispersive spectrographs, as they lead to a multiplex disadvantage (Hirschfeld, 1976; Davis et al., 2001). Due to the multiplex measurement, the intensity noise is simultaneously affecting all spectral channels, rather than just the spectral region in which it occurs. This is particularly relevant in our case, as the supercontinuum generation process usually leads to intensity fluctuations. There are possible ways to deal with source intensity fluctuations, e.g., by using a balanced detection in the FTS (Mertz, 1967; Burroughs and Chamberlain, 1971). In a balanced detection the second output from the FTS is also measured. This output receives the same information as the other but the interference pattern is just exactly opposite (also called a negative interferogram). To remove the source intensity fluctuations, the corrected interferogram I is calculated from the two interferograms i_1 and i_2 by:

$$I = \frac{i_1 - i_2}{i_1 + i_2} \tag{3.8}$$

Further correction is required to account for the different gains and spectral responses of the two detectors, as well as possible differences in phase between both outputs (Ahern and Pritchet, 1974). Thus, intensity fluctuation noise can be reduced by two orders of magnitude using a balanced detection method (Foltynowicz et al., 2011b,a). Our FTS does not offer the capability of a balanced detection.

3.4 Calibration of a Fourier transform spectrograph

To mitigate these numerous potential measurement error sources, the FTS measurements can be calibrated. Calibration of the frequency scale of an FTS spectrum may be performed by using frequency standards. Since the frequency scale is well defined and linear, higher order corrections are not necessary. In fact, the calibration can be performed by computing only a single dispersion factor (Learner and Thorne, 1988; Redman et al., 2011):

$$k_{\text{eff}} = \frac{f_{\text{ref}}}{f_{\text{FTS}}} - 1, \tag{3.9}$$

where f_{ref} is the known absolute frequency of the reference line and f_{FTS} is the frequency measured by the FTS for this line. This dispersion factor then serves as a correction for the entire frequency scale:

$$f_{\text{corr}} = (1 + k_{\text{eff}}) f, \tag{3.10}$$

where f is the original frequency scale. The precision of this dispersion correction can be increased by increasing the number of reference lines. Using a frequency comb, even a two-factor calibration is possible, where an additional offset is also taken into account (Huke et al., 2019b):

$$f_{\text{corr}} = (1 + k_{\text{eff}}) f + \delta k(k_{\text{eff}}), \tag{3.11}$$

where δk is an offset that linearly depends on the factor k_{eff}. The two-factor calibration can improve the calibration precision by an order of magnitude (Huke et al., 2019b). Since for an LFC the spacing between the lines is constant, this two-factor calibration can be performed using the equation

$$f_{\text{corr}} = (f - f_{\text{CEO,FTS}}) \frac{f_{\text{rep,ref}}}{f_{\text{rep,FTS}}} + f_{\text{CEO,ref}}, \tag{3.12}$$

where $f_{\text{rep,ref}}$ and $f_{\text{CEO,ref}}$ are the stabilized comb frequency values and $f_{\text{rep,FTS}}$ and $f_{\text{CEO,FTS}}$ are the ones measured by the FTS.

3.5 Fourier transform spectrograph setup

At our institute, we use a commercially available FTS, the IFS 125HR (Bruker Optics). It has one fixed arm with a length of 45 cm. The total travel distance of the retroreflector in the other arm is 250 cm. The setup can be used to record fully symmetric interferograms with a maximum OPD of 45 cm or asymmetric interferograms with a maximum OPD of 205 cm. There are two main contributions to the resolution limit. The dominant limit of our setup is given by

the maximum OPD. Using Eq. 3.7 this maximum OPD for asymmetric interferograms gives a bound to the resolution of 176 MHz for all frequencies. The minimum entrance aperture diameter of the FTS is 0.5 mm, which in combination with the focal length of the collimating mirror ($f_{col} = 418$ mm) leads to a limiting resolution of 53.7 MHz at 300 THz. The next larger aperture with a diameter of 1 mm would lower the resolution to 214 MHz but increases the amount of light in the interferometer.

The FTS is operated at ambient room temperature around 20 °C. It can be evacuated to a level of ≈2.5 µbar, reducing measurement errors caused by the remaining atmosphere.

Different beam splitters and detectors for different frequency regimes are available. For observations in the visible and near infrared wavelength ranges a quartz beam splitter and a Si-detector are used. For near and mid infrared observations a CaF beam splitter and an InGaAs- and an InSb-detector are available, while light sources in the mid to far infrared regime can be measured with a KBr beam splitter and an MCT-detector (for an overview on beam splitter materials and the appropriate frequency ranges see Tab. 5.2 in Griffiths and Haseth (2007, p. 137)).

A frequency stabilized HeNe-laser (SIOS model SL04) is launched in parallel with the science light in the FTS and provides the OPD reference. According to measurements by the manufacturer, it is stabilized to within ≈1 MHz corresponding to a relative stability of $2.2 \cdot 10^{-9}$.

To reduce the light lost at the pinhole and to enable simultaneous observations with two light sources, the source chamber before the entrance aperture has been modified (Schäfer et al., 2020a). A filter wheel allows the selection of different optics, to switch between single source and two source measurements. The light from two different sources can be combined via a dichroic beam splitter, so that the light from one source above the cut off wavelength and light from the other source below the cut off wavelength is combined. Both sources are then recorded in the same interferogram but their spectra do not overlap. The current options are two beam splitters with cut off wavelengths of 650 nm or 805 nm (Thorlabs DMLP650L or DMLP805L respectively). A single light source can be measured by switching the filter wheel to either an empty slot or to a mirror, depending on the input port being used.

3.6 **Current comb calibration performance**

Using the setup described above, in combination with the LFC described in Ch. 2, a calibration of the FTS has been demonstrated (Huke et al., 2019b). The LFC is located in a different laboratory than the FTS. Light from the LFC is transported to the FTS via a 100 m long multimode fiber (CeramOptec, low-OH, Ø= 200 mm, NA=0.22). The light exiting this fiber has a highly inhomogeneous spatial distribution (Huke et al., 2021). To provide some spatial scrambling, i.e., to homogenize the spatial distribution, we butt-couple the long fiber to a short hexagonal fiber (CeramOptec, Ø= 525 mm, NA=0.26).

For calibration, the repetition rate and offset frequency of the LFC are stabilized and monitored. The recorded interferograms have to be phase corrected and the line center of each comb line in the spectrum is fitted. From the fitted line center values, the two comb frequencies are calculated. In combination with the actual, stabilized comb frequency values, the frequency axis can be corrected. With a supercontinuum spectrum of the LFC spanning from about 310 to 370 THz, containing about 65,000 usable comb lines, a single measurement uncertainty of $\approx$65 kHz or 0.15 m s^{-1} has been achieved (Huke et al., 2019b).

Part II

IMPROVING FREQUENCY COMB CALIBRATION

4

DESIGNED NONLINEAR FIBER

Most laser frequency comb (LFC) applications require a supercontinuum broadening of its optical spectrum. The supercontinuum broadening is usually achieved using nonlinear media. It is necessary to employ the f-2f technique used to control the offset frequency. Also, spectral broadening increases the utility of the LFC as a broader spectral coverage enables a larger range of measurements and increases the spectral region which can be calibrated in dispersive spectrographs. In retrospect, it is not surprising that the first demonstrations of LFCs (Reichert et al., 1999; Jones et al., 2000) came shortly after the invention of the photonic crystal fiber (PCF), which reduced the cost of creating octave spanning supercontinuua (Ranka et al., 2000). To achieve this, much research was required.

The first observations of nonlinear broadening of maser or laser light in materials were reported in the 1960s (Stoicheff, 1963; Jones and Stoicheff, 1964; Brewer, 1967; Shimizu, 1967). The first generation of white light was achieved in 1970 by Alfano and Shapiro (1970). They were able to generate a spectrum spanning 300 nm in glass using a pulsed laser. This phenomenon is now known by the term “supercontinuum” generation (Manassah et al., 1985). The generation of supercontinuum spectra coincided with the appearance of self-trapped filaments (Alfano and Shapiro, 1970; Werncke et al., 1972). Self-trapped filaments only occur only at very strong light intensities. The strong electric field of the light changes the refractive index via the optical Kerr-effect and thereby the light focusses itself (Chiao et al., 1964). The self-focussing then increases other nonlinear effects which lead to a spectral broadening, such as self-phase modulation or four wave mixing. While the relevant effects for the spectral broadening were known or suspected initially, a thorough theoretical explanation of supercontinuum generation in bulk materials was given much later by Gaeta (2000).

Nonlinear broadening can also be observed in the simpler case of optical waveguides or fibers (Ippen, 1970; Stolen, 1975; Stone, 1975). The powers required are much lower than in bulk materials, as the confinement of the

light in the fiber core results in high, maintained power densities (Stolen, 1975; Lin and Stolen, 1976). In fibers, the key processes for nonlinear broadening were identified to be stimulated Raman scattering, self phase modulation, cross phase modulation and four wave mixing (Lin and Stolen, 1976; Stolen et al., 1984; Baldeck and Alfano, 1987; Ilev et al., 1996).

When pulsed laser sources in the anomalous group velocity dispersion (GVD) regime (see also Sec. 2.3.2) of fused silica (>1.3 µm) became available, optical solitons could be observed (Mollenauer et al., 1980). Solitons are pulses or wave packets, which maintain their shape while propagating, i.e., they are not dispersed. In solitons further nonlinear broadening processes were discovered: the soliton self-frequency shift and soliton-fission, i.e., the splitting of a soliton into two or more independent solitons (Mitschke and Mollenauer, 1986; Gordon, 1986; Beaud et al., 1987; Kodama and Hasegawa, 1987; Gouveia-Neto et al., 1988).

With a PCF the generation of supercontinuum spectra places even lower requirements on the laser input power. A PCF consists of a very small core, surrounded by a periodic pattern of air holes in the cladding (see Fig. 4.12b) (Knight et al., 1996). This photonic crystal cladding leads to a much higher refractive index difference than for a conventional step-index fibers. By engineering the photonic crystal cladding the zero dispersion wavelength—the onset point of the anomalous GVD-regime—can be shifted from 1.3 µm down into visible wavelength ranges (Mogilevtsev et al., 1998). This enables the propagation of solitons at these wavelength ranges. Additionally, the effective area of the PCF can be designed to be very small, which further increases the nonlinearity (Broderick et al., 1999). Ranka et al. (2000) exploited these effects to generate an octave-spanning supercontinuum with a mode-locked Ti:sapphire laser with a pulse energy of 0.8 nJ. Before the invention of these nonlinear fibers, such a feat required pulse energies a factor of a thousand higher (Dudley et al., 2006). This meant that broadband supercontinuum spectra were now widely available which enabled the self-referenced LFCs.

By tapering a fiber—i.e., heating and stretching it to reduce the diameter—even in regular multi-mode fibers, similar spectral broadening can be observed (Birks et al., 2000). The fundamental principle is similar to that of a PCF, as both can be approximately described as a thin glass rod suspended in air (Birks et al., 2000; Ravi, 2020). For tapered fibers the GVD then depends

on the fiber waist diameter instead of the air hole geometry around the fiber core.

The output spectra of nonlinear fibers can be predicted using simulations (Coen et al., 2001; Husakou and Herrmann, 2001). Due to the complex interaction of multiple nonlinear effects in a nonlinear fiber there are no straightforward analytical formulas to consider. While different effects become more dominant in different power and wavelength regimes, these regimes overlap. Due to this, it is not possible to just isolate a single effect when simulating supercontinuum broadening processes. However, using a generalized nonlinear Schrödinger equation (GNLSE) it is possible to take all relevant effects and their interaction into account and to predict and reproduce experimental results (Coen et al., 2001; Husakou and Herrmann, 2001; Ravi et al., 2018).

We aim to design a tapered fiber that generates a stable, broad and flat supercontinuum from our Ti:sapphire laser (see Ch. 2). To do this we use a dual approach by tapering a PCF to a specific geometry as demonstrated by Ravi et al. (2018). We simulate different taper geometries to predict the output spectra. Additionally, we construct a mounting stage to facilitate the in- and outcoupling of the light into the fiber and to keep the fiber in a stable environment.

In this chapter, we first describe a grid simulation of tapering geometries and the final taper design we obtained from it. Then, we describe the optical setup and the manufactured tapered fibers. Finally, results from this work are discussed.

4.1 Simulation of fiber taper geometries

We want to design a tapering geometry of a PCF, with the aim of achieving a flat and stable output spectrum of the LFC. During the tapering process multiple parameters can be influenced, such as the diameter at the taper waist, its length, but also the length of the transition between untapered fiber and taper waist. By using a simulation we can judge the quality of the output spectrum without having to actually produce the tapered fiber. This allows us to test a wide range of taper parameters. We are using a grid of different parameters since the process is nonlinear and therefore multiple different regions of good parameter sets may exist.

The ideal spectrum for us would be a flat top, with a width that covers the wavelength range from 750 to 1000 nm and is stable in time. In reality, this is

most likely not possible, so we have to try to approximate this ideal spectrum. The simulated example spectrum in Fig. 4.1 shows some characteristics of supercontinuum spectra we aim to avoid.

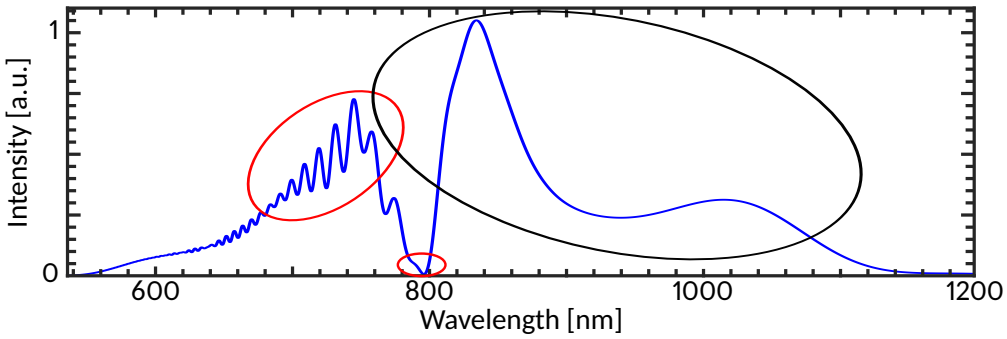

Figure 4.1: Example of a simulated supercontinuum spectrum. The large red circle shows short scale variations caused by the modulational instability. The small red circle indicates a region with a very low spectral intensity. The black circle indicates a broad, slowly varying spectral region with a low dynamic range, which is what we would like to achieve.

One feature often observed in supercontinuum spectra are short scale variations caused by the modulational instability. These are typically not stable in time (Dudley and Coen, 2002). This means that the peaks change in wavelengths and intensity. As this causes errors in the calibration, we want to avoid these instable features. Other spectral features can be dips in the spectrum, even to the point that there is no light covering a spectral region. Since this region then cannot be calibrated, or in the case of a Fourier transform spectrograph (FTS) less lines are available for calibration, this is also undesirable. Finally, the supercontinuum broadening can be so strong that a large amount of the laser power is in spectral regions where it is not useful. While for many applications the light from the LFC is still more than enough, this can become an issue if a spectrum control setup is used (see Ch. 6).

In order to judge the quality of the spectra from our simulations we defined four quality check parameters. These are as follows:

1. The maximum of the moving standard deviation with a window of about 2.9 THz (corresponding to about 6.1 nm at 800 nm). We empirically found that this window size is appropriate to detect peaks in the spectrum caused by the modulational instability.
2. The mean dynamic range in the spectral range from 750 to 1000 nm, since this is the wavelength region we are interested in. If large portions

of the spectrum have a low intensity in this wavelength range, this value will drop.

3. The fraction of the spectral power outside the spectral range from 750 to 1000 nm.
4. The overall spectral bandwidth where light with an intensity higher than 30 dB below the maximum is generated. Below this threshold the comb lines intensity is so low that they are not used for calibration of our FTS anymore. Thus, this is a measure of the bandwidth of the usable supercontinuum.

For the simulation of different fiber taper geometries, we adapt an existing code (Ravi, 2020, App. A). The input for this code are the parameters of the laser pulse and the geometrical shape of the tapered fiber. The output is the evolution of the pulse during propagation and the corresponding change in the optical spectrum. To calculate this, the code solves the GNLSE for the given input parameters as well as the nonlinear parameters of the fiber, the fiber dispersion and Raman response. Since these parameters are very specific to the PCF, they are only included for one specific nonlinear fiber (Crystal Fiber NL-2.8-850-02). These parameters were also calculated by Ravi (2020, App. A) using a commercial software. They have to be calculated for the same photonic crystal geometry at different diameters, in order to be able to solve the GNLSE correctly for the tapered parts of the fiber which are smaller in diameter than the original one. Consequently, we obtained the same fiber for our setup.

A measure of coherence is also included in the code. It is calculated by repeatedly solving the GNLSE with random noise seeds and comparing the different outputs. This simulates shot-to-shot noise, i.e., how the output spectrum might vary from pulse to pulse. Raman noise is not included in this simulation of coherence as shot-to-shot noise is dominant in our conditions (Ravi et al., 2018; Corwin et al., 2003). Shot-to-shot coherence can be relevant in FTS measurements, as the interference pattern of different pulses is recorded at higher optical pathlength differences (OPDs) (see Ch. 3). A spectral dependence of shot-to-shot coherence may then lead to erroneous measurements when the interference of two different pulses is recorded in the interferogram.

4.1.1 Grid simulation

For the grid simulation, we embedded the code by Ravi into a framework which enabled a systematic variation of the input parameters. The code considers five different geometrical taper parameters (Ravi et al., 2018). These are illustrated in Fig. 4.2 and defined as follows:

- length of the fiber before the taper L_0
- length of the taper waist L_w
- diameter of the taper waist d_w
- length of fiber after the taper L_1
- up and down taper lengths L_{t1} and L_{t2} (always equal length)

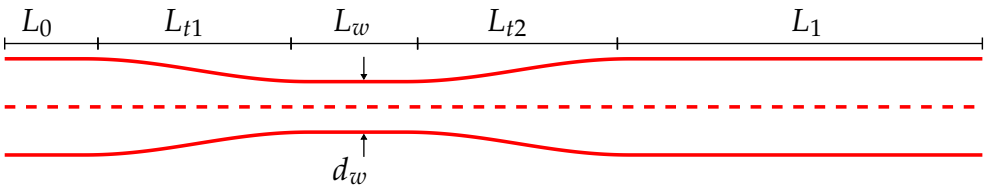

Figure 4.2: Schematic drawing of a tapered fiber and the different taper parameters.

We varied four of these parameters with seven equally spaced values in each range being simulated (see Tab. 4.1) leading to 2401 simulated spectra. The initial fiber length was fixed to $L_0 = 0.1\,\text{mm}$, since a longer length before the taper generally leads to more variable spectra. The input pulse duration was fixed at 40 fs, which is a rough estimate of the pulse length of our laser since we could not measure the pulse length before the fiber. Further input pulse parameters are the central wavelength of 797 nm and the input power of 500 mW, which are taken from measurements by the manufacturer and us respectively.

From the output spectra of the simulations, we then calculated the spectrum quality parameters for the different fiber taper geometries. We then reduced

Table 4.1: Range of the different fiber taper parameters used in the grid simulation.

Parameter	Lower limit	Upper limit
L_{t1} and L_{t2} [mm]	3.9	6.2
d_w [µm]	1.625	1.986
L_w [mm]	0.16	0.24
L_1 [mm]	1.8	7.2

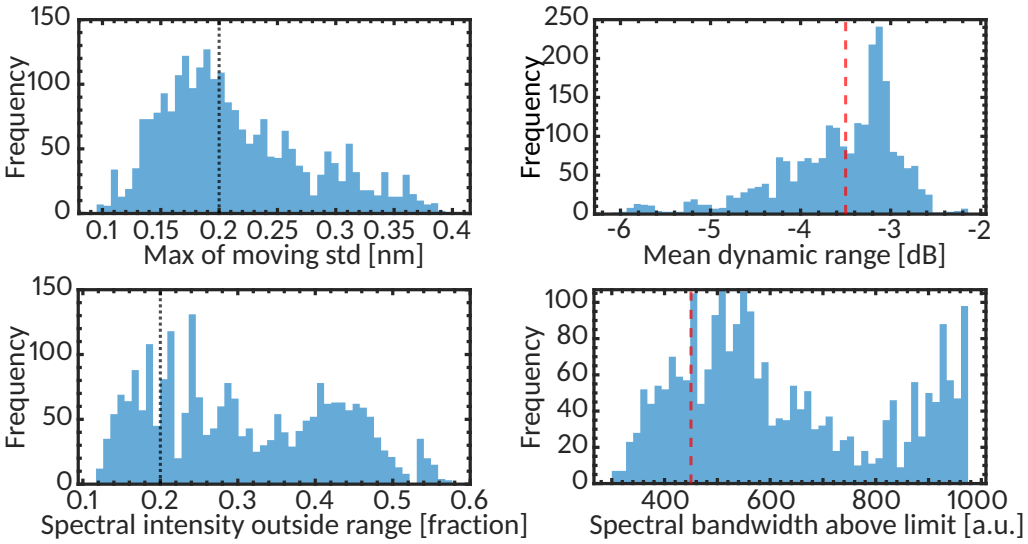

Figure 4.3: Histograms of the simulation quality parameters. The distribution of the maximum of the moving standard deviation is shown in the top left, the mean dynamic range in the top right, the fraction of power below the threshold in the bottom left and the spectral bandwidth in the bottom right. The black dotted lines indicate upper bounds while the red dashed lines indicate lower bounds for the selection criteria.

the data set to the best performing geometries according to our spectrum quality parameters. The cutoffs we set are as follows (see Fig. 4.3):

The maximum of the moving standard deviation was set to 0.2, which includes about 49.8 % of the whole data set. While this is not a very strong cutoff, it is enough to exclude the short scale spectrum variations. We set the cutoff for the mean dynamic range to a lower limit of −3.5 dB, including about 54.4 % of the whole data set. This prevents a dominance of regions with no intensity. In combination, these two parameters cut down the data set to 708, about a third of the data set. The fraction of spectral intensity lost was limited to 0.2, which is a strong cutoff and by itself only includes 22.2 % of the whole data set. However, since there is a large amount of light lost in the spectrum control setup (see Ch. 6), we optimized this value since we are satisfied with the other two. After enforcing this criterion 337 taper geometries remain, which already have relatively similar output spectra. Finally, we set the width of the spectrum above 30 dB to 350 nm, a condition which is fulfilled by about 80.9 % of the whole dataset. This leads to broader spectra and cuts down the selection to 76 taper geometries.

An overplot of the resulting spectra from all selected taper geometries in Fig. 4.4 shows that all spectra have similar characteristics. Each consists only of two to three overlapping peaks and only some exhibit a minimal

additional structure. We inspected one of the selected taper geometries more thoroughly. From the time domain output of the simulation shown in Fig. 4.6, it becomes apparent that each of these peaks corresponds to a soliton. The plot shows the onset of two soliton fission processes during the fiber propagation. This indicates that these output spectra are more stable than a broader, more variable supercontinuum which is caused by a stronger impact of the modulational instability (Dudley and Coen, 2002).

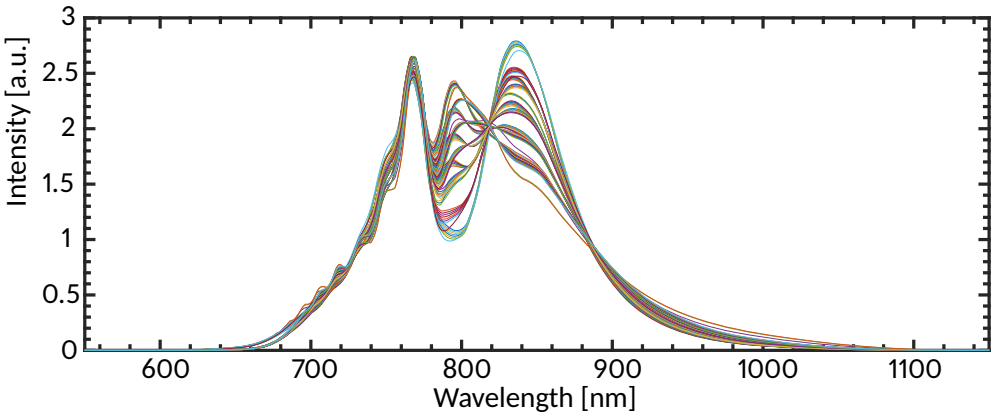

Figure 4.4: Spectra resulting from the 76 taper geometries selected from the grid of taper parameters by the criteria shown in the histograms (see Fig. 4.3).

4.1.2 Verification of final taper design

We computed the mean and standard deviation over the fiber parameters in the 76 selected simulations which are shown in Fig. 4.5. The higher standard deviations for L_w and L_1 imply that the grid steps we chose for these two parameters have a comparably lower impact than the grid steps for L_{ti} and d_w. In order to more efficiently simulate a new grid, the step size of these two variables could be increased.

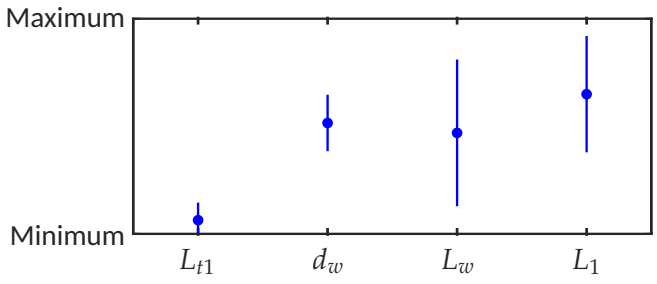

Figure 4.5: The mean values and standard deviation of the simulation parameters of the 76 selected spectra relative to the simulated range. Minimum and maximum refers to the respective values specified in Tab. 4.1.

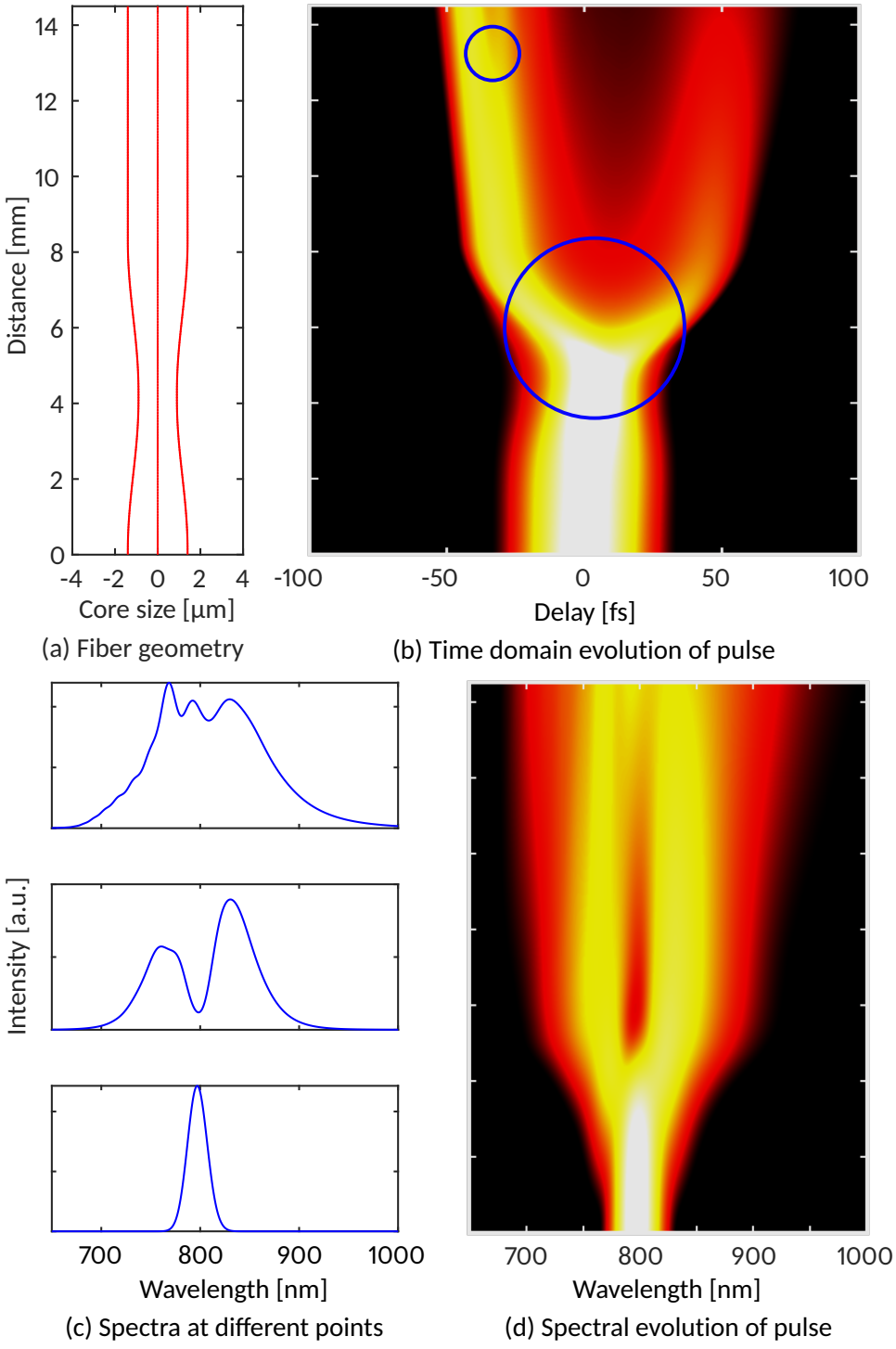

Figure 4.6: Panel (a): Geometry of the tapered fiber. Panel (b): Simulated evolution of the pulse during propagation through the fiber. The blue circles indicate where soliton fission occurs. Panel (c): The three simulated spectra correspond to the input spectrum (bottom), the spectrum after the first soliton fission (middle) and the output spectrum (top). Panel (d): Simulated evolution of the spectrum during propagation through the fiber.

We used the mean parameters from the simulations selected from the grid as our final taper design (for the taper parameters see Tab. 4.2 in Sec. 4.2.2). To ensure that the mean geometry would suit our needs, we made further simulations with this geometry. In these simulations we varied the input pulse parameters. Since the exact value of the pulse duration of our laser is not known, we wanted to make sure that this would not lead to a completely different supercontinuum spectrum. The input power and the pulse duration have similar effects since both affect the pulse peak power which is a crucial factor in the nonlinear broadening process. Therefore, we checked that we could compensate a wide range of pulse durations from 20 to 100 fs by varying the input power in the range from 100 to 1000 mW .

The final taper geometry we chose fulfills two purposes:

1. In a ”low” peak input power ($\approx$ 11 to 16 kW) regime, the output is smooth and slowly varying from about 650 to 1000 nm. This is similar to the result from the grid simulations (see Fig. 4.7a). This smooth output should also be stable in time and thus be more suitable for calibration of an FTS or echelle spectrograph.

2. In a ”high” peak input power ($\approx$ 19 to 25 kW) regime, the output is more variable and thus probably less useful for calibration purposes. The supercontinuum, however, extends over the range from 532 to 1064 nm (see Fig. 4.7b). This enables us to perform beat mode experiments with a (frequency doubled) Nd:YAG laser.

From each of these regimes, we selected one parameter set to simulate the shot-to-shot coherence (We only simulated one each, since this simulation is very time consuming). The parameters we used are 40 fs and 500 mW for the low peak power regime and 1000 mW for the high input power regime. These simulations show good coherence over the full spectral region where the intensity is sufficient (see Fig. 4.8). Typically, the coherence is better than 0.9998, meaning that shot-to shot coherence should not be an issue.

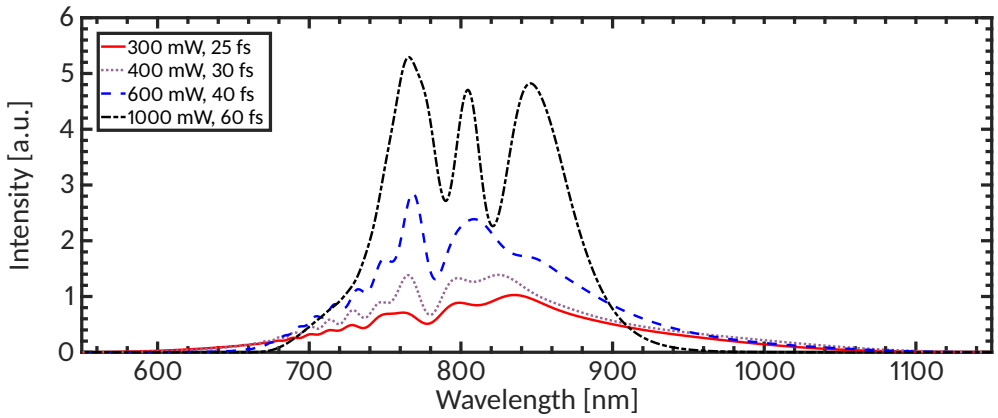

(a) Low peak power

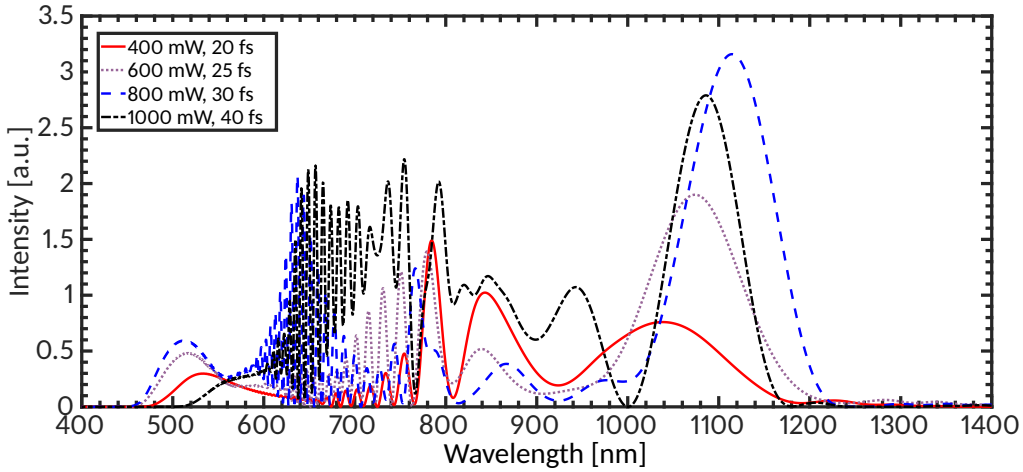

(b) High peak power

Figure 4.7: Simulations of the final taper geometry for different input powers and pulse durations. Panel (a): "Low" peak power regime. Panel (b): "High" peak power regime. Similar results are realized by choosing the right laser input powers for different pulse durations.

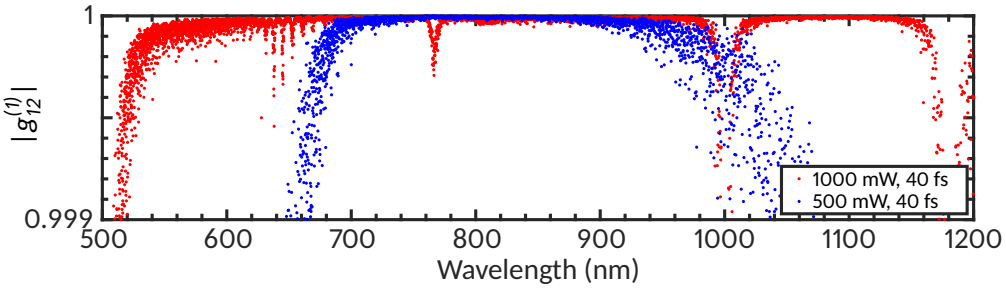

Figure 4.8: Simulated shot-to-shot coherence for two different input powers and a pulse duration of 40 fs of the final fiber taper geometry. Red dots indicate the coherence for 1000 mW, blue dots for 500 mW input power.

4.2 Nonlinear broadening setup

4.2.1 Fiber coupling stage

The setup for the designed nonlinear fiber replaces a coupling to a PCF with an FC/PC-connector inside the housing of the taccor comb unit. Using the existing structure leads to some restrictions in building the fiber coupling stage. However, placing the setup inside this housing has the advantage of a shielded environment which is temperature stabilized since the floor of the encasing is water cooled. Before the coupling stage, a $\lambda/2$-plate is used to adjust the polarization of the laser beam before it is coupled into the nonlinear fiber. Two three axis mounted mirrors and one piezo mounted mirror with tip-tilt capabilities allow fine alignment of the input beam. A CAD-model of the fiber coupling stage that follows is shown in Fig. 4.9.

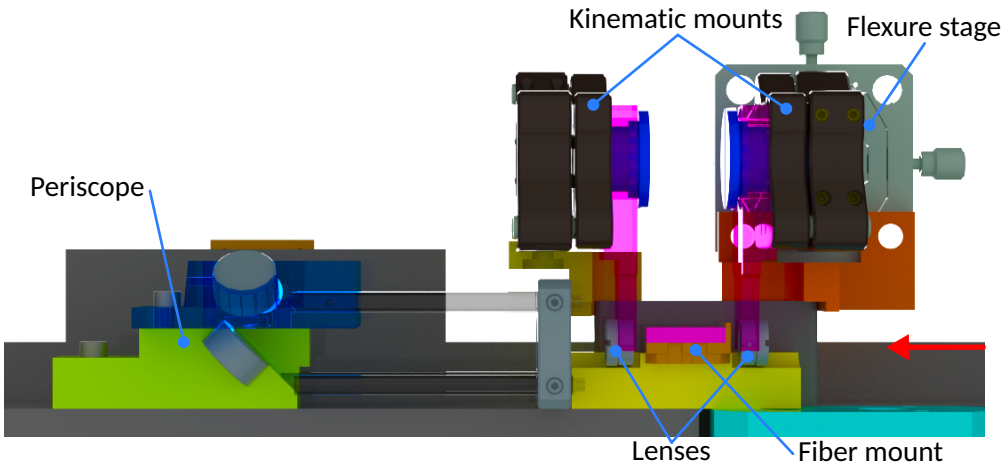

Figure 4.9: CAD rendering of the fiber coupling stage, showing a cut through the fiber axis. The light enters from the right side (red arrow) and is focussed into the fiber by a lens. The fiber itself is placed in the fiber mount consisting of two parts (pink and orange). Both lenses are fixed to the arms (pink), which are in turn attached to two 3 axis mirror mounts with a custom screw (dark blue). The adjustment stage holding the incoupling lens is mounted on an x-y flexure stage (grey). Behind the outcoupling lens a cage plate holds four cage roads. The cage roads position the custom built periscope (lime and light blue), which reflects the light out of the laser compartment.

The focusing lens (Thorlabs C230TMD-B) has a focal length of 8 mm. It is mounted on an arm which connects to a three axis mirror mount (Thorlabs KC05-T) for angular and coarse z-adjustment of the lens. For fine z-adjustment this mirror mount is connected to a flexure stage (Thorlabs CP1XY). The mount

of the collimating lens (Thorlabs C230TMD-B) on the backside of the fiber is similar, but not connected to a flexure stage as the z-position is not as crucial. The fiber itself is mounted in a small aluminium block (see Fig. 4.10) positioned by two rods. The fiber mount can be removed from the setup to exchange the fiber. The bottom part of the fiber mount has an L-shape with a conus hole on the front side. This is to block stray laser light going through the space between the two parts of the block, as was the case for an earlier version. The fiber mount serves as a heat sink and offers great positional stability even during a complete exchange, exceeding that of a standard FC/PC-coupling. Both lenses can be glued in place and all alignment elements removed, when the setup is finalized. Behind the outcoupling lens we added a small periscope with fixed mirrors, to reflect the light out of a small hole in the laser encasing.

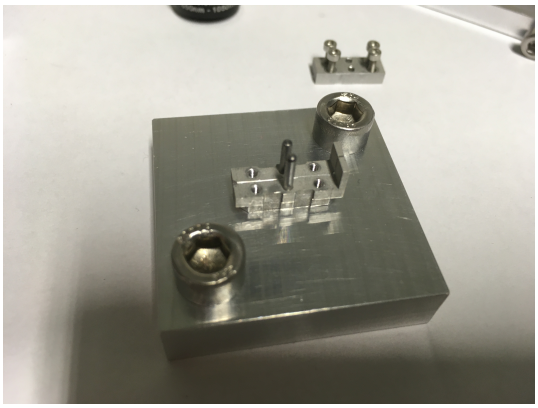

Figure 4.10: Fotograph of the fiber mount on the stage for placing the fiber in the block. The positioning rods are the same as in the actual setup. The fiber lies in the indentation of the fiber mount and can be seen by its reflection. In the back the top part of the fiber mount can be seen.

4.2.2 Designed tapered fibers

We aquired some of the NL-2.8-850-02 (Crystal fiber) PCF and sent it to Vytran for tapering. Vytran produced three samples of the designed tapered fiber. During the manufacturing process, small variations of the tapering parameters occur. The manufacturer uses micrographs to measure the actual values of the tapering process (see Fig. 4.12a). An overview of the final taper design parameters and the actual parameters of the three tapered fibers are given in Tab. 4.2. We simulated the real fiber taper geometries and found only marginal differences in the output spectra (see Fig. 4.11). The simulation of fiber 3 was

omitted for illustrative purposes, as its parameters fall in between the other two. We decided to use fiber 1 in our setup.

Table 4.2: Taper parameters of the three delivered fibers as measured by the manufacturer and the respective specified values. No measurement values were provided for L_0 and L_1, subsequently the overall length is also undetermined.

Parameter	Specification	Fiber 1	Fiber 2	Fiber 3
length before taper L_0 [mm]	0.1			
down taper length L_{t1} [mm]	4.0	4.27	3.93	3.94
waist length L_w [mm]	0.2	0.21	0.19	0.19
waist diameter d_w [µm]	1.8	1.84	1.76	1.77
up taper length L_{t2} [mm]	4.0	4.27	3.93	3.94
length after taper L_1 [mm]	6.2			
overall fiber length [mm]	14.5			

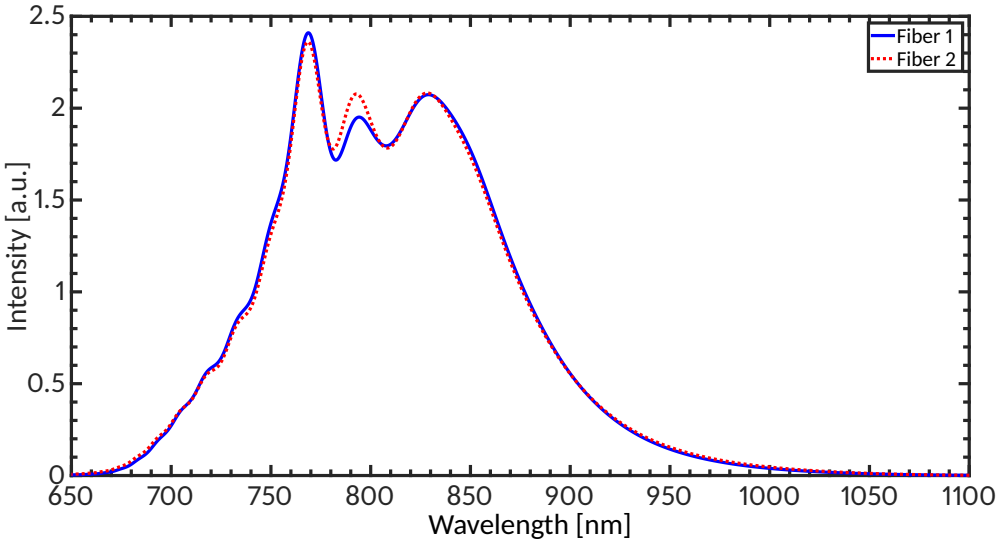

Figure 4.11: Simulated output spectra for the measured geometries of fiber 1 (blue solid line) and fiber 2 (red dotted line) (see Tab. 4.2) for 40 fs pulse duration and 500 mW input power.

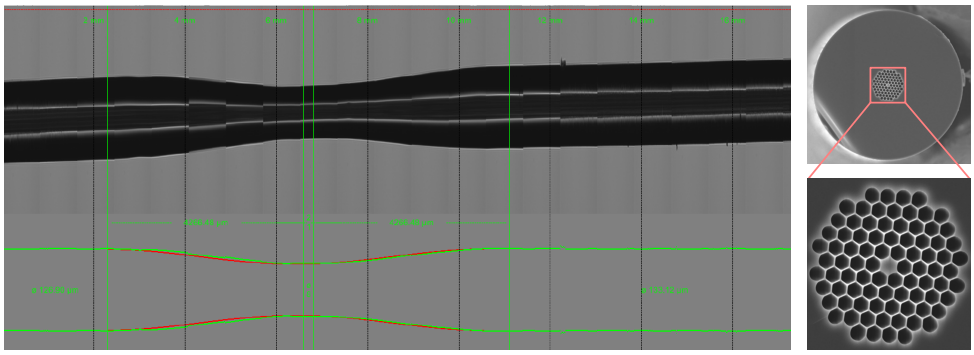

(a) Fiber taper measurement (b) Fiber front

Figure 4.12: Panel (a): Micrograph of the tapered fiber and the measurement of the taper parameters. Panel (b): Image of the fiber front face, showing the microstructure and airholes surrounding the fiber core.

4.3 Results and discussion

While we were able to couple light from the LFC into the fiber no significant spectral broadening was observed. The incoupling alignment is crucial and our setup does not provide enough degrees of freedom to couple sufficient light into the fiber core. We only achieved an output power of about 70 mW. In combination with the fact that the simulation slightly underestimates the required power (Ravi et al., 2018) a null result is plausible. Thus, we will have to forego the advantages of placing the fiber in the shielded environment of the laser encasing. Instead, we plan to built an external fiber coupling stage.

In principle, the tapered nonlinear fiber should create a supercontinuum that is much improved over the one that is generated by the nonlinear fiber currently used in the setup (NL-PM-750, 50 cm). A comparison between a measured spectrum from the current fiber and a simulation of the designed tapered fiber is shown in Fig. 4.13. The simulated spectrum exhibits much less structure and has a particularly smooth optical spectrum towards the near infrared from 750 nm.

Using the grid simulation, we were able to find a regime in which the soliton fission process is the dominant cause of supercontinuum generation. Since the simulated supercontinuum does not seem to be strongly affected by the modulational instability, its spectral envelope should also be stable in time. Furthermore, the designed tapered fiber should also provide a supercontinuum spectrum with a relatively low dynamic range.

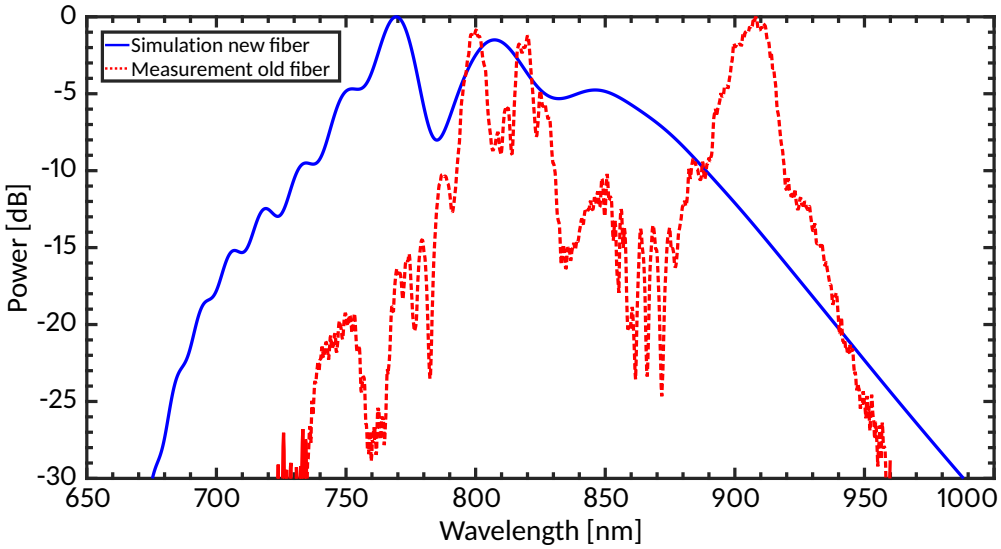

Figure 4.13: Comparison of the measured output from the nonlinear fiber currently in use (red dashed line) and the simulation of the tapered fiber (blue solid line).

For future applications, the grid could be expanded, both in the parameter space that is being explored, as well as the quality parameters that are being used to gauge the quality of the spectra. This might lead to even better supercontinuum spectra, since we also found multiple potentially useful parameter sets. The laser parameters could also be included in the grid simulation, as these are also parameters which can be altered to some degree. However, doing so would lead to long computation times for high power and thin waist configurations. Therefore, maybe some form of optimization as suggested by Ravi et al. (2018) would be required.

A further option which could be explored in designing supercontinuum spectra is the use of multiple tapered fibers in parallel. Certain geometries lead to significant broadening even at lower input powers of 200 mW. This means that a single laser like the one we use could power up to four or five tapered fibers. These could then be designed in such a way that a coaddition of the output light, possibly with variable proportions leads to a very flat spectrum. Using a grid of existing simulated spectra, this would be a feasible optimization problem.

5

CALIBRATION FROM THE INTERFEROGRAM

In the standard procedure of calibrating the Fourier transform spectrograph (FTS) with a laser frequency comb (LFC), all comb lines with sufficient signal-to-noise-ratio (SNR) are fitted to determine their line center. From the calculated line positions, the repetition rate and offset frequency of the LFC are computed and compared to the values to which the two frequencies were stabilized. The difference is used to calibrate the spectrum (see Sec. 3.4; Huke et al. (2019b). However, there is a correlation between the uncertainty in the line fits and variability in the spectral envelope (see Fig. 1.2). Furthermore, additional steps are necessary in order to compute a phase correction of the spectrum (Huke et al., 2019a). One of these additional steps is a truncation of the interferogram which reduces the resolution of the calculated spectrum.

Therefore, we tried to simplify this correction process and the line fitting by retrieving the offset frequency and repetition rate values directly from the interferogram rather than from the spectrum. This is possible because the FTS measurement of a coherent pulsed light source differs from that of a continuous light source. For example, there is not just a single interference fringe but multiple ones each time two pulses overlap spatially at the detector. The special characteristics of the interferogram are exploited in the sub nominal method, where an LFC is used to obtain absorption spectra with a resolution that is higher than the nominal resolution limit of the FTS (Maslowski et al., 2016; Rutkowski et al., 2016). Our method of retrieving the comb frequencies from the interferogram builds on some of the concepts used in the sub nominal method.

We applied the method of retrieving the comb frequncies from interferograms to measurements of the LFC with the FTS. Since we found some discrepancies in the comb frequency values retrieved from the spectrum and those retrieved from the interferograms, we simulated LFC interferograms mimicking the measurement data. The first goal of the simulations was to verify that the method works theoretically. The second goal was to determine the measurement effects as well as random and systematic errors which cause

the discrepancies between the comb frequency values obtained from the corrected spectra and those obtained from the interferograms.

This chapter starts with a description of the method of retrieving the comb frequencies directly from the interferogram. Then, a description of measurements, the results of applying the method and the calibration performance follows. Furthermore, we describe how to simulate LFC interferograms and compare results from simulated interferograms and measured interferograms.

5.1 Interferogram analysis

In the following, we describe a method to determine the comb frequencies—the repetition rate f_{rep} and the offset frequency f_{CEO}—directly from the interferogram. Since these are not independent measurements, we calculate the expected correlation of the errors in the two measurements.

5.1.1 Measuring the repetition rate

When recording an interferogram of a conventional white light source, there is one main interference peak at zero optical pathlength difference (OPD). Due to the highly coherent, pulsed output of the LFC, its interferogram has different characteristics than one of a conventional white light source. There is an interference peak, in the following referred to as burst, each time two laser pulses overlap spatially on the detector. At these points, the OPD corresponds to an integer multiple of the spatial separation b of two consecutive pulses (see Fig. 5.1). The distance between two consecutive burst centers is given by

$$b = \frac{c}{n f_{\text{rep}}}, \tag{5.1}$$

where c is the speed of light and n the refractive index of the medium (Balling et al., 2012). We can use this relationship to calculate the repetition rate if we know b:

$$f_{\text{rep}} = \frac{c}{nb}. \tag{5.2}$$

To get the distance b between two burst centers, we have to determine the exact position or OPD of each burst's center. For this purpose, we select a region of the interferogram around each burst center. From the selected data, we calculate the envelope of each burst using the Fourier transform method (Takeda et al., 1982). We then interpolate the envelope using spline interpolation. The OPD of the burst center is given by the OPD where the maximum amplitude of the interpolated envelope occurs (see Fig. 5.2).

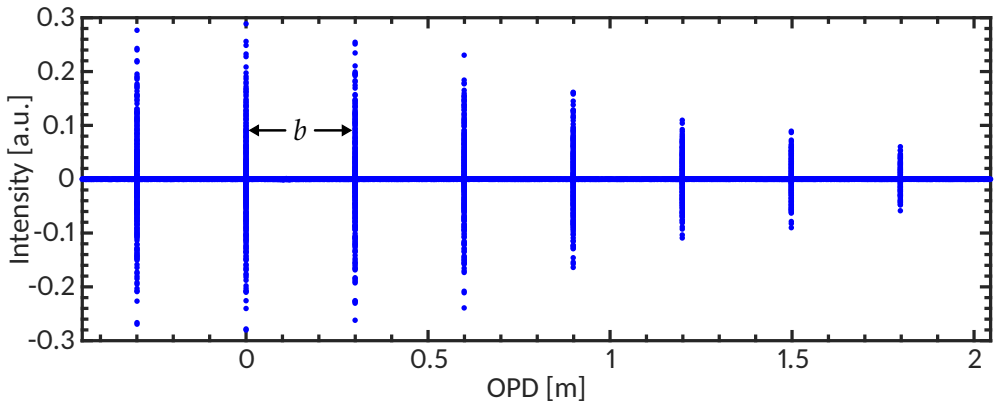

Figure 5.1: A typical interferogram of an LFC. The distance b between two bursts is determined by the repetition rate.

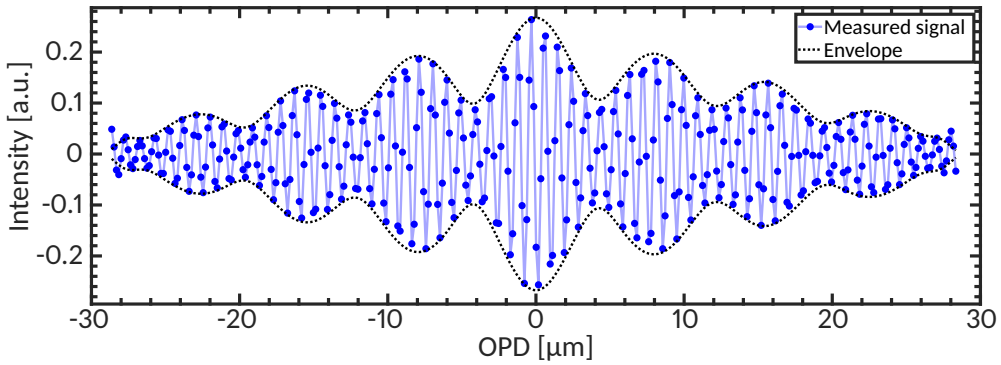

Figure 5.2: A typical burst from the interferogram (blue dots) and the corresponding calculated burst envelope (black dotted line).

For an interferogram with l bursts, we obtain $l - 1$ values for f_{rep}. We calculate a weighted mean of f_{rep} using the square of the mean amplitude of the respective bursts as weights. Naively, one would expect a lower error for a measurement from first to last burst, rather than for consecutive bursts. However, there are systematic errors in the burst center determination for different burst pairs (see Sec. 5.2.1). E.g., the burst amplitude is reduced at higher OPDs due to the self apodization caused by the input fiber (Schäfer et al., 2020a). Other instrumental effects which result in a stretching of the OPD-axis cause further systematic errors. Therefore, we use the weighted mean approach.

5.1.2 Measuring the offset frequency

Ideally, two bursts in the interferogram of an LFC are identical except for a shift in phase of the interference signal with respect to the envelope of the burst. This is the so called carrier-envelope-offset (CEO) phase. The magnitude

of this phase shift is $m\Delta\varphi$, where m is the integer number of the respective burst and $\Delta\varphi$ is the CEO phase causing f_{CEO} (for more detail see Sec. 2.1 and Eq. 2.19) (Huke et al., 2019a).

This is illustrated in Fig. 5.3 using a simulation of the interference of Gaussian pulses with a shift of $\Delta\varphi$ of the carrier wave with respect to the pulse envelope. For illustration purposes, we overlay all burst envelopes on top of each other to show the phase difference of the carrier waves with respect to their envelope. The burst $m = -1$ is shifted by $-\Delta\varphi$ with respect to the the burst $m = 0$. The burst $m = 1$ is shifted in the opposite direction by $\Delta\varphi$ with respect to the the burst $m = 0$. Further bursts are shifted by a multiple of $\Delta\varphi$ in the same manner. In this idealized simulation, the maximum of the carrier wave coincides with the maximum of the envelope. In a real setting, where dispersion occurs in the interferometer this is typically not the case.

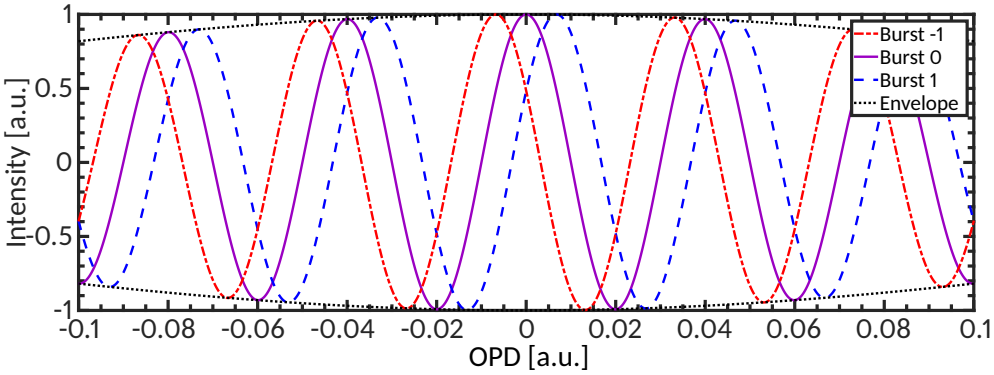

Figure 5.3: Illustration of the interference signal shift with respect to the envelope (black dotted line) for the central bursts of an interferogram of Gaussian pulses with a phase shift between carrier wave and envelope. All burst envelopes are overlayed on top of each other for better visualization of the phase shift in the interference signal.

To determine the phase difference $\Delta\varphi$ in a real measurement, we first normalize each burst by dividing it by its envelope calculated in the previous step (see Sec. 5.1.1). This allows us to fit a simple cosine model to each normalized burst center m:

$$u_m(x_m) = \cos(k_{\mathrm{BC}} x_m + 2\pi\varphi_m), \tag{5.3}$$

with the fit coefficients k_{BC} corresponding to the burst center wavenumber and φ_m being a constant phase. The OPD x_m is shifted so that the center determined in the previous step is at zero. An example of this fit is shown in Fig. 5.4. After unwrapping the phases, we can determine the CEO phase by

$$\Delta\varphi = \varphi_{m+1} - \varphi_m. \tag{5.4}$$

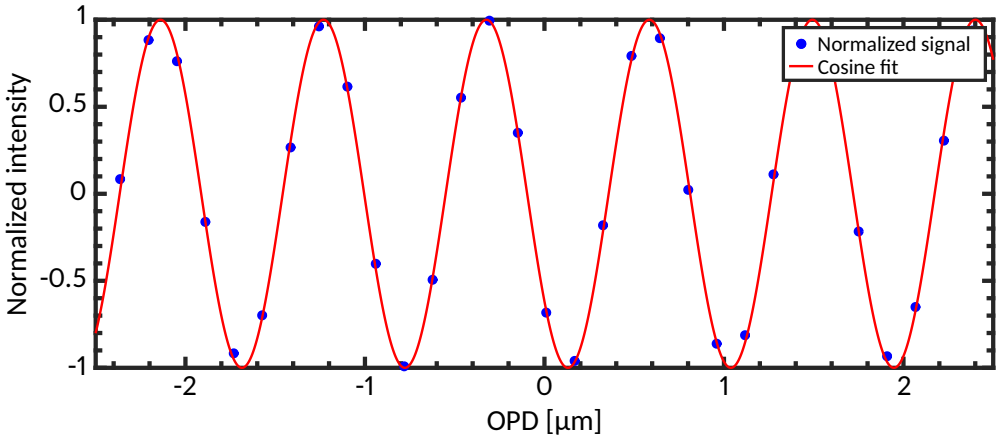

Figure 5.4: Cosine fit (red line) to the normalized signal around a burst center (blue dots).

Using Eq. 2.19, the offset frequency can then be calculated with the equation

$$f_{\mathrm{CEO}} = \Delta\varphi 2\pi f_{\mathrm{rep}}. \tag{5.5}$$

As with the repetition rate, we obtain $l-1$ values for f_{CEO} for an interferogram with l bursts. From these values, we calculate a weighted mean by using the squared mean burst amplitudes as weights as before.

5.1.3 Expected correlation of errors

The measured values of both f_{rep} and f_{CEO} directly depend on the determined distance between the bursts b. If there is an error in the measured distance b, resulting errors in both Δf_{rep} and Δf_{CEO} will be correlated. Since errors caused by false values of b are dominant, other error sources are not considered here. The relationship between both errors will be explored in this section.

The dependency of f_{rep} on the distance determination can be derived from Eq. 5.2. An error in the determination of the distance between bursts Δb causes an error in the repetition rate of

$$\Delta f_{\mathrm{rep}} = \Delta b \frac{\mathrm{d}f_{\mathrm{rep}}}{\mathrm{d}b} \tag{5.6}$$

$$= \Delta b \frac{\mathrm{d}}{\mathrm{d}b}\frac{c}{nb} \tag{5.7}$$

$$= -\Delta b \frac{c}{nb^2} \tag{5.8}$$

$$= -f_{\mathrm{rep}}\frac{\Delta b}{b}. \tag{5.9}$$

For f_{CEO} the dependency on Δb can be derived from Eqs. 5.3, 5.4 and 5.5. In the cosine fit described by Eq. 5.3, an error in the burst center measurement leads to a shift of the OPD vector x_m. In the fit, this error is transferred to φ_m, scaling with k_{BC}:

$$\Delta(\varphi_m) = k_{\mathrm{BC}} \Delta x_m \tag{5.10}$$

Using Eq. 5.4, we can then determine the error of $\Delta\varphi$ depending on Δb:

$$\Delta(\Delta\varphi) = k_{\mathrm{BC}} \Delta x_{m+1} - k_{\mathrm{BC}} \Delta x_m = k_{\mathrm{BC}} \Delta b \tag{5.11}$$

We can then express the error in the offset frequency depending solely on Δb as

$$\begin{aligned}
\Delta f_{\mathrm{CEO}} &= \Delta b \frac{\mathrm{d} f_{\mathrm{CEO}}}{\mathrm{d} b} && (5.12)\\
&= \Delta b \frac{\mathrm{d}}{\mathrm{d} b} \Delta\varphi f_{\mathrm{rep}} && (5.13)\\
&= \Delta b f_{\mathrm{rep}} \frac{\mathrm{d}}{\mathrm{d} b} \Delta\varphi + \Delta b \Delta\varphi \frac{\mathrm{d}}{\mathrm{d} b} f_{\mathrm{rep}} && (5.14)\\
&= \Delta b f_{\mathrm{rep}} k_{\mathrm{BC}} + \Delta\varphi \Delta f_{\mathrm{rep}}. && (5.15)
\end{aligned}$$

So, even though both depend on the error in b, the effect on the offset frequency error is much larger as it scales with k_{BC}, the instantaneous burst center wavenumber, while the repetition rate scales with the reciprocal burst distance.

From Eqs. 5.9 and 5.15, we can determine the relationship between both errors:

$$\begin{aligned}
\frac{\Delta f_{\mathrm{rep}}}{\Delta f_{\mathrm{CEO}}} &= -\frac{f_{\mathrm{rep}} \Delta b}{b \left(\Delta b f_{\mathrm{rep}} k_{\mathrm{BC}} - \Delta\varphi \frac{f_{\mathrm{rep}} \Delta b}{b} \right)} && (5.16)\\
&= -\frac{1}{k_{\mathrm{BC}} b - \Delta\varphi}. && (5.17)
\end{aligned}$$

5.2 **Laser frequency comb measurements**

With the LFC and FTS described in Ch. 2 and Ch. 3, respectively, we recorded 28 single-sided interferograms. We set the maximum OPD to 205 cm and the asymmetric OPD (the OPD before the center burst) to 45 cm, leading to eight full bursts in each interferogram. We used the minimum aperture of 0.5 mm and a sampling rate of 5 kHz. We evacuated the FTS to a level of about 2.5 µbar (see Fig. 5.5). During the first ten measurements, the pressure was still adjusting from a level of about 4 µbar. Both temperature and pressure

are relatively stable from the 10th measurement onwards. We stabilized and monitored the repetition rate and the offset frequency of the LFC. The LFC was spectrally broadened using a nonlinear fiber (NL-PM-750, 50 cm). To avoid saturation of the FTS detector, we discarded a fraction of the light.

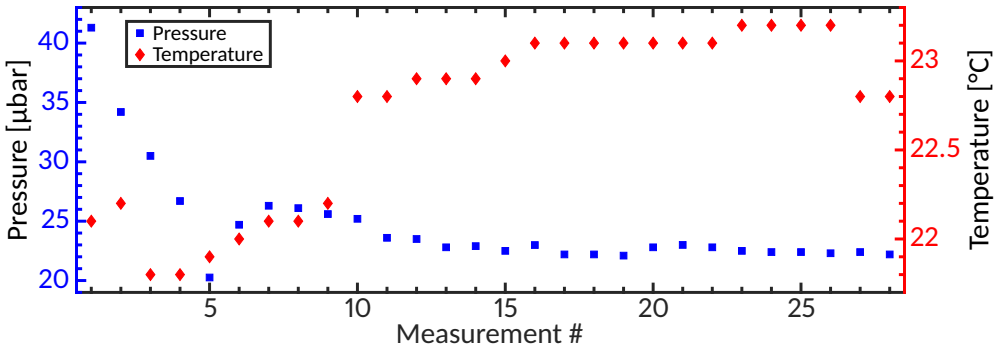

Figure 5.5: The FTS temperature (red diamonds) and pressure (blue squares) over the course of the measurements.

5.2.1 Applying the interferogram retrieval method

From the measured interferograms, we calculated the repetition rate and offset frequency. For both, we then calculated the difference to the values to which they were stabilized (see Fig. 5.6):

$$\Delta f = f_{\mathrm{FTS}} - f_{\mathrm{set}}, \tag{5.18}$$

where f_{FTS} is the value of the repetition rate or offset frequency calculated from the interferogram and f_{set} is the value to which the respective frequency was stabilized. As the variation of the stabilized frequencies is negligible, they can serve as an absolute reference (see Sec. 2.5). Both Δf_{rep} and Δf_{CEO} are offset from zero and follow a corresponding opposite trend (see Fig. 5.6). The systematic error of the measurement is 34 ± 13 Hz for the repetition rate and -13.1 ± 2.7 MHz for the offset frequency.

Each interferogram contains seven pairs of consecutive bursts and thus seven values each for Δf_{rep} and Δf_{CEO} can be retrieved. We calculate the single measurement precision, i.e., the expected precision in one interferogram. For this, we calculate the weighted standard deviation over all seven burst pair measurements in each interferogram by using the squared mean burst amplitudes as weights again. The expected single measurement precision then is the mean of the standard deviations over all interferograms. The single measurement precision of the repetition rate is 81 Hz. Expressing this as a

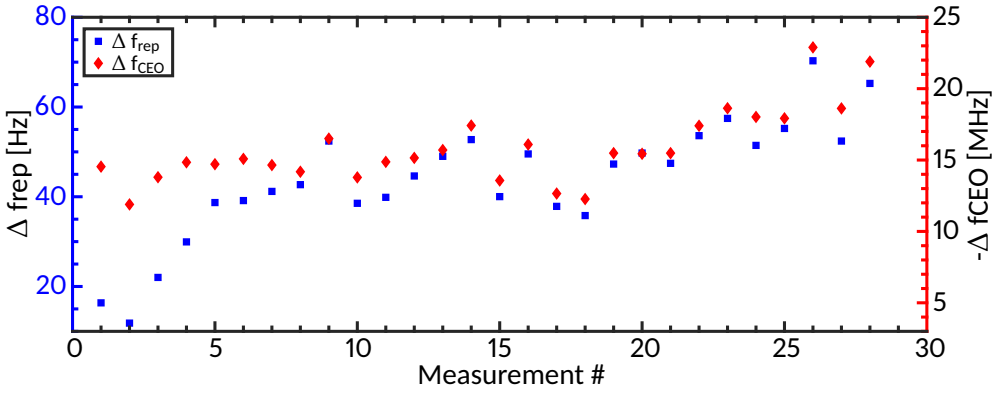

Figure 5.6: Average error of f_{rep} (blue squares) and -f_{CEO} (red diamonds) from each interferogram.

distance yields a value of 24 nm. This is comparable to results from Wu et al. (2014). For the offset frequency, the single measurement precision is 18 MHz corresponding to a phase measurement precision of 115 mrad. This is not as precise as previous measurements with a Michelson-correlator (Xu et al., 1996) or f-2f measurements. However, it is comparable to other interferometric measurements without the use of frequency doubling where an RMS jitter of 120 mrad was reached (Jójárt et al., 2012).

In order to compare Δf_{rep} and Δf_{CEO}, we can also express the error in the offset frequency measurement as a distance. For this, we use the measured phase shift $\Delta\varphi$ and compare it with the expected phase shift calculated using Eq. 5.5. Then, assuming the mean wavelength of the spectrum corresponds to the instantaneous wavelength λ_{inst}, we can calculate the phase error $\Delta(\Delta\varphi)$ in terms of a length scale as

$$\Delta x_{\text{phase}} = \Delta(\Delta\varphi)\lambda_{\text{inst}}. \tag{5.19}$$

A comparison shows that the errors of both Δf_{rep} and Δf_{CEO} occur on very similar length scales (see Fig. 5.7).

Correlation of errors

The expected correlation between the errors of both frequencies is visible in Fig. 5.6. The Pearson correlation coefficient between Δf_{rep} and Δf_{CEO} is negative and significant with a value of -0.87. The correlation becomes even more pronounced, when considering the values between consecutive burst pairs, rather than the ones averaged over an interferogram as illustrated by Fig. 5.8.

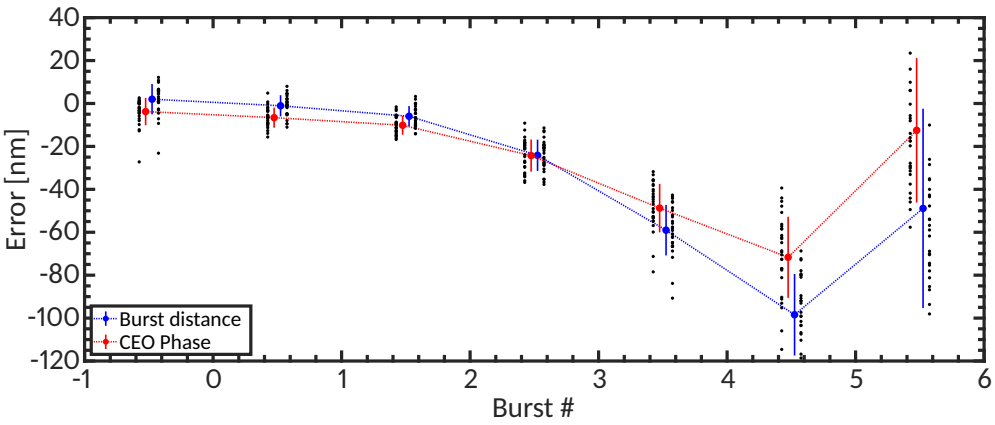

Figure 5.7: The error of each f_{CEO} and f_{rep} measurement between two bursts expressed in terms of length (black dots). The error in the CEO-phase (mean value shown in red) measurement is offset to the left and the error of the burst distance (mean value shown in blue) is offset to the right for clarity.

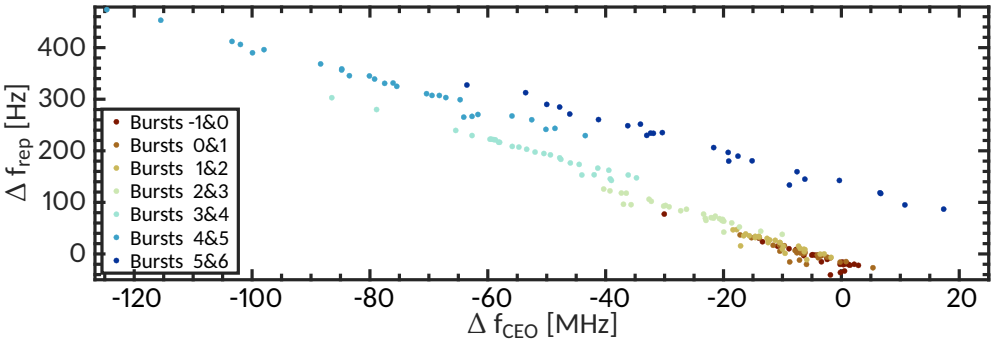

Figure 5.8: Measurement error of f_{rep} and f_{CEO} for the individual inter-burst measurements.

The expected relationship between both errors caused by an error in the burst distance measurement is derived in Sec. 5.1.3 (see Eq. 5.16). To calculate the exact value, we use mean values of $k_{\mathrm{BC}} \approx 1.098 \times 10^6\ \mathrm{m}^{-1}$ (corresponding to 329.2 THz), which is the burst center wavenumber from the fit given by Eq. 5.3 and $b \approx 0.2996$ m from our measurements. We neglect $\Delta\varphi$ which is on the order of one. The expected slope of the correlation of errors is then

$$\frac{\Delta f_{\mathrm{rep}}}{\Delta f_{\mathrm{CEO}}} \approx -3.039 \times 10^{-6} = -3.039\ \mathrm{Hz\,MHz}^{-1}. \tag{5.20}$$

A fit of linear models to the errors for each set of burst pairs is shown in Fig. 5.9. The average slope over all burst pairs is $-3.058\ \mathrm{Hz\,MHz}^{-1}$ (see Fig. 5.9). The expected and measured values differ by only 0.62 %. Since the expected correlation was derived from the assumption of an error caused only by the burst center determination this seems to be the dominant cause of error.

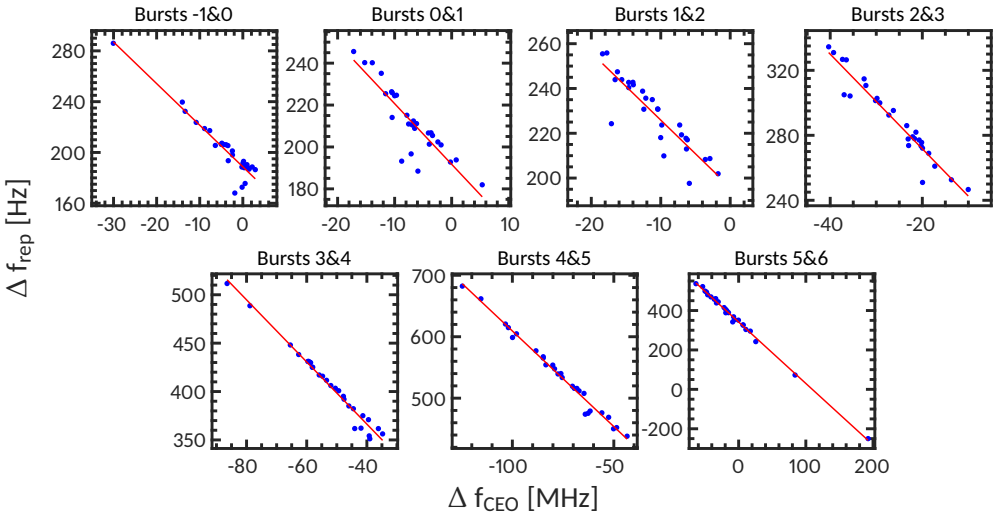

Figure 5.9: Linear fits to the measurement error of f_{rep} and f_{CEO} for each set of inter-burst measurements.

Error systematics

Fig. 5.8 shows that for each pair the values of Δf_{rep} and Δf_{CEO} scatter around a different center. The sets of the last four burst pairs show stronger systematic offsets. This means that the inaccuracy increases for higher burst numbers, i.e., higher OPDs. Therefore, the single measurement precisions are improved when including only the central bursts of the interferogram.

To investigate a possible cause of the systematic errors we calculated the refractive index from the measured temperature and pressure values using the updated Edlén equation (Bönsch and Potulski, 1998). The Pearson correlation coefficient between the refractive index and the repetition rate has a value of -0.71, significant at the 5 % level. However, when excluding the first ten interferograms where a large variation in temperature and pressure is observed, the correlation coefficient drops to -0.30. As the number of samples is then only 18, this is not significant anymore.

We calculated the difference and the mean of Δf_{rep} and Δf_{CEO} expressed as a distance for each burst pair and each interferogram, which is shown in Fig. 5.10. The difference is mainly dependent on the burst number or OPD and also slightly on the pressure (see Figs. 5.10b, 5.11). The difference of the errors is much less variable than the mean of the errors. This indicates the correlation between the two errors again.

The difference between both errors is a proxy of the dispersion inside the FTS, as it corresponds to the difference in group and phase velocity. There is a clear systematic OPD dependence of the dispersion proxy. We calculated

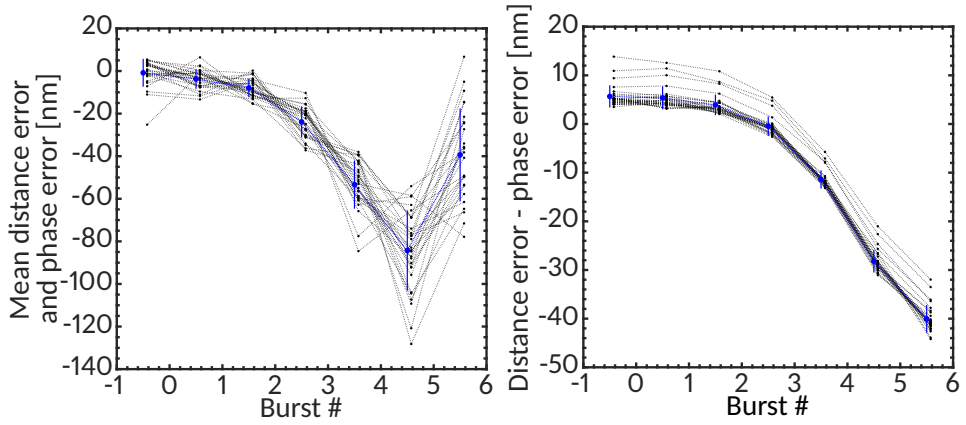

(a) Mean of errors (b) Difference of errors

Figure 5.10: Mean and difference of the errors in the burst distance and CEO-phase measurements. Mean values over each burst pair measurement are shown in blue and individual measurements slightly offset in black.

the deviation of each difference measurement from the mean difference measurement of the corresponding burst pair. This can then be used as a proxy of the dispersion in the FTS over the course of the measurement since it does not depend on the OPD anymore. A comparison of this dispersion proxy with the pressure over the course of the measurement is shown in Fig. 5.11. The dispersion proxy is clearly correlated with the pressure. This is

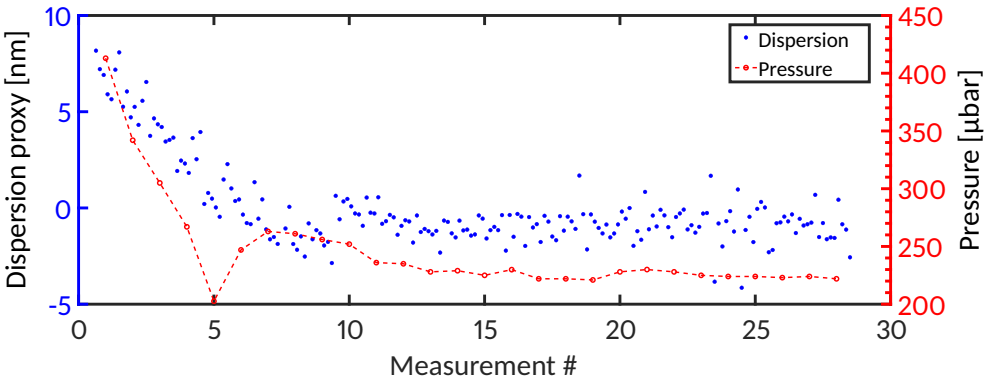

Figure 5.11: A proxy of the dispersion, measured as the difference in the error for the measurement of the burst center position and the CEO phase over the course of the measurements (blue dots). The pressure in the FTS during the measurement is shown as the red dots connected by the dashed line.

especially apparent from the first five measurements while the evacuation was still ongoing. There is a lag between the dispersion proxy measurement and pressure. The pressure sensor is in a different location than the interferometer

beam path, so the pressure might differ locally while the evacuation is still ongoing.

5.2.2 Calibration with coefficients from the interferogram

We used the difference between the comb frequencies measured from the interferogram and the frequency to which they were stabilized in order to calibrate the FTS as described in Sec. 3.4 (see also Eq. 3.12). A comparison of this calibration method with the calibration using correction factors calculated from fitting each comb line in the spectrum as demonstrated by Huke et al. (2019b) is shown in Fig. 5.12.

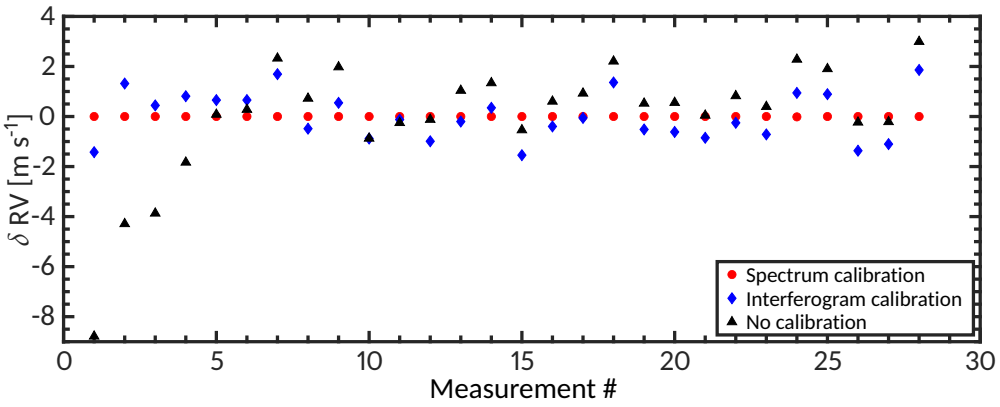

(a) Line fit position

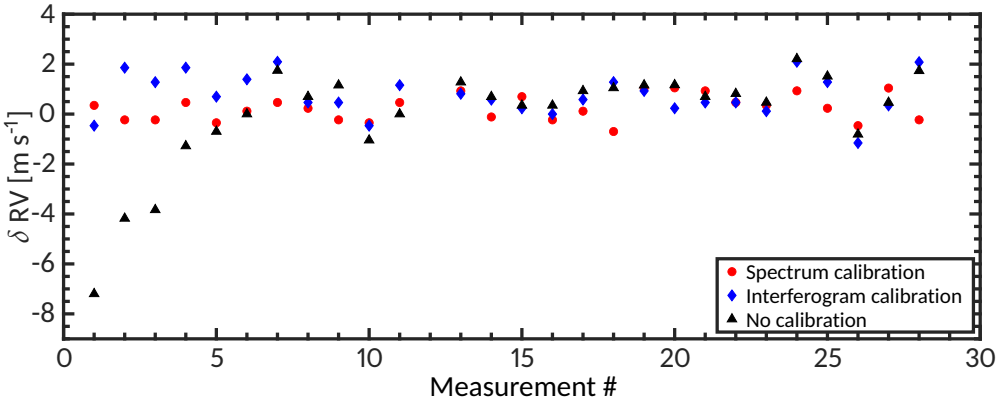

(b) Cross correlation

Figure 5.12: Comparison of interferogram and spectrum, i.e., line fit calibration. Panel (a): Mean deviation of the fitted comb line positions for the uncalibrated (black triangles), interferogram calibrated (blue diamonds) and spectrum calibrated (red circles) spectra. The spectrum calibration shows no deviation as the calibration coefficients are calculated from the fitted comb line positions. Panel (b): Lag of the maximum of the cross correlation with the 12th spectrum for the uncalibrated, interferogram calibrated and spectrum calibrated spectra (legend as in panel (a)).

We used two different measures to compare the two different calibration approaches. For the first measure, we simply calculated the difference of each fitted comb line position from the value expected from the stabilized values of the comb frequencies. Since this is also how the spectrum calibration factors are calculated, the spectrum calibration shows almost no remaining drift. For the second measure, we calculated the cross correlation of one spectrum with all other spectra of the measurement set. The lag at the maximum of the cross correlation was then interpreted as the remaining instrumental drift between the respective spectra. To estimate the overall calibration precision, we calculated the standard deviation of the full measurement set for each calibration and drift measure (see Tab. 5.1). Both calibration methods show an improvement over no calibration. The spectrum calibration performs better than the interferogram calibration for both measures.

Table 5.1: Comparison of the estimated overall measurement precision for different calibration and precision measures.

Method	δ RV [m s^{-1}] (line fit position comparison)	δ RV [m s^{-1}] (cross correlation)
Spectrum calibration	0.0028	0.5241
Interferogram calibration	0.9700	0.8302
No calibration	2.3823	2.0709

5.3 **Simulated interferograms**

To verify the method described in Sec. 5.1 and to explain the discrepancy in the frequency measurements from the interferograms with those from the spectra, we simulated interferograms of the LFC using MATLAB. To simulate an LFC interferogram, we superimpose the interferograms of N=100,000 monochromatic light sources (for the interferogram of a monochromatic light source see Eq. 3.4). This approximates the LFC as a Dirac-comb in frequency space. The equation for a simulated LFC interferogram is then given by

$$I(x) = \sum_{j=j_0}^{N+j_0} a_j \cos\left(\frac{2\pi}{c} f_j x\right), \tag{5.21}$$

where j_0 is the mode number of the mode with the lowest frequency, a_j is the amplitude of the mode, f_j the frequency of the mode given by the comb

equation (Eq. 2.18) and x is the OPD. The values of x are determined by the spatial sampling rate, the number of samples and the point of zero OPD.

We tried to keep the simulated datasets as close as possible to the parameters in our measurements. A number of parameters were fixed, while some parameters were varied to create a full data set. In all simulations we fixed the repetition rate at ≈1 GHz, the sample rate at ≈158 nm (a quarter of the HeNe-reference laser wavelength) and the number of sample points at 15.8 million. Using this framework, we created multiple data sets with varying parameters and increasing complexity.

The first dataset was used as a test case, to verify that our algorithm can correctly measure the offset frequency (for the repetition rate this type of measurement had been demonstrated by Balling et al. (2012)). Therefore, we kept most parameters constant, setting the zero OPD point at the ≈2.8 millionth sample point and using the same spectral envelope for each interferogram. In order to set the value of the amplitude a_j of each mode, we used a measurement of the LFC spectrum. We interpolated the measured spectral envelope of the LFC at the frequencies f_j. The interpolated values are then used for a_j. Correspondingly, the value of j_0 is ≈300,000, since the lowest frequencies in our LFC measurements were at about 300 THz. We only varied the offset frequency using values from 100 to 500 MHz in steps of 25 MHz resulting in 17 interferograms. In this dataset, we can fully recover the repetition rate with errors being on the order of the numerical precision limits. The offset frequency can also be recovered from all simulated interferograms, with the standard deviation over the whole data set below 0.1 MHz (see Fig. 5.13).

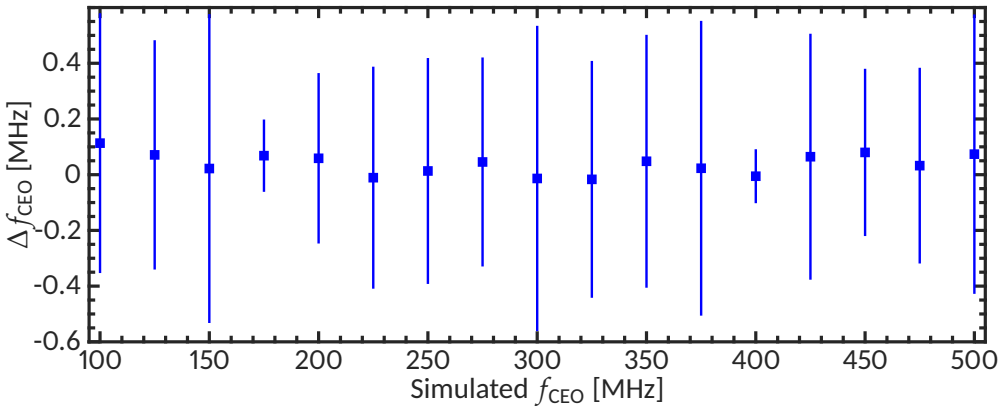

Figure 5.13: The error of the offset frequency Δf_{CEO} measured directly from the first simulated interferogram data set.

Since we verified that the method works in an ideal setting, we added measurement effects to our simluation, in order to understand how the measurement errors are caused. The following datasets all consist of 28 interferograms with the parameter inputs mirroring those from the real measurements. In all following simulations, we used zero OPD points retrieved from each measured interferogram in the calculation of x. Therefore, zero OPD always occurs in between two sample points. As a result no interferogram is fully symmetric anymore.

In the first data set emulating a measurement data set, we kept the comb frequencies f_{CEO} and f_{rep} at the values to which they were stabilized during the measurement. Also, the bursts were weighted with their mean amplitude corresponding to the measurement, i.e., lower burst amplitudes for bursts further away from the center burst (see Fig. 5.1). Additionally, we varied the mode amplitudes a_j, to replicate the spectral envelopes of each of the measurements. Applying the interferogram retrieval method to this data set shows increased errors for both comb frequencies compared with the initial ideal data set. However, the results are still two to four orders of magnitude better than the real dataset and show no systematic clustering (see Fig. 5.14).

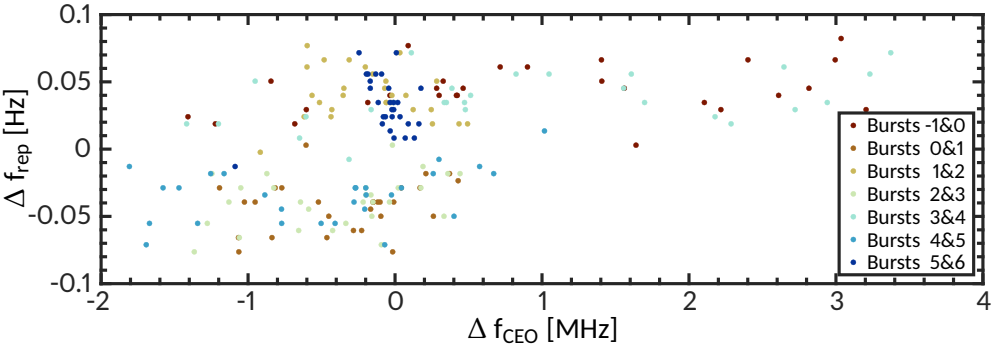

Figure 5.14: The errors of f_{CEO} and f_{rep} measured from the simulated interferogram data set including varying spectral envelopes and zero point offsets.

Next, we created three data sets including two different error sources and the combination of them. The first error source is a frequency dependent coherence as measured by Huke et al. (2021), leading to a reduced amplitude depending on OPD and wavelength. In order to simulate this, we calculated the attenuation in two different frequency regimes (320 THz and 356 THz) in the individual spectra calculated from each burst in the measurements. We fitted the attenuation as a function of burst number with a Gaussian and inter-

and extrapolated the width linearly over the whole frequency range and OPD range (see Fig. 5.15). The second error source is the frequency dependent beamsplitter phase. We calculated this from a double-sided interferogram of a halogen lamp. We interpolate the phase values Φ_j at the corresponding frequencies f_j and add it as a phase in Eq. 5.21:

$$I(x) = \sum_{j=j_0}^{N+j_0} a_j \cos\left(\frac{2\pi}{c} f_j x + \Phi_j\right). \tag{5.22}$$

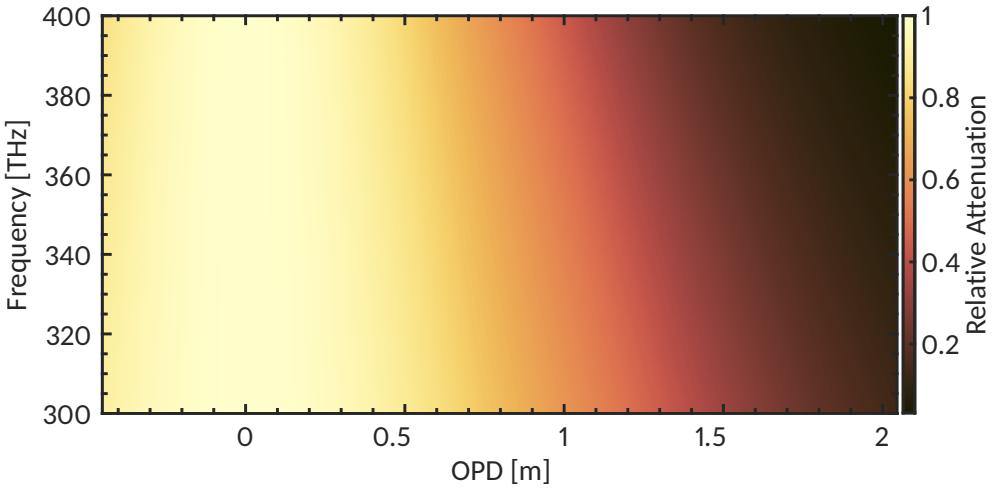

Figure 5.15: Interpolation of the frequency dependent coherence effect used in the simulated interferograms (Huke et al., 2021). This and subsequent colormaps were created using ”Scientific colour maps” (Crameri, 2021).

In all these simulations, we also included the variation of the zero OPD point and the spectral envelope retrieved from the measurements as before. We applied the interferogram retrieval algorithm to this dataset. The errors are shown in Fig. 5.16. Including the effects of frequency dependent coherence or the spectral phase Φ_j increases the errors, particularly for the offset frequency. For each on its own, the increase is small. It is slightly stronger for the beam splitter phase, which causes a few outliers with an error more than ten times larger than the previous data set. In combination, however, they lead to a much stronger increase than one would expect from just adding the errors of the single effects. In this case, the errors are only about a factor of ten smaller than in the measurement data set. The combination of both effects also leads to the distinct clustering of the values from each burst pair as it was observed in the real measurement. However, the distribution of the clusters is mirrored compared to the real measurement.

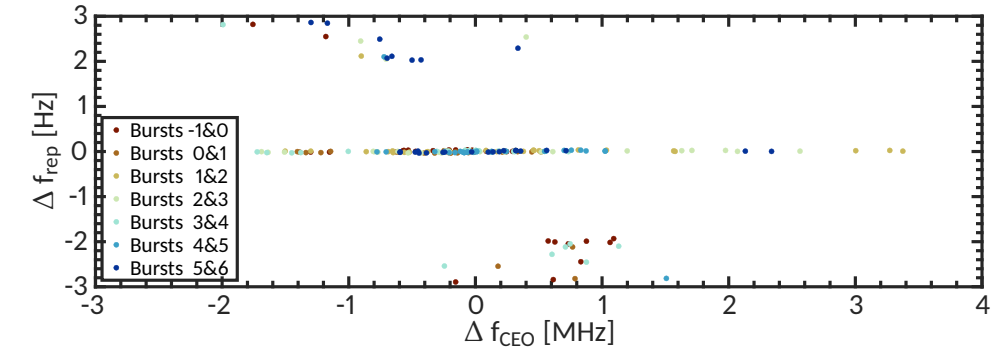

(a) Beam splitter phase

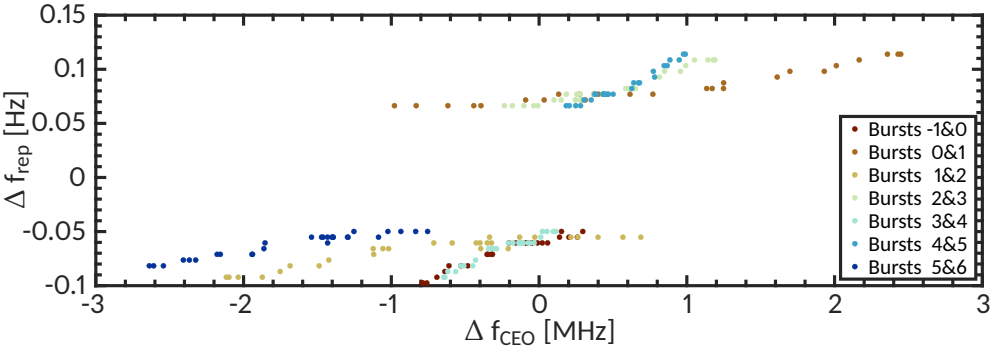

(b) Frequency dependent coherence

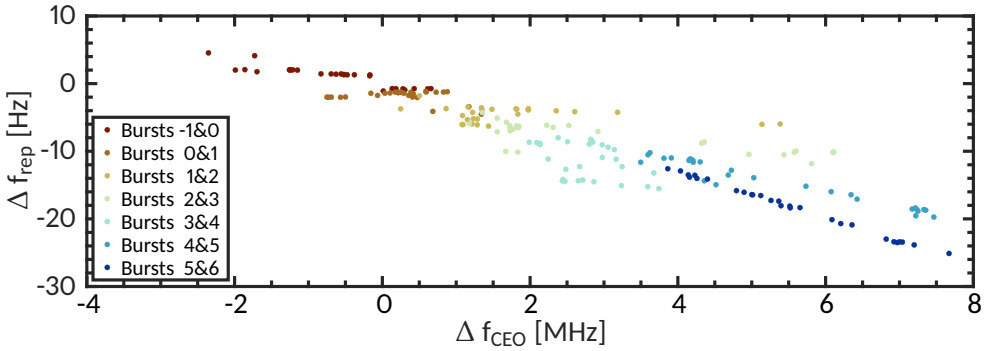

(c) Beam splitter phase & frequency dependent coherence

Figure 5.16: The errors of f_{CEO} and f_{rep} measured from the simulated interferogram data set including varying spectral envelopes and zero point offsets, the beam splitter phase and frequency dependent coherence.

In the next dataset, we included varying burst spectra (Huke et al., 2021). The spectrum of each burst in each measured interferogram is calculated so that the variation of the spectral envelope during a single measurement can be taken into account. In the simulated interferograms, the coefficients a_j are adjusted individually for each burst and each interferogram to emulate the measurements. This dataset also includes the beam splitter phase and zero OPD variations as described above, but not the frequency dependent

coherence since this is inherently included in the burst spectra. Calculating the repetition rate and the offset frequency from this data set, we observe that the clustering of the different burst pair measurements is reduced compared to the previous data set (see Fig. 5.17). However, the errors for both f_{CEO} and f_{rep} are increased by a factor of about two.

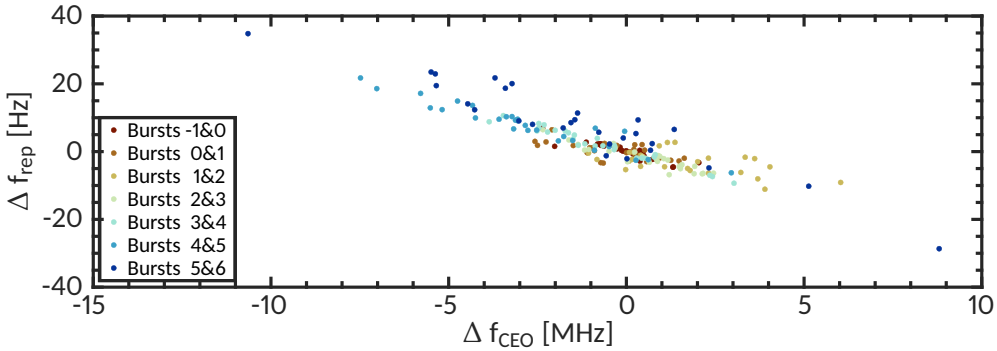

Figure 5.17: The errors of f_{CEO} and f_{rep} measured from the simulated interferogram data set including varying spectral envelopes for each burst, the beam splitter phase and zero point offsets.

We observed systematic differences in repetition rate between different burst pairs in our measurements (see Fig. 5.7). This effect could be explained by a stretching of the OPD axis. We thus calculated the stretching of the x vector necessary to reproduce the repetition rate measurements and included it in the simulation. This dataset also included the beam splitter phase, zero OPD variations and burst spectra. Adding this stretching of the interferogram OPD axis reproduces the errors in the repetition rate measurement but does not significantly affect the measurement of the offset frequency measurement (see Fig. 5.18).

We also observed systematic differences in the offset frequency between different burst pairs in our measurements (see Fig. 5.7). This could be the result of a systematic phase shift for each burst. We calculated the phase shift for each burst from the measurements and added a corresponding additional phase factor Φ_b for each burst in the corresponding simulated interferograms. This dataset also included the beam splitter phase, zero OPD variations and burst spectra, but not the stretching of the OPD axis. Similar to the previous data set, we now see the characteristic clustering of the burst pair measurements. However, the clustering occurs in the errror of the offset frequency and not the error of the repetition rate (see Fig. 5.19).

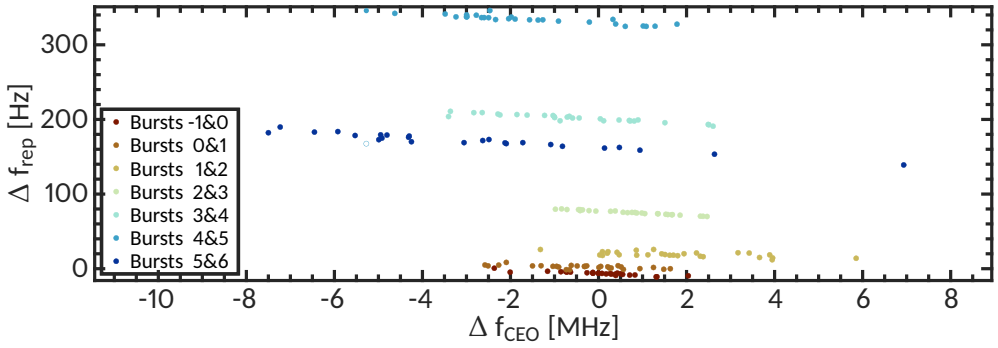

Figure 5.18: The errors of f_{CEO} and f_{rep} measured from the simulated interferogram data set including a stretching of the interferogram axis, varying spectral envelopes for each burst, the beam splitter phase and zero point offsets.

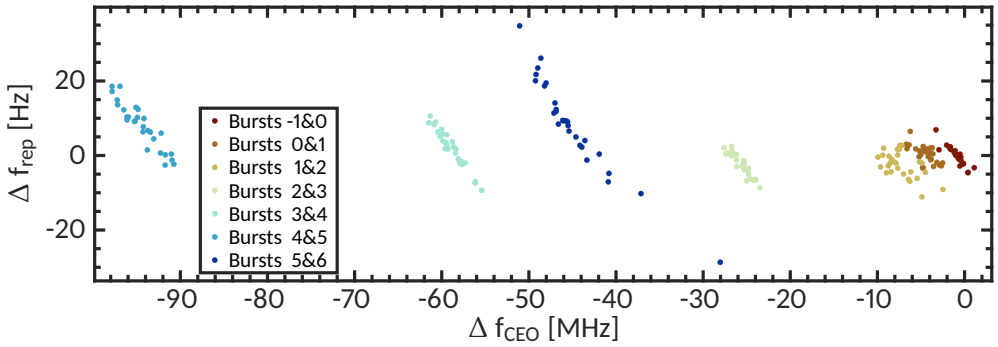

Figure 5.19: The errors of f_{CEO} and f_{rep} measured from the simulated interferogram data set including a different phase error for each burst, varying spectral envelopes for each burst, the beam splitter phase and zero point offsets.

In the final dataset, we included both the stretch of x and the burst phase factors, as well as the beam splitter phase, zero OPD variations and burst spectra. This data set reproduces the systematics in the measured results (see Fig. 5.20). Only the spread of the individual clusters is smaller.

Subsequently, we added Gaussian noise to each interferogram before retrieving the comb frequencies. With this dataset, we can then reproduce the measurement results, except for a small offset in Δf_{CEO} for the last burst pair (see Fig. 5.21).

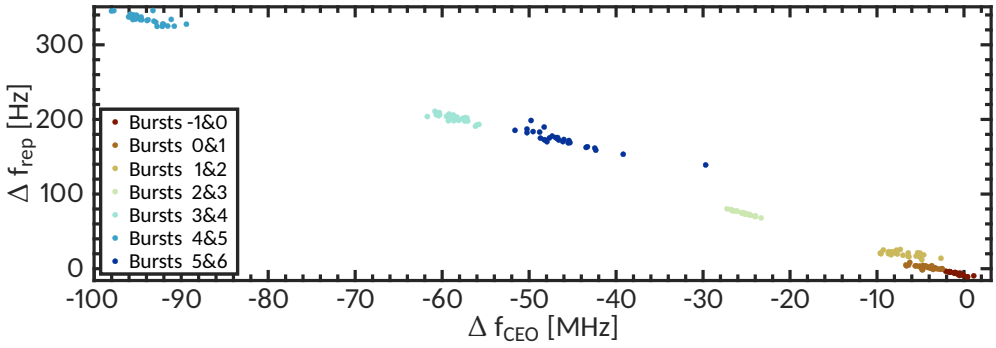

Figure 5.20: The errors of f_{CEO} and f_{rep} measured from the simulated interferogram data set including a stretching of the interferogram axis, varying spectral envelopes for each burst, the beam splitter phase and zero point offsets.

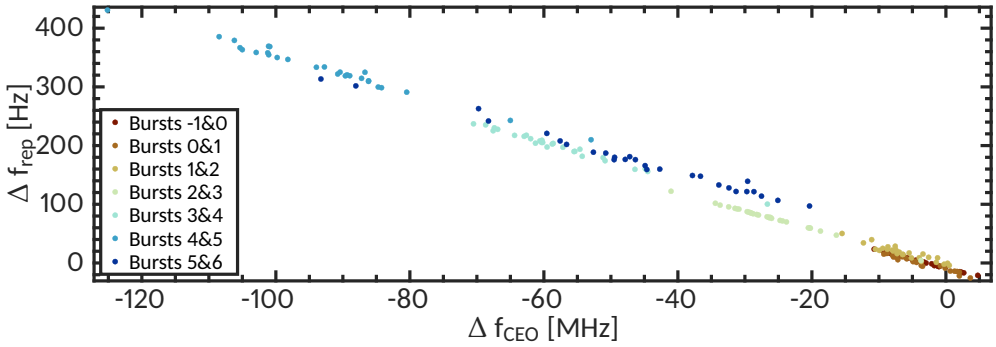

Figure 5.21: The errors of f_{CEO} and f_{rep} measured from the simulated interferogram data set including a stretching of the interferogram axis, varying spectral envelopes for each burst, the beam splitter phase, zero point offsets and Gaussian noise.

5.4 **Discussion**

We showed that it is feasible to retrieve the comb frequencies f_{CEO} and f_{rep} directly from the interferogram measured with a commercial FTS. In an ideal simulated interferogram, we can retrieve the repetition rate and the offset frequency with a very high accuracy and precision.

Measurement effects, however, reduce the measurement precision and accuracy of the method. The measurements show that pressure can play a role. Once the FTS is fully evacuated, the dispersion appears to stay constant in time. However, there is an additional dispersion dependence on OPD, causing systematic phase errors. If these were caused by residual atmosphere, we would expect a linear dependence on OPD, which is not observed.

We could reproduce these systematic phase errors in simulated interferograms, by introducing an artificial phase shift for each burst and simultaneously stretching the OPD axis. The phase errors may be a result of the finite aperture effect, since it follows a similar trend as the coherence measurements made with the FTS for different input fibers (Schäfer et al., 2020a). To determine the exact cause, further investigation is required.

From the slope of the correlation of errors Δf_{CEO} and Δf_{rep}, we can infer that most measurement noise is caused by errors in the burst center determination. The results from the simulated interferograms indicate that the change of the spectral envelope from burst to burst is the main reason for the errors of the burst center determination. This seems plausible, as this would lead to a change in the pulse shape and instantaneous frequency at the burst center, both of which can affect the burst center determination. A further factor could be simple Gaussian intensity noise. The precision of the measurements could be reproduced by including these two effects in the simulations.

The simulations indicate that frequency dependent coherence does not play a major role. While its implementation led to a clustering of Δf_{CEO} and Δf_{rep}, the effect was opposite of that observed in the measurements. Possibly, the interaction is more complex and the whole spectrum instead of just two small spectral bands have to be taken into account.

Compared to no calibration, the calibration of the spectra using the comb frequencies calculated from the interferogram improves the measurement precision. The improvement is strongest, if the pressure in the FTS changes. There is, however, a discrepancy between the comb frequencies calculated from the interferogram and the ones calculated from the spectrum. We suspect, that this difference may be explained by the systematic effects uncovered using the simulations. The overall calibration performance using the coefficients from the interferogram is worse than calibration using coefficients from the spectrum. Hence, we recommend using the established calibration method with the comb frequencies calculated from the spectrum. Further investigation of this discrepancy, particularly with a more stable LFC spectrum, may help to understand the underlying instrumental effects and improve the results.

6

SPECTRUM CONTROL SETUP

Laser frequency combs (LFCs) have many characteristics which make them an, in principle, ideal calibration light source: a broad spectral coverage, an equal and dense line spacing and a high accuracy and precision of the line positions. However, there are some technological challenges.

Murphy et al. (2007) and Schmidt et al. (2007) recognized the variability of the spectral envelope as one of the main technological challenges hindering the successful use of LFCs as calibration light sources. When an LFC is broadened in a nonlinear fiber, the spectral envelope often has a high dynamic range on very short wavelength scales. This can be mitigated by using a designed nonlinear fiber to create a smooth spectral envelope. Even then, another issue remains: The nonlinear broadening process is sensitive to changes in the polarization, input power and the incoupling into the fiber so that the spectral envelope undergoes changes on timescales of minutes. These changes in the spectral envelope will result in measured radial velocity (RV) shifts which reduces the calibration precision.

The instability and high dynamic range of the spectral envelope are not only detrimental when calibrating a dispersive spectrograph as well as an Fourier transform spectrograph (FTS). Due to the high dynamic range, a large number of comb lines is close to or below the noise floor. These lines cannot be used for calibration anymore (Huke et al., 2019b). The temporal variability is an even larger issue for the FTS, since it causes noise in all spectral channels simultaneously (Hirschfeld, 1976; Davis et al., 2001).

To maximize the calibration performance of LFCs, it is thus necessary to control the spectral envelope so it remains stable in time and has a low dynamic range. Ideally, the spectral envelope should be tailored to the wavelength dependent efficiency of the instrument to maximize the signal-to-noise-ratio (SNR) across the whole spectrum.

Murphy et al. (2007) suggested to use a Fourier transform optical pulse shaping setup to achieve control over the spectral envelope of the LFC. This type of setup acts in the Fourier domain of the laser pulse. By modulating

the intensity of each spectral component with a spatial light modulator (SLM), arbitrary waveforms may be generated. While this technology was originally developed to control the shape and phase of ultrafast optical pulses it can also be used to manipulate the spectrum of the light (Desbois et al., 1973; Froehly et al., 1983; Weiner et al., 1988).

Probst et al. (2013, 2015, 2020) successfully demonstrated the control over the spectral envelope of an LFC for the calibration unit of the HARPS spectrograph in the visible wavelength range using such an approach. A spectrum control setup for the near infrared has thus far not been demonstrated. There are many interesting science cases for the near infrared, e.g., the search for planets around M-dwarfs and the observation of exoplanet atmospheres (Reiners et al., 2010; Snellen et al., 2010). Additionally, this wavelength region can be used for simultaneous calibration of the FTS during solar observations.

We aim to build a spectrum control setup in the near infrared to alleviate the problems for the calibration of the FTS and to improve the LFC calibration for future spectrographs such as ELT-HIRES (Marconi et al., 2020). Our spectrum control setup is based on the previous work by Probst et al. (2013, 2015). Their setup stabilizes the spectral envelope to reduce systematic RV errors and can be used to tailor the spectral envelope for a maximization of the SNR of the calibration measurements. The spectral envelope is usually shaped to a flat top so that the number of photons per pixel in the spectrograph's detector is constant over the spectral range. Parts of this work have previously been published (Debus et al., 2021).

This chapter is structured as follows. First, we give a small overview of the theoretical background of a spectrum control setup and of SLMs. Then, we describe the design specifications and the resulting optical layout of our setup. This is followed by a description of the alignment procedure, calibration and the control loop of the setup. Finally, we present and discuss measurements and their results.

6.1 **Background**

6.1.1 Fourier transform optical pulse shaping setup

A basic Fourier transform optical pulse shaping setup schematic is shown in Fig. 6.1. The fundamental principle of a Fourier transform optical pulse shaping setup is that the light is spectrally dispersed and the spectral components are focused onto a modulator array. After the modulator array, the light is

recollimated and recombined by a second dispersing element. The modulator array can be a physical mask or SLM. Nowadays, the more flexible SLMs are usually used, since a physical mask can only serve a single specific purpose. The general term SLM describes a programmable device which manipulates incident light in amplitude, phase or polarization (or combinations thereof) in space and time (Lazarev et al., 2012).

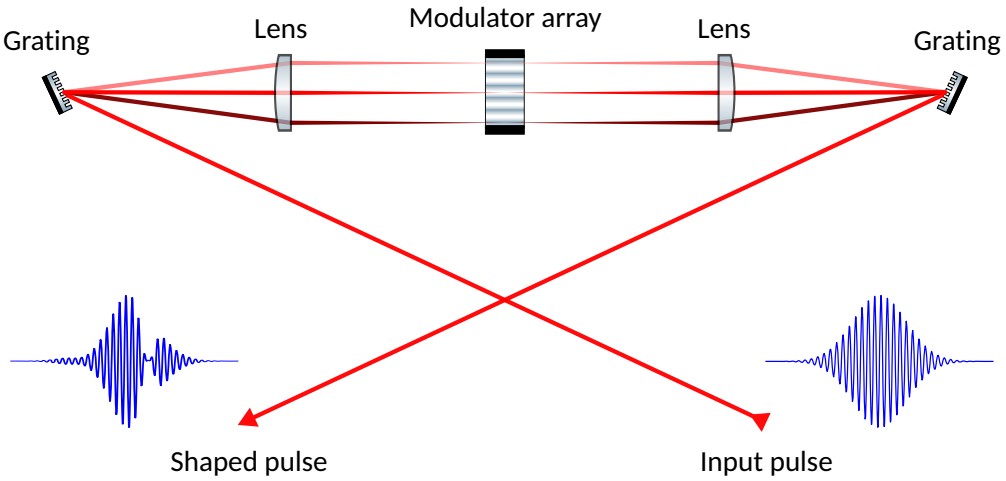

Figure 6.1: Schematic Fourier transform pulse shaping setup. Adapted from Weiner (2011).

The standard Fourier transform optical pulse shaping setup is built in a 4-f configuration which means that the focal lengths of collimator and focusing element are equal and both dispersers and the modulator array are at the respective foci. Compared with earlier setups, this configuration is free of temporal dispersion, i.e., if no modulator array is present the pulse remains unchanged (Froehly et al., 1983; Martinez et al., 1984). A thorough review of Fourier transform optical pulse shaping setups is given by Weiner (2011).

6.1.2 Liquid crystal on silicon spatial light modulators

Since our goal is to actively control the spectrum, we have to use an SLM. In our setup, we use a liquid crystal on silicon (LCOS) SLM. Liquid crystals (LCs) have several properties which, in combination, make them suitable for this application. The first one is that they have properties between liquid and solid materials. Depending on the temperature, they exhibit intermediate phases or so called mesophases (Chandrasekhar et al., 1977). In these phases, both the degree of orientational and positional order decreases, but not to the same extent. For example, in the so called nematic phase there is still orientational

order of the LCs while there is little positional order (Chandrasekhar et al., 1977).

A further useful property of LCs is birefringence (Zhang et al., 2014). The birefringence of a medium is defined as the difference of the refractive indices of the two axis perpendicular to the optical axis:

$$\text{birefringence} = n_e - n_o, \tag{6.1}$$

where n_e is the refractive index of the extraordinary axis and n_o is the refractive index of the ordinary axis. A schematic representation of an LC and the corresponding refractive indices is shown in Fig. 6.2a. If the optical axis is aligned with the long axis of the LC, its birefringence is zero, while it becomes maximal if the long axis of the LC is perpendicular to the optical axis. The birefringence causes a phase retardation for one direction compared to the other, similar to a waveplate.

Furthermore, LCs have a significant dipole moment, due to the elongated ellipsoidal shape of the molecules. Thus, a torque can be applied to an LC by applying an electric field.

In combination, these properties can be used to create an SLM. Due to the birefringence, the orientation of the LCs determines how the light's phase, polarization or both are affected. The orientation of the liquid crystals can easily be changed due to the low positional order and fluid behavior. Because of the dipole moment this can be done by applying a voltage.

A schematic of an LCOS SLM in Fig. 6.2b shows the different layers of a reflective SLM. For a reflective type, the top layer is usually a glass. The second layer is transparent and also conductive. Below these two layers, there are two alignment layers with a layer filled with LCs in between. The alignment layers' surface structure forces the orientation of LC monolayer at the surface interface into a certain direction (Jerome, 1991). This direction is called the rubbing direction. Without an external electrical field, the orientation is thus determined by the alignment layers. By applying a voltage, the orientation of the LCs can be changed. A conductive and reflective layer below the alignment layer contains the pixel array and is used to apply the voltage. The CMOS backplane on the bottom of the display controls the individual pixels.

There are multiple standard configurations of alignment layers, depending on whether a phase only, amplitude only or complex amplitude modulation is desired (Lazarev et al., 2012; Bougrenet de la Tocnaye and Dupont, 1997). Both vertically aligned nematic (VAN) or parallel aligned nematic (PAN) type displays

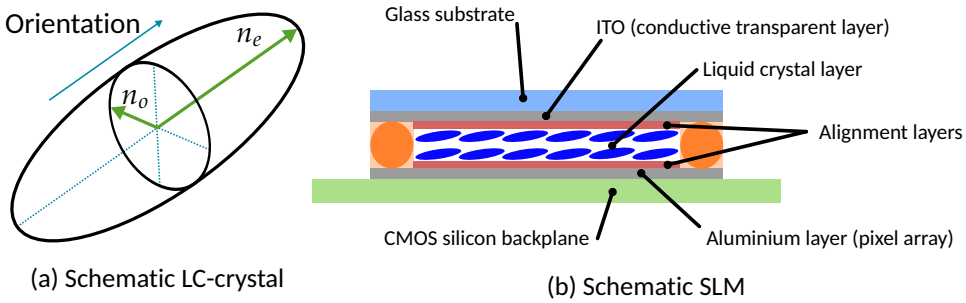

(a) Schematic LC-crystal

(b) Schematic SLM

Figure 6.2: Panel (a): Schematic of a liquid crystal used in LCOS displays. The different optical axis and index of refraction are indicated. Panel (b): Schematic layout of an LCOS SLM. Adapted from Zhang et al. (2014).

are suitable for amplitude modulation. In these types, the rubbing direction of both alignment layers is parallel. Thus, the initial orientation direction of the LCs is uniform if no voltage is applied. The difference between the two is that in the VAN type display, the initial orientation of the LCs is normal to the display surface (see Fig. 6.3), while it is parallel in the PAN type displays. An advantage of VAN type displays is that the birefringence is zero if no voltage is applied. In PAN type displays, the LCs at the surface are always parallel to the surface and thus slightly force the direction of the neighboring LCs, so that zero birefringence cannot be reached. Therefore, VAN type displays can reach a higher contrast ratio.

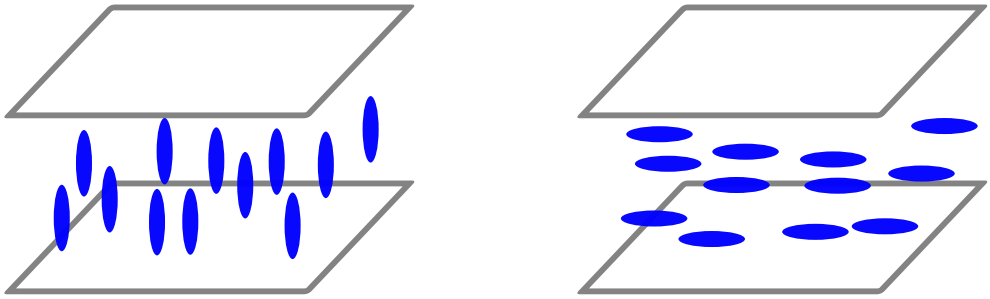

Off-State

On-State

Figure 6.3: LC orientation in a VAN-type SLM. Adapted from Zhang et al. (2014).

6.1.3 Jones-calculus

In the following, we use the Jones-Calculus approach (Jones, 1941) to describe the effect of an SLM on the polarization state of light and how it can be used to manipulate the amplitude. The Jones vector of linearly polarized light at an angle α is given by

$$E(\alpha) = \begin{pmatrix} \cos\alpha \\ \sin\alpha \end{pmatrix}, \tag{6.2}$$

where the first entry describes the horizontal and the second entry the vertical axis. A polarizer at an arbitrary angle θ can be described by the matrix:

$$T_{\text{pol}}(\theta) = \begin{pmatrix} \cos^2\theta & \cos\theta\sin\theta \\ \cos\theta\sin\theta & \sin^2\theta \end{pmatrix}. \tag{6.3}$$

The effect of an SLM with its ordinary axis aligned parallel to the horizontal axis and its extraordinary axis aligned parallel to the vertical axis can be described as (Glückstad and Palima, 2009, Appendix A)

$$T_{\text{SLM,0}} = \begin{pmatrix} e^{i\frac{2\pi}{\lambda}dn_o} & 0 \\ 0 & e^{i\frac{2\pi}{\lambda}dn_e} \end{pmatrix} \tag{6.4}$$

$$= e^{i\frac{2\pi}{\lambda}dn_o} \begin{pmatrix} 1 & 0 \\ 0 & e^{i\delta} \end{pmatrix}, \tag{6.5}$$

with $\delta = \frac{2\pi}{\lambda}d(n_e - n_o)$. In the case of a VAN-type display the extraordinary refractive index depends on rotation of the LCs:

$$n_e = \sin(2\pi\varphi(U)), \tag{6.6}$$

where the angle φ of the LC-orientation is a function of the applied voltage U. Thus, δ is the voltage dependent phase retardation caused by the SLM. Using the two-dimensional rotation matrix

$$R(\phi) = \begin{pmatrix} \cos\phi & -\sin\phi \\ \sin\phi & \cos\phi \end{pmatrix}. \tag{6.7}$$

we can calculate the Jones matrix of an SLM with the LCs extraordinary axis oriented perpendicular to the optical axis with an arbitrary rotation angle ϕ

$$T_{\text{SLM}}(\delta,\phi) = R^{-1}(\phi)\cdot T_{\text{SLM,0}}\cdot R(\phi) \tag{6.8}$$

$$= e^{i\frac{2\pi}{\lambda}dn_o} \begin{pmatrix} \cos^2\phi + e^{i\delta}\sin^2\phi & \cos\phi\sin\phi(e^{i\delta}-1) \\ \cos\phi\sin\phi(e^{i\delta}-1) & \sin^2\phi + e^{i\delta}\cos^2\phi \end{pmatrix}. \tag{6.9}$$

The uniform phase offset described by $e^{i\frac{2\pi}{\lambda}dn_o}$ only affects the phase, but not the polarization or amplitude and can therefore be neglected. Using these relations, we can now describe a system consisting of a polarizer, an SLM and an analyzer by

$$E_{\text{sys}} = E(\alpha) \cdot T_{\text{pol}}(\theta_p) \cdot T_{\text{SLM}}(\delta, \phi) \cdot T_{\text{pol}}(\theta_a). \tag{6.10}$$

We can assume the incoming light to be polarized horizontally and the polarizer to be horizontal as well ($\alpha = \theta_p = 0$) without any loss of generality, as the whole system is rotationally symmetric. The Jones vector of incoming horizontally polarized light then becomes

$$E(0) \cdot T_{\text{pol}}(0) = \begin{pmatrix} 1 \\ 0 \end{pmatrix}. \tag{6.11}$$

As we are only interested in the output power P, we take the norm of E_{sys}:

$$P(\theta_a, \phi, \delta) = \left|\left|E_{\text{sys}}\right|\right|. \tag{6.12}$$

For the two cases of $\theta_a = 0$ (analyzer parallel to polarizer) and $\theta_a = \frac{\pi}{2}$ (analyzer perpendicular to polarizer) this becomes

$$P(0, \phi, \delta) = \left|(\cos^2\phi + e^{i\delta}\sin^2\phi)\right| \tag{6.13}$$

$$P(\frac{\pi}{2}, \phi, \delta) = \left|\cos\phi \sin\phi (e^{i\delta} - 1)\right|. \tag{6.14}$$

Fig. 6.4 shows contour plots of the resulting power, depending on ϕ and δ for both cases. The plot shows that the power control range becomes maximal when the extraordinary axis of the LCs is at an angle of 45° with respect to the polarizer. Furthermore, the case of crossed polarizers is less sensitive to misalignments than the case of parallel polarizers.

6.2 Design specifications of the spectrum control setup

There are three main considerations for the design specifications of our setup, the wavelength range, the contrast ratio and the spectral resolution, i.e., the smallest controllable wavelength range.

We want to use the LFC as a calibrator for the FTS for simultaneous solar observations. For our solar observations, the visible wavelength regime is the most interesting. The calibration light should not overlap with this spectral region, hence we want to calibrate in the near infrared. The supercontinuum

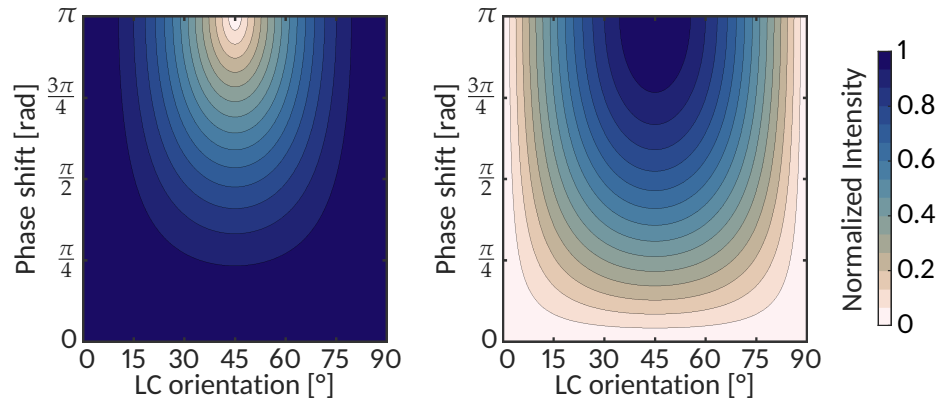

(a) Analyzer parallel to Polarizer (b) Analyzer perpendicular to Polarizer

Figure 6.4: Calculated amplitude response for two different Analyzer orientations, depending on SLM orientation and strength of phase shift.

generated by our LFC only extends to about 1000 nm. Thus, we want to be able to control the wavelength range from 700 to 1000 nm.

The supercontinuum of the LFC exhibits a strong dynamic range with large regions exceeding 20 dB (see Fig. 6.5a). For parts of the spectrum, the measured intensity is around −30 dB. Since this is the noise floor of the measurements, the intensity may be even lower. To mitigate this high dynamic range, we aim for a contrast ratio of at least 100:1—corresponding to 20 dB—or better.

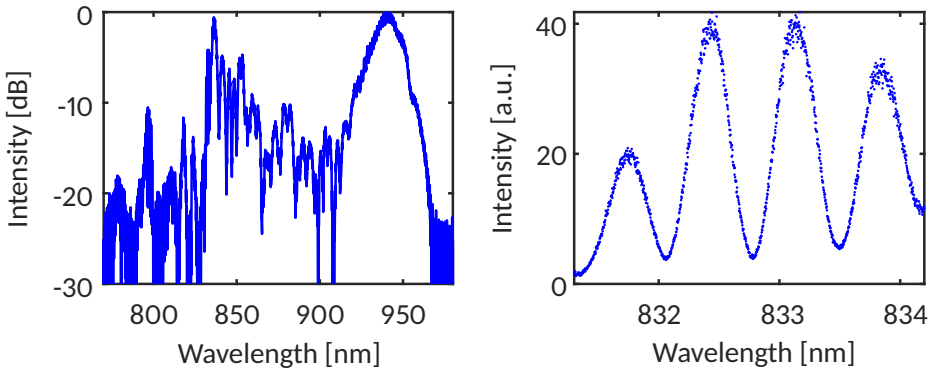

(a) Full spectrum (b) Zoom into a small oscillatory region

Figure 6.5: A typical supercontinuum spectral envelope of the LFC in our lab. Panel (a): Full spectrum with a typical dynamic range of 20 dB and more. Panel (b): A short scale oscillatory pattern typical for the supercontinuum broadening.

Additionally, the spectral envelope exhibits oscillatory patterns in some regions (see Fig. 6.5b). The separation between these peaks can be as low as 0.7 nm. In order to control such regions, it should be possible to sample them

with at least two elements. Therefore, the ideal resolution of the spectrum control setup should be on the order of 0.35 nm.

There are also some further design considerations. We try to minimize the cost and keep the setup as simple as possible. Therefore, we restrict ourselves to regular off-the-shelf components. Additionally, since it also serves as a prototype for the ELT-HIRES calibration unit, we want to keep the setup transportable. Last, we aim to optimize the efficiency. Even though the LFC delivers a large amount of power, not too much light should be wasted since a large fraction of the light is discarded when flattening the spectral envelope.

6.3 Optical layout of the spectrum control setup

We base our setup on the standard optical layout of a Fourier transform optical pulse shaping setup. However, our modulator array is a reflective SLM so that the light is reflected back through the focussing lens onto the dispersing grating. The forward-backward configuration is more compact and requires less parts. This optical configuration is quite similar to that of a regular grating spectrograph, with the detector replaced by the modulator array (see Fig. 6.6). When we planned and constructed the setup, we could make use of relations used in building grating spectrographs (Eversberg and Vollmann, 2015). With

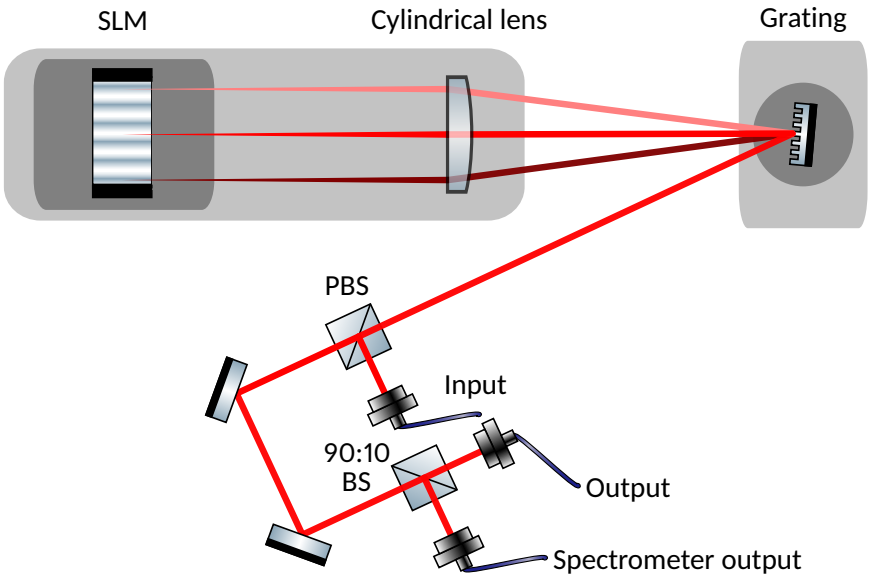

Figure 6.6: Spectrum control setup schematic. Red lines indicate combined light, dark red and light red indicate dispersed light. Grey boxes and circles indicate linear stages and rotation stages respectively.

respect to a regular spectrograph, we have to fulfill the additional constraint of the 4-f configuration, meaning that the grating is at the focal point of the focusing lens.

6.3.1 Analytical calculations

There are multiple tradeoffs we have to consider. The relevant equations and our considerations are introduced in this section. The setup is developed around two components which had been acquired prior to this work. These are the LCOS SLM HED-6001-NIR (Holoeye) and the BlueWave NIR2 Spectrometer (StellarNet). An overview of their properties is given in Tab. 6.1.

Unfortunately, the resolution of the spectrometer of $\Delta\lambda = 0.5$ nm is larger than the required 0.35 nm . As discussed before, a better resolution is required to be able to control the oscillatory patterns of the highest frequency in the spectral envelope of the LFC (see Fig. 6.5b). Since this is not attainable with the available spectrometer, we try to match the resolution of the spectrum control setup to that of the spectrometer. The resolution $\Delta\lambda$ of an optical grating is given by (Eversberg and Vollmann, 2015):

$$\Delta\lambda = \lambda \frac{\cos(\Theta_{\text{out}})}{amd_{\text{grat}}}, \tag{6.15}$$

Table 6.1: Specifications of the HED-6001-NIR (Holoeye) SLM and the BlueWave NIR2 (StellarNet) spectrometer.

(a) HED-6001-NIR

Resolution	1920 × 1080
Active area	15.36 × 8.64 mm
Pixel pitch	8 µm
Fill factor	93 %
Contrast ratio	>400:1 @830 nm
	>1000:1 @1064 nm
Reflectivity	64% @830 nm
	78 % @1064 nm
Frame rate	60 Hz
Addressing	8 Bit
Display type	VAN

(b) BlueWave NIR-2

Resolution	0.5 nm
Coverage	600 to 1000 nm
Integration	1 ms to 65 s
SNR	1000:1
Accuracy	< 0.25 nm
Repeatability	< 0.05 nm
Stability	< 0.001 nm $^{\circ}C^{-1}$
Coupling	SMA fiber

where λ is the wavelength, a is the grating constant, i.e., the distance between two rules of the grating, m is the diffraction order, d_{grat} is the width of the illuminated grating surface and Θ_{out} is the refracted angle. This angle itself depends on the grating, as well as the wavelength and the incidence angle Θ_{in}:

$$\Theta_{\text{out}}(\lambda, \Theta_{\text{in}}) = \arcsin\left(\frac{m\lambda}{a} - \sin(\Theta_{\text{in}})\right). \tag{6.16}$$

Using these relations, we calculate the resolution as a function of wavelength for different commercially available gratings with incident angles in the vicinity of the blaze angle for a beam diameter of 4 mm (see Fig. 6.7). Collimating the beam to a larger diameter proportionally increases the resolution as long as it does not become larger than the projected size on the grating.

From commercially available gratings we selected a reflective grating with a grating constant of 1/600 mm, a blaze angle of 17.6° and an aluminium coating. These parameters result in optimized efficiency at a wavelength of 1 µm (Thorlabs GR13-0610). This grating will give a resolution of 0.3 to 0.4 nm in the selected wavelength range.

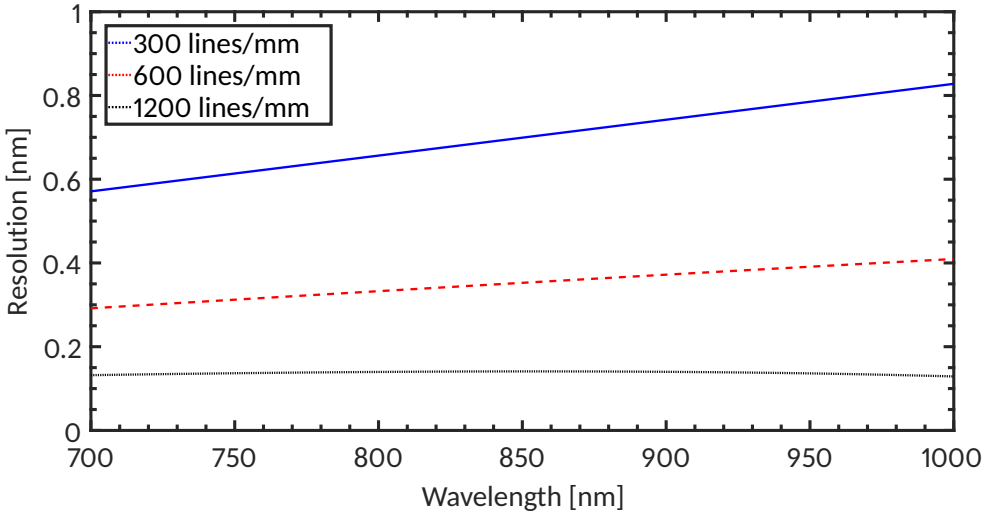

Figure 6.7: Simulated resolution as a function of wavelength for three commercially available gratings with varying grating constants for a collimated beam diameter of 4 mm.

With the specified grating, we can calculate the optimal incidence angle on the grating. For this, we have several constraints. First, the wavelength range from 700 to 1000 nm has to fall on the SLM. Second, for the sake of simplicity, we want to keep the beam path in one plane. We have to take care that no optomechanical component is blocking the beam path as well as leave some

space for alignment of the setup. To reduce optical abberations, we also try to keep the grating surface close to perpendicular with respect to the optical axis of the lens. This ensures that the whole grating surface is in the focal plane of the lens. This is the case for an opening angle of 30.7° at a central wavelength of 850 nm. Finally, we want to stay as close as possible to the blaze or Littrow angle of 17.6° to maximize efficiency. The space constraints lead to a minimal opening angle of about 25° for our wavelength range. A more precise evaluation of optical abberations and beam blocking is carried out using Zemax (see Sec. 6.3.3). Since the opening angle of 25° lies in between the two optimal values, we are satisfied with taking the middle value as a tradeoff.

The other main component we have to select is the focusing/collimation lens. Again, multiple factors play a role in this selection. First of all, the focal length of the "camera" lens f_{cam} has to be low enough, so that the whole spectral range fits on the SLM. This can be determined by the equation

$$f_{\mathrm{cam}} = -\frac{d_{\mathrm{SLM}}}{\Theta_{\mathrm{out}}(\lambda_{\mathrm{high}}) - \Theta_{\mathrm{out}}(\lambda_{\mathrm{low}})}, \tag{6.17}$$

where d_{SLM} is the width of the SLM and λ_{low} and λ_{high} are the lower and upper bound of the wavelength interval we want to capture. This gives the upper limit of 88 mm for the focal length.

The next aspect to consider is the inverse linear dispersion, which describes the width of a wavelength interval falling onto a pixel. It is given by

$$\frac{\mathrm{d}x}{\mathrm{d}\lambda} = \frac{\mathrm{d}\lambda}{\mathrm{d}\Theta_{\mathrm{out}}} \cdot \frac{1}{f_{\mathrm{cam}}} \cdot d_{\mathrm{pix}}, \tag{6.18}$$

where d_{pix} is the size of a single pixel on the SLM display. Ideally, we would like a resolution element, i.e., the point-spread-function of single wavelength, to fall on 2 to 3 pixels. This prevents the limited fill factor of the pixels from causing oscillations in the spectral envelope. Fig. 6.8 shows the inverse linear dispersion as a function of focal length at the central wavelength of 850 nm. The linear dispersion is on the order of 0.2 nm/pixel, while the resolution is about 0.4 nm, corresponding to about two pixels. However, the resolution cannot only only be limited by the grating resolution, but also by the image size of the aperture—in our case the input fiber—on the SLM. It is is given by

$$s' = s \cdot \frac{cos(\Theta_{\mathrm{in}})}{cos(\Theta_{\mathrm{out}})} \cdot \frac{f_{\mathrm{cam}}}{f_{\mathrm{col}}}, \tag{6.19}$$

where $s = 5.3\,\mu m$ is the size of the fiber core—we use the specified mode field diameter (MFD) at 850 nm—and f_{col} is the focal length of the fiber collimator. The change of image size due to the anamorphotic magnification is only marginal over the given wavelength range. Depending on the focal lengths of the cylindrical lens ($f_{cam} = 60$ to 80 mm) and the initial collimator ($f_{col} = 15$ mm or $f_{col} = 33$ mm), we get an image size of 9 to 26 µm. This is about 1 to 3 times the pixels size of 8 µm. Combining this with the inverse linear dispersion of 0.177 nm/pixel, we get a similiar value as the resolution limit given by the grating.

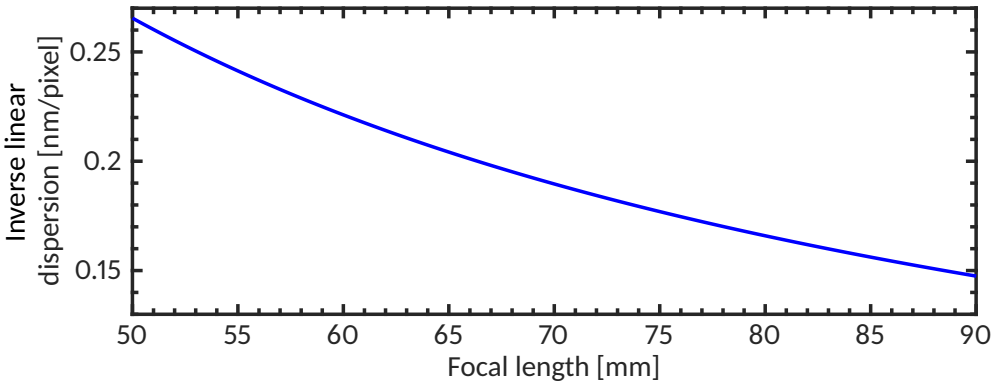

Figure 6.8: Calculated inverse linear dispersion at 850 nm as a function of collimator focal length.

One constraint for the choice of lens is the high power of the LFC, which is high enough to potentially damage the SLM. In order to reduce the power incident on individual SLM pixels, we use a cylindrical lens which spreads the power across multiple pixels in the vertical direction. Furthermore, initial Zemax simulations showed that the image quality of a regular cylindrical lens is quite poor due to chromatic aberrations. Thus, we are further restricted to cylindrical achromatic lenses. This led us to choose the AC254-075-B (Thorlabs), a cylindrical achromatic doublet with a focal length of 75 mm and a clear aperture of 25.4 mm.

There is also a constraint on the beam width to ensure a vignetting-free image on the SLM. It is determined by the size of the SLM and the distance s_{cam}, focal length and width of the lens d_{cam}. The vignetting free beam width is given by the equation

$$d_{beam} \leq \left(d_{cam} - s_{cam} \tan\left(\frac{d_{SLM}}{f_{cam}} \right) \right) \cos\Theta_{in}. \tag{6.20}$$

Due to the constraint of the 4-f configuration, s_{cam} is equal to the focal length of the camera f_{cam}. Since the chosen wavelength interval is not illuminating the whole SLM width, we have to replace d_{SLM} using Eq. 6.17:

$$d_{\text{beam}} \leq \left(d_{\text{cam}} - f_{\text{cam}} \tan\left(\Theta_{\text{out}}(\lambda_{\text{high}}) - \Theta_{\text{out}}(\lambda_{\text{low}})\right)\right) \cos\Theta_{\text{in}}. \quad (6.21)$$

This equation tells us that we can avoid vignetting as long as we have a collimated beam size smaller than 10.6 mm using this lens and grating. The beam width depends on the focal length of the collimator and the input fiber numerical aperture (NA), which is 0.12 in our case. Since we want to use a mirror collimator, we had the choice between two collimators: the RC04FC-P01 giving a beam diameter of only 4 mm and the RC08FC-P01 leading to a beam diameter of 8.5 mm. The larger beam diameter of the RC08FC-P01 improves the resolution to better than 0.2 nm and the longer focal length also decreases the image size on the SLM to 11 µm. This means that a single resolution element falls on slightly more than a single pixel. However, each pixel only has a fill factor of 90 %. Therefore, this would lead to modulation of the spectral envelope. Additionally, an experimental comparison of the two collimators also showed that the response of a single active pixel column of the SLM was barely detectable by the spectrometer when using the RC08FC-P01. This leads to issues in the wavelength calibration process. For these reasons, we chose the RC04FC-P01 collimator for our setup. If the spectrometer were to be upgraded to one with a higher resolution, this choice should be revisited. In this case, the larger collimator RC08FC-P01 should be advantageous since it increases the resolution so that the design requirement of 0.35 nm can be reached.

6.3.2 Instrumental profile

Using the previous considerations we can calculate a model of the instrumental line shape (ILS) of the spectrum control setup, i.e., the spectral bandwidth which is affected by a single SLM pixel column (see also Kalyoncu et al. (2012)). We assume a simple Gaussian profile as the light distribution exiting the single mode fiber with the specified MFD as the width of the profile. Using Eq. 6.19 we calculate the magnified image of the profile incident on the SLM. We convolve this profile with the diffraction pattern caused by the grating. This convolution is then the spatial distribution of a monochromatic beam of light (see Fig. 6.9a).

An active pixel column can be modeled with a boxcar function with the width of the active area of a single pixel which is 7.2 µm (90 % of the full pixel width). We convolve the boxcar with the spatial distribution of monochromatic light calculated in the previous step. Finally, we change coordinates from spatial extension to wavelengths using the inverse linear dispersion (see Eq. 6.18). This is then the spectral response of a single active pixel column (see Fig. 6.9b). The full width at half-maximum (FWHM) of the model ILS is 0.62 nm, which is close to the specified resolution of the spectrometer of 0.5 nm.

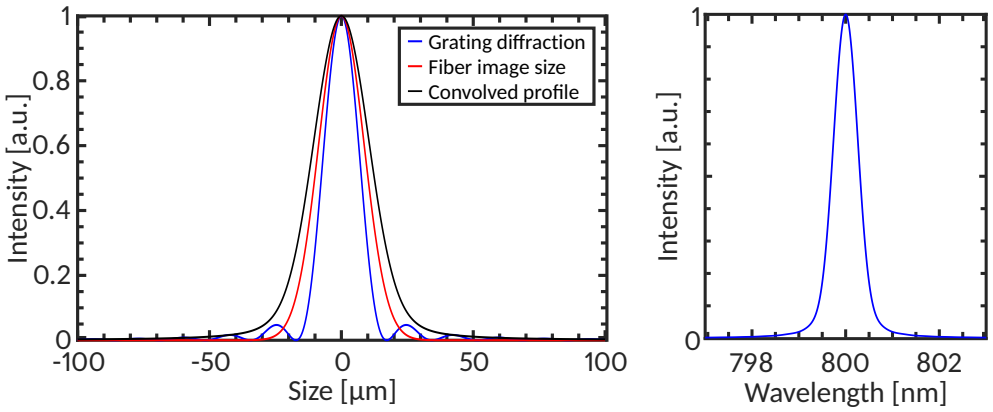

(a) Monochromatic light distribution

(b) Simulated ILS

Figure 6.9: Panel (a): Calculation of the distribution of a monochromatic beam of light incident on the SLM. The contribution from the grating diffraction (blue) and from the fiber image size (red) as well as the convolved profile are shown (black). Panel (b): Calculation of the instrumental profile of the spectrum control setup, i.e., the spectral distribution reflected by a single activated pixel.

6.3.3 Zemax simulations

Building on the results from the analytical calculations, we made a full simulation of the setup using Zemax, an optical raytracing software (see Fig. 6.10). This helps to check for optical aberrations which are not considered by the analytical equations. We can also understand which optical elements are more critical in terms of a precise alignment.

The simulations show how small we could make the setup without any vignetting. By reducing the size of the optics—for everything but lens and grating half inch optics suffice—and using the correspondingly smaller optomechanics a footprint of 100 $\times$ 180 mm is feasible.

The simulations also show that an acylindrical lens would lead to a worse image quality than an achromatic lens. Using the achromatic doublet AC254-075-B,

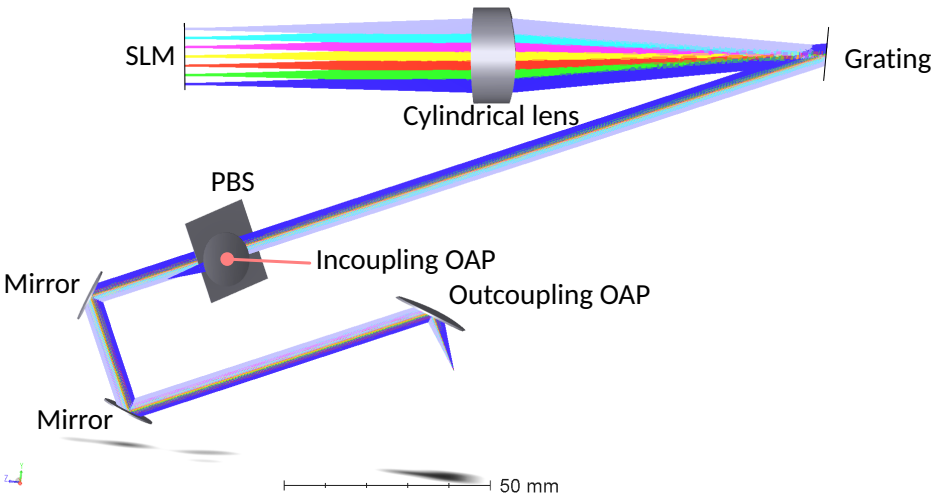

Figure 6.10: Raytracing simulation of the full spectrum control setup using Zemax.

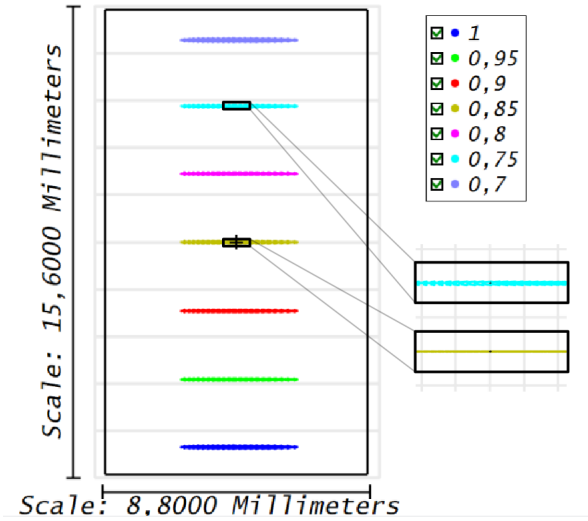

(a) Light distribution on SLM.

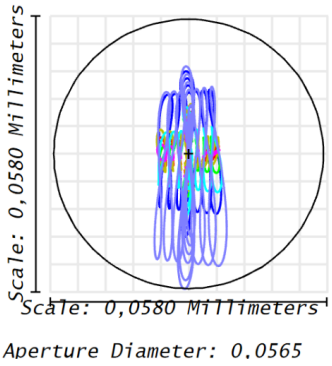

(b) Light distribution at outcoupling fiber focus.

Figure 6.11: Light distributions calculated with Zemax. The legend for the wavelengths in µm is the same for both plots. Panel (a): The light distribution for different wavelengths on the SLM display. Panel (b): Light distribution on the exit fiber front face. The distribution has a maximum extension of about 44 µm but shows some optical aberrations.

the remaining aberrations are mainly spherical aberrations. These lead to an increase of the image size towards the boundaries (see Fig. 6.11a). This can be mitigated and a more uniform focal width or instrumental profile achieved when the setup is aligned so that the wavelengths at the first and third quartile of the overall range are in focus.

Using the Zemax model, we also calculated the image size on the fiber coupling for the output (see Fig. 6.11b). This shows that the optical quality

is theoretically good enough for all light to be coupled into the output fiber. The light distribution width at the fiber front is about 44 µm, which is much smaller than the diameter of the core of the fiber (200 µm).

6.4 **Component verification**

6.4.1 Spatial light modulator

The general specifications of the HES-NIR-6001 (Holoeye) are given in Tab. 6.2a. Each pixel of the SLM can be set to 256 different voltage levels, so called gray values. In the SLM driver unit the voltage assigned to each gray value is stored in a look-up-table called ”gamma curve”. When the software sends a command to set a pixel to a certain gray value, the driver unit then applies the voltage stored in the gamma curve.

Liquid crystal orientation

The HES-NIR-6001 is an LCOS SLM with a VAN alignment of the LCs. This means that the intensity modulation works optimally with crossed polarizers aligned at 45° with respect to the LC axis (see Sec. 6.1.3).

To test the optimal alignment, we used a small setup, consisting of a HeNe-laser (Melles-Griot 25-LHR-111- 230), two turnable polarizers (Thorlabs LPVIS050-MP2) and a powermeter (Thorlabs PM100D). The laser and the powermeter, each with a polarizer in front, were placed next to each other facing the same direction. We placed the SLM about 1.5 m away from laser and powermeter. We then aligned the laser beam so that it reflected off the SLM onto the powermeter. The angle between incoming and outgoing light was only about 2°.

Initial tests suggested that the LC orientation axis is at 45° with respect to the edges of the display. We therefore conducted four measurements with all combinations of the polarizers aligned in paralellel with the SLM display edges. For each set of polarizer orientations, we stepped through the 256 gray values of the SLM and recorded the intensity. The results show that a higher contrast is achieved for crossed polarizers (see Fig. 6.12). Furthermore, the combination of incoming horizontal polarization and outgoing vertical polarization seems to be slightly favorable as it leads to a higher contrast. This could just be due to better polarizer alignment in this measurement over the other, but we nonetheless opted for this set of polarization directions in our setup.

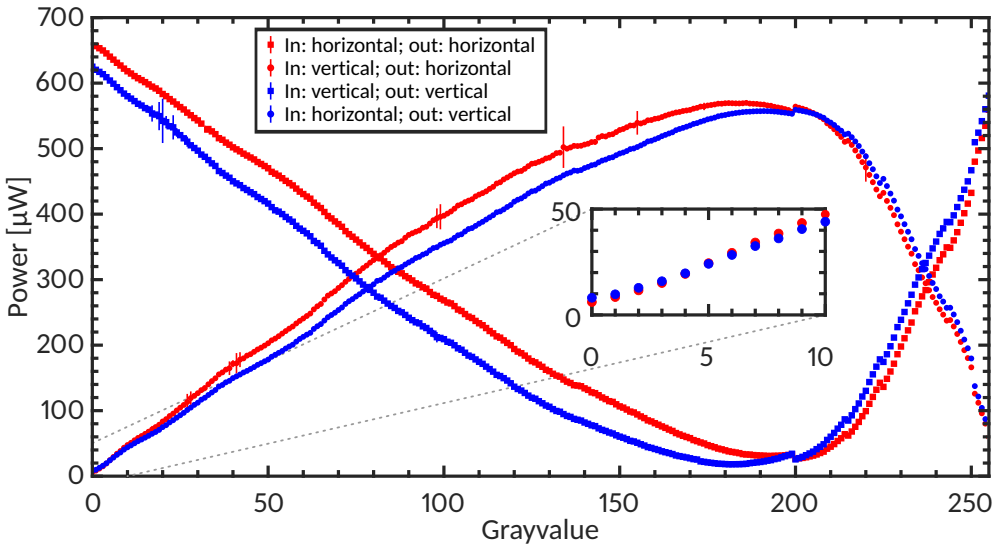

Figure 6.12: Measurement of the intensity response depending on the polarizer orientation. Crossed polarizers are indicated by dots, parallel polarizers by squares. Red indicates a horizontal analyzer and blue a vertical. The inset shows that at the lowest gray values the configuration with a horizontal analyzer reaches lower values than with a vertical analyzer. We define horizontal as the direction parallel to the long side of the SLM display and vertical as the direction parallel to the short side of the SLM display.

Bitplane sequence

The voltage of an SLM pixel is applied via a sequence of pulses. This means that each average voltage level of one frame is the sum of the voltage of these individual pulses. Thus, the phase of the light and thereby in our case the output power will flicker during one frame. The standard bitplane sequence is the 18-6 sequence with a frame rate of 60 Hz. This sequence has 1216 possible different mean voltage values, which is the highest number of all bitplanes. But, this sequence also has the highest RMS-AC-voltage value over a single cycle. We compared it with the 5-6 sequence, which only has 382 different mean voltage values, but has a much lower RMS-AC-voltage value. Additionally, it has a frame rate of 240 Hz. This provides the possibility to address the SLM four times faster.

Using the spectrum control setup, we set the whole display to a gray value of 140, about half the possible output power. We then measured the output light using a fast photodiode (Thorlabs DET36A/M) and an oscilloscope (Rodhe&Schwarz RTM2150). In Fig. 6.13 the intensity fluctuations for the two different sequences are shown. The RMS AC-voltage for the 5-6 sequence

was 348 mV, while it was 1237 mV for the 18-6 sequence. The 5-6 sequence modulation is lower by a factor of 3.55, agreeing well with the manufacturers measurements (see Fig. A.1).

The biggest drawback of the 5-6 sequence is that the phase modulation depth is lower than π, meaning that we cannot reach the maximum intensity. When setting both sequences to maximum throughput, the output intensity for the 5-6 sequence was only 93 % of that achieved with the 18-6 sequence. In a spectral flattening application, this will raise the threshold of the dynamic range below which the spectrum cannot be controlled anymore. Since it only leads to a small reduction of the acuteness of the power level increments, the lower number of different phase values is not a major issue. Intensity variations, however, are a strong concern in FTS measurements. We therefore chose to use the 5-6 bitplane sequence in our FTS experiments.

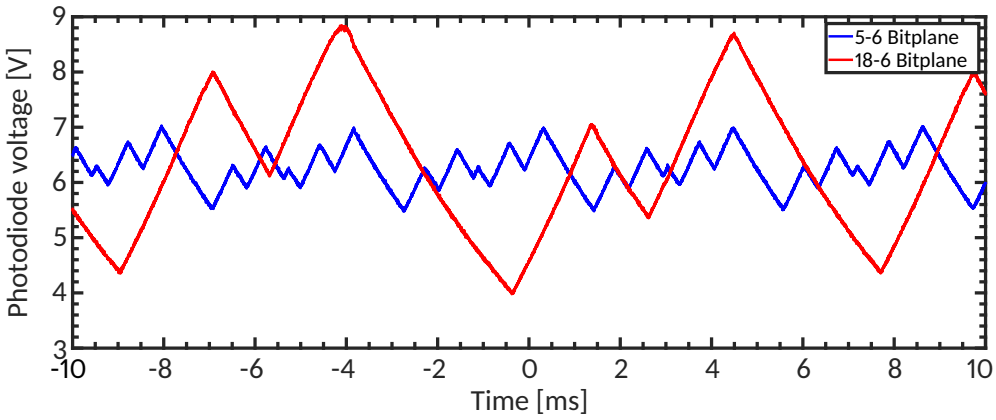

Figure 6.13: Intensity variations in the spectrum control setup output caused by the SLM bitplane adressing recorded with a photodiode. For the 5-6 bitplane (blue) with a framerate of 240 Hz four full frames are shown. For the 18-6 bitplane (red) with a framerate of 60 Hz only a single full frame is shown.

6.4.2 Spectrometer

The general specifications of the StellarNet BLUE-wave NIR2-25 are given in Tab. 6.2b. The manufacturer defines two closely space lines as resolved when the valley in between them is at half of the maximum intensity. The spectral resolution is then the distance from peak to valley. The spectral resolution corresponds to the half-width-half-maximum of a single line. The BLUE-wave NIR2-25 is specified to have a resolution of 0.5 nm. To verify the resolution and accuracy of the spectrometer, we performed measurements with two different lasers simultaneously.

One is a diode laser (Toptica DL 100) with wavelength of 780 nm and a linewidth of 30 to 300 kHz, the other a HeNe laser (Melles-Griot 25-LHR-111-230) with a wavelength of 632.8 nm with no specified linewidth, but a mode spacing of 687 MHz. In any case, the linewidth of the HeNe-laser is limited to less than 2 GHz by the gain curve, so both lasers' linewidth is much smaller than the nominal resolution of 0.5 nm of the spectrometer. This allows us to measure the ILS of the spectrometer and thereby verify the nominal resolution of the spectrometer.

Fig. 6.14 shows the mean of about 26,000 spectra in the spectral range of the HeNe-laser (Fig. 6.14a) and the diode-laser (Fig. 6.14b). A spline fit gives a FWHM of 1.810 $\pm$ 0.089 nm and a center position of 633.307 nm for the HeNe-laser. For the diode-laser the spline fit results in a FWHM of 2.625 $\pm$ 0.064 nm and a center position of 781.164 nm. This corresponds to a resolution of about 0.9 nm at 633 nm and 1.3 nm at 780 nm.

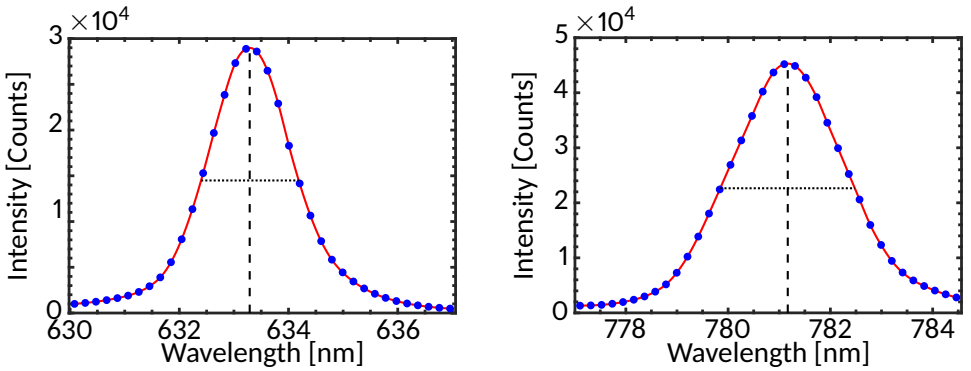

(a) HeNe-laser (b) Diode-laser

Figure 6.14: Measured spectrometer ILS using two different lasers. The measured data points (blue dots), a corresponding spline fit (red solid line), as well as the determined line center (black dashed line) and FWHM (black dotted line) are shown.

Both measurements indicate that the nominal resolution of 0.5 nm is not reached. Fig. 6.15 shows the measured line center deviation from the mean over a timespan of 86 minutes. The Pearson-correlation coefficient between the two line centers is insignificant with a value of –0.0353. The HeNe-laser line center seems to jump between three different positions. This is likely due to mode instability. Accounting for this and calculating the correlation for each of the subsets of HeNe line centers with the corresponding diode laser line centers still does not yield any significant outcome. We therefore conclude that the drift in line center position is mainly caused by an actual drift of the laser line center and not by the spectrometer.

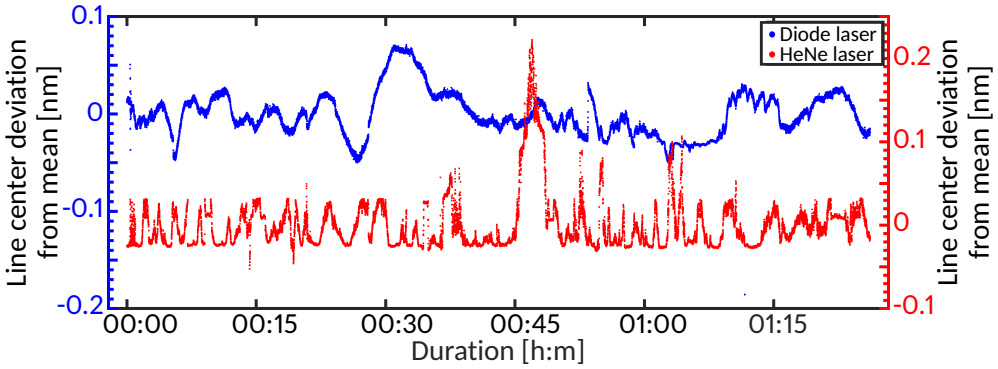

Figure 6.15: Drift of measured line center for a diode laser (blue dots) and a HeNe-laser (red dots).

6.5 Optical setup

6.5.1 Coupling stage

Light from the LFC is fed into a photonic crystal fiber (PCF) (NL-PM-750, 50 cm) inside the comb module. The fiber is plugged into a mirror collimator (Thorlabs RC04FC-P01) located outside the laser compartment. The collimated light is guided through a periscope to a series of beam splitters on a breadboard (see Fig. 6.16). These are a polarizing beam splitter (PBS) (Thorlabs CCM1-PBS252/M), a dichroic longpass with a cut off wavelength of 650 nm (Thorlabs DMLP650) and a second dichroic longpass with a cut off wavelength of 1000 nm (Thorlabs DMLP1000). This filters the unused polarization direction, light below 650 nm and light above 1000 nm. The light below 650 nm and above 1000 nm is going to be used in beat-mode experiments with a frequency doubled Nd:YAG laser at 532 nm and 1064 nm. The light reflecting of the second longpass is coupled into a polarization maintaining fiber (Thorlabs PM780-HP) using a lens collimator (Thorlabs F240FC-780). There is a high mismatch between the nonlinear fiber numerical aperture (NA=0.39) and the polarization maintaining fiber (NA=0.12) leading to a reduced coupling efficiency. Using the numerical aperture values of the fibers the maximum possible coupling efficiency can be calculated using

$$\mu = \frac{4a^2}{(1+a^2)^2} \tag{6.22}$$

$$a = \frac{\mathrm{NA}_1}{\mathrm{NA}_2}. \tag{6.23}$$

This leads to a maximum possible coupling efficiency of $\mu = 31.6\,\%$. This mismatch is therefore the largest lossfactor in this setup.

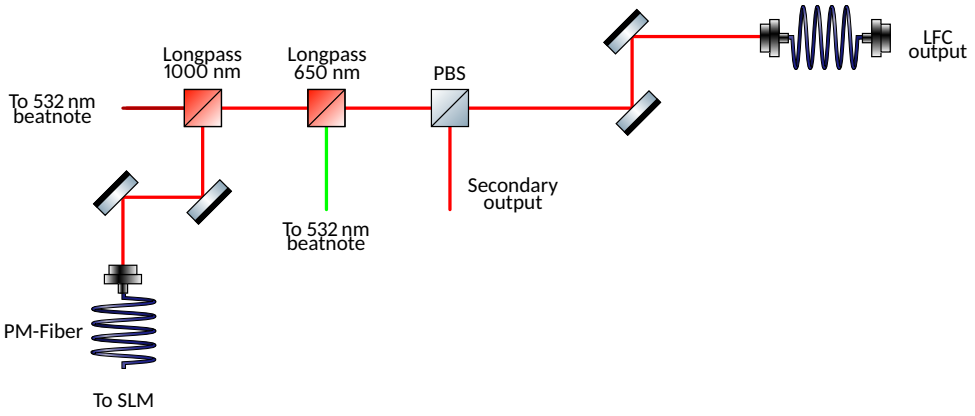

Figure 6.16: Schematic of the coupling stage.

6.5.2 Spectrum control setup

A photograph of the final optical setup is shown in Fig. 6.17. Light is coupled in at the input fiber port, reflected at the PBS, dispersed at the grating, focused by the cylindrical lens, manipulated and reflected by the SLM, collimated by the cylindrical lens, recombined by the grating, filtered by the PBS, folded by two mirrors and split to spectrometer (10 %) and science (90 %) output.

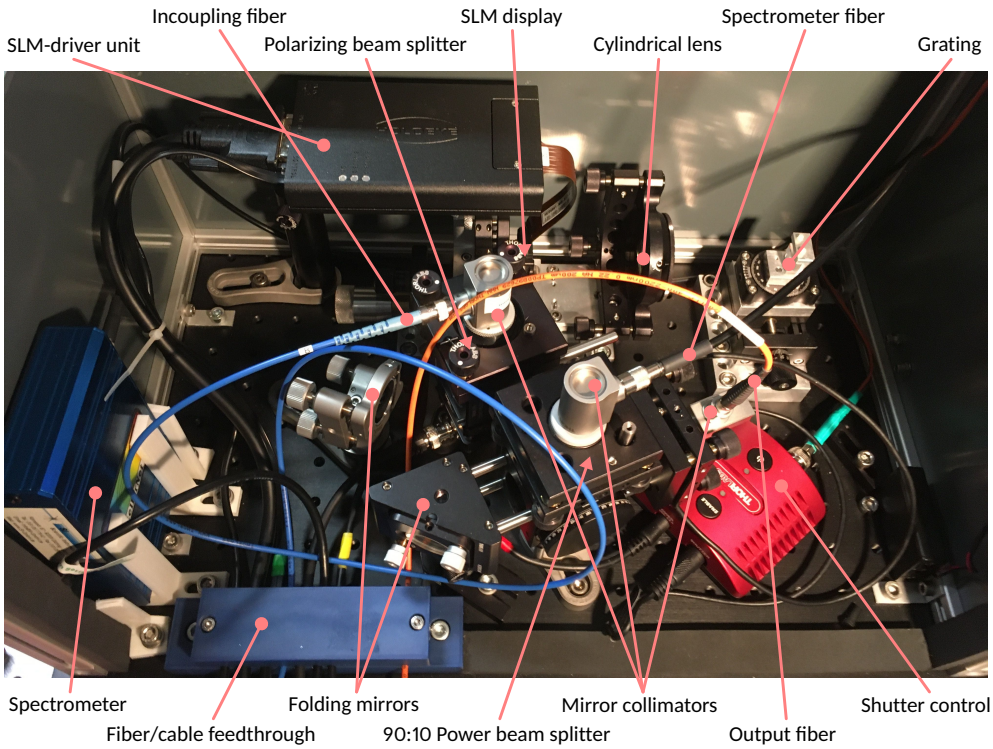

Figure 6.17: Photograph of the setup mounted on a 300 × 500 mm breadboard. Arrows indicate hidden elements.

The setup, including the enclosing box, fits on a 300 × 500 mm breadboard. Moreover, the number of optical components is kept to a minimum. In total, the setup consists of ten components. These are three mirror collimation packages for the input and output fibers (RC04FC/PC), two folding mirrors (1/2", silver coated), a PBS (PBS252), a 90:10 power beam splitter plate (BSN11R), a reflective ruled grating (GR13-0610), a cylindrical achromatic lens (AC254-075-B) and a spatial light modulator (HED 6001-NIR).

The theoretical efficiency calculated from component specifications for the science port is shown in Tab. 6.3 for wavelengths of 830 nm and 1064 nm (these were the only values given by HoloEye). The grating efficiencies are specified in Littrow configuration, so the values in our case are lower than the ones specified in the table. Overall, the theoretical throughput is in the range of 25 to 30 %.

The overall setup is quite simple with few sources for errors in the construction process. One thing to be careful about, however, is the orientation of the two beam splitters. For the PBS, it is important that the input is in reflection

Table 6.3: Efficiencies of the different optical components in percent at 830 nm and 1064 nm. Grating efficiencies are given for Littrow configuration only.

Component	830 nm	1064 nm
Collimator	>97.5	>97.5
PBS s-pol	99.5	99.5
Grating p-pol	72.0	88.0
Lens, coated	99.5	99.5
SLM	64.0	78.0
Lens, coated	99.5	99.5
Grating s-pol	64.0	51.0
PBS p-pol	97.0	98.0
Mirror	98.9	98.5
Mirror	98.9	98.5
90:10 BS p-pol	95.0	95.0
Collimator	>97.5	>97.5
Overall	>24.9	>29.6

and the output is in transmission. This is due to the fact that the extinction ratio is much higher in transmission. A lower extinction decreases contrast and therefore decreases the ability to compensate the dynamic range of the spectral envelope. In order to reduce the footprint, we orient the PBS so that the collimator from the input fiber is perpendicular to the beam plane.

The power beam splitter plate has a slight polarization dependence. This means that the nominal 90:10 split ratio is only achieved for unpolarized light. For s-polarized light (see Fig. A.4), meaning the polarization direction is in the plane of the beam splitter plate, the split ratio is about 81:18. For p-polarized light, the split ratio becomes 95:4 in the desired wavelength region. As our spectrometer is typically close to the lower limit of exposure times, we opt to maximize the power in the output port. Therefore, we ensure that the outgoing light is p-polarized with respect to the beam splitter plate. The spectrometer is coupled to the spectrometer output port with a hexagonal fiber (CeramOptec, 550 µm core width).

6.5.3 Optomechanics

To simplify the initial setup of the optical components and the alignment process, we make use of commercially available optomechanics and built custom adapter plates and mounts to combine all components. Additionally, we built a simple grating mount. A CAD-model of the central optical components and the corresponding optomechanical devices is shown in Fig. 6.18.

Grating stage

The most important part about the grating mount is that its rotation axis lies in the surface of the grating. This ensures that when the grating is rotated, e.g., to select a different spectral region, only marginal realignment of the beampath is required. To achieve this, we manufactured a custom grating mount, which is fixed on a rotation stage (Thorlabs MSRP01/M). The rotation stage is connected to a linear stage (OWIS older model, comparable to VT 45N) via a custom adapter plate, so that the grating can be aligned to be in line with the SLM and the cylindrical lens. The linear stage in turn sits on a custom adapter plate which can be mounted on a standard breadboard (25 mm grid of M6 bores). There are additional bores halfway in between, in case a lens with a different focal length is used in the future.

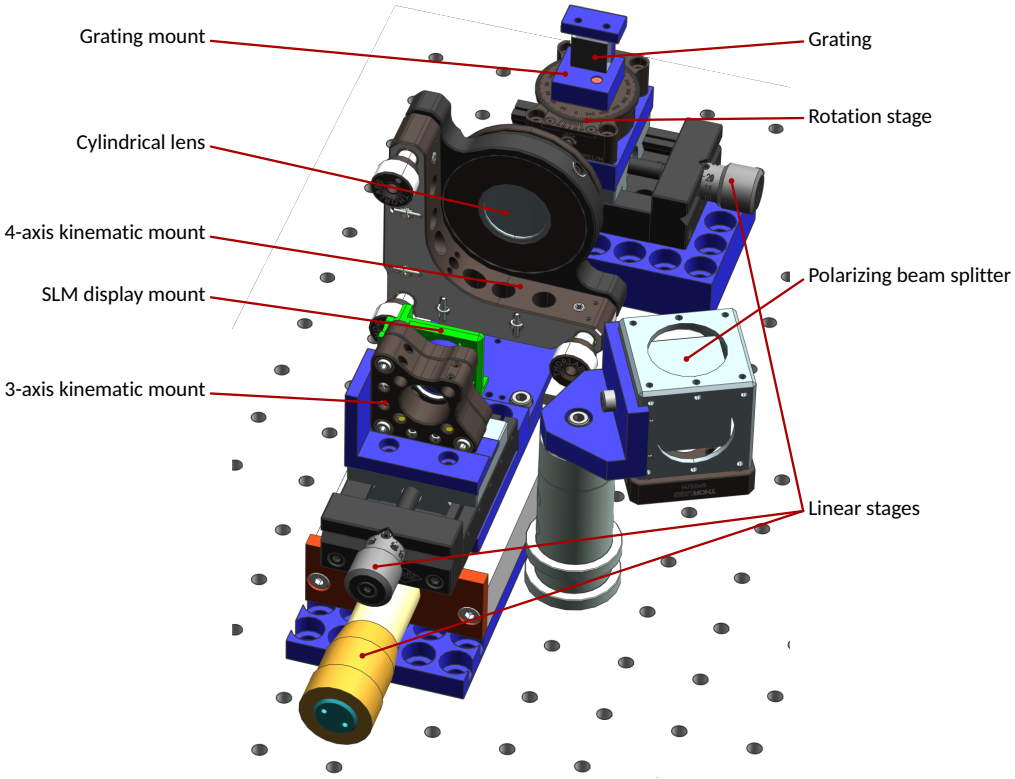

Figure 6.18: CAD model of the central components of the spectrum control setup. The designed mount and adapter plates connecting all parts are shown in blue.

Cylindrical lens and spatial light modulator stage

For the cylindrical lens and SLM two linear stages are used. The lower one moves both the cylindrical lens and SLM in unison and was custom built by our workshop for another project. The second one (OWIS older model, comparable to VT 45N) moves the SLM with respect to the lens. This way, the focus on the SLM and the distance between cylindrical lens and grating can be adjusted independently. The cylindrical lens is mounted in a 4-axis mount (Thorlabs KS1RS), allowing rotation, z-translation, tip and tilt. The holder for the SLM display is connected to a 3-axis mount (Thorlabs KC05-T) with a custom screw.

6.5.4 Enclosing box

To shield the setup from environmental influences and the user from laser radiation, as well as to protect the setup during a possible transport, we built an encasing structure around it. It is mounted on the same breadboard as the rest of the setup. Through a small port all necessary cables and fibers can be routed. Inside is a small button which is pressed by the lid when closed. The

button controls the shutter behind the incoupling fiber collimator, so that the shutter is closed automatically when the lid is opened.

6.6 Alignment procedures

The main axis of the setup is given by the SLM, cylindrical lens and optical grating. For coarse initial alignment, we use a halogen lamp coupled to a 105 µm multimodefiber. The incoupling beamsplitter is pointed, so the light is incident on the grating. We then rotate the grating, so that the visible part of the spectrum instead of the infrared falls on the SLM. With the visible light, we can then adjust the tip and tilt of SLM until the reflected and incident spot coincide on the grating. We rotate the grating again so the red part of the spectrum is just on the edge of the SLM in order to ensure that the near infrared part is incident on the SLM. Now we use the two folding mirrors to maximize the power on both output ports. In the next step, we want to place the desired wavelength in the center of the SLM. For this, we turn on only the central region of the SLM, which causes a peak to appear in the spectrometer measurements. Then, we just have to rotate the grating until the peak in the spectrum matches the desired wavelength. For the final alignment steps and throughput optimization, we switch to the polarization maintaining single mode fiber and the LFC.

6.6.1 Rotational alignment of cylindrical lens

To ensure that the focusing axis of the cylindrical lens is aligned with the SLM, we use the SLM and the spectrometer. We turn on a single horizontal pixel line on the SLM and take an exposure with the spectrometer. We then set every pixel to zero gray value and take a second exposure. Finally, we take a third exposure with the full SLM set to a high gray value. This is repeated for each pixel line. Using the formula

$$I_{\text{rel}}(\lambda, p) = \frac{I_p(\lambda) - I_0(\lambda)}{I_{\text{high}}(\lambda) - I_0(\lambda)}, \tag{6.24}$$

we get a normalized intensity distribution as a function of activated horizontal pixel line p and wavelength. This process is necessary due to the high variability of the LFC. By inverting a previous wavelength calibration (see Sec. 6.7.3) we can express the wavelength in terms of pixel columns. We can thus calculate the relative intensity distribution on the SLM (see Fig. 6.19).

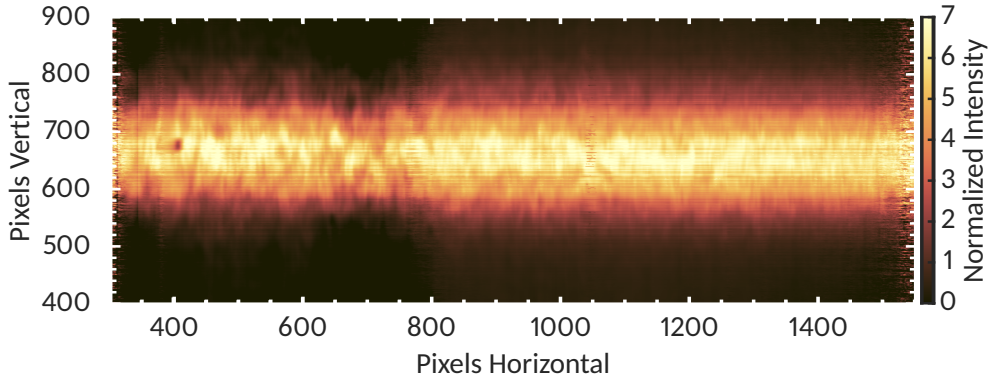

Figure 6.19: The normalized light distribution on the SLM is shown. The regions where little or no light was present were cropped.

We then fit the peak position along each pixel column. By fitting a linear curve to the peak position in terms of pixel rows as a function of pixel column, we can determine whether there is any rotational mismatch between the cylindrical lens and the SLM (see Fig. 6.20). Using this result, we can adjust the rotation accordingly. In the end we achieved a tilt between the two elements of 34', which is at the limit of what is possible with a manual rotation. Using a lens mount with a micron adjustment screw this could be improved further.

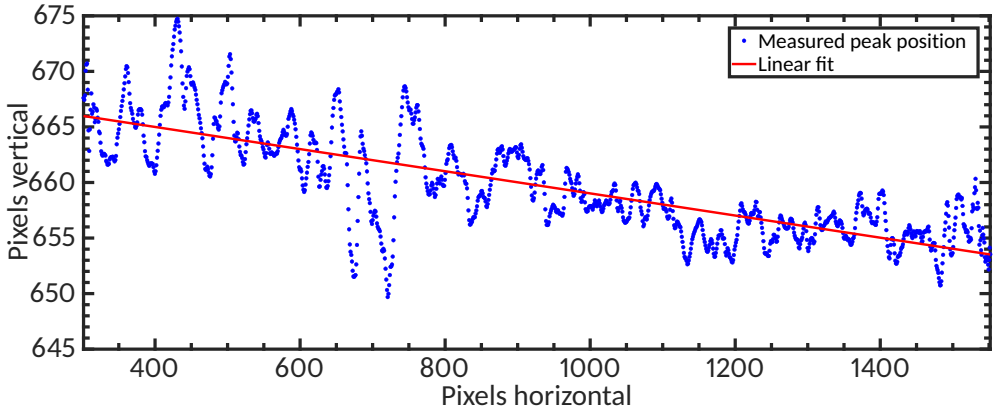

Figure 6.20: Measured peak positions on the vertical pixel axis as a function of horizontal pixels (blue dots) and a corresponding linear fit (red line) from which the rotational mismatch between SLM and cylindrical lens can be calculated.

6.6.2 Adjusting the focus

From the Zemax simulations we know (see Sec. 6.3.3) that the optimal alignment is not with the central wavelength in focus, but with the two wavelengths halfway between center and each edge in focus. To achieve this, we take three exposures with different SLM settings again. Similar to the previous step, we

take exposures with the SLM each turned fully off and on. This time, the third exposure consists of two pixel columns, i.e., pixel lines perpendicular to the dispersion direction, switched on. These are each at the first and third quartile of the current LFC spectrum, since the Zemax simulations showed that the focus of these wavelengths should be optimized (see Sec. 6.3.3). After correcting the exposures similar to Eq. 6.24, we get a spectrum with two peaks caused by the activated pixel columns. We fit a generalized Gaussian to each of these peaks. By adjusting the focus using the linear stage on which only the SLM is mounted, we minimize the FWHM of the measured lines .

6.7 **Calibration of the spectrum control setup**

The spectrum control setup calibration involves three steps. First, the gray values of the SLM have to be assigned to the correct voltage so that the intensity output of the system linearly depends on the gray values. This is the calibration of the gammacurve. In the second step, the wavelength dependent intensity response of the spectrometer has to be crosscalibrated with that of the FTS. These two calibration steps usually only have to be performed after major changes to the setup. The third calibration step is to map wavelengths to SLM pixels. This should be done each time the spectrum control setup is used. The high frequency of this calibration is necessary as the setup is not environmentally controlled and slight shifts of the wavelength position by more than 4 µm already disturb the control loop.

6.7.1 Gammacurve calibration

We want the intensity response of the setup to be linear with respect to gray value, to improve stability of the control loop and to ensure that the control steps are equal at all intensity levels. Therefore, we have to adjust the gamma curve of the SLM. Since the intensity response is also wavelength dependent, we chose to adjust the gammacurve so that the response is linear for the central wavelength of 850 nm.

To improve the gamma curve, we first have to measure the intensity response of the system as a function of gray value and wavelength. Due to the variability of the LFC, we have to take three exposures with different settings while iterating over each gray value g (similar to Sec. 6.6.1). To measure the background (I_0) all pixels are set to a gray value of zero for the first exposure. For the second exposure, all pixels are set to a fixed high gray value (I_{high}). This

is to track short term changes in the spectral envelope. For the last exposure, all pixels are set to the respective gray value g. The relative intensity for each g is then

$$I_{\text{rel}}(\lambda, g) = \frac{I_g(\lambda) - I_0(\lambda)}{I_{\text{high}}(\lambda) - I_0(\lambda)}. \tag{6.25}$$

We repeat this procedure for ten exposures of each setting for every gray value and average the results to reduce the impact of noise. For further noise reduction, we also average the relative intensity response over a small spectral window of 5 nm width around 850 nm, the wavelength for which we want to optimize the gamma curve. Then, we fit a smoothing spline to the relative intensity response. Using the original gammacurve that relates g to the applied voltage, we can rewrite $I_{\text{rel}}(\lambda, g)$ as a function of applied voltage. Then, we determine the corresponding voltage at increments of $\frac{1}{255}$ of the relative intensity. These voltages are then assigned to the gray values for the new, improved gamma curve, which gives a linear relative intensity response from zero to one for 850 nm.

For different bitplane sequences, a different number of possible voltage levels can be set (1216 for the 18-6 bitplane, 384 for 5-6 bitplane). Additionally, the voltage range covered by the different bitplane sequences differs. Therefore, the gammacurve has to be recalibrated when using a new bitplane sequence for the first time. We calculated an improved gamma curve for both the 18-6 and the 5-6 bitplane (see Fig. 6.21). For the 5-6 bitplane there is a small issue. At a gray value of about 140, a jump occurs in the intensity response (see Fig. 6.21b). The manufacturer states that this is caused by the internal switching of bits, as each voltage is encoded internally by a different bit setting and some bits can cause larger jump. A more sophisticated gamma curve calibration could be done by identifying the voltage levels at which these jumps occur and fit according chunks between these jumps. However, for us the current gamma curve is sufficient.

Using the improved gamma curves, we measured the relative intensity response for each bitplane sequence. We then fitted a linear trend to the spectral intensity response in each wavelength. The relative residual to the linear response is typically lower than 5 % and does not exceed 12 % for the 18-6 bitplane (see Fig. 6.22). For the 5-6 bitplane the residual is lower than 8 % and does not exceed 11 % in regions with sufficient light (see Fig. 6.23). The jump observed in the linear intensity response is also clearly apparent in the residuals, leading to a sign flip at a gray value of about 140.

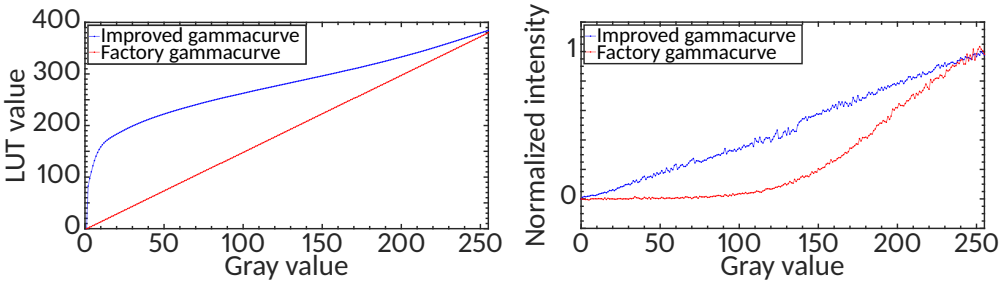

(a) Gammacurves (b) Intensity response

Figure 6.21: Panel (a): Comparison of factory (red) and improved gammacurve (blue) for the 5-6 bitplane sequence. Panel (b): Comparison of the corresponding intensity responses.

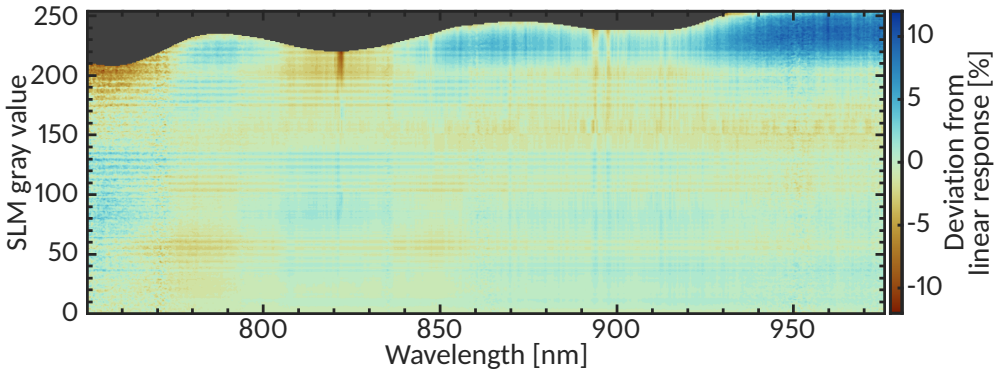

Figure 6.22: The residuals from a linear response in each wavelength for the 18-6 bitplane sequence.

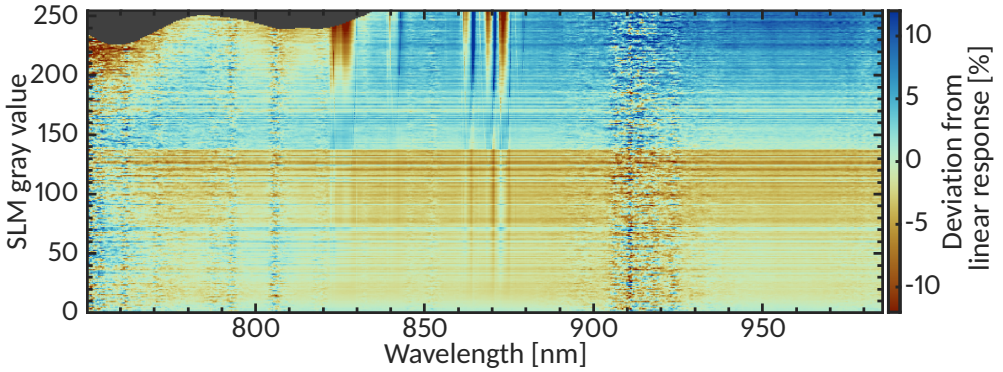

Figure 6.23: The residuals from a linear response in each wavelength for the 5-6 bitplane sequence.

The residual plot for the 18-6 bitplane in Fig. 6.22 also shows the regions at high gray values where the intensity reaches its maximum and starts to fall again. To a lesser degree, this is also the case for the 5-6 bitplane. The gray values, where the maximum is reached, are stored in a look-up-table. Using this look-up-table we can prevent the control loop from overshooting, i.e.,

driving the intensity over this maximum and thereby reducing the intensity when an increase is necessary. With the look-up-table, we are also able to set the SLM to maximum throughput for all wavelengths simultaneously.

6.7.2 Cross calibration with Fourier transform spectrograph

We expect the intensity responses of the spectrometer and of the FTS to be different. This can be due to optical losses in the fibers and other optics, different detector efficiencies and the difference in the measurement process. We want to cross-calibrate both intensity responses. With the cross calibration, we can achieve the desired spectral envelope for FTS measurements using the spectrum control setup (Probst et al., 2013).

We performed low-resolution, double-sided measurements with the FTS while the spectrum control setup was set to give a spectrum with a flat top in the spectrometer measurements. A plot of both measurements is shown in Fig. 6.24. The FTS measurements show a lot more structure compared to the spectrometer measurements. Due to the low resolution of the spectrometer, this is expected. The intensity response of the FTS is also clearly different than that of the spectrometer, with intensities increasing with wavelength.

We want to approximate the intensity response of the FTS. For this, we created a mask from the spectral regions where the spectrum deviates by more than 2 % from the set point in the spectrometer measurements. We applied this mask to the FTS spectrum and then fitted a quadratic function to the remaining data. Since the exact underlying function is not known, we opted for the simplest model.

To apply the cross calibration, the desired output spectrum set in the control loop, has to be divided by the quadratic fit function. Then, the correct intensity response is achieved in the FTS measurements. This is only a coarse correction and does not account for any small scale absorption features. However, the low resolution of the spectrometer and its asymmetric ILS make it hard to compare the two spectral responses on a smaller scale. To improve these results, better data would be required. As the deviations are much lower than an order of magnitude, this is not a major concern, but could be improved in the future.

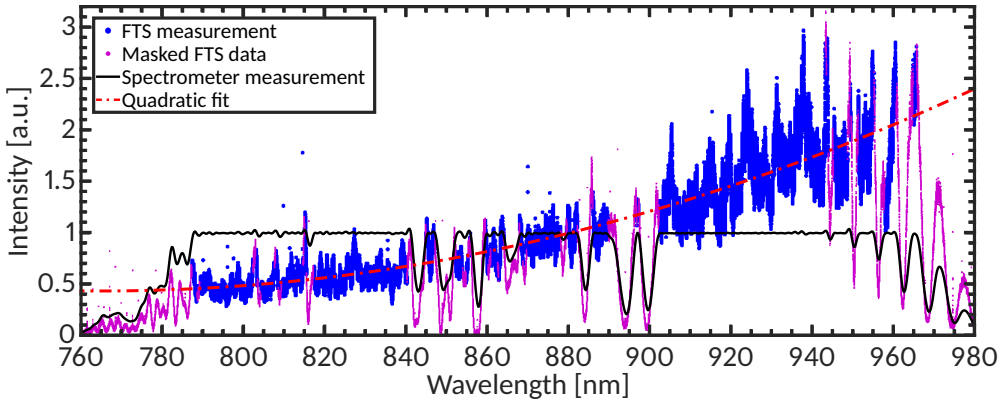

Figure 6.24: Simultaneous measurement of the flattened LFC with the spectrometer (black solid line) and FTS (blue dots). Excluded FTS data points (pink dots) and a quadratic fit to the FTS data (red dash-dotted line) are also shown.

6.7.3 Wavelength calibration

In order to control a specific wavelength region with the SLM we need to measure which wavelength region is incident on which pixel column of the SLM. The measurement procedure is also similar to that of the rotational alignment procedure and gammacurve calibration and also consists of sets of three exposures (see Sec. 6.6.1 and Sec. 6.7.1). We again take an exposure each with all pixels set to zero and with all pixels set to a high gray value to subtract the background and to measure the spectral variability. For the third exposure, one pixel column p is set to a high gray value. The normalized intensity response is then

$$I_{\text{rel}}(\lambda, p) = \frac{I_p(\lambda) - I_0(\lambda)}{I_{\text{high}}(\lambda) - I_0(\lambda)}. \tag{6.26}$$

The normalized intensity response then shows a peak at the wavelength incident on the active pixel column. Since the results are prone to outliers, we repeat the measurements ten times. To speed up the process, we turn on multiple pixel columns at regular intervals for each measurement. We found that in our case a pixel spacing of 50 leads to a sufficient separation of the peaks in each normalized intensity spectrum. We then iteratively shift the active pixel columns by one pixel, until each pixel column is covered. However, we cannot uniquely identify which peak belongs to which pixel. The light from the LFC does not fully illuminate the SLM. Therefore, we do not know which is the first or last pixel column which causes a peak in the spectrum. In order to match the peaks to the corresponding active pixel columns, we take two additional sets of exposures, each with only a single pixel column

turned on. We chose two pixel columns at the first and third quartile of the illuminated region on the SLM. The linear curve between the two pixel column – wavelength datapoints provides the preliminary wavelength solution. The preliminary wavelength solution allows us to uniquely identify each peak with its corresponding pixel column from the previous step. In principle, a single measurement would suffice to anchor the wavelength solution. However, we found that the additional measurement improves stability and simplifies the data evaluation.

For the evaluation of the aquired data, we first remove any outliers in the spectra by discarding any datapoints which deviate from the median by more than three standard deviations. Then, each peak is fitted with a spline fit and the center of gravity of each line is determined to be the center wavelength of that pixel. Fitting an analytic function instead, e.g., a skewed, generalized Gaussian, leads to higher residuals and worse overall calibration performance due to the large spectrometer ILS and the variability of the line shapes caused by LFC intensity fluctuations. We found that the spline fit leads to the most consistent results.

We then fit a polynomial to the obtained pixel-wavelength data. We exclude outliers by removing all data points with a residual larger than one standard deviation of the residuals and fit the polynomial again (see Fig. 6.25). To determine the optimal degree of the polynomial for the fit, we used the Bayesian information criterion (BIC) (Schwarz, 1978):

$$\mathrm{BIC} = n \ln(\mathrm{RSS}/n) + k \ln(n), \tag{6.27}$$

where n is the number of data points, RSS is the sum of squared residuals and k is the number of parameters of the model. The lowest values of the BIC are reached for third and fourth degree polynomials, with the third degree being slightly lower. Thus, we use a third degree polynomial fit. This fit is then our wavelength solution and can be used to control the spectral envelope.

The fit residuals in terms of pixels (see Fig. 6.25) typically exceed 0.5 pixels for of about half of the pixels, which can lead to instabilities in the control loop (Probst et al., 2013). The large calibration residuals are caused by the low resolution of the spectrometer. The average inverse linear dispersion is on the order of 0.177 nm/pixel, while the resolution of the spectrometer is 1.3 nm corresponding to more than seven pixels. Therefore, we were not able to improve the wavelength calibration.

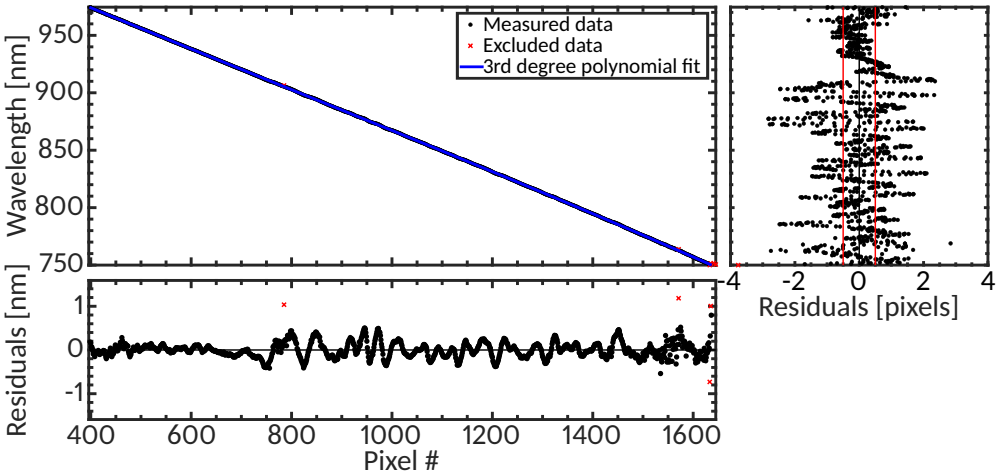

Figure 6.25: Top left panel: Wavelength calibration measurement (black dots), with excluded outliers (red crosses) and a third degree polynomial fit (blue line). Top right panel: Residuals in terms of pixels. The red lines indicate the 0.5 pixel threshold. Bottom left panel: Residuals in terms of wavelength.

6.8 Controlling the spectrum

We implemented the control software for the spectrum control setup using LabVIEW (see Fig. 6.26). The software enables us to set the spectral envelope to an arbitrary shape (within the limits of the control range).

In each iteration of the control loop, a spectrum of the output is measured using the spectrometer. The sampling of the spectrum by the spectrometer does not match the pixel spacing of the SLM. Therefore, the spectrum is interpolated at the points corresponding to the center wavelengths of each pixel column using the wavelength solution. A virtual multivariable PI-controller compares the measured spectrum to the desired set point and adjusts the gray value setting of each pixel column accordingly. The gain values of the PI-controller can be adjusted if necessary, e.g., when the exposure time of the spectrometer and thus the time interval of one iteration is changed. So far, we have implemented three analytic functions for the spectral envelope set point: a linear, a Gaussian and a sine function. The function and their coefficients can be adjusted during runtime.

Multiple graphs let us monitor the current spectrum and the current set point. Both are shown in terms of pixels and wavelength (see Fig. 6.26). Additionally, the deviation from the set point in terms of wavelength and the control output, i.e., the current grayvalue of each pixel column are displayed. Both the spectra and the control values can be stored.

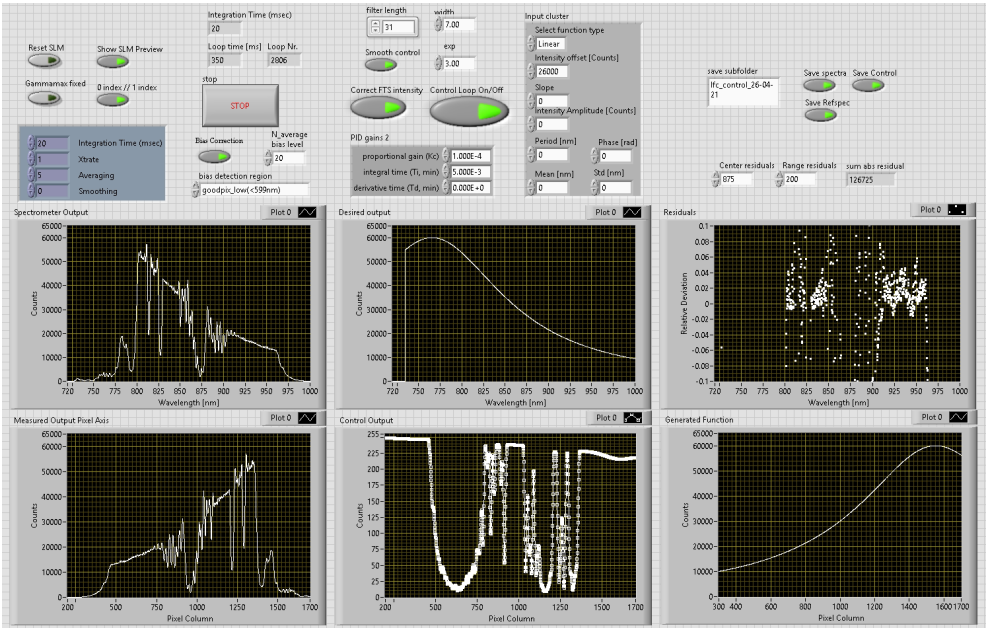

Figure 6.26: Screenshot of the front panel of the control loop VI. The graphs show (from left to right, top to bottom) the measured spectrum, the desired spectrum, the deviation from the desired spectrum, the measured spectrum interpolated to pixel columns, the current SLM gray values in each pixel column and the desired spectrum in pixel columns.

The measured FWHM of a peak of a single active pixel column is on the order of 2 nm. Since the separation of the pixels in terms of wavelength is only about 0.17 nm, each spectral bin is heavily affected by neighboring pixel columns if multiple pixels are active. This can lead to an oscillatory pattern in the control values, where a single pixel column is set to a high gray value, while its neighboring columns are set to zero. To mitigate this effect, we implemented the possibility to activate a smoothing of the control output with a generalized Gaussian kernel. The width and exponent of the kernel can be adjusted.

Additionally, there are options to apply the intensity cross calibration with the FTS (see Sec. 6.7.2) and to fix the maximum gray values in each wavelength (see Sec. 6.7.1). Furthermore, the exposure time and other acquisition parameters and the bias correction of the spectrometer can be adjusted.

6.9 Characterizing the spectrum control setup

We performed two sets of measurements to characterize the spectrum control setup and to check whether the design specifications were met. For the

following measurements, we used the LFC and the coupling stage described in Sec. 6.5.1 to couple the light into the spectrum control setup.

6.9.1 Contrast and efficiency

To evaluate the trade off between contrast and efficiency, we performed measurements with two different settings of the internal potentiometers in the SLM driver unit. These potentiometers determine the voltage range which is covered from the lowest to the highest gray value. However, the range of these potentiometers is limited. If we include the lowest voltage possible, i.e., the one which leads to the minimal output, then the voltage leading to the maximum output cannot be reached anymore. Thus, we can optimize the potentiometer setting either for contrast or for efficiency. If we chose to optimize for contrast, we include the lowest voltage. If we optimize for efficiency, we include the voltage corresponding to the maximum throughput.

For the measurements, we used a powermeter (Thorlabs PM100D) and measured the power at the input fiber and the output fiber at the science port for different settings of the SLM using the 5-6 bitplane. Additionally, we recorded spectra on the spectrometer port to measure the spectral contrast ratio. For both output measurements and both potentiometer settings, we set the SLM to zero and to maximum throughput to measure the contrast ratio.

With the powermeter, the measured input power of linearly polarized light coupled into the setup was 20.2 mW. In Tab. 6.4 the measured output powers and corresponding contrast ratios and efficiencies are shown. The overall efficiency of the setup is 17.1 % with the potentiometer optimized for contrast and 19.2 % with the potentiometer optimized for efficiency. The overall contrast ratio was 359:1 and 318:1, respectively. These values depend on the LFC spectrum, since both contrast ratio and efficiency are functions of wavelength. Thus, results will differ if the supercontinuum spectrum is different.

The spectral contrast ratio measured with the spectrometer for both potentiometer settings is shown in Fig. 6.27. The potentiometer setting optimized for contrast performs slightly better with a contrast ratio about 30 to 80 higher than for the potentiometer setting optimized for efficiency in the wavelength range up to 870 nm. The contrast ratio of 400:1 at 850 nm as specified by the manufacturer is achieved. However, there is a large drop in contrast ratio from 900 to 950 nm. We would actually expect a further increase, as the

Table 6.4: Measured output power for different potentiometer settings and derived efficiencies and contrast ratios.

	Potentiometer optimized for contrast		Potentiometer optimized for efficiency	
SLM setting	zero	max	zero	max
Output power	9.62 µW	3.45 mW	12.2 µW	3.88 mW
Efficiency	17.1 %		19.2 %	
Contrast ratio	358.63		318.03	

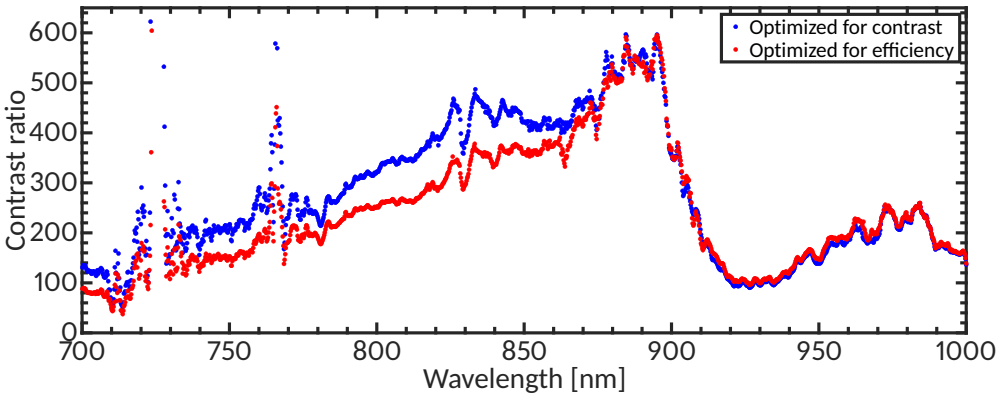

Figure 6.27: The measured spectral contrast ratio for the 5-6 bitplane. Two different potentiometer settings were used, one optimized for contrast (blue dots) and one optimized for efficiency (red dots).

specified contrast ratio is 1000:1 at 1064 nm. This is also roughly the value we get if we linearly extrapolate the slope from 750 to 900 nm. Additionally, the contrast ratio is similar for both potentiometer settings in the region from 900 to 950 nm.

To further investigate the drop in contrast, we use measurements of the light distribution on the SLM. The light distribution had been recorded for the the rotational alignment of lens and SLM (see Sec. 6.6.1). In that measurement, we had already fitted Gaussians along the pixel columns, i.e., perpendicular to the dispersion direction. We calculate residuals to the Gaussian fits of the light distribution along the pixel columns which are shown in Fig. 6.28. This reveals a structure which looks like a complex diffraction pattern. Since the image of the single mode fiber should have a Gaussian shape, we would expect the pattern to be more smooth. The pattern also changes in the exact same region from 910 to 940 nm where the largest drop in contrast is observed. As

this pattern emerges from multiple measurements at different times this also cannot be explained by intensity variations of the LFC. Furthermore, the width of the fitted Gaussians does not show a strong trend up to about 900 nm (see Fig. 6.29). However, there also is a sudden change at around 910 nm, mirroring the change in contrast ratio. Therefore, we assume the contrast ratio and the light distribution to be connected in some way.

We have no satisfactory explanation for the drop in contrast at 900 nm and the corresponding change in the light distribution. One cause could be the PBS. Extinction ratio measurements of the PBS by the manufacturer show that a different regime starts in this wavelength region (see Fig. A.3). While the extinction ratio smoothly varies up until about 880 nm, the data becomes more variable for higher wavelengths. If the manufacturers measurements in this region are not precise enough, this could explain the drop in contrast ratio. This should be investigated further by checking if the issue persists when a different type of PBS is used.

Another explanation for the drop in contrast could be the grating. The grating efficiency not only depends on wavelength, but also on the polarization. If the efficiency for the outgoing polarization compared with the incoming polarization direction drops at this wavelength, it could cause the decrease in spectral contrast ratio. However, this seems less likely, since the grating should not affect the vertical light distribution.

Our measurements show that we can use the internal potentiometers to adjust the phase retardation caused by the SLM at each gray value. We

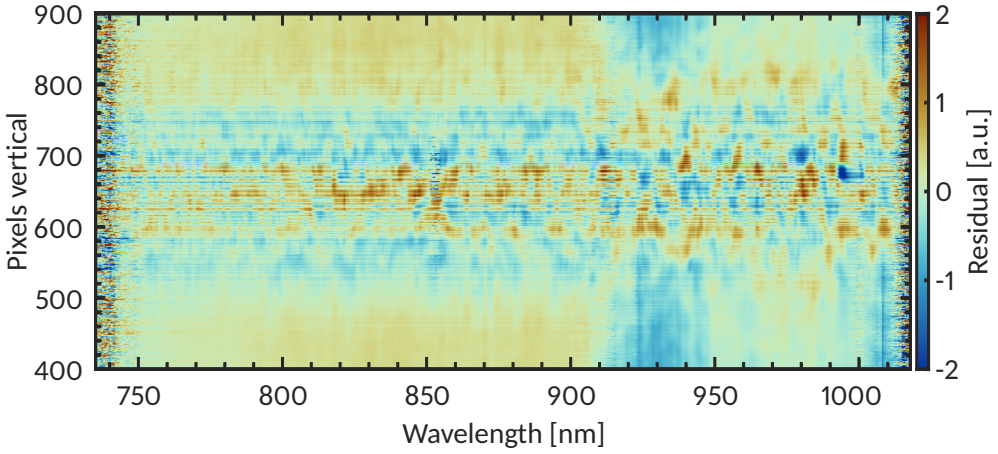

Figure 6.28: The residuals from a Gaussian fit to each pixel column of the light distribution on the SLM display are shown. The regions where little or no light was present were cropped.

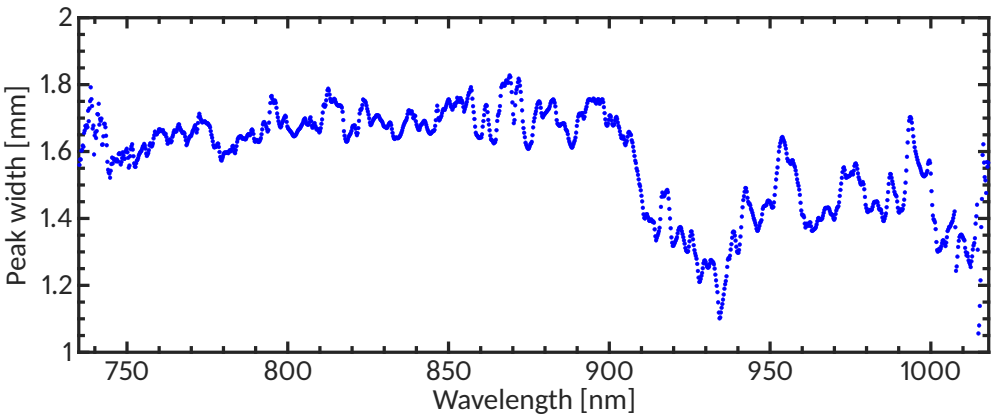

Figure 6.29: The fitted width of the light distribution in the vertical direction. The width is given as the one σ width of the Gaussian fit.

are, however, at the limit of the settings, so there is a trade off between contrast ratio and efficiency. If we adjust the settings so that the throughput is higher, the darkest state of the SLM cannot be reached anymore. This means that we sacrifice contrast. We value contrast over efficiency, so we optimize the potentiometers for maximum contrast. The 18-6 bitplane offers better contrast ratio and efficiency, since it can reach a phase retardation of π for all wavelengths, while still reaching the lowest phase retardation at a gray value of zero. However, this advantage is offset by the stronger phase flicker of the final output, so that we use the 5-6 bitplane instead for FTS measurements.

The measured efficiency of the setup is about 60 % of the theoretical value. The theoretical value, however, is an overestimation since the grating efficiencies were only specified for the Littrow configuration. In the spectrum control setup, most losses occur at the SLM and the grating. The largest improvement of the efficiency could probably be achieved by finding a more optimal grating, which is efficient for the corresponding polarization directions and respective incident angles. Manufacturer data on this is sparse, so that a full simulation of the grating would be necessary to make an informed choice.

The overall output could most easily be increased without changing the setup itself. Instead, using a different polarization maintaining input fiber whose NA better matches that of the nonlinear fiber would yield the largest gain in output power. About 75 % of the light is lost during the incoupling. This is much higher than the specified insertion loss. High NA polarization maintaining single mode fibers are commercially available, so a replacement could easily be found.

6.9.2 Spectrum control setup line shape

To measure the ILS of the spectrum control setup, i.e., its resolution, we have to use the FTS, since the spectrometer does not resolve the spectral response of a single active pixel column. Using the FTS at a resolution of $\approx 3.2\,\mathrm{pm}$ we measured the output at the science port. For comparison, we simultaneously measured with the spectrometer on the other port during the FTS measurements. We recorded two interferograms: one with pixel columns separated by 100 pixels activated and one with the SLM fully set to zero in order to subtract the background.

The measured spectrum control setup ILS is shown in Fig. 6.30. To the spectrometer data, we fitted a cubic spline while a smoothing spline was used for the FTS data. The FWHM of the ILS ranges from 1.8 nm at 750 nm to 1.3 nm at 950 nm for the spectrometer. The spectrometer measurements also exhibit a long tail on the high wavelength side of the line center, with about 10 % of the maximum line intensity 3 nm from the line center. The FWHM is 0.469 ± 0.096 nm in the FTS measurements and stays constant over the wavelength range. This again shows the low resolution of the spectrometer. A comparison of the FTS measurement with an analytical model (see Sec. 6.3.2)) shows good agreement.

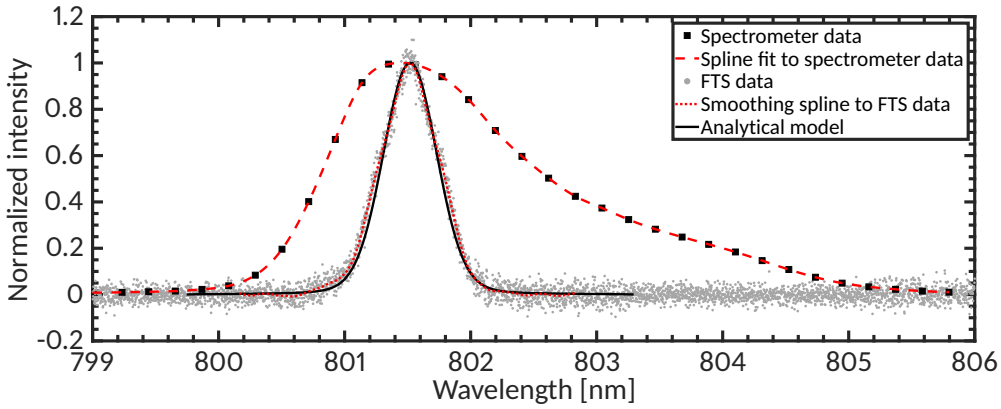

Figure 6.30: Background corrected measurement of the spectrum with a single active SLM pixel column with the spectrometer (black squares) and FTS (grey dots). Corresponding spline (red dashed line) and smoothing spline (red dotted line) fits as well as an analytical model (black line, see Sec. 6.3.2) are shown.

The agreement indicates a good alignment of the spectrum control setup and shows that we can predict the resolution of the control setup. Unfortunately, the ILS of the spectrometer is much broader than specified by the manufacturer. This also leads to a mismatch between the resolution of the

spectrum control setup and the spectrometer. Ideally, the spectrometer resolution should be similar or better to achieve a good calibration and stability of the control.

6.9.3 Evaluation of the design goals

We were able to meet our design goals for the contrast ratio and for the spectral range. To fully exploit the available spectral range, a broader supercontinuum of the LFC would be required. Since a higher contrast ratio would improve the overall performance, the cause of the drop in contrast ratio should also be found and eliminated if possible. While we did not reach the desired resolution, this was done on purpose to match the low resolution of the spectrometer. The only change required to reach the resolution of 0.35 nm, would be to switch all fiber collimators to ones with a longer focal length (e.g. , the RC-08FC-P01). So, if the spectrometer were upgraded, the spectrum control setup could easily be changed to also reach this design goal.

6.10 **Spectrally flattened comb**

We wanted to verify the performance of the spectrum control setup with the activated control loop to see if we could achieve a flat and stable spectral envelope with which we can improve the calibration. For these measurements, we also used the spectrally broadened LFC and filtered the light with the coupling stage described in Sec. 6.5.1 before the spectrum control setup. In a preliminary measurement, we only measured the output with the spectrometer, while in the second measurement the science output was measured with the FTS while simultaneously monitoring the spectrometer output.

In both sets, we first performed a wavelength calibration of the spectrum control setup (see Sec. 6.7.3). To test the setup under real conditions for future applications, we also locked both the offset frequency and repetition rate of the comb. Particularly, the offset frequency stabilization might also influence the stability of the output spectrum of the nonlinear fiber since it affects the pump power of the laser.

We first conducted a measurement to internally verify that the spectrum control setup is working as intended. For this initial measurement set, we used the 18-6 bitplane and did not employ the intensity cross-calibration with the FTS. Using the control loop software, the whole spectrum was set to a flat spectral envelope. The level of intensity was chosen so that the lowest

gray values—the ones at highest spectral intensities—were at a value of ten. This way, there is some room for the control to act in case the intensity at these points increases further. We let the control run for more than 4.5 hours, storing the measured spectra as well as the control values. To compare the stabilized, flat spectrum to the original input, we also took 369 reference spectra with the SLM set to maximum throughput.

For the measurements with the FTS, we activated the intensity cross calibration correction and used the 5-6 bitplane setting of the SLM due to the sensitivity of the FTS to intensity modulations. As with the earlier FTS measurements, we used the 100 m multimodefiber connecting the laser laboratory with the FTS and evactuated the FTS (see Sec. 3.5).

To investigate how this affects the noise caused by the SLM modulation (see Sec. 6.4.1), we recorded interferograms at different sampling rates ranging from 5 to 40 kHz with active spectral flattening. In all other respects, the same measurement parameters as described in Sec. 5.2 were used.

In a second measurement set, with the same parameters as above, we used an FTS sampling rate of 40 kHz since we learned that this reduces the impact of the intensity modulation caused by the SLM. We recorded 18 interferograms. The SLM was set to maximum throughput for the first four and last four measurements, while the control loop with the intensity cross-calibration was active for the ten measurements in between.

6.10.1 Results - Spectrometer

With the active control loop we were able to flatten a spectral region from 739 to 922 nm to a set point at about −17 dB with respect to the maximum spectral intensity (see Fig. 6.31) for the 18-6 bitplane. The control loop is stable over time. For a measurement duration longer than 4.5 hours, over 94 % of the spectral region stayed within 1 dB of the set point (see Fig. 6.35a). No deviation larger than 8 dB from the set point was detected in this spectral region (see Fig. 6.32). The largest deviation was in the region around 773 nm where the initial intensity is 23 dB lower than the maximum of the unflattened spectrum.

Fig. 6.31 and Fig. 6.33 show that the variability of the spectral envelope influences the stability of the controlled spectrum. The flattened spectrum exhibits less fluctuations in regions where the initial spectrum is smoother, i.e., from about 740 to 770 nm and to a lesser extent from about 850 to 885 nm.

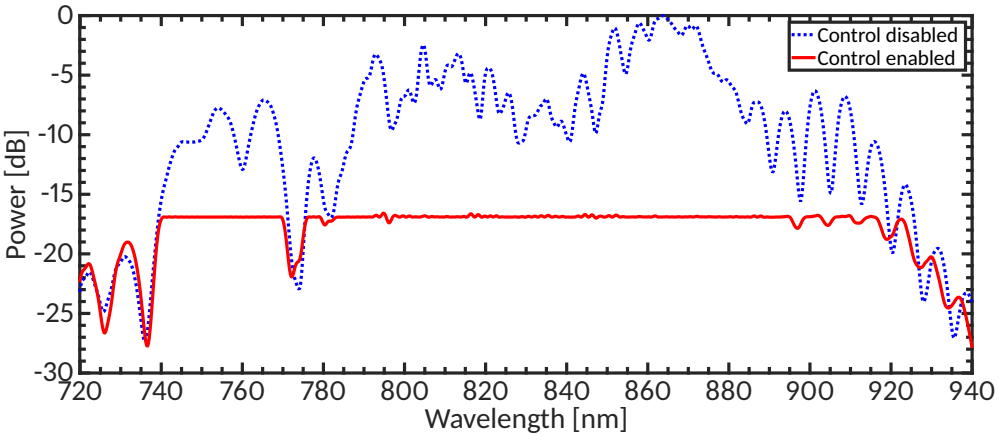

Figure 6.31: Measured LFC spectrum with control disabled (blue dotted line) and control enabled (red solid line) with the 18-6 bitplane. The spectrum with control enabled was averaged over a measurement time of over 4.5 h.

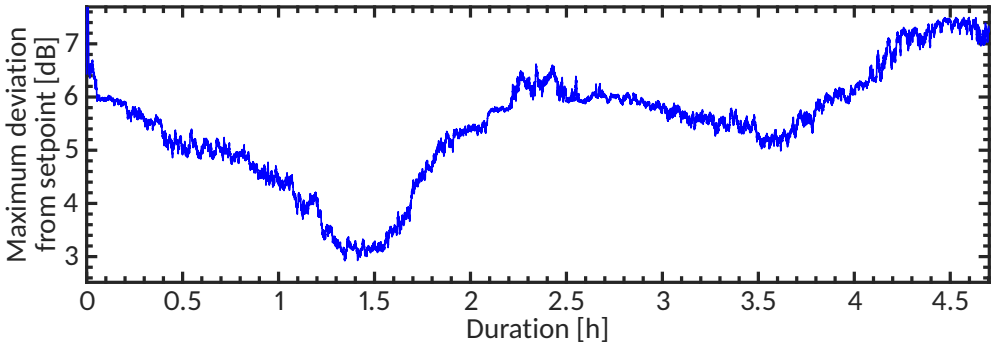

Figure 6.32: Maximum deviation from the set point throughout the measurement.

When we compare this with the results from measurements with the spectrum control setup settings optimized for FTS measurements, i.e., the 5-6 bitplane and the intensity cross calibration, both the dynamic range and the stability are reduced (see Fig. 6.34). In these measurements, 90 % of the spectral range from 777 to 977 nm are within 3 dB of the set point of −14.4 dB (see Fig. 6.35b).

Comparing the two different control setup settings (see. Figs. 6.35, 6.36), we see that the 18-6 bitplane setting without cross calibration outperforms the 5-6 bitplane with the activated intensity cross calibration. A larger fraction of the spectrum stays closer within the set point and the spectral intensity variations are lower due to the higher achievable contrast. In the regions where good control was achieved, e.g., around 815 nm or around 826 nm, however, the 5-6 bitplane achieves a slightly better stability (see Fig. 6.36).

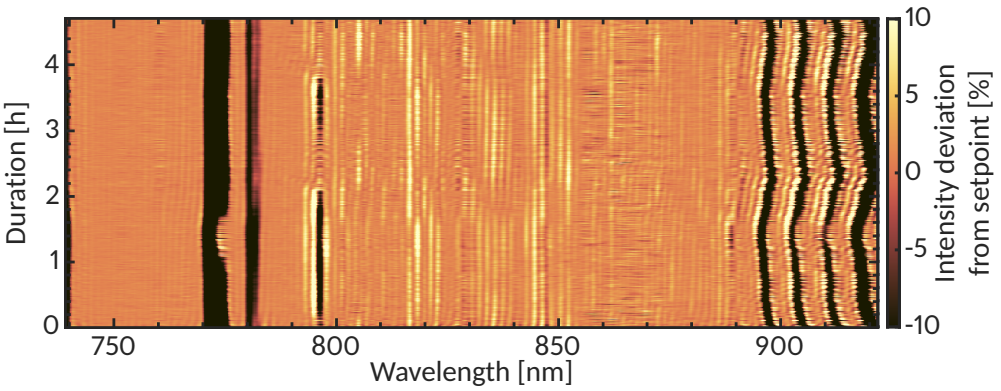

Figure 6.33: The deviation of the controlled LFC spectrum from the set point over the course of the measurement.

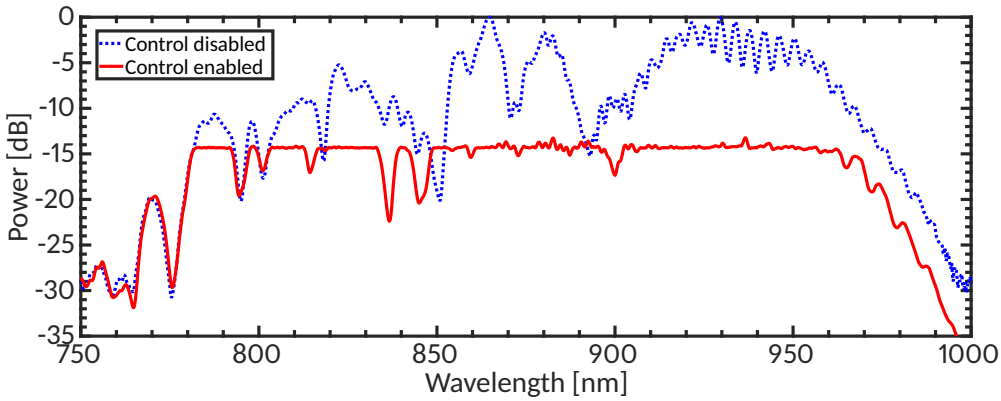

Figure 6.34: Measured LFC spectrum with control disabled (blue dotted line) and control enabled (red solid line) with the 5-6 bitplane and activated intensity cross calibration. To make the results more comparable with the 18-6 bitplane measurements (see Fig. 6.31) the spectra are corrected with the cross calibration function. The spectrum with control enabled was averaged over a measurement time of over 45 minutes.

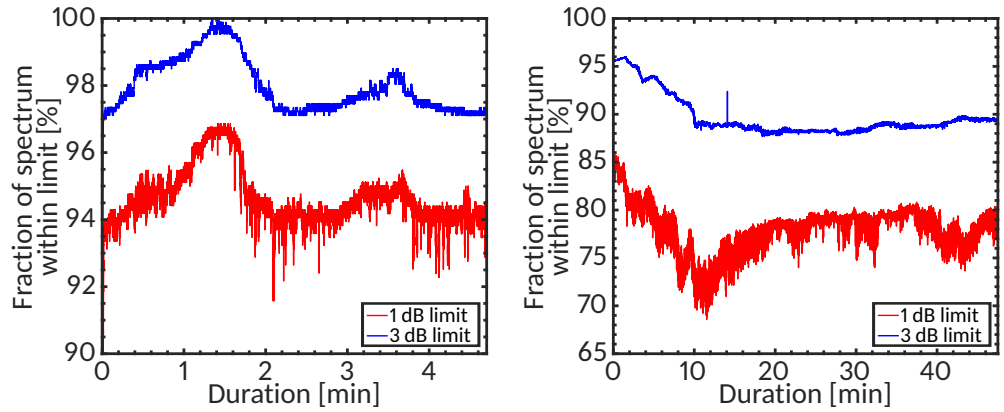

(a) 18-6 bitplane

(b) 5-6 bitplane

Figure 6.35: The fraction of the output spectrum which stayed within a range of ± 1 dB (red) and ± 3 dB (blue) of the set point for the different bitplane settings.

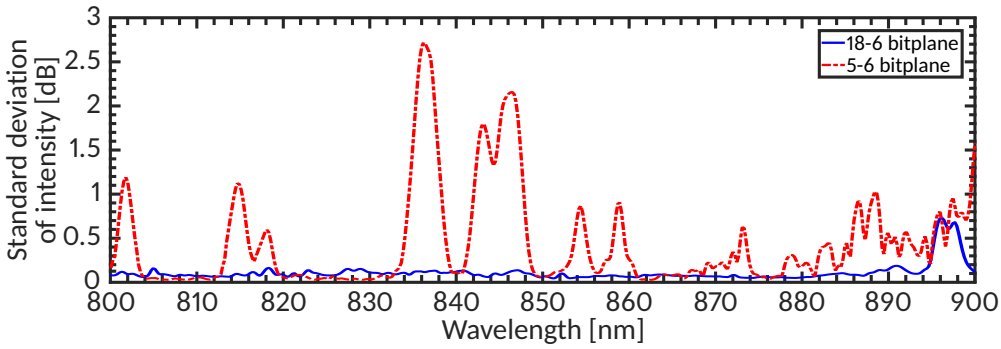

Figure 6.36: Comparison of the standard deviation of the intensity over the course of the measurement between the 18-6 bitplane setting (blue solid line) and the 5-6 bitplane setting with activated intensity cross calibration (red dash-dotted line).

6.10.2 Results - Fourier transform spectrograph

Impact of spatial light modulator

As discussed in Sec. 6.4.1, the SLM causes an intensity modulation pattern with a frequency of 60 Hz or 240 Hz depending on the bitplane sequence. The pattern also depends on the gray value. In the case of the activated control loop, each pixel column with a different gray value will imprint a different modulation pattern onto the corresponding wavelength range. The overall intensity is then the superposition of all modulated wavelength ranges. This means that the mean intensity term in the interferogram equation (see Eq. 3.4) is no longer constant, but modulated with a superposition of approximately triangular waveforms.

We observe these patterns in all our interferograms recorded with the spectrum control setup (see e.g., Fig. 6.37). In the interferogram, the amplitude caused by the SLM modulation exceeds that of the modulation caused by the scanning of the interferometer except in small regions around the bursts. Compared with an interferogram recorded without the SLM (see Fig. 5.1), there is an increased modulation amplitude between the bursts (see Fig. 6.37a). Even at zero optical pathlength difference (OPD), the interferometric modulation is only about a factor of seven stronger than the modulation caused by the SLM (see Fig. 6.37b). In between two bursts, the interferometric modulation is not visible at all and completely hidden by the SLM modulation (see Fig. 6.37c).

To gain insight on the impact the modulation has on the spectrum, we can approximately describe the modulation as a superposition of triangular waves. The Fourier series expansion of a triangular wave $I_t(t)$ is given by

$$I_t(t) = \frac{8}{\pi^2} \sum_{k=0}^{\infty} (-1)^k (2k+1)^{-2} \sin(2\pi f_t (2k+1)t), \tag{6.28}$$

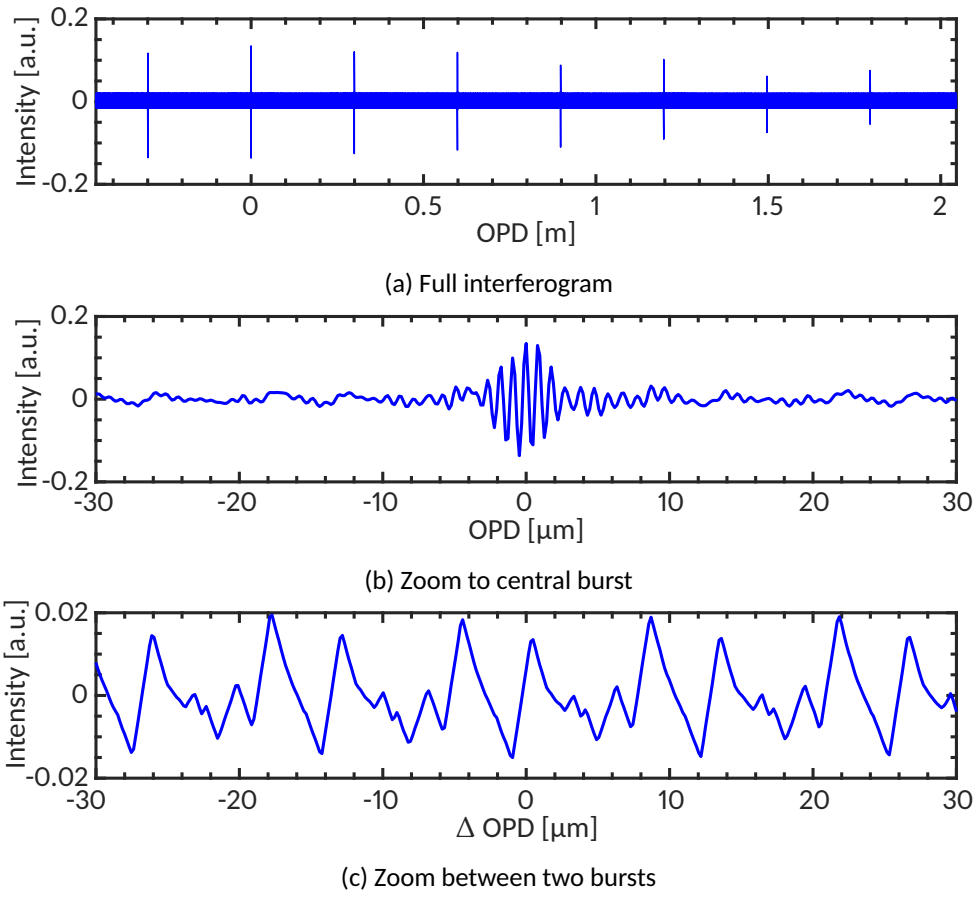

(a) Full interferogram

(b) Zoom to central burst

(c) Zoom between two bursts

Figure 6.37: Interferogram with SLM induced modulation. Panel (a): The full interferogram, showing the large modulation band between the bursts. Panel (b): The central burst which is deformed by the distinct triangular-modulation. Panel (c): A region between two bursts, where the signal is completely dominated by the triangular modulation pattern.

with the fundamental frequency of the triangular wave f_t and the mode number k. This function has infinite harmonics, although they decrease in amplitude for the higher modes. Each mode will thus cause a peak in the spectrum calculated from the interferogram.

Calculating the Fourier transform of the measured interferograms, we observe exactly this behavior. The peaks caused by the SLM modulation are apparent in spectral regions with low optical intensity (see Fig. 6.38b) but are not immediately obvious in regions with higher optical intensity (see Fig. 6.38). However, the SLM peaks still affect the line shapes of the comb lines if they overlap in regions with optical intensity (see Fig. 6.38c).

Furthermore, the amplitude of the modulation is stronger at intermediate gray values and becomes weaker for gray values close to the maximum or zero

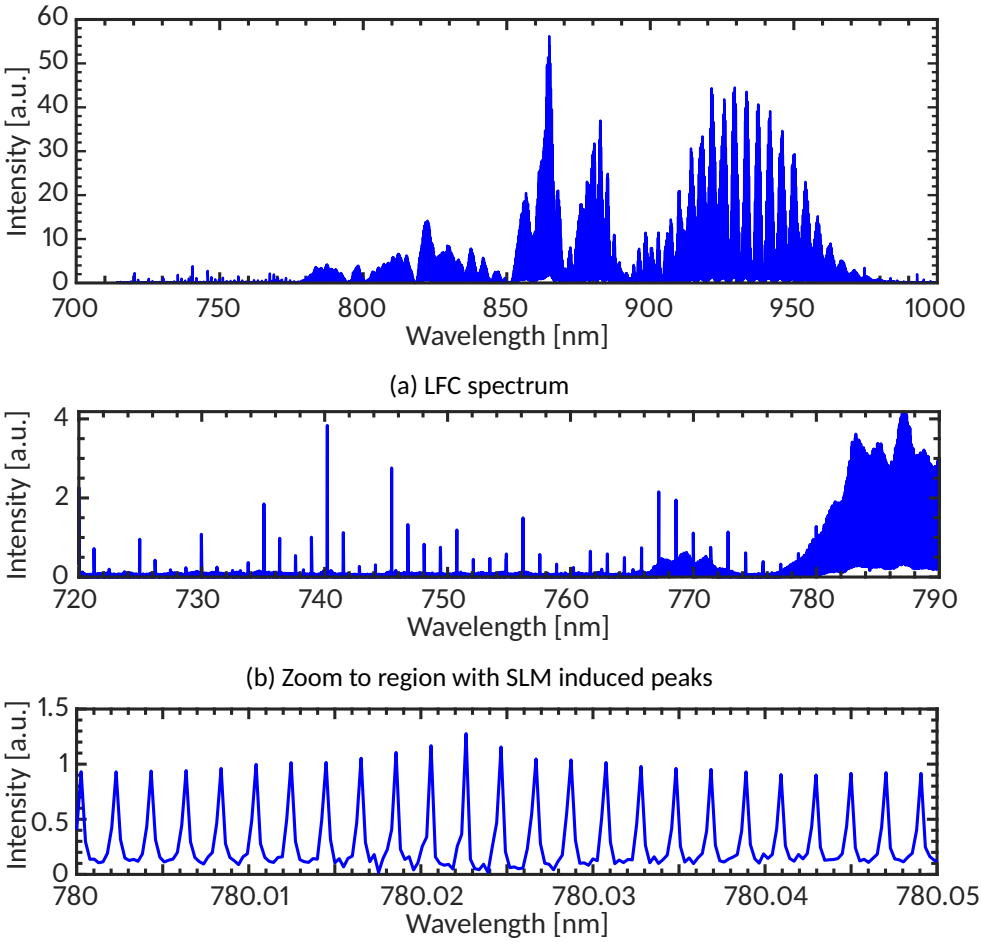

(a) LFC spectrum

(b) Zoom to region with SLM induced peaks

(c) Zoom to a single SLM peak in optical spectrum

Figure 6.38: LFC spectrum with peaks caused by the SLM modulation. Panel (a): The full spectrum, seemingly unaffected. Panel (b): A region with lower intensity, showing many small peaks at periodic intervals caused by the SLM. Panel (c): Zoom to the level of individual comb lines, with the lineshapes around 780.0225 nm being deformed by the SLM induced peak.

(see Fig. A.1). When the control loop is activated, a large number of pixels are set to an intermediate gray value and thus the strength of the modulation is increased. The noise caused by the SLM modulation is therefore higher when the control is enabled than when the SLM is set to maximum throughput.

A comparison of an interferogram sampled with 5 kHz and one with 40 kHz shows that the frequency of the SLM modulation decreases compared to the optical modulation for higher sampling rates (see Fig. 6.39a). Due to the lower frequency and the power of the modes scaling with the mode number k^{-2} (see Eq. 6.28), the power of the modes in the optical regime is reduced (see Fig. 6.39b). The number of modes, however, is increased, because the lower

fundamental frequency also means that the modes are spaced more closely. For the 5 kHz sampling, the measured intensity of the SLM modes exceeds that of the optical spectrum by factors of more than 20. For the 40 kHz sampling, the intensity of the SLM modes is at levels corresponding to half the optical intensity.

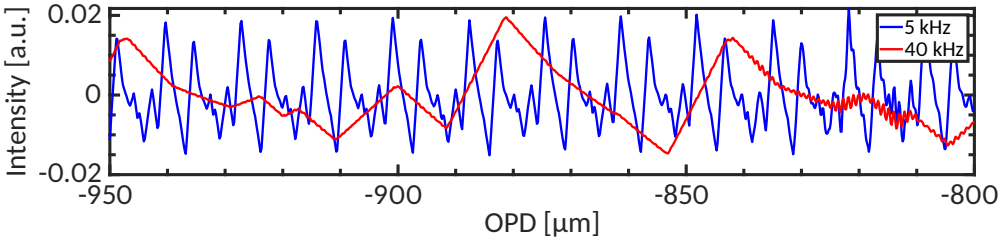

(a) Interferogram

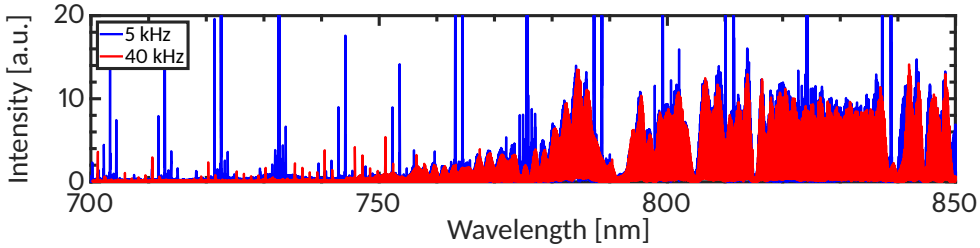

(b) Spectrum

Figure 6.39: Comparison between a measurement at 5 kHz samplerate (blue line) and 40 kHz samplerate (red line). Panel (a): Parts of the respective interferograms. Panel (b): Parts of the respective spectra. The intensity axis was clipped to show the comparably low strength of the SLM modes in the wavelength region from 700 to 730 nm.

The SLM modulation also heavily affects the phase spectrum as the modulation introduced by the SLM causes a strong asymmetric component in the interferogram. This leads to erratic phase strings shown in Fig. 6.40. The fitting of the individual phase strings often fails and it is not feasible to perform the phase correction algorithm for LFC spectra (see Sec. 3.3.2). Therefore, we only computed simple power spectra for our subsequent analysis.

Regardless of the SLM setting, i.e., active control loop or maximum throughput, the SLM modulation disturbs the algorithm to measure f_{rep} and f_{CEO} from the interferogram (see Sec. 5.1). The average precisions are 267 Hz and 37 MHz respectively, factors of 26 and 13 worse than in the results shown in Ch. 3 when the spectrum control setup was not used. Also, the f_{CEO} measurement on average is off by 176 MHz or 55 %. Therefore, we did not attempt to use the interferogram retrieval algorithm on the interferograms with the spectrum control setup.

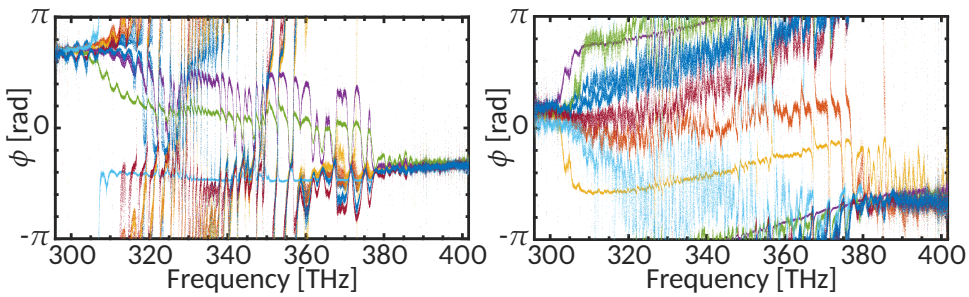

(a) Maximum throughput (b) Flattened envelope

Figure 6.40: Typical phase spectrum when the spectrum control setup is used (resulting from the interferogram treatment to obtain individual phase strings outlined in Sec. 3.3.2). Panel (a): Phase spectrum from a measurement with the SLM set to maximum throughput. Panel (b): Phase spectrum from a measurement with the control loop activated.

Spectrally flattened comb

To evaluate the improvement of the dynamic range by the flattening of the spectral envelope, we compare the results from an interferogram recorded with the control loop activated and an interferogram recorded with the SLM set to maximum throughput (see Fig. 6.41). The flattening results in a highly reduced dynamic range of the spectrum. 90 % of the spectral range are within 3 dB of the set point.

In the corresponding spectrometer measurements 96 % are within 3 dB of the set point. With the higher resolution of the FTS, more variability of the spectral envelope becomes apparent. The regions where the spectrometer measures small constant deviations from the set point, correspond to regions with very steep slopes in the spectral envelope. These slopes are unresolved in the spectrometer measurements.

Line fitting

In the FTS measurements, we can detect 3 % more comb lines in the flattened spectra compared to the unflattened spectra (see Fig. 6.42a). Theoretically, a maximum increase of about 11 % in the number of detected lines is possible. This full potential is not reached as there are still regions with too little light generated in the supercontinuum. As we have to use the 5-6 bitplane in the FTS measurements, we are limited in contrast and cannot set the spectrum to a lower overall intensity to decrease the dynamic range further.

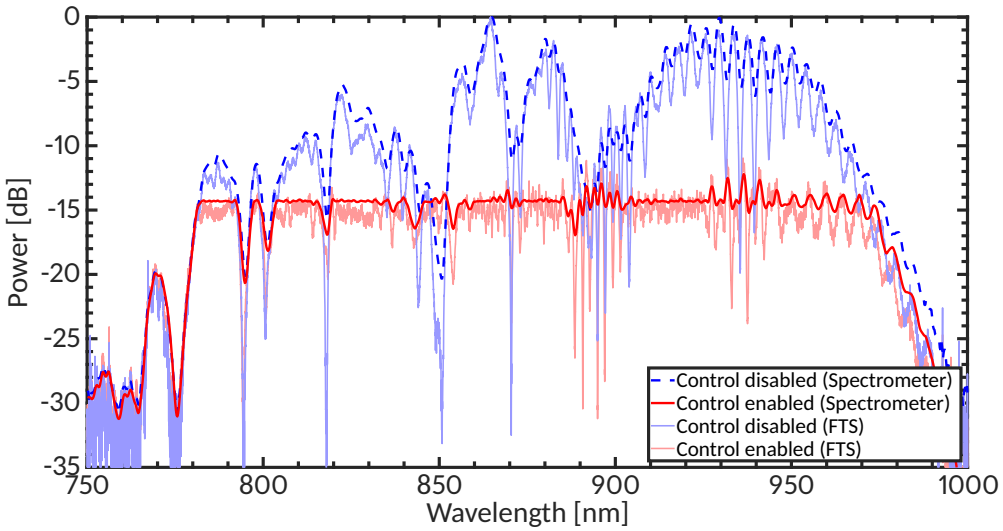

Figure 6.41: A measurement of the LFC with control disabled (blue) and control enabled (red). The thick lines are spectrometer measurements, the thin weak lines are the FTS measurements. The resolving power of the FTS measurement was reduced to $R = 100.000$ in order to only show the spectral envelope and not the individual comb lines. The spectrometer measurements are scaled with the cross-calibration function for better comparison (see Sec. 6.7.2).

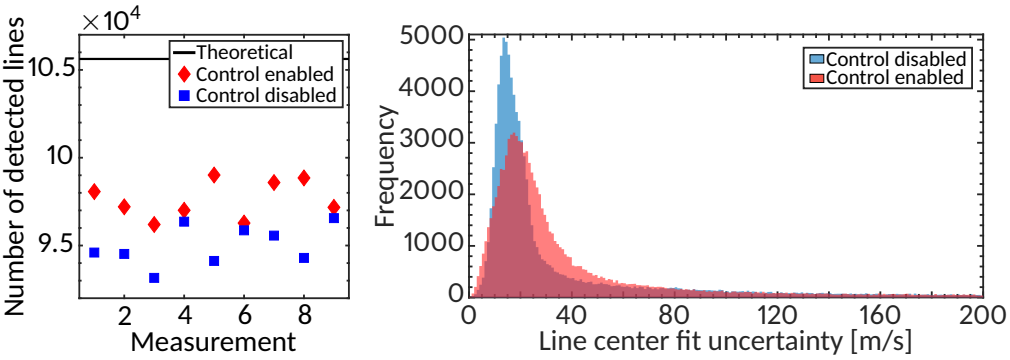

(a) Number of detected lines

(b) Line fit uncertainty

Figure 6.42: Panel (a): Number of fitted comb lines for control of the spectral envelope disabled (red) and enabled (blue) as well as the theoretical limit of comb lines in the spectral range. Panel (b): Histogram of the line fit uncertainty of spectra with control disabled (blue) and enabled (red). For better visibility the histogram was truncated at 200 m s^{-1}. The number of observations at higher uncertainties are $N_{enabled} = 6180$ and $N_{disabled} = 5485$, about 6 % of the overall observations in each set.

The increased SLM modulation amplitude of the activated control leads to an 8 % lower line center fit precision in the flat spectra compared to the maximum throughput spectra (see Fig. 6.42b). We did not attempt a calibration of the spectra since the lower line fit precision will lead to a worse performance than the one demonstrated by Huke et al. (2019b).

Spectral envelope stability

Overall, the spectra become more stable in time when the control is active. We plotted a histogram of the deviation from the mean intensity in each sample point for data sets with active control and with the SLM set to maximum throughput in Fig. 6.43. The comparison between spectra with control enabled and disabled shows that systematic drifts are eliminated by the control loop. While there is still fluctuation around a mean value over the measurements, this is now symmetrically distributed and does not exhibit systematic drifts in time. Without stabilization, only 50.2 % of the values fall within 25 % of the mean intensity. With active control of the spectrum 83.6 % of the intensity values fall within 25 % of the spectral bins mean.

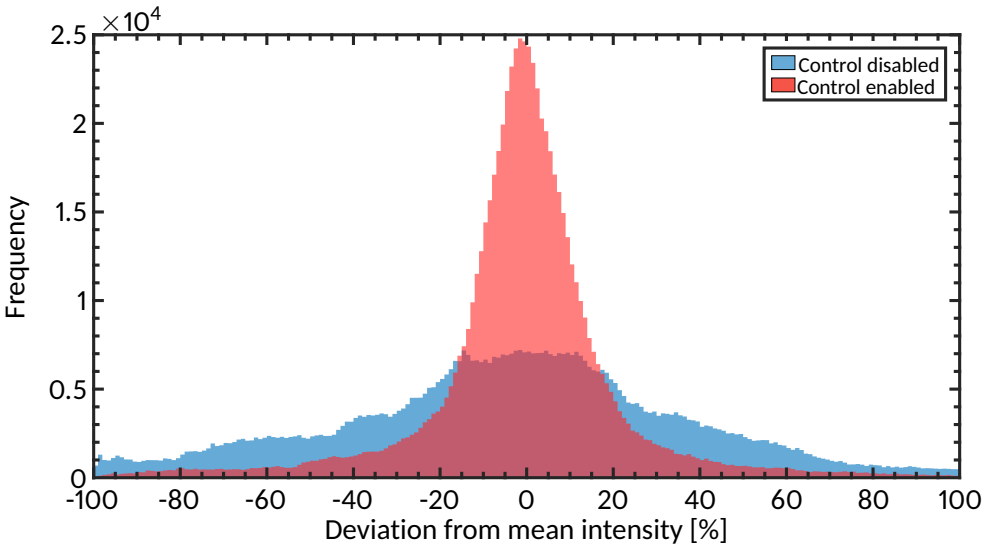

Figure 6.43: Histogram of the deviation from the mean intensity in each sample point of stabilized (red) and unstabilized (blue) LFC spectra.

6.11 Discussion

The control of the spectrum is stable and stays within 1 dB of the set point for about 95 % in the spectral region from 739 to 922 nm in the spectrometer measurements when using the 18-6 bitplane. The main limit here is the large initial dynamic range of the LFC spectrum. Overall, the spectral flattening is

an improvement from the initial state, reducing the dynamic range by almost two orders of magnitude.

The direct comparison shows that spectrum control setup worked much better when the 18-6 bitplane was used instead of the 5-6 bitplane. The 18-6 bitplane allows a higher contrast ratio and thus a better control. Another reason for the differing performance in the FTS measurements is the applied cross calibration function. This also leads to an effective reduction of the achievable contrast. When applying the cross calibration function the intensity is reduced for higher wavelengths and increased at lower wavelengths (see Sec. 6.7.2). The spectral contrast of the spectrum control setup is lowest at high wavelengths (see Sec. 6.9.1). Thus, the control loop only has a low dynamic range to work with in this spectral region and constantly operates near a gray value of zero leading to the strong deviations from the set point. For this reason, the flattening level could only go down to −14.4 dB instead of −17 dB.

In regions where good control was achieved, such as around 815 nm or around 826 nm, the variability seems to be lower when using the 5-6 bitplane (see Fig. 6.36). This could be due to the fact that the SLM modulation occurs on timescales of only 4 ms instead of 16 ms when using the 18-6 bitplane. The exposure time we use with the activated control is typically 5 ms, with an averaging over 20 frames. Therefore, the measured variability in regions with stable control could actually be caused by the SLM modulation.

In some spectral regions oscillatory patterns emerge, typically on scales of 2 nm. Regions which exhibit these oscillatory patterns, typically are those where the initial LFC spectrum is more variable. This may have multiple reasons. First of all, these patterns typically emerge in the spectral region from 900 to 950 nm where the contrast of our setup is low (see Fig. 6.27) reducing the control capabilities of the SLM. Secondly, our wavelength calibration has residuals larger than 0.5 pixels (see Fig. 6.25), which can cause such oscillations to emerge due to the control loop acting on the wrong pixels. The third and main reason is the limited resolution of the spectrometer, which broadens spectral features to a large extent, corresponding to about ten SLM pixels (see ILS). This also causes the control loop to act on wrong pixels, since the measured intensity is attributed to the wrong wavelength and thereby the wrong pixel.

The biggest improvement to this setup would therefore be a spectrometer with a resolution of 0.5 nm or better. This should simultaneously improve

and simplify wavelength calibration and most importantly the control loop stability.

Another improvement would be a designed nonlinear fiber which could deliver a smoother initial LFC spectrum. This would eliminate a majority of the instabilities in the control loop. Additionally, a smoother LFC spectrum would also increase the output power when flattening is enabled, as less light has to be discarded by the control loop.

The FTS measurements confirmed that the spectrum control setup is working and that we are able to flatten the LFC spectrum. Despite the additional noise caused by the SLM modulation, more comb lines could be fitted in the flattened spectra. Furthermore, we could show that the stability of the spectral envelope is enhanced and the remaining scatter follows a well defined distribution as opposed to systematic drifts. Thus, the goal of creating more usable comb lines by reducing the dynamic range and the goal of stabilizing the spectral envelope was achieved. The intensity cross calibration functions as intended as well. However, some challenges also became apparent.

The measurements also clearly show that the spectrometers resolution is too low to fully take advantage of the setups capabilities. Using a spectrometer with a higher resolution of 0.5 nm or better, the control should be fine enough to deal with the spectral intensity variations of our current LFC setup.

To reduce the impact of the modulation caused by the SLM, we can increase the sample rate of the FTS to 40 kHz, which improves the results slightly. Since the SLM modulations are not in phase over different measurements, the noise can be reduced by the square root of the number of measurements by averaging the interferograms. However, this leads to the disadvantage that drifts occurring throughout a measurement set cannot be corrected.

Unfortunately, we cannot improve calibration performance by using this spectrum control setup in conjunction with the FTS. This is due to the modulation caused by the SLM. The additional noise and phase errors degrade the overall quality of the spectra to a point, where it is better to use the LFC without the spectrum control setup instead. A way to mitigate the effect of the SLM modulation would be the use of a balanced detection, i.e., also recording the second output of the FTS (see Sec. 3.3.3). Instead of using a true balanced detection, another possibility would be to split off a fraction of the LFC light and measure it using a photodiode which is triggered by the HeNe-reference

laser fringes. This should then mirror the mean intensity recorded in the interferogram and could be used to correct the noise caused by the SLM. While the FTS in our setup does not provide the possibility of measuring the negative interferogram, the signal of its reference laser is accessible via an output port. While it is not trivial to implement, we are confident that such a scheme can improve the calibration performance of the flattened LFC.

For use with an echelle spectrograph, the results from our spectral flattening setup are very promising. The SLM intensity modulation does not affect dispersive spectrographs to the same extent. This is because in each measurement that is longer than a few modulation periods, the intensity flicker is automatically averaged in each spectral bin. Since the intensity modulation is not an issue, the better performing 18-6 bitplane could be used in an echelle spectrograph. The 18-6 bitplane performs better in all aspects except the intensity modulation, i.e., it leads to a smoother spectral envelope and a lower remaining dynamic range. However, there is slight evidence that the 18-6 bitplane—maybe due to the intensity flicker—causes slightly higher intensity noise in the spectrometer measurements (see Fig. 6.36). It should be investigated if this impedes calibration. However, this is unlikely since averaging times in astronomical applications are usually much longer than the 40 ms used in our spectrometer measurements. Therefore, our spectrum control setup could improve the calibration of an echelle spectrograph with an LFC.

7

CONCLUSION

Laser frequency combs (LFCs) have many characteristics which make them ideal calibration light sources for high resolution spectrographs but technological challenges prevent a routine use. One major issue limiting the calibration precision is the instability and high dynamic range of the spectral envelope. The present work explored three different paths aimed at mitigating or circumventing this issue. The first idea is to generate a more stable and flat spectral envelope from the start by designing a tapered nonlinear fiber. Additionally, we tried to circumvent the problems caused by the spectral envelope in Fourier transform spectrograph (FTS) calibration via retrieving the calibration parameters directly from the interferogram rather than the spectrum. Furthermore, we aimed to improve the stability and reduce the dynamic range of the spectral envelope by building an optical setup to control the spectral envelope.

The LFC at the Institute for Astrophysics in Göttingen offers good stability of both the repetition rate and the offset frequency. A weak phase modulation is present in the data of the stabilized frequencies, but it is unclear whether this is a measurement artifact. Even in a worst case scenario, this modulation only leads to a comb line broadening to about 50 kHz (50 mm s^{-1} in terms of radial velocities). Thus, it will not influence any calibration measurements in the optical or near infrared regime. However, the instability and high dynamic range of the spectral envelope limit the calibration precision.

To achieve a stable, flat and broad spectral envelope, we designed a tapered nonlinear fiber. We created a grid of simulations of different taper geometries and defined several parameters which can serve as quality factors in an evaluation of the results. The designed fiber was manufactured and we devised a setup for its use. While we were unable to obtain measurement results in time for this work, we expect a significant improvement in the characteristics of the supercontinuum based on the simulations.

To simplify the calibration of the FTS and to circumvent the issue of spectral envelope instability, we developed a scheme to retrieve the repetition

rate and the offset frequency directly from the interferogram. We verified that the method works both on measured and on simulated interferograms. The measurements show systematic phase differences between the measurement of the offset frequency and the repetition rate, hinting at systematic instrumental errors of the FTS. The simulations enabled an identification of key measurement effects responsible for reducing measurement precision, namely the change of the spectral envelope from burst to burst, the limited, frequency-dependent coherence, the beam splitter phase, random measurement noise and the systematic phase errors of the FTS. The method is more susceptible to measurement noise than the established method of calibration using line fits of phase corrected spectra, even when accounting for the systematic effects. Correspondingly, the interferogram calibration has a lower precision than the spectrum calibration. Therefore, more work is required to eliminate the measurement errors and make the interferogram calibration competitive.

To extend the capabilities of controlling LFC supercontinuum spectra to the near infrared, we constructed a spectrum control setup. Based on previous work, we developed a compact and cost-efficient spectrum control setup. The setup achieves continuous, stable control of the spectral envelope, mitigating temporal fluctuations and reducing the dynamic range. Measurements of a spectrally controlled LFC with an FTS confirm that the dynamic range and temporal stability of the comb spectrum are improved also at high resolution. In these measurements, more comb lines could be detected and the spectral envelope was more consistent over the measurements, compared to measurements without active control. This indicates that the setup should improve calibration of high resolution spectrographs. However, these measurements also showed that the intensity modulations caused by the spatial light modulator (SLM) driving scheme leads to increased noise in the FTS measurements, preventing an improvement of the calibration of the FTS. One issue reducing the spectrum control setup performance is that the spectrometer used for the control loop does not reach its specified resolution. This reduces the resolution of the control which leads to increased dynamic range and impedes wavelength calibration, which in turn reduces the stability of the control.

At the current state none of our attempts lead to an improvement in the calibration performance of the FTS. However, this work can be a starting point

in improving LFC calibration of high resolution spectrographs in general. Each of the approaches show potential with different possible next steps that could be taken.

The designed tapered nonlinear fiber, once in use, should immediately provide improved characteristics of the spectral envelope and thus improve calibration precision. Furthermore, the parameter space of the grid simulations could be explored further. This might lead to even better geometries. For this, not only could the parameter space of the fiber geometry be expanded, but also the laser parameters such as pulse length and power could be included. Due to the long computing times, an optimization algorithm instead of a grid simulation could make this a more feasible course of action.

To improve the interferogram retrieval method, more theoretical work is necessary. Most importantly, the nature of the discrepancies to the conventional method should be understood to achieve an equally good calibration. A more stable spectral envelope may make this easier since it would remove a major source of measurement noise.

The spectrum control setup could be improved by using a spectrometer with a higher resolution, reducing both residual instabilities and further reducing the dynamic range of the controlled spectrum. Using a spectrum control setup with an FTS is only beneficial if the SLM modulation is removed from the FTS interferogram with a balanced detection. Then, a spectrum control setup may lead to an improved calibration. The SLM modulation would not cause issues in echelle spectrographs, where the setup can provide an increased calibration precision. Thus, this setup could be used in future instruments, such as ELT-HIRES.

To conclude, LFCs are promising calibration light sources for high resolution spectrographs. While more work is necessary to further improve the calibration precision, especially in the light of instabilities of the spectral envelope, a resolution of these problems is feasible.

BIBLIOGRAPHY

Ahern, F. J. and C. Pritchet (Oct. 1974). "Ratio Method of Fourier Spectrometry: an Improvement." In: *Applied Optics* 13.10, p. 2240. doi: 10.1364/ao.13.002240

Ahro, M., J. Kauppinen, and I. Salomaa (2000). "Detection and correction of instrumental line-shape distortions in Fourier Spectroscopy." In: *Applied Optics* 39.33, pp. 6230–6237

Aitken, R. G. (1898). "Spectroscopic Binary Stars." In: *Publications of the Astronomical Society of the Pacific* 10.60, pp. 26–34. issn: 00046280, 15383873

Alfano, R. R. and S. L. Shapiro (Mar. 1970). "Emission in the Region 4000 to 7000 Å Via Four-Photon Coupling in Glass." In: *Physical Review Letters* 24.11, pp. 584–587. doi: 10.1103/physrevlett.24.584

Allan, D. W. (1966). "Statistics of atomic frequency standards." In: *Proceedings of the IEEE* 54.2, pp. 221–230

Baldeck, P. and R. Alfano (1987). "Intensity effects on the stimulated four photon spectra generated by picosecond pulses in optical fibers." In: *Journal of Lightwave Technology* 5.12, pp. 1712–1715. doi: 10.1109/jlt.1987.1075465

Ballard, S. et al. (Dec. 2011). "The Kepler-19 System: A Transiting 2.2R$\oplus$ Planet and a Secon Planet Detected via Transit Timing Variations." In: *The Astrophysical Journal* 743.2, p. 200. doi: 10.1088/0004-637x/743/2/200

Balling, P., P. Masika, P. Kren, and M. Dolezal (2012). "Length and refractive index measurement by Fourier transform interferometry and frequency comb spectroscopy." In: *Measurement Science and Technology* 23.9, p. 094001

Baranne, A., D. Queloz, M. Mayor, G. Adrianzyk, G. Knispel, D. Kohler, D. Lacroix, J.-P. Meunier, G. Rimbaud, and A. Vin (Oct. 1996). "ELODIE: A spectrograph for accurate radial velocity measurements." In: *Astronomy & Astrophysics* 119, pp. 373–390

Bauer, F. F., M. Zechmeister, and A. Reiners (Sept. 2015). "Calibrating echelle spectrographs with Fabry-Perot etalons." In: *Astronomy & Astrophysics* 581, A117. doi: 10.1051/0004-6361/201526462

Beaud, P., W. Hodel, B. Zysset, and H. Weber (Nov. 1987). "Ultrashort pulse propagation, pulse breakup, and fundamental soliton formation in a single-mode optical fiber." In: *IEEE Journal of Quantum Electronics* 23.11, pp. 1938–1946. doi: 10.1109/jqe.1987.1073262

Beaulieu, J.-P. et al. (Jan. 2006). "Discovery of a cool planet of 5.5 Earth masses through gravitational microlensing." In: *Nature* 439.7075, pp. 437–440. doi: 10.1038/nature04441

Beer, R., R. H. Norton, and C. H. Seaman (1971). "Astronomical Infrared Spectroscopy with a Connes-Type Interferometer. I. Instrumental." In: *Review of Scientific Instruments* 42.10, pp. 1393–1403

Beloy, K. et al. (Mar. 2021). "Frequency ratio measurements at 18-digit accuracy using an optical clock network." In: *Nature* 591.7851, pp. 564–569. doi: 10.1038/s41586-021-03253-4

Birks, T. A., W. J. Wadsworth, and P. St. J. Russell (2000). "Supercontinuum generation in tapered fibers." In: *Opt. Lett.* 25.19, pp. 1415–1417. doi: 10.1364/OL.25.001415

Bond, I. A. et al. (Apr. 2004). "OGLE 2003-BLG-235/MOA 2003-BLG-53: A Planetary Microlensing Event." In: *The Astrophysical Journal* 606.2, pp. L155–L158. doi: 10.1086/420928

Bönsch, G. and E. Potulski (1998). "Measurement of the refractive index of air and comparison with modified Edlén's formulae." In: *Metrologia* 35.2, p. 133

Borucki, W. J. et al. (Jan. 2010). "Kepler Planet-Detection Mission: Introduction and First Results." In: *Science* 327.5968, pp. 977–980. doi: 10.1126/science.1185402

Bougrenet de la Tocnaye, J. L. de and L. Dupont (Mar. 1997). "Complex amplitude modulation by use of liquid-crystal spatial light modulators." In: *Applied Optics* 36.8, p. 1730. doi: 10.1364/ao.36.001730

Brewer, R. G. (July 1967). “Frequency Shifts in Self-Focused Light.” In: *Physical Review Letters* 19.1, pp. 8–10. doi: 10.1103/physrevlett.19.8

Broderick, N. G. R., T. M. Monro, P. J. Bennett, and D. J. Richardson (Oct. 1999). “Nonlinearity in holey optical fibers: measurement and future opportunities.” In: *Optics Letters* 24.20, p. 1395. doi: 10.1364/ol.24.001395

Brogi, M. and M. R. Line (Feb. 2019). “Retrieving Temperatures and Abundances of Exoplanet Atmospheres with High-resolution Cross-correlation Spectroscopy.” In: *The Astronomical Journal* 157.3, p. 114. doi: 10.3847/1538-3881/aaffd3

Burroughs, W. J. and J. Chamberlain (Apr. 1971). “Submillimetre-wave solar observations using a double-output Michelson interferometer.” In: *Infrared Physics* 11.1, pp. 1–23. doi: 10.1016/0020-0891(71)90030-3

Butler, R. P., H. R. A. Jones, F. Feng, M. Tuomi, G. Anglada-Escudé, and Sandy Keiser (Dec. 2019). “A Reanalysis of the UVES M Dwarf Planet Search Program.” In: *The Astronomical Journal* 158.6, p. 251. doi: 10.3847/1538-3881/ab4905

Butler, R. P., G. W. Marcy, E. Williams, C. McCarthy, and P. Dosanjh (June 1996). “Attaining Doppler Precision of 3m/s.” In: *Publications of the Astronomical Society of the Pacific* 108, pp. 500–509

Campbell, B. and G. A. H. Walker (Aug. 1979). “Precision radial velocities with an absorption cell.” In: *Publications of the Astronomical Society of the Pacific* 91, p. 540. doi: 10.1086/130535

Campbell, B., G. A. H. Walker, and S. Yang (1988). “A search for substellar companions to solar-type stars.” In: *The Astrophysical Journal* 331, pp. 902–921

Carson, C. G. and I. V. Haljasmaa (Nov. 2015). “Proper calculation of a modulation half cycle from the Allan deviation.” In: *Metrologia* 52.6, pp. L31–L33. doi: 10.1088/0026-1394/52/6/l31

Chandrasekhar, S., B. K. Sadashiva, and K. A. Suresh (Nov. 1977). “Liquid crystals of disc-like molecules.” In: *Pramana* 9.5, pp. 471–480. doi: 10.1007/bf02846252

Chiao, R. Y., E. Garmire, and C. H. Townes (Oct. 1964). “Self-Trapping of Optical Beams.” In: *Physical Review Letters* 13.15, pp. 479–482. doi: 10.1103/physrevlett.13.479

Coen, S., A. H. L. Chau, R. Leonhardt, J. D. Harvey, J. C. Knight, W. J. Wadsworth, and P. St. J. Russell (Sept. 2001). “White-light supercontinuum generation with 60-ps pump pulses in a photonic crystal fiber.” In: *Optics Letters* 26.17, p. 1356. doi: 10.1364/ol.26.001356

Connes, J. (1963). *Spectroscopic Studies Using Fourier Transformation*. Vol. 3157. US Naval Ordnance Test Station

Connes, J. and P. Connes (July 1966). “Near-Infrared Planetary Spectra by Fourier Spectroscopy I: Instruments and Results.” In: *Journal of the Optical Society of America* 56.7, p. 896. doi: 10.1364/josa.56.000896

Connes, P., M. Martic, and J. Schmitt (1996). “Demonstration of Photon-Noise Limit in Stellar Radial Velocities.” In: *The Search for Extra-Solar Terrestrial Planets: Techniques and Technology*. Springer Netherlands, pp. 61–76. doi: 10.1007/978-94-011-5808-4_5

Connes, P. and G. Michel (Sept. 1975). “Astronomical Fourier spectrometer.” In: *Appl. Opt.* 14.9, pp. 2067–2084. doi: 10.1364/AO.14.002067

Cooley, J. W. and J. W. Tukey (May 1965). “An algorithm for the machine calculation of complex Fourier series.” In: *Mathematics of Computation* 19.90, pp. 297–297. doi: 10.1090/s0025-5718-1965-0178586-1

Cornachione, M. A. et al. (Nov. 2019). “A Full Implementation of Spectro-perfectionism for Precise Radial Velocity Exoplanet Detection: A Test Case With the MINERVA Reduction Pipeline.” In: *Publications of the Astronomical Society of the Pacific* 131.1006, p. 124503. doi: 10.1088/1538-3873/ab4103

Corwin, K. L., N. R. Newbury, J. M. Dudley, S. Coen, S. A. Diddams, B. R. Washburn, K. Weber, and R. S. Windeler (Sept. 2003). “Fundamental amplitude noise limitations to supercontinuum spectra generated in a microstructured fiber.” In: *Applied Physics B: Lasers and Optics* 77.2-3, pp. 269–277. doi: 10.1007/s00340-003-1175-x

Crameri, F. (2021). *Scientific colour maps*. en. doi: 10.5281/ZENODO.4491293

Curiel, S., G. N. Ortiz-León, A. J. Mioduszewski, and R. M. Torres (Aug. 2020). “An Astrometric Planetary Companion Candidate to the M9 Dwarf TVLM 513–46546.” In: *The Astronomical Journal* 160.3, p. 97. doi: 10.3847/1538-3881/ab9e6e

Davis, S. P., M. C. Abrams, and J. W. Brault (2001). *Fourier transform spectrometry*. Elsevier. isbn: 0-12-042510-6

Debus, M., P. Huke, D. Meyer, and A. Reiners (2021). “Spectral envelope control for a flat frequency comb spectrum.” In: *Journal of Astronomical Telescopes, Instruments, and Systems* 7.2, pp. 1–11. doi: 10.1117/1.JATIS.7.2.025005

Desbiens, R., J. Genest, P. Tremblay, and J.-P. Bouchard (July 2006). “Correction of instrument line shape in Fourier transform spectrometry using matrix inversion.” In: *Applied Optics* 45.21, p. 5270. doi: 10.1364/ao.45.005270

Desbois, J., F. Gires, and P. Turnois (Feb. 1973). “A new approach to picosecond laser pulse analysis shaping and coding.” In: *IEEE Journal of Quantum Electronics* 9.2, pp. 213–218. doi: 10.1109/jqe.1973.1077462

Diddams, S. A. (Oct. 2010). “The evolving optical frequency comb [Invited].” In: *Journal of the Optical Society of America B* 27.11, B51. doi: 10.1364/josab.27.000b51

Diddams, S. A., D. J. Jones, J. Ye, S. T. Cundiff, J. L. Hall, J. K. Ranka, R. S. Windeler, R. Holzwarth, T. Udem, and T.W. Hänsch (May 2000). “Direct link between microwave and optical frequencies with a 300 THz femtosecond laser comb.” In: *Physical Review Letters* 84.22, pp. 5102–5105. doi: 10.1103/physrevlett.84.5102

Doerr, H.-P., T. Steinmetz, R. Holzwarth, T. Kentischer, and W. Schmidt (Mar. 2012). “A Laser Frequency Comb System for Absolute Calibration of the VTT Echelle Spectrograph.” In: *Solar Physics* 280.2, pp. 663–670. doi: 10.1007/s11207-012-9960-5

Dudley, J. M. and S. Coen (July 2002). “Coherence properties of supercontinuum spectra generated in photonic crystal and tapered optical fibers.” In: *Optics Letters* 27.13, p. 1180. doi: 10.1364/ol.27.001180

Dudley, J. M., G. Genty, and S. Coen (Oct. 2006). “Supercontinuum generation in photonic crystal fiber.” In: *Reviews of Modern Physics* 78.4, pp. 1135–1184. doi: 10.1103/revmodphys.78.1135

Dumusque, X. et al. (Nov. 2015). “HARPS-N Observes the Sun as a Star.” In: *The Astrophysical Journal* 814.2, p. L21. doi: 10.1088/2041-8205/814/2/l21

Dupuy, T. J., M. C. Liu, K. N. Allers, B. A. Biller, K. M. Kratter, A. W. Mann, E. L. Shkolnik, A. L. Kraus, and W. M. J. Best (July 2018). “The Hawaii Infrared Parallax Program. III. 2MASS J0249–0557 c: A Wide Planetary-mass Companion to a Low-mass Binary in the β Pic Moving Group.” In: *The Astronomical Journal* 156.2, p. 57. doi: 10.3847/1538-3881/aacbc2

Eckstein, J. N. (1978). “High resolution spectroscopy using multiple coherent interactions.” PhD thesis

Eckstein, J. N., A. I. Ferguson, and T. W. Hänsch (1978). “High-resolution two-photon spectroscopy with picosecond light pulses.” In: *Physical Review Letters* 40.13, p. 847

Eversberg, T. and K. Vollmann (2015). *Spectroscopic Instrumentation: Fundamentals and Guidelines for Astronomers*. Springer Praxis Books. Springer. doi: 10.1007/978-3-662-44535-8

Fellgett, P. (1958). “I. — les principes généraux des méthodes nouvelles en spectroscopie interférentielle - A propos de la théorie du spectromètre interférentiel multiplex.” In: *Journal de Physique et le Radium* 19.3, pp. 187–191

Fischer, D. A. et al. (May 2016). “State of the Field: Extreme Precision Radial Velocities.” In: *Publications of the Astronomical Society of the Pacific* 128.964, p. 066001. doi: 10.1088/1538-3873/128/964/066001

Foltynowicz, A., T. Ban, P. Masłowski, F. Adler, and J. Ye (Nov. 2011a). “Quantum-Noise-Limited Optical Frequency Comb Spectroscopy.” In: *Phys. Rev. Lett.* 107 (23), p. 233002. doi: 10.1103/PhysRevLett.107.233002

Foltynowicz, A., P. Maslowski, T. Ban, F. Adler, K. C. Cossel, T. C. Briles, and J. Ye (2011b). “Optical frequency comb spectroscopy.” In: *Faraday Discussions* 150, p. 23. issn: 1364-5498. doi: 10.1039/c1fd00005e

Forman, M. L., W. H. Steel, and G. A. Vanasse (Jan. 1966). “Correction of Asymmetric and Interferograms Obtained and in Fourier and Spectroscopy.” In: *J. Opt. Soc. Am.* 56.1, pp. 59–64

Forrester, A. T., R. A. Gudmundsen, and P. O. Johnson (1955). “Photoelectric mixing of incoherent light.” In: *Physical Review* 99.6, p. 1691

Franzen, A. (2006). *ComponentLibrary*. url: http://www.gwoptics.org/component_library/

Froehly, C., B. Colombeau, and M. Vampouille (1983). “II Shaping and Analysis of Picosecond Light Pulses.” In: *Progress in Optics*. Elsevier, pp. 63–153. doi: 10.1016/s0079-6638(08)70277-4

Gaeta, A. L. (Apr. 2000). “Catastrophic Collapse of Ultrashort Pulses.” In: *Physical Review Letters* 84.16, pp. 3582–3585. doi: 10.1103/physrevlett.84.3582

Gardner, F. M. (2005). *Phaselock techniques*. John Wiley & Sons

Genest, J. and P. Tremblay (Sept. 1999). “Instrument line shape of Fourier transform spectrometers: analytic solutions for nonuniformly illuminated off-axis detectors.” In: *Applied Optics* 38.25, p. 5438. doi: 10.1364/ao.38.005438

– (Nov. 2002). “Impact of optical aberrations on the line shape of Fourier-transform spectrometers.” In: *Elsevier, Vibrational Spectroscopy* 29, pp. 3–13

Glenday, A. G. et al. (Mar. 2015). “Operation of a Broadband Visible-Wavelength Astro-Comb with a High-Resolution Astrophysical Spectrograph.” In: *Optica* 2.3, pp. 250–254. doi: 10.1364/OPTICA.2.000250

Glückstad, J. and D. Palima (2009). *Generalized Phase Contrast*. Springer Netherlands. doi: 10.1007/978-90-481-2839-6

Gordon, J. P. (Oct. 1986). “Theory of the soliton self-frequency shift.” In: *Optics Letters* 11.10, p. 662. doi: 10.1364/ol.11.000662

Gouveia-Neto, A. S., A. S. L. Gomes, and J. R. Taylor (Feb. 1988). “Femto soliton Raman generation.” In: *IEEE Journal of Quantum Electronics* 24.2, pp. 332–340. doi: 10.1109/3.130

Griffin, R. (June 1973). “On the Possibility of Determining Stellar Radial Velocities to 0.01 km s-1.” In: *Monthly Notices of the Royal Astronomical Society* 162.3, pp. 243–253. doi: 10.1093/mnras/162.3.243

Griffiths, P. R. and J. A. de Haseth (2007). *Fourier Transform Infrared Spectrometry*. Wiley & Sons. doi: ISBN:978-0-471-19404-0

Hall, J. L. (2006). “Nobel Lecture: Defining and measuring optical frequencies.” In: *Reviews of Modern Physics* 78.4, p. 1279

Hänsch, T. W. (2006). “Nobel lecture: passion for precision.” In: *Reviews of Modern Physics* 78.4, p. 1297

Harris, F. J. (1978). “On the use of windows for harmonic analysis with the discrete Fourier transform.” In: *Proceedings of the IEEE* 66.1, pp. 51–83. doi: 10.1109/proc.1978.10837

Hatzes, A. P. (May 2016). “The Architecture of Exoplanets.” In: *Space Science Reviews* 205.1-4, pp. 267–283. doi: 10.1007/s11214-016-0246-3

Hatzes, A. P. and W. D. Cochran (1993). “Long-period radial velocity variations in three K giants.” In: *The Astrophysical Journal* 413, pp. 339–348

Hatzes, A. P., W. D. Cochran, M. Endl, B. McArthur, D. B. Paulson, Gordon A. H. Walker, B. Campbell, and S. Yang (Dec. 2003). “A Planetary Companion to γ Cephei A.” In: *The Astrophysical Journal* 599.2, pp. 1383–1394. doi: 10.1086/379281

Hatzes, A. P. et al. (Sept. 2006). “Confirmation of the planet hypothesis for the long-period radial velocity variations of βGeminorum.” In: *Astronomy & Astrophysics* 457.1, pp. 335–341. doi: 10.1051/0004-6361:20065445

Hawker, G. A. and I. R. Parry (Feb. 2019). “High-resolution spectroscopy and high contrast imaging with the ELT: looking for O2 in Proxima b.” In: *Monthly Notices of the Royal Astronomical Society* 484.4, pp. 4855–4864. doi: 10.1093/mnras/stz323

Haywood, R. D. et al. (Feb. 2016). “The Sun as a planet-host star: proxies fromSDOimages for HARPS radial-velocity variations.” In: *Monthly Notices of the Royal Astronomical Society* 457.4, pp. 3637–3651. doi: 10.1093/mnras/stw187

Helsby, N. C. (2003). “GPS disciplined offset-frequency quartz oscillator.” In: *Frequency control symposium and pda exhibition jointly with the 17th European frequency and time forum, 2003. Proceedings of the 2003 IEEE international*. IEEE, pp. 435–439

Henry, G. W., G. W. Marcy, R. P. Butler, and S. S. Vogt (Dec. 1999). “A Transiting “51 Peg–like” Planet.” In: *The Astrophysical Journal* 529.1, pp. L41–L44. doi: 10.1086/312458

Hewitt, A. V., A. S. Milsom, and P. R. Standen (1968). “The radial velocity curve of VZ CANCRI.” In: *The Observatory* 88, pp. 262–264

Hillman, G., J. Tulip, and H. Seguin (Feb. 1970). “Pulse Repetition Rate Control and Stabilization in a Passively Q-Switched CO_2 Laser.” In: *Applied Optics* 9.2, p. 515. doi: 10.1364/ao.9.000515

Hirschfeld, T. (Mar. 1976). “The Implications of Fluctuation Noise in Multiplex Spectroscopy.” In: *Applied Spectroscopy* 30.2, pp. 234–236. doi: 10.1366/000370276774456291

Holzwarth, R., T. Udem, T. W. Hänsch, J. C. Knight, W. J. Wadsworth, and P. St. J. Russell (Sept. 2000). “Optical Frequency Synthesizer for Precision Spectroscopy.” In: *Phys. Rev. Lett.* 85 (11), pp. 2264–2267. doi: 10.1103/PhysRevLett.85.2264

Hopcroft, M. A. (2016). *allan*. Retrieved April 26, 2017. MATLAB Central File Exchange. url: www.mathworks.com/matlabcentral/fileexchange/13246-allan (visited on 04/26/2016)

– (2017). *allan_overlap*. Retrieved July 7, 2016. MATLAB Central File Exchange. url: www.mathworks.com/matlabcentral/fileexchange/26441-allan%5C_overlap (visited on 07/15/2016)

Hubbard, E. N., J. R. P. Angel, and M. S. Gresham (1979). “Operation of a long fused silica fiber as a link between telescope and spectrograph.” In: *The Astrophysical Journal* 229, pp. 1074–1078

Huke, P., M. Debus, and A. Reiners (May 2019a). “Phase-correction algorithm for Fourier transform spectroscopy of a laser frequency comb.” In: *J. Opt. Soc. Am. B* 36.5, pp. 1260–1266. doi: 10.1364/JOSAB.36.001260

– (July 2021). “Multimode fiber-coupling of a Michelson-type Fourier Transform Spectrometer.” In: *Optical Sensors and Sensing Congress*. Optical Society of America

Huke, P., M. Debus, M. Zechmeister, and A. Reiners (2019b). “Characterization and calibration of a Fourier-transform spectrometer using a laser frequency comb.” In: *J. Opt. Soc. Am. B* 36.7, pp. 1899–1906. doi: 10.1364/JOSAB.36.001899

Huke, P. et al. (June 2017). “Phase A: calibration concepts for HIRES.” In: *Optical Measurement Systems for Industrial Inspection X*. Vol. 10329. SPIE, p. 103292M. doi: 10.1117/12.2271782

Husakou, A. V. and J. Herrmann (Oct. 2001). “Supercontinuum Generation of Higher-Order Solitons by Fission in Photonic Crystal Fibers.” In: *Physical Review Letters* 87.20, p. 203901. doi: 10.1103/physrevlett.87.203901

Ilev, I., H. Kumagai, K. Toyoda, and I. Koprinkov (May 1996). “Highly efficient wideband continuum generation in a single-mode optical fiber by powerful broadband laser pumping.” In: *Applied Optics* 35.15, p. 2548. doi: 10.1364/ao.35.002548

Ippen, E. P. (Apr. 1970). “Low-Power Quasi-cv Raman Oscillator.” In: *Applied Physics Letters* 16.8, pp. 303–305. doi: 10.1063/1.1653204

Jacquinot, P. (Jan. 1960). “New developments in interference spectroscopy.” In: *Reports on Progress in Physics* 23.1, pp. 267–312. doi: 10.1088/0034-4885/23/1/305

Jerome, B. (Mar. 1991). “Surface effects and anchoring in liquid crystals.” In: *Reports on Progress in Physics* 54.3, pp. 391–451. doi: 10.1088/0034-4885/54/3/002

Jójárt, P., Á. Börzsönyi, B. Borchers, G. Steinmeyer, and K. Osvay (2012). “Agile linear interferometric method for carrier-envelope phase drift measurement.” In: *Optics letters* 37.5, pp. 836–838

Jones, D. J., S. A. Diddams, J. K. Ranka, A. Stentz, R. S. Windeler, J. L. Hall, and S. T. Cundiff (Apr. 2000). "Carrier-Envelope Phase Control of Femtosecond Mode-Locked Lasers and Direct Optical Frequency Synthesis." In: *Science* 288.5466, pp. 635–639. doi: 10.1126/science.288.5466.635

Jones, R. C. (July 1941). "A New Calculus for the Treatment of Optical SystemsI Description and Discussion of the Calculus." In: *Journal of the Optical Society of America* 31.7, p. 488. doi: 10.1364/josa.31.000488

Jones, W. J. and B. P. Stoicheff (Nov. 1964). "Inverse Raman Spectra: Induced Absorption at Optical Frequencies." In: *Physical Review Letters* 13.22, pp. 657–659. doi: 10.1103/physrevlett.13.657

Kalas, P., J. R. Graham, E. Chiang, M. P. Fitzgerald, M. Clampin, E. S. Kite, K. Stapelfeldt, C. Marois, and J. Krist (Nov. 2008). "Optical Images of an Exosolar Planet 25 Light-Years from Earth." In: *Science* 322.5906, pp. 1345–1348. doi: 10.1126/science.1166609

Kalyoncu, S. K., Y. Huang, Q. Song, and O. Boyraz (Nov. 2012). "Analytical study on arbitrary waveform generation by MEMS micro mirror arrays." In: *Optics Express* 20.25, p. 27542. doi: 10.1364/oe.20.027542

Kauppinen, J., T. Kärkkäinen, and E. Kyrö (May 1978). "Correcting errors in the optical path difference in Fourier spectroscopy: a new accurate method." In: *Applied Optics* 17.10, p. 1587. doi: 10.1364/ao.17.001587

Kauppinen, J. and P. Saarinen (Jan. 1992). "Line-shape distortions in misaligned cube corner interferometers." In: *Appl. Opt.* 31.1, pp. 69–74. doi: 10.1364/AO.31.000069

Kerber, F., G. Nave, C. J. Sansonetti, P. Bristow, and M. R. Rosa (2007). *Vol. 364 - The Future of Photometric, Spectrophotometric and Polarimetric Standardization, ed C. Sterken, page 461*. Astronomical Society of the Pacific Conference Series. isbn: 978-1-58381-232-7

Kerr, J. (Nov. 1875). "A new relation between electricity and light: Dielectrified media birefringent." In: *The London, Edinburgh, and Dublin Philosophical Magazine and Journal of Science* 50.332, pp. 337–348. doi: 10.1080/14786447508641302

Knight, J. C., T. A. Birks, P. St. J. Russell, and D. M. Atkin (Oct. 1996). "All-silica single-mode optical fiber with photonic crystal cladding." In: *Optics Letters* 21.19, p. 1547. doi: 10.1364/ol.21.001547

Kodama, Y. and A. Hasegawa (May 1987). "Nonlinear pulse propagation in a monomode dielectric guide." In: *IEEE Journal of Quantum Electronics* 23.5, pp. 510–524. doi: 10.1109/jqe.1987.1073392

Kurucz, R. L. (1984). "Solar Flux Atlas from 296 to 1300 nm." In: *National Solar Observatory Atlas* 1

Lagrange, A.-M., M. Desort, and N. Meunier (Mar. 2010a). "Using the Sun to estimate Earth-like planets detection capabilities." In: *Astronomy and Astrophysics* 512, A38. doi: 10.1051/0004-6361/200913071

Lagrange, A.-M. et al. (June 2010b). "A Giant Planet Imaged in the Disk of the Young Star β Pictoris." In: *Science* 329.5987, pp. 57–59. doi: 10.1126/science.1187187

Lazarev, G., A. Hermerschmidt, S. Krüger, and S. Osten (2012). "LCOS spatial light modulators: trends and applications." In: *Optical Imaging and Metrology: Advanced Technologies*, pp. 1–29

Learner, R. C. M. and A. P. Thorne (Oct. 1988). "Wavelength calibration of Fourier-transform and emission and spectra with applications to Fe and I." In: *Opt. Soc. Am. B* 5.10, pp. 2045–2059. doi: 10.1364/JOSAB.5.002045

Learner, R. C. M., A. P. Thorne, I. Wynne-Jones, J. W.J. W. Brault, and M. C. Abrams (Oct. 1995). "Phase correction of emission line Fourier transform spectra." In: *J. Opt. Soc. Am. A* 12.10, pp. 2165–2171

Lesko, D. M. B., H. Timmers, S. Xing, A. Kowligy, A. J. Lind, and S. A. Diddams (Mar. 2021). "A six-octave optical frequency comb from a scalable few-cycle erbium fibre laser." In: *Nature Photonics* 15.4, pp. 281–286. doi: 10.1038/s41566-021-00778-y

Li, C.-H., A. J. Benedick, P. Fendel, A. G. Glenday, F. X. Kärtner, D. F. Phillips, D. Sasselov, A. Szentgyorgyi, and R. L. Walsworth (Apr. 2008). "A laser frequency comb that enables radial

velocity measurements with a precision of 1 cm s-1." In: *Nature* 452.7187, pp. 610–612. issn: 1476-4687. doi: 10.1038/nature06854

Lin, C. and R. H. Stolen (Feb. 1976). "New nanosecond continuum for excited-state spectroscopy." In: *Applied Physics Letters* 28.4, pp. 216–218. doi: 10.1063/1.88702

Liske, J. et al. (May 2008). "Cosmic dynamics in the era of Extremely Large Telescopes." In: *Monthly Notices of the Royal Astronomical Society* 386.3, pp. 1192–1218. doi: 10.1111/j.1365-2966.2008.13090.x

Lovis, C. and F. Pepe (2007). "A new list of thorium and argon spectral lines in the visible." In: *A&A* 468.3, pp. 1115–1121. issn: 1432-0746. doi: 10.1051/0004-6361:20077249

Manassah, J. T., R. R. Alfano, and M. Mustafa (Feb. 1985). "Spectral distribution of an ultrafast supercontinuum laser source." In: *Physics Letters A* 107.7, pp. 305–309. doi: 10.1016/0375-9601(85)90641-3

Marconi, A. et al. (Dec. 2020). "ELT-HIRES, the high resolution spectrograph for the ELT: the Phase A study and the path to construction." In: *Ground-based and Airborne Instrumentation for Astronomy VIII*. Vol. 11447. SPIE, p. 1144726. doi: 10.1117/12.2560489

Marcy, G. W. and K. J. Benitz (1989). "A search for substellar companions to low-mass stars." In: *The Astrophysical Journal* 344, pp. 441–453

Marcy, G. W. and R. P. Butler (Apr. 1992). "Precision radial velocities with an iodine absorption cell." In: *PASP* 104, p. 270. doi: 10.1086/132989

Marois, C., B. Macintosh, T. Barman, B. Zuckerman, I. Song, J. Patience, D. Lafreniere, and R. Doyon (Nov. 2008). "Direct Imaging of Multiple Planets Orbiting the Star HR 8799." In: *Science* 322.5906, pp. 1348–1352. doi: 10.1126/science.1166585

Martinez, O. E., J. P. Gordon, and R. L. Fork (Oct. 1984). "Negative group-velocity dispersion using refraction." In: *Journal of the Optical Society of America A* 1.10, p. 1003. doi: 10.1364/josaa.1.001003

Maslowski, P. et al. (Feb. 2016). "Surpassing the path-limited resolution of Fourier-transform spectrometry with frequency combs." In: *Phys. Rev. A* 93 (2), p. 021802. doi: 10.1103/PhysRevA.93.021802

Matos, L., D. Kleppner, O. Kuzucu, T. R. Schibli, J. Kim, E. P. Ippen, and F. X. Kaertner (July 2004). "Direct frequency comb generation from an octave-spanning, prismless Ti:sapphire laser." In: *Optics Letters* 29.14, p. 1683. doi: 10.1364/ol.29.001683

Mayor, M. and D. Queloz (1995). "A Jupiter-Mass Companion to a Solar-Type Star." In: *Nature* 378, pp. 355–359. doi: 10.1038/378355a0

Mayor, M. et al. (2003). "Setting new standards with HARPS." In: *The Messenger* 114, p. 20

McCracken, R. A., J. M. Charsley, and D. T. Reid (June 2017a). "A decade of astrocombs: recent advances in frequency combs for astronomy [Invited]." In: *Optics Express* 25.13, p. 15058. doi: 10.1364/oe.25.015058

McCracken, R. A., É. Depagne, R. B. Kuhn, N. Erasmus, L. A. Crause, and D. T. Reid (Mar. 2017b). "Wavelength calibration of a high resolution spectrograph with a partially stabilized 15-GHz astrocomb from 550 to 890 nm." In: *Optics Express* 25.6, p. 6450. doi: 10.1364/oe.25.006450

Mertz, L. (1966). "Auxiliary Computation for Fourier Spectrometry." In: *Infrared Physics* 7, pp. 17–23

– (Mar. 1967). "Rapid Scanning Fourier Transform Spectrometry." In: *Journal de Physique* Colloque C 2.supplement au 3-4, pp. C 2-87 - 2–91. doi: .org/10.1051/jphyscol:1967218

Meunier, N., A.-M. Lagrange, and M. Desort (Sept. 2010). "Reconstructing the solar integrated radial velocity using MDI/SOHO." In: *Astronomy and Astrophysics* 519, A66. doi: 10.1051/0004-6361/201014199

Mitschke, F. M. and L. F. Mollenauer (Oct. 1986). "Discovery of the soliton self-frequency shift." In: *Optics Letters* 11.10, p. 659. doi: 10.1364/ol.11.000659

Mogilevtsev, D., T. A. Birks, and P. St. J. Russell (Nov. 1998). "Group-velocity dispersion in photonic crystal fibers." In: *Optics Letters* 23.21, p. 1662. doi: 10.1364/ol.23.001662

Mollenauer, L. F., R. H. Stolen, and J. P. Gordon (Sept. 1980). “Experimental Observation of Picosecond Pulse Narrowing and Solitons in Optical Fibers.” In: *Physical Review Letters* 45.13, pp. 1095–1098. doi: 10.1103/physrevlett.45.1095

Morgner, U., R. Ell, G. Metzler, T. R. Schibli, F. X. Kärtner, J. G. Fujimoto, H. A. Haus, and E. P. Ippen (June 2001). “Nonlinear Optics with Phase-Controlled Pulses in the Sub-Two-Cycle Regime.” In: *Physical Review Letters* 86.24, pp. 5462–5465. doi: 10.1103/physrevlett.86.5462

Mou, Y. and J. W. Rabalais (July 2009). “Detection and Identification of Explosive Particles in Fingerprints Using Attenuated Total Reflection-Fourier Transform Infrared Spectromicroscopy.” In: *Journal of Forensic Sciences* 54.4, pp. 846–850. doi: 10.1111/j.1556-4029.2009.01060.x

Murphy, M. T. et al. (2007). “High-Precision Wavelength Calibration of Astronomical Spectrographs with Laser Frequency Combs.” In: *Monthly Notices of the Royal Astronomical Society* 380.2, pp. 839–847. issn: 1365-2966. doi: 10.1111/j.1365-2966.2007.12147.x

Muterspaugh, M. W., B. F. Lane, S. R. Kulkarni, M. Konacki, B. F. Burke, M. M. Colavita, M. Shao, W. I. Hartkopf, A. P. Boss, and M. Williamson (Oct. 2010). “The Phases Differential Astrometry Data Archive. V. Candidate Substellar Companions to Binary Systems.” In: *The Astronomical Journal* 140.6, pp. 1657–1671. doi: 10.1088/0004-6256/140/6/1657

Nave, G., F. Kerber, E. Den Hartog, and G. Lo Curto (July 2018). “The dirt in astronomy’s genie lamp: ThO contamination of Th-Ar calibration lamps.” In: *Observatory Operations: Strategies, Processes, and Systems VII*. Vol. 10704. SPIE, p. 1070407. doi: 10.1117/12.2312286

Nyquist, H. (Apr. 1928). “Certain Topics in Telegraph Transmission Theory.” In: *Transactions of the American Institute of Electrical Engineers* 47.2, pp. 617–644. doi: 10.1109/t-aiee.1928.5055024

Osterbrock, D. E., J. P. Fulbright, A. R. Martel, M. J. Keane, S. C. Trager, and G. Basri (Mar. 1996). “Night-Sky High-Resolution Spectral Atlas of OH and O2 Emission Lines for Echelle Spectrograph Wavelength Calibration.” In: *Publications of the Astronomical Society of the Pacific* 108, p. 277. doi: 10.1086/133722

Osterink, L. M. and J. D. Foster (Aug. 1968). “A Mode-Locked Nd:YAG Laser.” In: *Journal of Applied Physics* 39.9, pp. 4163–4165. doi: 10.1063/1.1656941

Pepe, F., M. Mayor, G. Rupprecht, G. Avila, P. Ballester, J.-L. Beckers, W. Benz, J.-L. Bertaux, F. Bouchy, B. Buzzoni, et al. (2002). “HARPS: ESO’s coming planet searcher. Chasing exoplanets with the La Silla 3.6-m telescope.” In: *Messenger* 110, pp. 9–14

Pepe, F. et al. (Jan. 2021). “ESPRESSO at VLT.” In: *Astronomy & Astrophysics* 645, A96. doi: 10.1051/0004-6361/202038306

Phillips, D. F. et al. (June 2012). “Calibration of an astrophysical spectrograph below 1 m/s using a laser frequency comb.” In: *Optics Express* 20.13, p. 13711. doi: 10.1364/oe.20.013711

Picqué, N. and T. W. Hänsch (Feb. 2019). “Frequency comb spectroscopy.” In: *Nature Photonics* 13.3, pp. 146–157. doi: 10.1038/s41566-018-0347-5

Porter, C. D. and D. B. Tanner (Mar. 1983). “Correction of phase errors in fourier spectroscopy.” In: *International Journal of Infrared and Millimeter Waves* 4.2, pp. 273–298. doi: 10.1007/bf01008607

Probst, R. A., G. Lo Curto, G. Ávila, A. Brucalassi, B.-L. Canto Martins, I. de Castro Leão, M. Esposito, …, and Y. Wu (Aug. 2016). “Relative stability of two laser frequency combs for routine operation on HARPS and FOCES.” In: *Ground-based and Airborne Instrumentation for Astronomy VI*. Vol. 9908. Proceedings of the SPIE, p. 990864. doi: 10.1117/12.2231434

Probst, R. A., T. Steinmetz, T. Wilken, G. K. L. Wong, H. Hundertmark, S. P. Stark, P. S. J. Russell, T. W. Hänsch, R. Holzwarth, and T. Udem (2013). “Spectral flattening of supercontinua with a spatial light modulator.” In: *Techniques and Instrumentation for Detection of Exoplanets VI*. Vol. 8864. Proceedings of the SPIE, 88641Z. doi: 10.1117/12.2036601

Probst, R. A., Y. Wu, T. Steinmetz, S. P. Stark, T. W. Hänsch, T. Udem, and R. Holzwarth (2015). "Spectrally flattened, broadband astronomical frequency combs." In: *2015 Conference on Lasers and Electro-Optics (CLEO)*. IEEE, pp. 1–2

Probst, R. A. et al. (July 2014). "A laser frequency comb featuring sub-cm/s precision for routine operation on HARPS." In: *Ground-based and Airborne Instrumentation for Astronomy V*. Ed. by Suzanne K. Ramsay, Ian S. McLean, and Hideki Takami. SPIE. doi: 10.1117/12.2055784

Probst, R. A. et al. (Feb. 2020). "A crucial test for astronomical spectrograph calibration with frequency combs." In: *Nature Astronomy* 4.6, pp. 603–608. doi: 10.1038/s41550-020-1010-x

Queloz, D., G. W. Henry, J. P. Sivan, S. L. Baliunas, J. L. Beuzit, R. A. Donahue, M. Mayor, D. Naef, C. Perrier, and S. Udry (Nov. 2001). "No planet for HD 166435." In: *Astronomy and Astrophysics* 379.1, pp. 279–287. doi: 10.1051/0004-6361:20011308

Quirrenbach, A., P. J. Amado, and et. al. (Aug. 2016). "CARMENES: an overview six months after first light." In: *Ground-based and Airborne Instrumentation for Astronomy VI*. Vol. 9908. Proceedings of the SPIE, p. 990812. doi: 10.1117/12.2231880

Quirrenbach, A. et al. (Oct. 2012). "CARMENES. I: instrument and survey overview." In: *Ground-based and Airborne Instrumentation for Astronomy IV*. Vol. 8446. SPIE, 84460R. doi: 10.1117/12.925164

Ranka, J. K., R. S. Windeler, and A. J. Stentz (2000). "Visible continuum generation in air–silica microstructure optical fibers with anomalous dispersion at 800 nm." In: *Opt. Lett.* 25.1, pp. 25–27. doi: 10.1364/OL.25.000025

Ravi, A. (2020). "Topics in precision astrophysical spectroscopy." PhD thesis. Harvard University, Graduate School of Arts &Sciences.

Ravi, A., M. Beck, D. F. Phillips, A. Bartels, D. Sasselov, A. Szentgyorgyi, and R. L. Walsworth (2018). "Visible-Spanning Flat Supercontinuum for Astronomical Applications." In: *Journal of Lightwave Technology* 36.22, pp. 5309–5315. doi: 10.1109/JLT.2018.2872423

Redfield, S., M. Endl, W. D. Cochran, and L. Koesterke (Jan. 2008). "Sodium Absorption from the Exoplanetary Atmosphere of HD 189733b Detected in the Optical Transmission Spectrum." In: *The Astrophysical Journal* 673.1, pp. L87–L90. doi: 10.1086/527475

Redman, S. L., J. E. Lawler, G. Nave, L. W. Ramsey, and S. Mahadevan (Aug. 2011). "The infrared spectrum of uranium hollow cathode lamps from 850nm to 4000nm: wavenumbers and line identifications from fourier transform spectra." In: *The Astrophysical Journal Supplement Series* 195.2, p. 24. issn: 1538-4365. doi: 10.1088/0067-0049/195/2/24

Reichert, J., R. Holzwarth, T. Udem, and T. W. Hänsch (1999). "Measuring the frequency of light with mode-locked lasers." In: *Optics communications* 172.1-6, pp. 59–68

Reiners, A., R. K. Banyal, and R. G. Ulbrich (Sept. 2014). "A Laser-Lock Concept to Reach cm/s-Precision in Doppler Experiments with Fabry-Perotrot Wavelength Calibrators." In: *Astronomy & Astrophysics* 569, A77, A77. doi: 10.1051/0004-6361/201424099

Reiners, A., J. L. Bean, K. F. Huber, S. Dreizler, A. Seifahrt, and S. Czesla (Jan. 2010). "Detecting Planets Around Very Low Mass Stars with the Radial Velocity Method." In: *The Astrophysical Journal* 710.1, 432â443. issn: 1538-4357. doi: 10.1088/0004-637x/710/1/432

Reiners, A., U. Lemke, F. Bauer, B. Beeck, and P. Huke (Oct. 2016a). "Radial velocity observations of the 2015 Mar. 20 eclipse." In: *Astronomy & Astrophysics* 595, A26. doi: 10.1051/0004-6361/201629088

Reiners, A., N. Mrotzek, U. Lemke, J. Hinrichs, and K. Reinsch (Feb. 2016b). "The IAG solar flux atlas: Accurate wavelengths and absolute convective blueshift in standard solar spectra." In: *Astronomy & Astrophysics* 587, A65. doi: 10.1051/0004-6361/201527530

Riley, W. J. (2008). *Handbook of Frequency Stability Analysis*. NIST

Rutkowski, L., P. Maslowski, A.C. Johansson, A. Khodabakhsh, and A. Foltynowicz (2016). "Optical Frequency Comb Fourier Transform Spectroscopy with Sub-Nominal Resolution." In: *Physics: Instrumentation and Detectors* arXiv. doi: arXiv:1612.04808

Saarinen, P. and J. Kauppinen (May 1992). "Spectral line-shape distortions in Michelson interferometers due to off-focus radiation source." In: *Appl. Opt.* 31.13, p. 2353

Sandage, A. (1962). “The Change of Redshift and Apparent Luminosity of Galaxies due to the Deceleration of Selected Expanding Universes.” In: *The Astrophysical Journal* 136, p. 319

Sanderson, R. B. and E. E. Bell (Feb. 1973). “Multiplicative Correction of Phase Errors in Fourier Spectroscopy.” In: *Applied Optics* 12.2, p. 266. doi: 10.1364/ao.12.000266

Sanford, R. F (1933). “On the Spectrum and Radial Velocity of U Monocerotis.” In: *The Astrophysical Journal* 77, p. 120

Sarmiento, L. F. et al. (Aug. 2014). “Characterizing U-Ne hollow cathode lamps at near-IR wavelengths for the CARMENES survey.” In: *Ground-based and Airborne Instrumentation for Astronomy V*. Vol. 9147. Proceedings of the SPIE, p. 914754. doi: 10.1117/12.2056501

Schäfer, S., E. W. Guenther, A. Reiners, J. Winkler, M. Pluto, and J. Schiller (July 2018). “Two Fabry-Pérots and two calibration units for CARMENES.” In: *Ground-based and Airborne Instrumentation for Astronomy VII*. Vol. 10702. SPIE, p. 1070276. doi: 10.1117/12.2315241

Schäfer, S., P. Huke, D. Meyer, and A. Reiners (Dec. 2020a). “Fiber-coupling of Fourier transform spectrographs.” In: *Ground-based and Airborne Instrumentation for Astronomy VIII*. Vol. 11447. SPIE, 114473Q. doi: 10.1117/12.2561599

Schäfer, S. and A. Reiners (2012). “Two Fabry-Perot Interferometers for High Precision Wavelength Calibration in the Near-Infrared.” In: *Proc. SPIE* 8446, pp. 844694-844694–8. doi: 10.1117/12.926232

Schäfer, S., K. Royen, A. Zapke, M. Ellwarth, and A. Reiners (Dec. 2020b). “Observing the integrated and spatially resolved Sun with ultra-high spectral resolution.” In: *Ground-based and Airborne Instrumentation for Astronomy VIII*. Vol. 11447. SPIE, 11447A9. doi: 10.1117/12.2560156

Schmidt, P. O., S. Kimeswenger, and H. U. Käufl (2007). “A new Generation of Spectrometer Calibration Techniques Based on Optical Frequency Combs.” In: *The 2007 ESO Instrument Calibration Workshop*, pp. 409–412. doi: 10.1007/978-3-540-76963-7_55

Schmidt, T. M. et al. (Feb. 2021). “Fundamental physics with ESPRESSO: Towards an accurate wavelength calibration for a precision test of the fine-structure constant.” In: *Astronomy & Astrophysics* 646, A144. doi: 10.1051/0004-6361/202039345

Schwab, C., J. Stuermer, Y. V. Gurevich, T. Fuehrer, S. K. Lamoreaux, T. Walther, and A. Quirrenbach (Sept. 2015). “Stabilizing a Fabry-Perot etalon to 3 cm/s for spectrograph calibration.” In: *Publications of the Astronomical Society of the Pacific* 127.955, pp. 880–889. doi: 10.1086/682879

Schwarz, G. (Mar. 1978). “Estimating the Dimension of a Model.” In: *The Annals of Statistics* 6.2. doi: 10.1214/aos/1176344136

Seemann, U. et al. (Aug. 2014). “Wavelength calibration from 1-5 µm for the CRIRES+high-resolution spectrograph at the VLT.” In: *Ground-based and Airborne Instrumentation for Astronomy V*. Vol. 9147. SPIE, 91475G. doi: 10.1117/12.2056668

Shannon, C. E. (Jan. 1949). “Communication in the Presence of Noise.” In: *Proceedings of the IRE* 37.1, pp. 10–21. doi: 10.1109/jrproc.1949.232969

Shimizu, F. (Nov. 1967). “Frequency Broadening in Liquids by a Short Light Pulse.” In: *Physical Review Letters* 19.19, pp. 1097–1100. doi: 10.1103/physrevlett.19.1097

Siegman, A. E. (1986). *Lasers*. Ed. by Aidan Kelly. University Science Books. doi: 0-935702-11-3

Snellen, I. A. G., R. J. de Kok, J. L. Birkby, B. Brandl, M. Brogi, C. Keller, M. Kenworthy, H. Schwarz, and R. Stuik (Mar. 2015). “Combining high-dispersion spectroscopy with high contrast imaging: Probing rocky planets around our nearest neighbors.” In: *Astronomy & Astrophysics* 576, A59. doi: 10.1051/0004-6361/201425018

Snellen, I. A. G., R. J. de Kok, E. J. W. de Mooij, and S. Albrecht (June 2010). “The orbital motion, absolute mass and high-altitude winds of exoplanet HD 209458b.” In: *Nature* 465.7301, pp. 1049–1051. doi: 10.1038/nature09111

Snyder, J. J. (1981). “An ultra-high resolution frequency meter.” In: *Thirty Fifth Annual Frequency Control Symposium*. IEEE, pp. 464–469

Spence, D. E., P. N. Kean, and W. Sibbett (Jan. 1991). “60-fsec pulse generation from a self-mode-locked Ti:sapphire laser.” In: *Optics Letters* 16.1, p. 42. doi: 10.1364/ol.16.000042

Stahl, O., A. Kaufer, and S. Tubbesing (1999). “The FEROS spectrograph.” In: *Optical and Infrared Spectroscopy of Circumstellar Matter*. Vol. 188, p. 331

Stoicheff, B. P. (Nov. 1963). “Characteristics of stimulated raman radiation generated by coherent light.” In: *Physics Letters* 7.3, pp. 186–188. doi: 10.1016/0031-9163(63)90377-9

Stolen, R. H. (1975). “Phase-matched-stimulated four-photon mixing in silica-fiber waveguides.” In: *IEEE Journal of Quantum Electronics* 11.3, pp. 100–103

Stolen, R. H., C. Lee, and R. K. Jain (Aug. 1984). “Development of the stimulated Raman spectrum in single-mode silica fibers.” In: *Journal of the Optical Society of America B* 1.4, p. 652. doi: 10.1364/josab.1.000652

Stone, J. (Feb. 1975). “cw Raman fiber amplifier.” In: *Applied Physics Letters* 26.4, pp. 163–165. doi: 10.1063/1.88100

Strassmeier, K. G., I. Ilyin, and M. Steffen (Apr. 2018). “PEPSI deep spectra I. The Sun-as-a-star.” In: *Astronomy & Astrophysics* 612, A44. doi: 10.1051/0004-6361/201731631

Stürmer, J., A. Seifahrt, C. Schwab, and J. L. Bean (June 2017). “Rubidium-traced white-light etalon calibrator for radial velocity measurements at the cm s-1 level.” In: *Journal of Astronomical Telescopes, Instruments, and Systems* 3.2, p. 025003. doi: 10.1117/1.jatis.3.2.025003

Takeda, M., H. Ina, and S. Kobayashi (1982). “Fourier-transform method of fringe-pattern analysis for computer-based topography and interferometry.” In: *JosA* 72.1, pp. 156–160

The Royal Swedish Academy of Sciences (Oct. 4, 2005). *New light on modern optics*. url: www.nobelprize.org/prizes/physics/2005/press-release/

Tiesinga, E., P. J. Mohr, D. B. Newell, and B. N. Taylor (2021). “CODATA recommended values of the fundamental physical constants: 2018.” In: *Reviews of Modern Physics* 93.2, p. 025010

Udalski, A., B. Paczynski, K. Zebrun, M. Szymanski, M. Kubiak, I. Soszynski, O. Szewczyk, L. Wyrzykowski, and G. Pietrzynski (2002). “The optical gravitational lensing experiment. Search for planetary and low-luminosity object transits in the galactic disk. Results of 2001 campaign.” In: *Acta Astronomica* 52.1, pp. 1–37

Udem, T., A. Huber, B. Gross, J. Reichert, M. Prevedelli, M. Weitz, and T. W. Hänsch (Oct. 1997). “Phase-Coherent Measurement of the Hydrogen 1S-2S Transition Frequency with an Optical Frequency Interval Divider Chain.” In: *Physical Review Letters* 79.14, pp. 2646–2649. doi: 10.1103/physrevlett.79.2646

Valenti, J. A., R. P. Butler, and G. W. Marcy (Oct. 1995). “Determining Spectrometer Instrumental Profiles Using FTS Reference Spectra.” In: *Publications of the Astronomical Society of the Pacific* 107, pp. 966–976

Vig, J. R., E. S. Ferre-Pikal, J. C. Camparo, L. S. Cutler, L. Maleki, W. J. Riley, S. R. Stein, C. Thomas, F. L. Walls, and J. D. White (1999). “IEEE standard definitions of physical quantities for fundamental frequency and time metrology-random instabilities.” In: *IEEE Standard* 1139, p. 1999

Walker, G. A. H. (Jan. 2012). “The first high-precision radial velocity search for extra-solar planets.” In: *New Astronomy Reviews* 56.1, pp. 9–15. doi: 10.1016/j.newar.2011.06.001

Walker, G. A. H., A. R. Walker, A. W. Irwin, A. M. Larson, S. Yang, and D. C. Richardson (Aug. 1995). “A Search for Jupiter-Mass Companions to Nearby Stars.” In: *Icarus* 116.2, pp. 359–375. doi: 10.1006/icar.1995.1130

Wallace, L., K. H. Hinkle, W. C. Livingston, and S. P. Davis (June 2011). “An Optical and Near-Infrared (2958–9250 Å) Solar Flux Atlas.” In: *The Astrophysical Journal Supplement Series* 195.1, p. 6. doi: 10.1088/0067-0049/195/1/6

Weiner, A. M. (2011). “Ultrafast optical pulse shaping: A tutorial review.” In: *Optics Communications* 284.15, pp. 3669–3692

Weiner, A. M., J. P. Heritage, and E. M. Kirschner (Aug. 1988). “High-resolution femtosecond pulse shaping.” In: *Journal of the Optical Society of America B* 5.8, p. 1563. doi: 10.1364/josab.5.001563

Werncke, W., A. Lau, M. Pfeiffer, K. Lenz, H.-J. Weigmann, and C.D. Thuy (Feb. 1972). “An anomalous frequency broadening in water.” In: *Optics Communications* 4.6, pp. 413–415. doi: 10.1016/0030-4018(72)90113-7

Wildi, F., F. Pepe, B. Chazelas, G. Lo Curto, and C. Lovis (Sept. 2011). “The performance of the new Fabry-Perot calibration system of the radial velocity spectrograph HARPS.” In: *Techniques and Instrumentation for Detection of Exoplanets V*. Vol. 8151. SPIE, 81511F. doi: 10.1117/12.901550

Wolszczan, A. and D. A. Frail (1992). “A Planetary System around the Millisecond Pulsar PSR1257 + 12.” In: *Nature* 355, pp. 145–147. doi: 10.1038/355145a0

Wu, H., F. Zhang, S. Cao, S. Xing, and X. Qu (May 2014). “Absolute distance measurement by intensity detection using a mode-locked femtosecond pulse laser.” In: *Opt. Express* 22.9, pp. 10380–10397. doi: 10.1364/OE.22.010380

Xu, L., C. Spielmann, A. Poppe, T. Brabec, F. Krausz, and T. W. Hänsch (1996). “Route to phase control of ultrashort light pulses.” In: *Optics letters* 21.24, pp. 2008–2010

Ycas, G. G. et al. (Mar. 2012). “Demonstration of on-sky calibration of astronomical spectra using a 25 GHz near-IR laser frequency comb.” In: *Optics Express* 20.6, p. 6631. doi: 10.1364/oe.20.006631

Zhang, Z., Z. You, and D. Chu (2014). “Fundamentals of phase-only liquid crystal on silicon (LCOS) devices.” In: *Light: Science & Applications* 3.10, e213

A

MANUFACTURER MEASUREMENTS

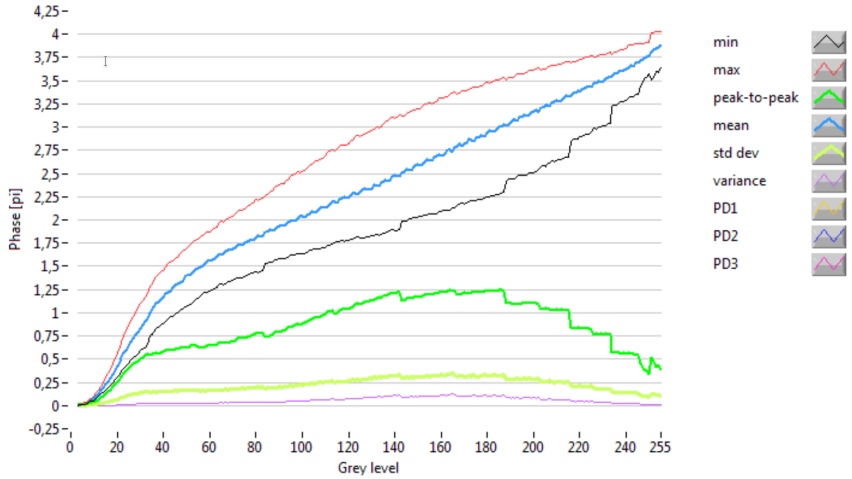

(a) 18-6 bitplane

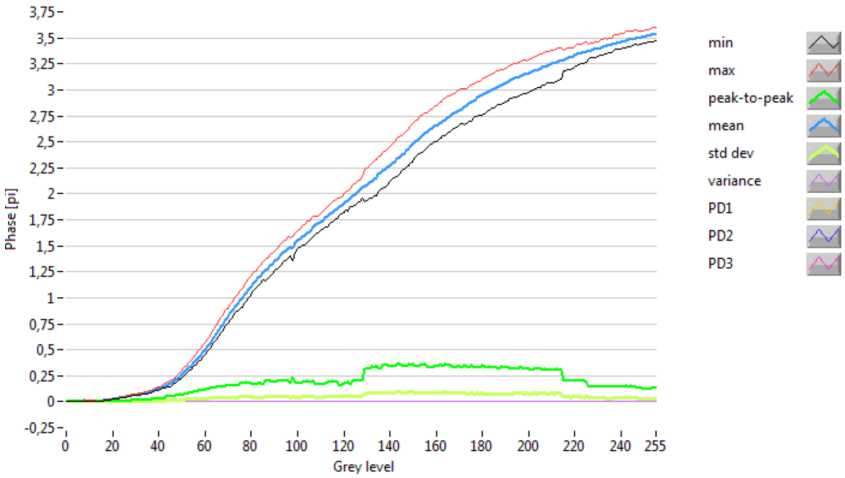

(b) 5-6 bitplane

Figure A.1: Measurements of the characteristics of the two different bitplanes. Particularly relevant are the mean (blue) curve, which shows the maximum achievable phase shift at 633 nm and the peak-to-peak (green) curve, showing how strongly the phase deviation varies over a single frame (Measurements from Holoeye).

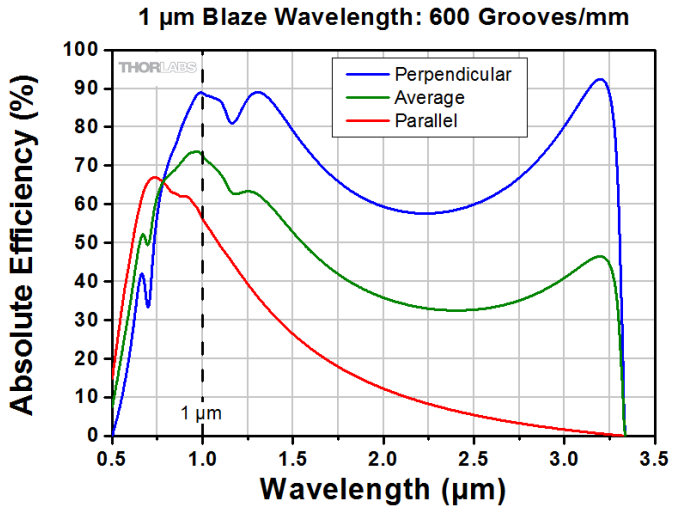

Figure A.2: Spectral efficiency of the ruled grating for the two polarization directions and unpolarized light in Littrow-configuration (Measurements from Thorlabs).

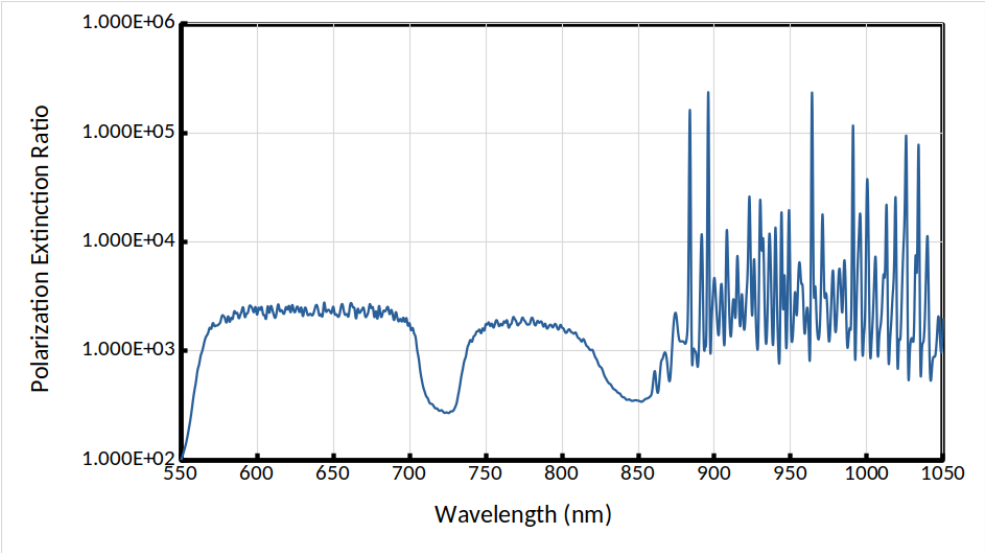

Figure A.3: Spectral extinction ratio for the transmission direction of the polarizing beam splitter PBS252 (Measurements from Thorlabs).

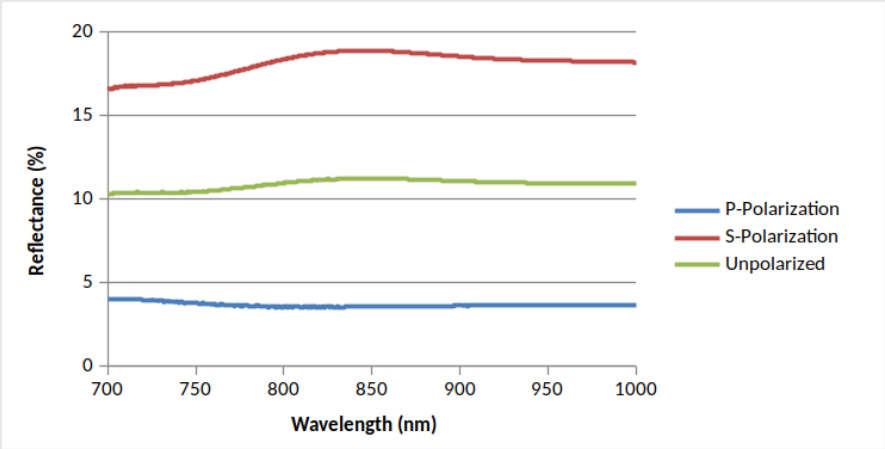

(a) Reflectance

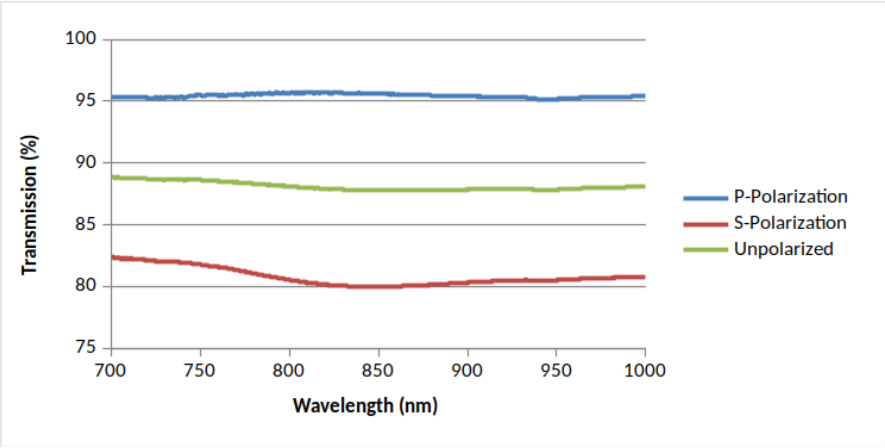

(b) Transmission

Figure A.4: Measurements of the typical reflectance and transmission values of the 90:10 beam splitter plate BSN11 for different polarization directions (Measurements from Thorlabs).

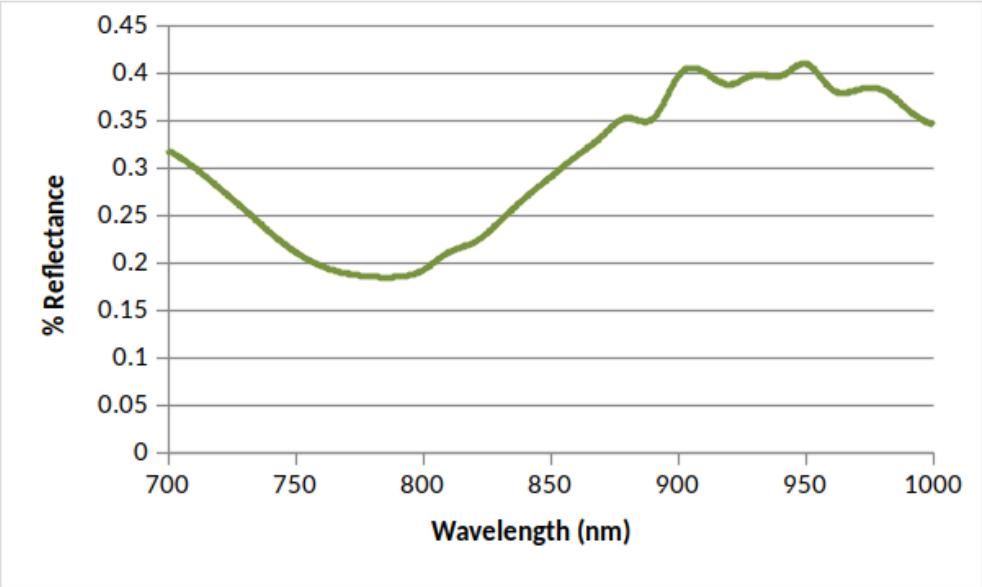

Figure A.5: Reflectance of the anti-reflection coating of the cylindrical lens ACY254-075-B (Measurements from Thorlabs).

DANKSAGUNGEN

Danke Philipp, für die gute Betreuung und Unterstützung, die Möglichkeit immer Fragen zu stellen und die stete Ermunterung auch komplexere Dinge selbst auszuprobieren und in Angriff zu nehmen.

Danke Ansgar, für das Ermöglichen der Promotion, für die gute Betreuung und das stets offene Ohr, für das Heranführen an wissenschaftliches Arbeiten und die vielen Hinweise zum Schreiben wissenschaftlicher Arbeiten.

Danke Claus, für den wertvollen Input bei den TACs und die Hilfe dabei, das Ziel im Auge zu behalten.

Danke Mathias und Sebastian, für das bereitwillige Teilen eurer Expertise und für eure geduldigen Antworten auf viele Fragen.

Danke David, für die Arbeit an den Gammakurven für den SLM.

Danke Julian, für die vielseitige Hilfe und Unterstützung bei allen möglichen Aufgaben.

Danke Johann und Peter, für die Konstruktionen verschiedenster spezieller Bauteile, die die optischen Aufbauten so sehr vereinfacht haben.

Danke an das gesamte Werkstatt-Team für die schnelle und präzise Herstellung dieser Bauteile.

Danke Heiko, für jedwede Hilfe egal ob mit IT oder 3D-Druck.

Danke Dennis, Max, Paddy und Sebastian für das Korrekturlesen dieser Arbeit.

Danke Ann-Charline für das Korrekturlesen, für die viele Geduld und Hilfe dabei meine Gedanken auch zu Papier zu bringen.